



Theoretical and Experimental Study of Structural Aspects of 2-acetyl-2-methyl Benzothiazoline

K. LAXMI

Department of Chemistry, Chaitanya Bharathi Institute of Technology (CBIT),
Gandipet, Hyderabad-500 075, India.

*Corresponding author E-mail: klaxmi_chm@cbit.ac.in

<http://dx.doi.org/10.13005/ojc/400315>

(Received: February 02, 2024; Accepted: May 04, 2024)

ABSTRACT

Schiffs base 2-acetyl-2-methyl benzothiazoline (AMBT) is prepared by the condensation of acetyl acetone with 2-aminothiophenol. The compound has been characterised by IR, ¹H NMR spectra. HyperChem 7.5 software is used to study the structural features of AMBT and theoretical data so obtained is compared with experimental spectral data. Quantum mechanical calculations were done by HyperChem 7.5 software. Ab Initio method is used for geometry optimization. Quantum calculation of molecular electronic structure and variables for Quantitative structure-activity relationships (QSAR) of AMBT were determined by applying Austin Model 1, or AM1 a semi-empirical method. Computation of HOMO and LUMO frontier orbital energies is also performed. The relationship between the structure and energy gap is studied. pH-metry studies confirm that in AMBT Molecule there exists only one proton which is dissociable.

Keywords: AMBT, Energy gap, Quantitative structure-activity relationships.

INTRODUCTION

As benzothiazolines contain two different hetero atoms linked by carbon in the ring many studies were made. It is reported that Benzothiazolines possess biological activities¹⁻⁴ and preparation of benzothiazolines is done by condensation of 2-aminothiophenol with aldehyde and ketones⁵. Derivatives of Benzothiazolines form an predominant group of ligands which can be bidentate as well as multidentate⁶⁻⁸.

In natural medicines there is wide application of carbon-nitrogen bonds and in various

natural bioactive products and pharmaceuticals. the structure of heterocycles is studied This is in view of their significant analgesics, antidiabetic, antiallergic, anticonvulsant, antidepressant, antimicrobials and antifungal properties. N-C-S group of benzothiazolines is known for pharmacological activity and is of appreciable chemotherapeutic interest. In order to understand the physiological activity of such compound a study is made on its capacity of chelation with traces of metal ions⁹⁻¹¹. The acidity of 2-acetyl-2-methyl benzothiazoline (AMBT), is estimated by determining its pKa value. In the present paper the structural properties of AMBT Fig.1 are described and a detailed discussion



of experimental data and theoretical data obtained by applying Hyperchem 7.5 Software¹² is done.

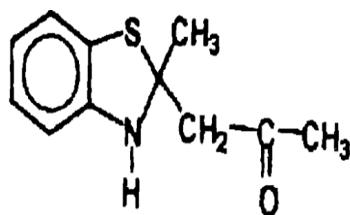


Fig. 1. Structure of 2-acetyl-2-methyl benzothiazoline

EXPERIMENTAL

Synthesis of 2-acetyl-2-methyl benzothiazoline

Synthesis of AMBT is done using the following procedure. Acetyl acetone 0.05 mole was melted in 15 mL methanol and cooled in an ice bath. The precooled 2-amino thio phenol (0.05 mole) dissolved in 10 mL methanol is added to the acetyl acetone solution. This solution is stirred briefly and was allowed to stand overnight, at -5°C to -10°C . The prismatic crystals so formed were collected by filtration and washed with chilled methanol and further recrystallised from warm methanol, m.p. 85°C - 86°C (lit. 85°C - 86°C).

Physical measurements

Employing Perkin elmer model no 435 infrared spectrometer, IR spectrum of 2-acetyl-2-methyl benzothiazoline (AMBT) was documented in KBr phase. Using Bruker WH-270 MHz FT-NMR spectrometer ¹H spectra of AMBT was analysed in CDCl_3 and DMSO-d_6 using tetra methylsilane (TMS) as standard. Micro Mass spectrometer of V.G70-70H type administering at 70eV using direct inlet system is used for recording Mass spectra of AMBT.

Potentiometric method using pH-metric titration technique as adopted by Irving-Rossotti is employed to determine proton dissociation constant (pK_a) of AMBT. Measurement of pH is done employing Digital pH meter. Digisun model: DI-707., by making use of combination or pH electrode. With the application of Hyperchem tools the molecule AMBT is constructed¹², and then by exercising Ab Initio optimized method of single point AM1. semi-empirical calculation the geometry optimization is executed.

RESULTS AND DISCUSSIONS

As per potentiometric titration data it is clear that in ligand 2-acetyl-2-methyl benzothiazoline

(AMBT) only one dissociable proton is present. Calculations indicated that the pK_a value of AMBT is 8.79 for titration carried out in Methanol : Water (50:50)% (v/v) medium at temperature of 303 K and at ionic strength of 0.1 M KNO_3 .

The acidified ligand titration curve runs below the acid curve indicating non protonation of ligand. From the calculation of n_A^- values it is evident that there is one dissociable proton. (Table 1, Figure 2).

Table 1: Data for obtaining Proton-Ligand stability constants of AMBT in Methanol: Water (50:50)% (v/v) medium at temperature of 303 K and at ionic strength of 0.1 M KNO_3

Ligand/Medium	pH	n_A^-	$\log 1-n_A^-/n_A^-$
AMBT	8.4	0.74	-0.43
50%v/vmethanol-water medium	8.5	0.68	-0.32
	8.6	0.62	-0.21
	8.7	0.56	-0.1
	8.8	0.49	0.02
	8.9	0.44	0.13
	9	0.37	0.23
	9.1	0.3	0.34

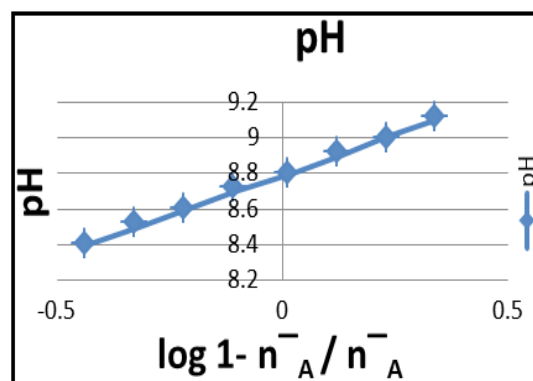


Fig. 2. Plots of $\log 1-n_A^-/n_A^-$ Vs pH of AMBT in Methanol: Water (50:50)% (v/v) medium at temperature of 303 K and at ionic strength of 0.1 M KNO_3

As the base is added enolisation of the ligand readily takes place and proton is dissociated from enol form in the pH region of 8 to 9. The dissociation constant value is comparable with the dissociation constant of acetyl acetone.

From the above titration data any ring cleavage or oxidative ring expansion are not evident. The proton from SH group in open ring Schiff base dissociates indicating release of one more proton, if ring cleavage occur to form tautomer of open ring type. There is no proof for such process for AMBT in solution under given experimental condition and hence the formation of open ring tautomer even at high pH is ruled out.

Formation of Binary metal chelates in solution

In the present study evidence for the interaction of various metal ions with AMBT has been obtained from the data of pH metric titrations of the AMBT ligand solution in presence and absence of metal ions.

The interaction of various bivalent metal ions Co(II) and Ni(II) ions with AMBT have been carried out by following Irving Rosotti pH titration technique in Methanol : Water (50:50)% (v/v) medium at temperature of 303 K and at ionic strength of 0.1 M KNO₃. The following observations indicate the complex formation (Figures 3 & 4, Tables 2 & 3).

1. On addition of metal ion solution to AMBT ligand solution, a decrease in pH is observed thereby suggesting the release of proton on coordination.
2. M(II)-AMBT titration curves lie below the AMBT ligand titration curve indicating complexation.
3. $-n$ values gradually increase and equilibrium is attained during titration.

The M(II)-AMBT stability constants indicate the extent of interaction between the metal ion and the compound AMBT.

Table 2: Data for obtaining formation curves of Co (II)-AMBT in Methanol:Water (50:50)% (v/v) medium at temperature of 303 K and at ionic strength of 0.1 M KNO₃

Co (II)-AMBT		
$-n$	$\log 1-n/n$	pL
0.78	-0.55	8.06
0.65	-0.27	8.3
0.59	-0.16	8.5
0.45	0.08	8.61
0.34	0.29	8.81
0.26	0.41	8.92

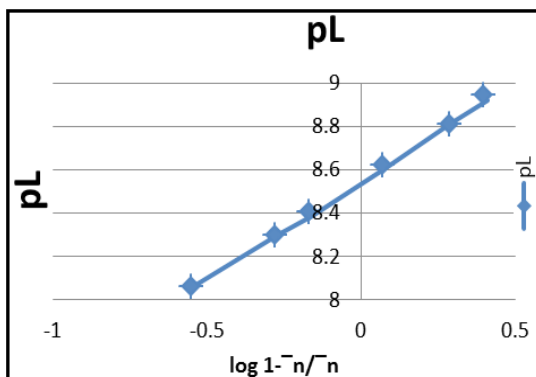


Fig. 3. Plots of pL Vs $\log 1-n/n$ of Co (II)-AMBT in Methanol : Water (50:50)% (v/v) medium at temperature of 303 K and at ionic strength of 0.1 M KNO₃

Table 3: Data for obtaining formation curves of Ni(II)-AMBT in Methanol:Water (50:50)% (v/v) medium at temperature of 303 K and at ionic strength of 0.1 M KNO₃

$-n$	Ni (II)-AMBT $\log 1-n/n$	pL
0.72	-0.41	8.32
0.67	-0.31	8.38
0.54	-0.07	8.52
0.36	0.25	8.71
0.27	0.43	8.81
0.15	0.75	9.01

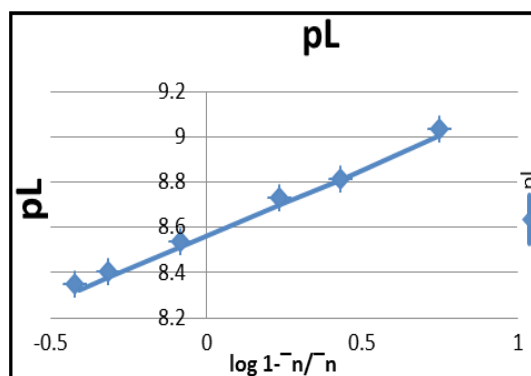


Fig. 4. Plots of pL Vs $\log 1-n/n$ of Ni (II)-AMBT in Methanol : Water (50:50)% (v/v) medium at temperature of 303 K and at ionic strength of 0.1 M KNO₃

With the help of Hyperchem tools the molecule 2-acetyl-2-methyl benzothiazoline was built and then by implementing Ab Initio method geometry optimization was done (Figs. 1 to 3). with the application of single point AM1 method approximation the spectral data is generated.

Certain input parameters like molecular geometry value, bond lengths values and values of coulombic, resonance influence the calculations performed to some extent. Prospective view and active conformation of 2-acetyl-2-methyl benzothiazoline (AMBT) as given by Hyperchem is shown in Figure 5 & 6.

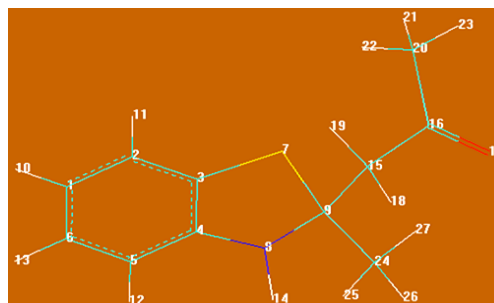


Fig. 5. Prospective view of 2-acetyl-2-methyl benzothiazoline (AMBT)

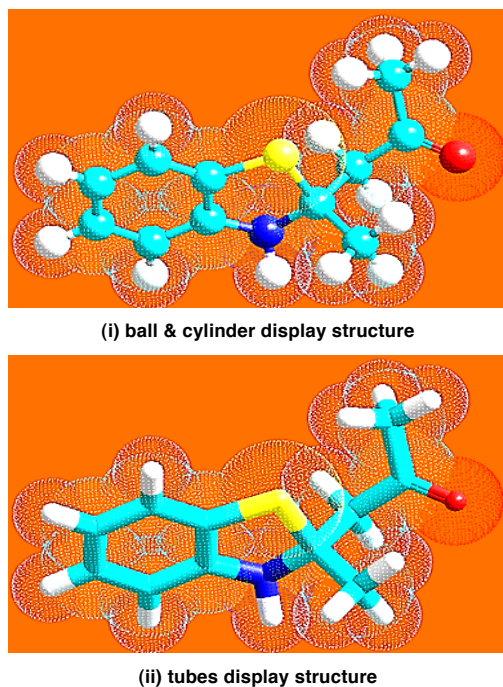


Fig. 6. Active conformations of 2-acetyl-2-methyl benzothiazoline

Hyperchem data of 2-acetyl-2-methyl benzothiazoline (AMBT) indicates that Single point energy as per Austin Model 1, or AM1 optimization is -2801.26 with Gradient of 1.618 and symmetry of C1.

IR spectrum of 2-acetyl-2-methyl benzothiazoline

A comparative study is done for experimentally obtained IR spectral data of AMBT with the theoretical spectral IR data of AMBT as obtained by applying Ab Initio method of optimization of Austin Model 1, or AM1 a semi-empirical method.

IR spectrum of AMBT shows peaks at 3277 cm^{-1} which is assigned to -NH stretching vibration. In addition to these the aromatic C-H stretching frequencies and C-H (-CH₃) stretching frequencies are observed at 3148 cm^{-1} and 2936 cm^{-1} respectively. The band observed at 1797 cm^{-1} is assigned to C=O. Aromatic stretching vibrations are observed at 1569-1498 cm^{-1} .

Table 4: IR Spectral data of AMBT (Experimental)*AMBT (semiempirical AM1)

Compound	ν_{NH}	ν_{CHaro}	$\nu_{\text{C-H(-CH}_3\text{)}}$	$\nu_{\text{C=O(-CO-CH}_3\text{)}}$	$\nu_{\text{C=C}}$	$\nu_{\text{N-H}}$ bending g	$\nu_{\text{S-H}}$
AMBT* Experimental	3277 cm^{-1}	3148 cm^{-1}	2936 cm^{-1}	1943 cm^{-1}	1797 cm^{-1}	1606, 1590 cm^{-1}	1345, 1283 cm^{-1}
AMBT(semiempirical AM1)	3417.5 cm^{-1}	3206-3185 cm^{-1}	3031 cm^{-1}	2059 cm^{-1}	1794 cm^{-1}	1568, 1521 cm^{-1}	1336, 1279 cm^{-1}

IR spectrum of AMBT generated by semi empirical single point AM1 (Fig. 7) method 11-17 indicates that -NH stretching vibration is obtained at 3417.5 cm^{-1} . Aromatic C-H stretching frequencies are observed at 3206-3185 cm^{-1} and C-H(-CH₃) stretching frequencies at 3031 cm^{-1} .

A good acceptance of experimental IR spectral data with theoretical IR data is perceived (Table 4)

¹HNMR spectrum of 2-acetyl-2-methyl benzothiazoline

Comparison of experimental ¹HNMR spectral data of AMBT with the theoretical NMR spectral data obtained by Austin Model 1, or AM1 a semi-empirical method is made.

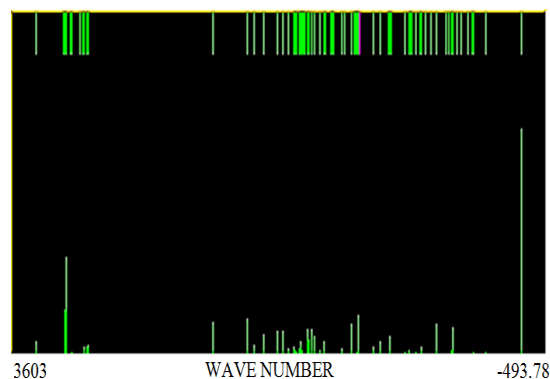


Fig. 7. IR spectrum of 2-acetyl-2-methyl benzothiazoline-experimental

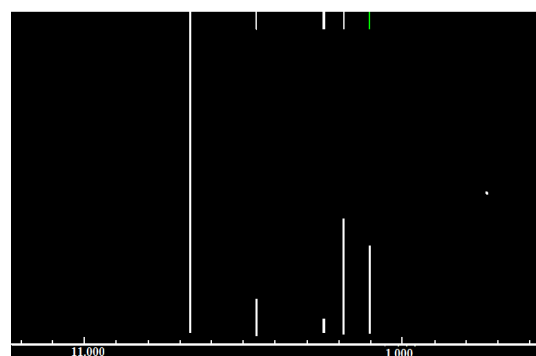


Fig. 8. ¹HNMR spectrum of 2-acetyl-2-methyl benzothiazoline (AMBT) as given by Austin Model 1, or AM1 a semi-empirical method

Table 5: Shielding data of 2-acetyl-2-methyl benzothiazoline (AMBT) as given by Austin Model 1, or AM1 a semi-empirical method

Index	1-10(H)	1-11(H)	1-12(H)	1-13(H)	1-14(H)	1-18(H)	1-19(H)	1-21(H)	1-22(H)	1-23(H)	1-25(H)	1-26(H)	1-27(H)
Shielding	16.271	16.271	16.271	16.271	18.368	20.476	20.476	21.118	21.118	21.118	21.898	21.898	21.898
Shift	7.68	7.68	7.68	7.68	5.583	3.475	3.475	2.833	2.833	2.833	2.053	2.053	2.053
Tau	2.32	2.32	2.32	2.32	4.417	6.525	6.525	7.167	7.167	7.167	7.947	7.947	7.947

Table 6: Coupling data of AMBT as given by Austin Model 1, or AM1 a semi-empirical method

Coupling	1-10(H)	1-11(H)	1-12(H)	1-13(H)	1-14(H)	1-18(H)	1-19(H)	1-21(H)	1-22(H)	1-23(H)	1-25(H)	1-26(H)	1-27(H)
1-10(H)	0	5.042	5.042	5.042	0.116	0.016	0.016	0	0	0	0.014	0.014	0.014
1-11(H)	5.042	0	5.042	5.042	0.116	0.016	0.016	0	0	0	0.014	0.014	0.014
1-12(H)	5.042	5.042	0	5.042	0.116	0.016	0.016	0	0	0	0.014	0.014	0.014
1-13(H)	5.042	5.042	5.042	0	0.116	0.016	0.016	0	0	0	0.014	0.014	0.014
1-14(H)	0.116	0.116	0.116	0.116	0	-0.397	-0.397	-0.042	-0.042	-0.042	-0.233	-0.233	-0.233
1-18(H)	0.016	0.016	0.016	0.016	-0.397	0	4.396	-0.602	-0.602	-0.602	-0.076	-0.076	-0.076
1-19(H)	0.016	0.016	0.016	0.016	-0.397	4.396	0	-0.602	-0.602	-0.602	-0.076	-0.076	-0.076
1-21(H)	0	0	0	0	-0.042	-0.602	-0.602	0	0.302	0.302	0.004	0.004	0.004
1-22(H)	0	0	0	0	-0.042	-0.602	-0.602	0.302	0	0.302	0.004	0.004	0.004
1-23(H)	0	0	0	0	-0.042	-0.602	-0.602	0.302	0.302	0	0.004	0.004	0.004
1-25(H)	0.014	0.014	0.014	0.014	-0.233	-0.076	-0.076	0.004	0.004	0.004	0	2.158	2.158
1-26(H)	0.014	0.014	0.014	0.014	-0.233	-0.076	-0.076	0.004	0.004	0.004	2.158	0	2.158
1-27(H)	0.014	0.014	0.014	0.014	-0.233	-0.076	-0.076	0.004	0.004	0.004	2.158	2.158	0

The experimental ¹H NMR spectral data of the AMBT in CDCl₃ recorded signal at 2.15 ppm (δ 3H, s, CH₃), 2.9 ppm (δ 3H, s, CH₃), 3.2 ppm (δ 2H, q, CH₂) and a peak at 5.4 ppm is attributable to NH. The multiplet recorded at 6.55–7.18 ppm corresponds to aromatic protons. This experimental data is in good concurrence with the data of theoretical method as obtained by semiempirical AM1 method, as given the following table ¹H NMR spectral data of the AMBT as recorded by semiempirical AM1 method¹¹⁻¹⁷ (Fig. 8, Tables 5 & 6) shows a peak at 2.833 ppm which is attributed to three protons of -CH₃ i.e

1-21(H), 1-22(H), 1-23(H) and a peak at 2.053 ppm due to three protons of one more -CH₃ i.e ¹⁻²⁵(H), 1-26(H), 1-27(H). Apart from this peak observed at 5.58 ppm is due to NH and 7.68 ppm multiplet is due to protons aromatic ring.

From the above comparative study (Table 7) it is clear that for 2-acetyl-2-methyl benzothiazoline (AMBT) there is good agreement between experimentally obtained ¹H NMR spectral data and spectral data obtained by semiempirical single point AM1 method.

Table 7: ¹H NMR Spectral data of AMBT (Experimental)*/AMBT (semiempirical AM1)

Compound	δ 4H, m, aromCH	δ -1H, s, NH	δ 2H, q, CH ₂	δ 3H, s, CH ₃	δ 3H, s, CH ₃
AMBT (Experimental)*	6.55–7.18 ppm	5.4 ppm	3.2 ppm	2.9 ppm	2.15 ppm
AMBT (semiempirical AM1)	7.68 ppm				
	1-10(H)	5.58 ppm	3.475 ppm	2.833 ppm	2.053 ppm
	1-11(H)	1-14(H)	1-18(H)	1-21(H)	1-25(H)
	1-12(H)		1-19(H)	1-22(H)	1-26(H)
	1-13(H)			1-23(H)	1-27(H)

Interpretation of Quantitative structure activity relationship studies (QSAR studies) and Molecular properties of AMBT

Empolying single point AM1 method QSAR properties of AMBT were determined. These include properties like surface area, volume, hydration energy,

log P, refractivity, polarisability, mass, total energy etc. (Table. 8). Molecular descriptors commonly used in quantitative structure activity relationship (QSAR) studies were computed¹⁸⁻²¹. This study amounts to analyse the relationship between structural descriptors of compounds and their physicochemical

properties and biological activities. Binding energy of AMBT is about -2801.26 kcal/mol as determined by AM1 calculation. AMBT has heat of formation of -5.186 kcal/mol and this shows its exothermic nature. Dipole moment value is 2.145 D. A good acceptance between trends of the theoretical molecular properties with the experimental results is observed²⁵⁻²⁷.

Table 8: QSAR and Molecular properties of 2-acetyl-2-methyl benzothiazoline (AMBT)

QSAR and Molecular properties of AMBT	
Overall Net charge	0.00 e
approx Surface area	347.31 °A ²
Grid Surface area	394.87 °A ²
Volume	629.72 °A ³
Energy of Hydration	-3.15 kcal/mol
Log P value	2.76
value of Refractivity	61.28 °A ³
value of Polarisability	23.27 °A ³
Molar Mass	207.29 amu
Total energy	-53244.06 kcal/mol
Energy of Binding	-2801.26 kcal/mol
value of Heat of formation	-5.186 kcal/mol
value of Electronic energy	-308034.78 kcal/mol
value of Nuclear energy	254790.72 kcal/mol
Dipole moment value	2.145 D
X Dipole	-2.043 D
Y Dipole	-0.5018 D
Z Dipole	-0.4209 D
RMS gradient	1.618 kcal/°A mol
X Gradient	0.3382 kcal/°A mol
Y Gradient	1.0999 kcal/°A mol
Z Gradient	1.1378 kcal/°A mol

Quantum Chemical Studies of 2-acetyl-2-methyl benzothiazoline (AMBT)

Quantum chemical calculations were employed for studying donor and acceptor properties of AMBT molecule. Fig. 9 &10 indicate the values of E_{HOMO} (energy of the highest occupied molecular orbitals), E_{LUMO} (energy of the lowest unoccupied molecular orbitals) and $E_{LUMO-HOMO}$ (the energy gap between them) for AMBT molecule.

Energies of Frontier molecular orbital E_{HOMO} and E_{LUMO} ²²⁻²⁴ is one of the most important factor for assessing the extent to which a chemical species is reactive. Value of E_{HOMO} is measure for ability of a molecule to donate electrons while the E_{LUMO} value indicates tendency of molecule for accepting electrons.

Hence high value of E_{HOMO} is an indication of inclination of AMBT molecule for donation of electron(s) to a suitable molecule which can accept electrons and which is provided with empty molecular orbital possessing low energy.

The values of E_{HOMO} is -8.179 eV, E_{LUMO} is 0.1067 eV and $E_{LUMO-HOMO}$ of 2-acetyl-2-methyl benzothiazoline (AMBT) is recorded to be -8.0723 eV. The correlation of static first hyperpolarizability and energy gap is considered. AMBT has a reduced $E_{LUMO-HOMO}$ energy gap indicating its significant donor character and this enables the compound for nonlinear optical applications.

The highest occupied molecular orbitals (HOMO) in AMBT, are localized on the, N-H bonds of the molecule (Fig. 9). while the lowest unoccupied molecular orbitals (LUMO) are present on the C=O of acetyl group, N-H, and aromatic C=C bonds of AMBT (Figure 10).

Ligand AMBT is considered as a potential donor molecule as well as acceptor molecule as HOMO and LUMO frontier orbitals are concentrated on all groups.

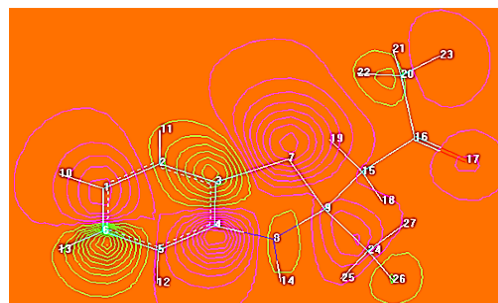


Fig. 9. HOMO (Highest occupied molecular orbital) of 2-acetyl-2-methyl benzothiazoline (AMBT) $E_{HOMO} = -8.179$ eV

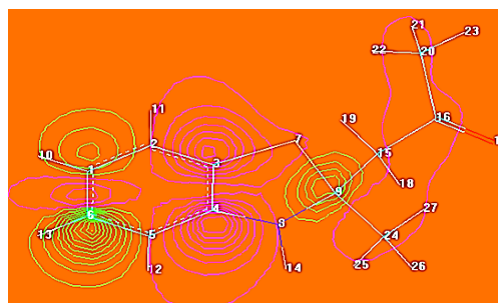


Fig. 10. LUMO (Lowest unoccupied molecular orbital) of 2-acetyl-2-methyl benzothiazoline (AMBT) $E_{LUMO} = 0.1067$ eV

$E_{LUMO-HOMO}$ gap (Frontier molecular orbital energy gap) namely (E_g) is indication of chemical activity of the molecule. In the present study $E_{LUMO-HOMO}$ gap of 2-acetyl-2-methyl benzothiazoline (AMBT) molecule as determined by Hyperchem is

8.2857 eV. As the value of $E_{LUMO-HOMO}$ gap (E_g) of AMBT is higher²⁵⁻²⁶ it indicates that there is smaller delocalization of electrons.

Total charge density of AMBT- Molecular graph

Charge density is defined as the electric charge measured per unit surface area, or per unit volume of a object or field. The charge density value indicates the amount of stored charge for a definite field. It is estimated in forms of volume, area, or length.

Semi-empirical methods of HyperChem include only the valence charge density but not inner-shell electrons. An illustration of areas around the molecule with equal electron probability density is obtained by electron density surface. Molecular graph²⁸ of AMBT showing total charge density is given in Fig. 11. This indicates the size of AMBT molecule and its tendency for electrophilic attack.



Fig. 11. Molecular graph of AMBT showing total charge density

Total spin density of AMBT-Molecular graph

Electron density is called as Spin density with respect to free radicals. Total spin density is difference of total electron density of electrons of two different spins. Employing Hyperchem software it is possible to estimate Spin density and can be displayed. This is possible for chemical systems with unpaired electrons. Molecular graph²⁷ of AMBT showing total spin density is given in Figure 12.

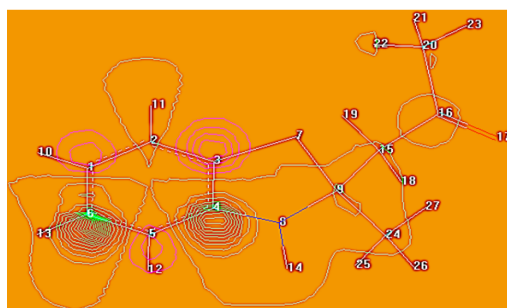


Fig. 12. Molecular graph of AMBT showing total spin density

Electrostatic potential of AMBT

The amount of work done for moving a unit charge from a reference point to a specific point without any acceleration inside the field is Electrostatic potential. Electrostatic potential is also known as electric field potential, electric potential, or potential drop.

Applying the routine MNDO and Polak–Ribiere conjugated gradient algorithm semi-empirical calculations were carried and the program MNDO is employed to perform semi-empirical computations. In AMBT molecule nucleophilic site is indicated by the areas close to the carbon atom and these are shown as green regions.

With the help of molecular electrostatic potential (MEP) it can be established that the reactive sites are present towards reactants which are positively or negatively charged. From this the possibility of presence of H-bonding and structure–activity relationships²⁸ in AMBT molecule are also established.

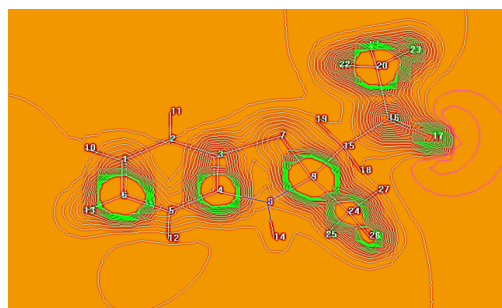


Fig. 13. Molecular graph of AMBT showing electrostatic potential

A strong correlation of electrostatic potential, electronegativity, partial charges, and dipole moment in AMBT is confirmed from Quantum chemical calculations. The relative polarity of a molecule is strongly recognized by molecular electrostatic potential plot of AMBT (Figure 13).

CONCLUSION

In this study structural data, ab initio and electronic and vibrational contribution to polarizabilities of 2-acetyl-2-methyl benzothiazoline (AMBT) were investigated. A valid knowledge of geometrical structure of AMBT is established from these numerical simulations. Theoretical study of Compound AMBT is performed applying Hyperchem 7.5 software and the results so obtained

were compared with Experimental data. A good agreement of experimental IR and NMR spectral data with theoretical spectral data obtained by using hyperchem is observed. Presence of only one dissociable proton in AMBT is indicated from the results obtained by Potentiometric titrations. Application of Hyperchem 7.5 software in determining QSAR properties and obtaining molecular graphs is well demonstrated in this Paper.

ACKNOWLEDGMENT

This research did not receive any specific grant from funding agencies in the public, commercial, or not-for-profit sectors.

Conflict of interest

The author declare that we have no conflict of interest.

REFERENCES

1. Radiation-Responsive Benzothiazolines as Potential Cleavable Fluorogenic Linkers for Drug Delivery, Dr. Wei Tuo, Dr. Jean-Philippe Renault, Aashini Rajpal, Dr. Serge Pin, IDr. Frédéric Taran, 28 March 2023., <https://doi.org/10.1002/chem.202300358>.
2. Sadiq R.; Musaddiq S.; Iqbal F.; Kanwal S.; Perveen S. Neuroprotective effects of 2-(2-thienyl) benzothiazoline on gross motor skill deficits in rotenone induced rat model of Parkinson's disease., *Pak J Pharm Sci.*, **2022**, 35(2), 435-440. PMID: 35642397.
3. Coudert P.; Couquelet J.; Sudre O.; Bastide J. Synthesis and analgesic activity of new spiro-derivatives of benzothiazoline., *J Pharm Belg.*, **1988**, 43(4), 258-62. French. PMID: 3236198.
4. Sharma K.; Singh RV.; Fahmi N. Palladium(II) and platinum(II) derivatives of benzothiazoline ligands: Synthesis, characterization, antimicrobial and antispermatogenic activity. *Spectrochim Acta A Mol Biomol Spectrosc.*, **2011** Jan;78(1):80-7. doi: 10.1016/j.saa.2010.08.076. Epub 2010 Oct 16. PMID: 20951633.
5. Fu Y.; Wang JY.; Zhang D.; Chen YF.; Gao S.; Zhao LX.; Ye F. Solvent-Free Synthesis and Safener Activity of Sulfonylurea Benzothiazolines., *Molecules.*, **2017**, 22;22(10), 1601. doi: 10.3390/molecules22101601. PMID: 28937640; PMCID: PMC6151413.
6. Teoh S.G., *Acta Cryst.*, **1991**, C47, 1347.
7. Zhu C.; Saito K.; Yamanaka M.; Akiyama T. Benzothiazoline: versatile hydrogen donor for organocatalytic transfer hydrogenation. *Acc Chem Res.*, **2015**, 17;48(2), 388-98. doi: 10.1021/ar500414x. Epub 2015 Jan 22. PMID: 25611073.
8. Mary, Y.S.; Yalcin, G.; Mary, Y. S., Spectroscopic, quantum mechanical studies, ligand protein interactions and photovoltaic efficiency modeling of some bioactive benzothiazolinone acetamide analogs. *Chem. Pap.*, **2020**, 74, 1957–1964. <https://doi.org/10.1007/s11696-019-01047-7>.
9. Garg, A.; Tandon, J. P. Mössbauer and other spectral studies of Fe(III) complexes of benzothiazolines., *Proc. Indian Acad. Sci. (Chem. Sci.)*, **1988**, 100, 463–468. <https://doi.org/10.1007/BF02841121>.
10. Zhou, J.W.; Li, Y.T.; Tang, Y. W., UV-Vis spectroscopic study of the solvatochromism and chelating reaction of a benzothiazoline merocyanine in mixed solvents., *J Solution Chem.*, **1995**, 24, 925–933. <https://doi.org/10.1007/BF00973446>.
11. Santes, V.; Rojas-Lima, S.; Santillan, R., Synthesis and Study of Isomeric Benzo[1,4]oxazines and Benzothiazolines by NMR Spectroscopy and X-ray Crystallography. *Monatsh. Fur Chem.*, **1999**, 130, 1481–1486. <https://doi.org/10.1007/s007060050307>.
12. HyperChem Software, Hypercube Inc Florida Science and Technology Park, 1115 Street, Gainesville, Florida, 326001, USA., **2006**, 12.
13. Mahajan, K.; Swami, M. & Singh, R.V. Microwave synthesis, spectral studies, antimicrobial approach, and coordination behavior of antimony(III) and bismuth(III) compounds with benzothiazoline., *Russ J Coord Chem.*, **2009**, 35, 179–185. <https://doi.org/10.1134/S1070328409030038>.
14. a. Padmaja A.; Laxmi K and Sarala Devi Ch., *J. Indian Chem. Soc.*, **2011**, 88, 183-187.
b. Padmaja A.; Aliya Begum.; Raghavaiah P and Sarala Devi Ch., *Indian J. Chem.*, **2011**, 50B, 326-329.
15. Laxmi K.; Bhargavi G.; Sireesha B and Sarala Devi Ch., *Bull. Chem. Soc. Ethiop.*, **2006**, 20(1), 161-166 [16].
16. Srinivas Reddy G.; Sireesha B.; Laxmi K and Sarala Devi Ch., *Bull. Pure Appl. Sci.*, **2005**, 24C,(1-2), 57-61.

17. Laxmi K and Sarala Devi Ch., *J. Electrochem Soc., India.*, **2000**, 49-2, 85-88.
18. Hansch C.; Leo A and Hoekman DH, Exploring QSAR, Fundamentals and applications in Chemistry and Biology., American Chemical Society Washington ,DC, USA., **1995**.
19. Srivastava A.K.; Jaiswal M.; Archana and Srivastava A., *Oxid. Commun.*, **2009**, 32, 55.
20. Chen, J.; Qian, L.; Shen, Y., A QSAR study and molecular design of benzothiazole derivatives as potent anticancer agents., *Sci. China Ser. B-Chem.*, **2008**, 51, 111–119. <https://doi.org/10.1007/s11426-007-0107-8>.
21. Mohapatra RK.; Dhama K.; El-Arabey AA.; Sarangi AK.; Tiwari R.; Emran TB.; Azam M.; Al-Resayes SI.; Raval MK.; Seidel V.; Abdalla M. Repurposing benzimidazole and benzothiazole derivatives as potential inhibitors of SARS-CoV-2: DFT, QSAR, molecular docking, molecular dynamics simulation, and in-silico pharmacokinetic and toxicity studies., *J King Saud Univ Sci.*, **2021**, 33(8), 101637. doi: 10.1016/j.jksus.2021.101637. Epub 2021 Oct 7. PMID: 34642560; PMCID: PMC8496942.
22. Sivaprakash S.; Prakash S.; Mohan S.; Sujin P. Jose.; Quantum chemical studies and spectroscopic investigations on 2-amino-3-methyl-5-nitropyridine by density functional theory., *Heliyon.*, **2019**, 5, 7., e02149,ISSN 2405-8440,<https://doi.org/10.1016/j.heliyon.2019.e02149>.
23. Maciej Spiegel.; Current Trends in Computational Quantum Chemistry Studies on Antioxidant Radical Scavenging Activity., *J Chem Inf Model.*, **2022**, 62(11), 2639-2658,DOI: 10.1021/acs.jcim.2c00104.
24. Ebenso EE.; Isabirye DA.; Eddy NO. Adsorption and quantum chemical studies on the inhibition potentials of some thiosemicarbazides for the corrosion of mild steel in acidic medium., *Int J Mol Sci.*, **2010**, 15;11(6), 2473-98. doi: 10.3390/ijms11062473. PMID: 20640164; PMCID: PMC2904928.
25. HyperChem Software, Hypercube Inc Florida Science and Technology Park,1115 Street, Gainesville,Florida,326001,USA., **2006**, 12.
26. Kumer, A.; Sarker, M. N., & Paul, S. The theoretical investigation of HOMO, LUMO, thermophysical properties and QSAR study of some aromatic carboxylic acids using HyperChem programming., *Int. J. Chem. Technol.*, **2019**, 3(1), 26-37. <https://doi.org/10.32571/ijct.478179>.
27. Joshi, B. D.; Mishra, R.; Tandon, P.; Oliveira, A. C. & Ayala, A. P. Quantum chemical studies of structural, vibrational, NBO and hyperpolarizability of ondansetron hydrochloride., *J. Mol. Struct.*, **1058**, 31–40. <https://doi.org/10.1016/j.molstruc.2013.10.062> (2014).

SwissADME Predictions of Pharmacokinetics and Drug-Likeness Properties of Atenolol

K. Laxmi

Professor of Chemistry Department of Chemistry, Chaitanya Bharathi Institute of Technology (CBIT), Gandipet,
Hyderabad -500 075, India Email ID: klaxmi_chm@cbit.ac.in

ABSTRACT

In the present paper Absorption, Distribution, Metabolism and Excretion (ADME) properties of Atenolol were presented employing Swiss ADME web tool. Atenolol obeys Lipinski's rule of five which is specified as drug likeness test. ADME properties of atenolol were appreciated by operating with SwissADME which is simple, accurate and powerful method. Atenolol exhibited good brain penetration and good GIT absorption

Keywords: Atenolol, SwissADME, drug discovery, Lipinski's rule of five

INTRODUCTION

Atenolol is a beta-blocker (Fig 1) used in managing hypertension (high blood pressure) and chronic angina (chest pain) and thereby reduces the risk of death after heart attack¹⁻³. By administering the drug Atenolol the amount of work to be done by heart muscle to push the blood through body will be reduced. As a result the heart's demand for oxygen is decreased and the symptoms of heart attack are managed.

At present computer aided reckoning of ADME (Absorption, Distribution, Metabolism and Excretion) of drugs is of considerable interest. This enabled to implement information which is revealing and trustworthy before experimentation.

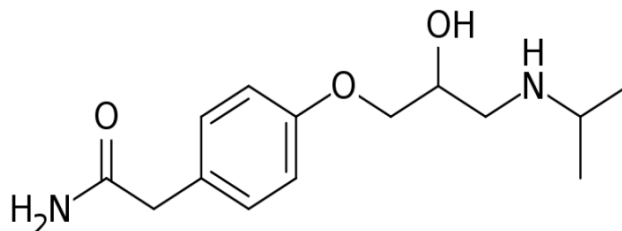


Fig 1. Structure of Atenolol

MATERIALS AND METHODS

Swiss institute of bioinformatics (<http://www.sib.swiss>) provided SwissADME software (www.swissadme.ch). Individual ADME behaviors of the compound is determined in Google web server that presents the page of Submission of SwissADME. A molecular sketcher built on Chem Axons Marvin JS (<http://www.chemaxon.com>) is employed to draw and edit 2D chemical structures. On right hand side of the submission page, the structure is transmitted and this constitutes the actual input for computation. Input molecule is defined by simplified molecular input line entry system (SMILES) and the results are learned in the form of tables, graphs and also an excel spread sheet. SwissADME gives a provision for output file consisting of one panel for each molecule (Fig.2). All the information of the molecule is obtained as a clear output and can be exported⁴.

Swiss ADME web tool furnishes with powerful predictive analytical tools physicochemical properties, pharmacokinetics, drug-likeness and medicinal chemistry friendliness^{5,6}. Swiss ADME also gives provision for new skilled technique of BOILED-Egg model⁷ which is efficacious for good interpretation of results.

Table 1. General Characteristics of Atenolol

General Characteristics of Atenolol	
molecule	Atenolol
Pubchem ID	2249
Molecular formula	C ₁₄ H ₂₂ N ₂ O ₃
Canonical SMILES	O=C(N)Cc1ccc(cc1)OCC(O)CNC(C)C
Molecular weight	266.341 g·mol ⁻¹

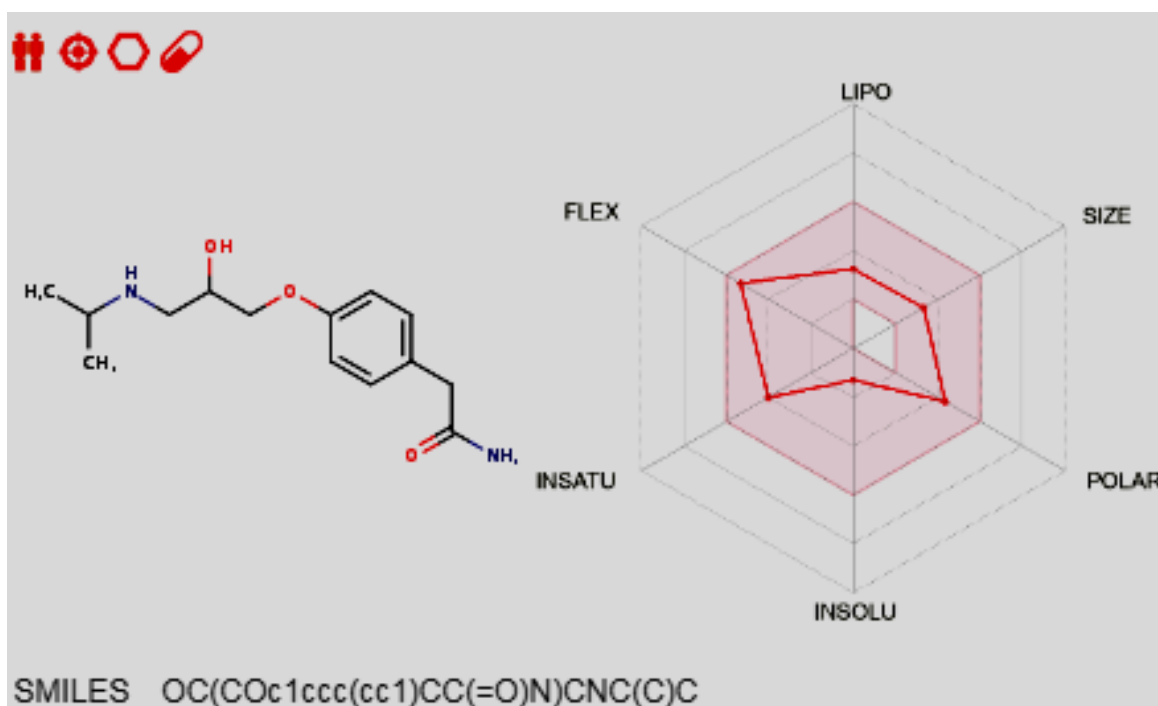


Fig.2 Schematic diagram of swiss ADME Software in webpage for Atenolol

Physicochemical properties of Atenolol

In this section using open babel version 2.3.0 the values of molecular and physicochemical characteristics were computed^{8,9}. This includes molecular formula, molecular weight, number of heavy atoms, number of aromatic heavy atoms, fraction csp³, number of rotatable bonds, number of H-bond acceptors, number of H-bond donors, molar refractivity, TPSA (Tables 1&2).

For determining PSA (molecular polar surface area) called TPSA (Topological PSA) a new method has been developed. This involves calculation of the summation of the tabulated surface contributions of polar fragments¹⁰. Physicochemical properties of Atenolol were presented in Table 2.

Table 2. Physicochemical properties of Atenolol

Physicochemical properties of Atenolol	
Formula	C ₁₄ H ₂₂ N ₂ O ₃
Molecular weight	266.34 g/mol
Num. heavy atoms	19
Num. arom. heavy atoms	6
Fraction Csp ³	0.045
Num. rotatable bonds	8
Num. H-bond acceptors	4
Num. H-bond donors	3
Molar Refractivity	73.61
TPSA	84.58 Å ²

Lipophilicity of Atenolol

Lipophilicity property of the compounds illustrate a prime role for molecular discovery activities in different fields¹¹⁻¹³. lipophilicity is quantitatively described as the partition coefficient between n-octanol and water system¹⁴. Classic log P predictors are classified into two types

1. This involves split of molecular structures in to molecular fragments known as fragmental approach or atomic approach eg. ALOGP^{15,16}, XLOGP^{17,18}.

2. second one involves molecules description based on count of specific atoms or groups eg. MLOGP (Moriguchi et al., 1992 and Moriguchi et al., 1994),

A hybrid technique is SILICOS-IT which is a combined method of molecular fragments and topological parameters¹⁴. Classic log P values of Atenolol predicted by SwissADME applying above methods are given in Table 3.

Table 3. Lipophilicity of Atenolol

Lipophilicity of Atenolol	
Log Po/w (iLOGP)	2.17
Log Po/w (XLOGP3)	0.16
Log Po/w (WLOGP)	0.45
Log Po/w (MLOGP)	0.69
Log Po/w (SILICOS-IT)	1.52
Consensus Log Po/w	1

Water solubility of Atenolol

SwissADME employs two methods for predicting the water solubility¹⁹⁻²¹ 1. One method involves the execution of ESOL model. In this method the Solubility class follows Log S Scale: Insoluble<-10 poorly<-6, moderately<-4 soluble<-2 very<0<-10 poorly<-6, moderately<-4 soluble< 2very<0 <highly)

2. the second method adapted from Ali et al, 2012 follows Solubility class of Log S Scale: Insoluble<-10 poorly<-6, moderately<-4 soluble< 2very<0<highly) Ali et al, 2012. The fundamental general solubility equation is differing in both the methods. The fundamental difference between the two methods is general solubility equation.²²



Log S values of Atenolol as predicted by ESOL model and Ali model were found to be -1.3 and -1.49 respectively. For Atenolol correlation of Log S values as given by ESOL model and Ali model is observed.

3. Apart from these two methods, SwissADME expanded third predictor which was executed by SILICOS-IT, for which the scale of Solubility class: Log S Scale: Insoluble<-10 poorly<-6, moderately<-4 soluble<-2 very<0<highly). All values are predicted by SwissADME as log S which is decimal logarithm of the molar solubility in water. log S value of Atenolol as predicted by SILICOS-IT is -3.29 (Table 4.)

Table 4. Water solubility of Atenolol

Water solubility of Atenolol	
(ESOL)	-1.3
Solubility	1.34e-01 mg/ml ; 5.04e-02 mol/l
Class	very soluble
Log S (Ali)	-1.49
Solubility	8.55e+00 mg/ml ; 3.21e-02 mol/l
Class	Very soluble
Log S (SILICOS-IT)	-3.29
Solubility	1.36e-01 mg/ml ; 5.11e-04 mol/l
Class	Soluble

Pharmacokinetics of Atenolol

The pharmacokinetics and drug likeness of Atenolol performed using SwissADME showed a high level of GI absorption. Atenolol is not the substrates for P-gp

The Swiss ADME model for Atenolol indicated “No” thereby inferring that drug Atenolol has greater probability to be non-substrate of P-gp (Table 5). It also indicates “No” for other factors suggesting that Atenolol is non-inhibitor²³⁻²⁵ of Cytochrome P 450 isoenzymes (CYP1A2, CYP2c9, CYP2C19, CYP2D6 and CYP3A4).

Table 5. Pharmacokinetics parameters of Atenolol

Pharmacokinetics of Atenolol	
GI absorption	High
BBB permeant	No
P-gp substrate	No
CYP1A2 inhibitor	No
CYP2C19 inhibitor	No
CYP2C9 inhibitor	No
CYP2D6 inhibitor	No
CYP3A4 inhibitor	No
Log Kp (skin permeation)	-7.81 cm/s



Log K_p is the skin permeability coefficient which is a multiple linear regression. If the value of Log K_p is more negative where K_p is expressed in cm/s, the molecule is considered to be, less skin permeant. SwissADME of Atenolol molecule showed Log K_p value of -7.81 cm/s and hence it is considered to be of less skin permeation.

Medicinal Chemistry of Atenolol

Medicinal chemists in their endeavours of drug discovery will focus on the results of this section of medicinal Chemistry as given by SwissADME. Pan Assay Interference compounds (PAINS) are molecules that show potent response in assays irrespective of the protein targets. These compounds were found to be active in other assays, considered as the source of starting points to explore more further²⁶⁻²⁹. SwissADME analysis did not assign any PAINS alert for atenolol molecule.

According to Brenk rule compounds which are smaller, less hydrophobic and not obeying “Lipinski’s rule of 5” can show Leadlikeness. Compound Atenolol does not follow Brenk’s rule and failed Leadlikeness as interpreted by SwissADME (Table 6).

In Atenolol the number of hydrogen-bond donors and acceptors to fewer being 4 and 3 respectively and the number of heavy atoms is only 19. This indicates that Atenolol is one of the compound with limited complexity having 8 rotatable bonds and one ring system and such compounds are considered to be medicinal.

Table 6. Medicinal Chemistry of Atenolol

Medicinal Chemistry of Atenolol	
PAINS	0 alert:
Brenk	0 alert
Leadlikeness	No;1 violations: Rotors>7
Synthetic accessibility	2.51

Drug likeness of Atenolol

The possibility of molecule to be used as an oral drug concerning to bioavailability is evaluated as Drug likeness. This feature is specified as red distorted hexagon within pink shade as obtained for Atenolol (fig.2) Swiss ADME allows filtering process for excluding peculiar molecules which are not suitable with an acceptable pharmacokinetics profile³⁰.

Table 7. Druglikeness parameters of Atenolol

Druglikeness of Atenolol	
Lipinski	Yes; 0 violations
Veber	Yes
Egan	Yes
Muegge	Yes
Bioavailability Score	0.55

SwissADME section provides provision for five filters each based on different rule and each with properties of diversified range which can define the molecule as drug like. A colonial rule of five is Lipinski (Pfizer) filter executed with Veber, Egan and Muegge methods (Table 7). In the output panel as given above no violation from any rule is noticed.

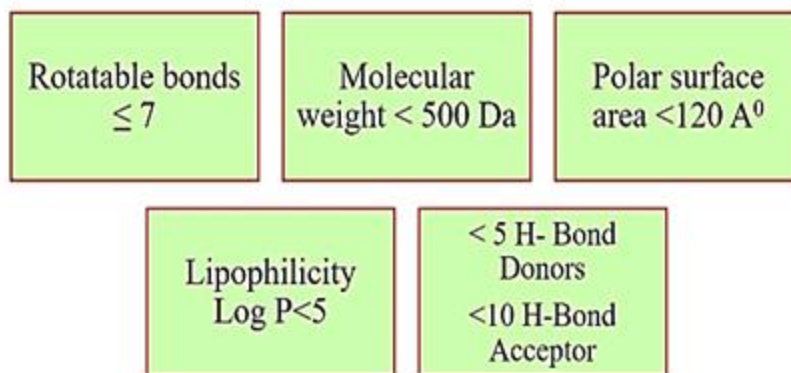


Fig 3. Good In vivo Drug absorption and Permeation Lipinski's rule of 5

Atenolol followed the filtered rule of Lipinski's rule of 5 as invoked in the SwissADME satisfying all the above requirements (fig.3) and no the violation shown. Hence Atenolol is considered as an efficient in vivo Drug.

BOILED-Egg model of Atenolol

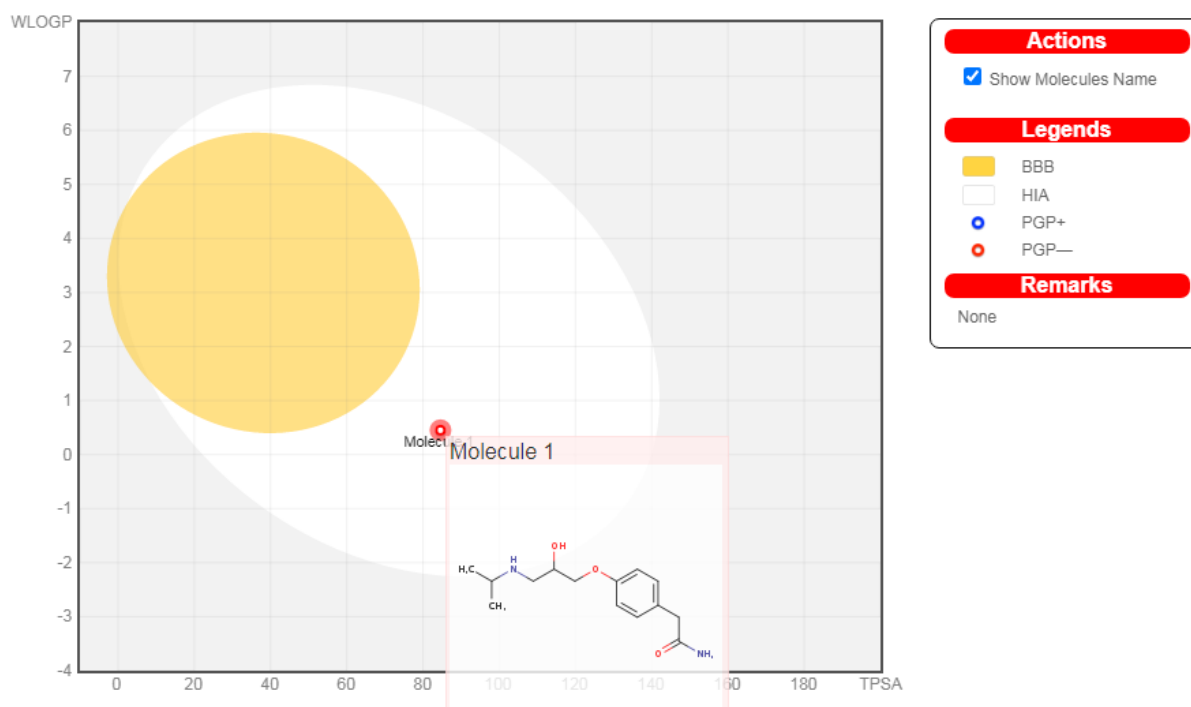


Fig 4: Schematic representation of perceptive evaluation of passive gastrointestinal absorption (HIA) and Brain penetration (BBB) with Atenolol molecules in the WLOGP-versus-TPSA using BOILED-Egg.

Evaluation of passive gastrointestinal absorption (HIA) and brain penetration (BBB) for Atenolol molecule is done by employing BOILED-Egg model³¹⁻³⁶. In this the high probability for passive absorption by GIT is indicated by white region and the high probability of brain penetration is denoted by yellow region (yolk). Apart from this blue coloured points are for molecules predicted to be effluated from the central nervous system by the P-glycoprotein P-gp (PGP+), while red coloured points are for molecules predicted not to be effluated from the central nervous system by the P-glycoprotein. In the present study the molecule of Atenolol is in the region outside the prediction site(Fig 4). Atenolol molecule is found to be present in white region of the BOILED-Egg thereby indicating high passive absorption of GIT and it is denoted red dot specifying non-substrate of P-gp.

CONCLUSION

In this research article a computational approach to statistical learning is given by focusing on the algorithmic and numeric motivations. In the present study a web tool SwissADME is used to appraise therapeutic potential of compound Atenolol. The relationships between various predictive models along with predictions for both brain and intestinal permeation are obtained. Evaluation of biophysical parameters like lipophilicity, drug likeness, water solubility and medicinal chemistry of Atenolol is done by applying SwissADME. Acquisition of knowledge of ADME properties further affirms that Atenolol can be employed both as in vitro and in vivo prescription drug.

REFERENCES

- [1]. Tomiyama H, Yamashina A (2014). "Beta -Blockers in the Management of Hypertension and/or Chronic Kidney Disease". *International Journal of Hypertension*. **2014**: 919256. doi:10.1155/2014/919256. PMC 3941231. PMID 24672712.
- [2]. DiNicolantonio JJ, Fares H, Niazi AK, Chatterjee S, D'Ascenzo F, Cerrato E, et al. (2015). "β-Blockers in hypertension, diabetes, heart failure and acute myocardial infarction: a review of the literature". *Open Heart*. **2** (1): e000230. doi:10.1136/openhrt-2014-000230. PMC 4371808. PMID 25821584
- [3]. Wiysonge CS, Bradley HA, Volmink J, Mayosi BM, Opie LH (January **2017**). "Beta-blockers for hypertension". *The Cochrane Database of Systematic Reviews*. **1** (1): CD002003. doi:10.1002/14651858.CD002003.pub5. PMC 5369873. PMID 28107561.
- [4]. Egan WJ, Merz KM, Baldwin JJ. Prediction of Drug Absorption Using Multivariate Statistics. *J. Med. Chem.* 2000; 43(21):3867-3877.
- [5]. Ndombera FT, Pharmacokinetic, Maiyoh GKK, Vivian CT. Physicochemical and Medicinal Properties of N-Glycoside Page 2 of 8 Anti-Cancer Agent more Potent than 2-Deoxy-D-Glucose in Lung Cancer Cells. *Cancer Sci Res Open Access*. 2019; 6(1):1-8.
- [6]. Lipinski CA, Lombardo F, Dominy BW, Feeney PJ. Experimental and computational approaches to estimate solubility and permeability in drug discovery and development settings. *Adv Drug Deliv Rev*. 2001; 46(1 3):3-26.
- [7]. Daina A, Zoete V. A BOILED-Egg to Predict Gastrointestinal Absorption and Brain Penetration of Small Molecules. *Chem Med Chem*. 2016; 11:1117 1121.
- [8]. Daina Antoine, Olivier Michielin, Vincent Zoete. SwissADME: a free web tool to evaluate pharmacokinetics, drug likeness and medicinal chemistry friendliness of small molecules. *Nature - Scientific Reports*. 2017; 7:42717.1-13.
- [9]. O'Boyle NM et al. Open Babel: An open chemical toolbox. *J. Chem inform*. 2011; 3: 33.
- [10]. Ertl Peter, Bernhard Rohde, Paul Selzer. Fast Calculation of Molecular Polar Surface Area as a Sum of Fragment Based Contributions and Its Application to the Prediction of Drug Transport Properties. *J. Med. Chem.* 2000; 43:3714-3717.
- [11]. Leeson PD, Springthorpe B. The influence of drug-like concepts on decision-making in medicinal chemistry. *Nat Rev Drug Discov*. 2007; 6:881-90
- [12]. Testa B, Crivori P, Reist M et al. The influence of lipophilicity on the pharmacokinetic behavior of drugs: concepts and examples. *Perspect Drug Discov Des*. 2000; 19:179-210.
- [13]. Arnott JA, Planey SL. The influence of lipophilicity in drug discovery and design. *Expert Opin. Drug Discov*. 2012; 7:863-875.
- [14]. Daina Antoine, Olivier Michielin, Vincent Zoete. iLOGP: A Simple, Robust, and Efficient Description of n Octanol/ Water Partition Coefficient for Drug Design Using the GB/SA Approach. *J of Chem Info and Modelling*. 2014; 54(12):3284-3301.
- [15]. Ghose AK, Crippen GM. Atomic physicochemical parameters for three-dimensional structure-directed quantitative structure-activity relationships. I. Partition coefficients as a measure of hydrophobicity. *J. Comput. Chem*. 1986; 7:565-577.
- [16]. Ghose AK, Viswanadhan VN, Wendoloski JJ. Prediction of hydrophobic (lipophilic) properties of small organic molecules using fragmental methods: An analysis of ALOGP and CLOGP methods. *J. Phys. Chem. A*. 1998; 102:3762-3772.
- [17]. Wang R, Fu Y, Lai L. A new atom-additive method for calculating partition coefficients. *J. Chem. Inf. Model*. 1997; 37:615-621.
- [18]. Cheng T, Zhao Y, Li X, Lin F, Xu, Y, Zhang X et al. Computation of octanol-water partition coefficients by guiding an additive model with knowledge. *J. Chem. Inf. Model*. 2007; 47:2140-2148.
- [19]. Lachman LH, Lieberman, Kanig JL. *The Theory and Practice of Industrial Pharmacy*, Lea & Febiger, 3rd edition, 1986.



- [20]. 43. Savjani KT, Gajjar AK, Savjani JK. Drug solubility: importance and enhancement techniques. *ISRN Pharm*, 2012, 195727.
- [21]. 44. Amidon GL, Lennernas H, Shah VP, Crison JR. A theoretical basis for a biopharmaceutical drug classification: the correlation of in vitro drug product dissolution and in vivo bioavailability," *Pharmaceutical Research*. 1995; 12(3):413-420.
- [22]. Yalkowsky SH, Valvani SC. Solubility and partitioning I: Solubility of nonelectrolytes in water. *J Pharm Sci*. 1980; 69:912-922.
- [23]. Lipinski CA, Lombardo F, Dominy BW, Feeney PJ. Experimental and computational approaches to estimate solubility and permeability in drug discovery and development settings. *Adv Drug Deliv Rev*. 2001; 46(1 3):3-26.
- [24]. Montanari F, Ecker GF. Prediction of drug-ABC transporter interaction-Recent advances and future challenges. *Adv. Drug Deliv. Rev*. 2015; 86:17-26.
- [25]. Ogu CC, Maxa JL. Drug interactions due to cytochrome P450. *Proc (Bayl Univ Med Cent)*. 2000; 13(4):421-423.
- [26]. Baell JB, Holloway GA. New substructure filters for removal of pan assay interference compounds (PAINS) from screening libraries and for their exclusion in bioassays. *J. Med. Chem*. 2010; 53:2719-2740.
- [27]. Brenk R, Schipani A, James D, Krasowski A, Gilbert IH, Frearson J et al. Lessons learnt from assembling screening libraries for drug discovery for neglected diseases. *Chem Med Chem*. 2008; 3(3):435-444.
- [28]. Hann MM, Keseru GM. Finding the sweet spot: the role of nature and nurture in medicinal chemistry. *Nature Rev. Drug Discov*. 2012; 11:355-365.
- [29]. Teague S, Davis A, Leeson P, Oprea T. The Design of Leadlike Combinatorial Libraries. *Angew. Chem. Int. Ed. Engl*. 1999; 38:3743-3748.
- [30]. Daina Antoine, Olivier Michielin, Vincent Zoete. SwissADME: a free web tool to evaluate pharmacokinetics, drug likeness and medicinal chemistry friendliness of small molecules. *Nature - Scientific Reports*. 2017; 7:42717.1-13.
- [31]. Fukuzumi S. fundamental concepts of catalysis in electron transfer. *electron transfer in chemistry*. 2001; 4; 2-67
- [32]. Gagne OC. Bond-length distributions for ions bonded to oxygen: metalloids and post-transition metals. *Acta Cryst*. 2018; B74; 49-62.
- [33]. Gagné OC. On the crystal chemistry of inorganic nitrides: Crystal-chemical parameters, bonding behavior, and opportunities in the exploration of their compositional space. *Chem Rxiv*. 2020; 11626974.
- [34]. Gagné OC, Hawthorne FC. Comprehensive derivation of bond-valence parameters for ion pairs involving oxygen. *Acta Cryst*. 2015; B71, 562-578.
- [35]. Gagné OC, Hawthorne FC. Bond-length distributions for ions bonded to oxygen: Alkali and alkaline-earth metals. *Acta Cryst*. 2016; B72: 602–625.
- [36]. Gagné OC, Hawthorne FC. Empirical lewis acid strengths for 135 cations bonded to oxygen. *Acta Cryst*. 2017; B73: 956-961.



THEORETICAL STUDY OF PROPERTIES OF SULFORAPHANE A CHEMO PREVENTIVE AGENT USING CHEMSKETCH AND CHEMICALIZE SOFTWARE

K. Laxmi

Professor of Chemistry

Department of Chemistry, Chaitanya Bharathi Institute of Technology (CBIT), Gandipet, Hyderabad -500 075, INDIA Email ID: klaxmi_chm@cbit.ac.in

Abstract: Sulforaphane (SFN) is a powerful phytochemical found mostly in dark green vegetables like broccoli and cruciferous vegetables like kale, cabbage cauliflower, and Brussels sprouts. SFN is known for its antioxidant, anti-inflammatory, and anti-apoptotic properties. Keeping in view of its therapeutic effects structure and properties of Sulforaphane (SFN) were studied by using Chems sketch & Chemicalize software of Chemaxon and the data obtained is interpreted.

Keywords: Sulforaphane, Properties, pka, Isoelectric Point, logP, logD, Solubility, Geometry, HNMR

Introduction

Sulforaphane (SFN) is compound within the isothiocyanate group of organosulphur compounds (fig.1). Sulforaphane (SFN) is highly effective in blocking carcinogenesis¹⁻⁴. In recent decades a wide research has been carried out on Sulforaphane considering it as a potential chemopreventive compound. Sulforaphane is also known for its efficient effect in the treatment of neurodegenerative disease, including Alzheimer's disease, Parkinson's disease, and multiple sclerosis. In view of its beneficial effects, Sulforaphane is recommended as a supplement to neutralize neurodegenerative diseases^{5,6} and for prevention and/or treatment of disorders like neoplasm and heart failure. SFN has been reported to conceal neurotoxicity induced by toxic factors like hydrogen peroxide, prion protein, hyperammonemia, and methamphetamine.

It has been reported that the progression of Alzheimer's disease, Parkinson's disease, cerebral ischemia, Huntington's disease, multiple sclerosis, epilepsy can be prevented by the use of SFN. This is possible by the potential effect of SFN in inhibiting the oxidative stress and neuro inflammation and also by promoting neurogenesis^{7,8}.

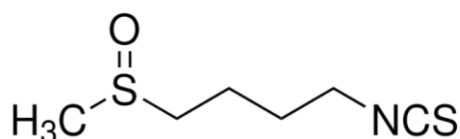


Fig.1 structure of sulforaphane

Results and Discussions

Hypothetical Study of Sulforaphane Using Chemsketch Software

ACD/Labs is one of the powerful software⁹⁻¹¹ used to obtain analytical data and to present reaction schemes. This software is used to focus on research as it is well equipped with prediction tools. A Chemical Naming Service is provided by ACD/Labs and this will use powerful software to quickly and accurately name compounds. ACD allows to generate systematic names according to IUPAC and CAS Index nomenclature rules.

ACD/ChemSketch enables to generate IUPAC names and also allows to calculate a variety of molecular descriptors. Molecular Formula of Sulforaphane is $C_6H_{11}NOS_2$ and its Molecular Weight is 177.28. IUPAC Name of Sulforaphane^{12,13}(fig.2) is 1-isothiocyanato-4-(methanesulfinyl)butane. InChI name of Sulforaphane.(Table.1) is 1S/C6H11NOS2/c1-10(8)5-3-2-4-7-6-9/h2-5H2,1H3. The structure of chemical species using short ASCII strings.(Table.1) is described by using the simplified molecular-input line-entry system^{14,15} (SMILES). It is a specification in the form of a line notation. Smiles notation of Sulforaphane.(Table.1) is S=C=NCCCCS(=O)C

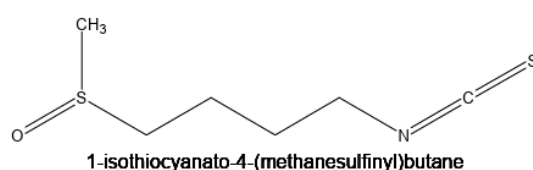


Fig.2 structure of sulforaphane with IUPAC name

Table.1 chemical naming of sulforaphane as determined by ACD/chemsketch

IUPAC name	1-isothiocyanato-4-(methanesulfinyl)butane
InChI	1S/C6H11NOS2/c1-10(8)5-3-2-4-7-6-9/h2-5H2,1H3
SMILES Notation	<chem>S=C=NCCCCS(=O)C</chem>

ACD/ChemSketch calculates the properties like molar volume, molar refractivity, parachor, of Sulforaphane (Table 2) from additive increments. The additive atomic increments were obtained using a database of density, surface tension, and calculated MW. Molar volume, molar refractivity, parachor, of Sulforaphane as given in the table are $150.6 \pm 7.0 \text{ cm}^3$, $49.16 \pm 0.5 \text{ cm}^3$ and $392.6 \pm 8.0 \text{ cm}^3$ respectively.

ACD/ChemSketch calculates the density from MW and the calculated molar volume and it determines the refractive index from the molar volume and molar refractivity. Density of Sulforaphane is $1.17 \pm 0.1 \text{ g/cm}^3$ and Index of Refraction is 1.566 ± 0.05 .

ACD/ChemSketch calculates the dielectric constant from calculated MV and a proprietary empirical additive function. Polarizability is calculated from the Molar Refractivity (MR). Polarizability of Sulforaphane $19.49 \pm 0.5 \cdot 10^{-24} \text{ cm}^3$

Nominal Mass (M_n) is the sum of the approximated monoisotopic masses of the elements forming the structure. Nominal Mass (M_n) of Sulforaphane SFN is 177 Da. Average Mass (M_{av}) is the calculated mass of a particle based on the atomic weights of the elements from which it is comp. Average Mass (M_{av}) of SFN as determined by ACD/ChemSketch is 177.28 Da.

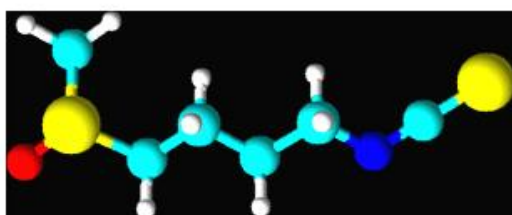
Table 2 properties of sulforaphane as determined by acd/chemsketch

Molecular Formula:	C₆H₁₁NOS₂
Formula Weight:	177.28
Composition:	C(40.65%) H(6.25%) N(7.90%) O(9.02%) S(36.17%)
Molar Refractivity:	49.16 ± 0.5 cm³
Molar Volume:	150.6 ± 7.0 cm³
Parachor:	392.6 ± 8.0 cm³
Index of Refraction:	1.566 ± 0.05
Surface Tension:	46.2 ± 7.0 dyne/cm
Density:	1.17 ± 0.1 g/cm³
Dielectric Constant:	Not available
Polarizability:	19.49 ± 0.5 10⁻²⁴cm³
RDBE:	3
Monoisotopic Mass:	177.028204 Da
Nominal Mass:	177 Da
Average Mass:	177.28 Da
M+:	177.027655 Da
M-:	177.028753 Da
[M+H]+:	178.03548 Da
[M+H]-:	178.036578 Da
[M-H]+:	176.01983 Da
[M-H]-:	176.020928 Da

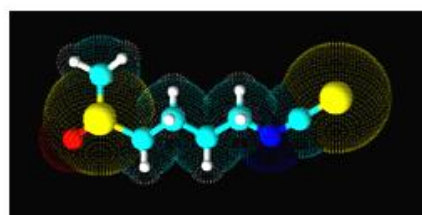
The logP prediction model of ACD/ChemSketch enables to estimate the value of the octanol-water partitioning coefficient (also referred to as K_{ow}) in the form of logarithmic ratio (logP) from structure. Chemists make use of ACD/LogP in different fields of chemical research. This is utilized even by the world's largest pharmaceutical companies like GlaxoSmithKline and Pfizer. Calculated log P of Sulforaphane is 0.23+/- 0.39.

3D Viewer –3D Optimised Forms of Sulforaphane

A powerful modeling and visualization program ACD/3D Viewer, provides various styles of structure 3D representation. These can be displayed in various forms like Ball and cylinder form, ball and cylinder form with dots. The 3D forms of Sulforaphane are given in figure 3.



ball and cylinder form



ball and cylinder form with dots

Fig. 3. 3D optimized structure of sulforaphane

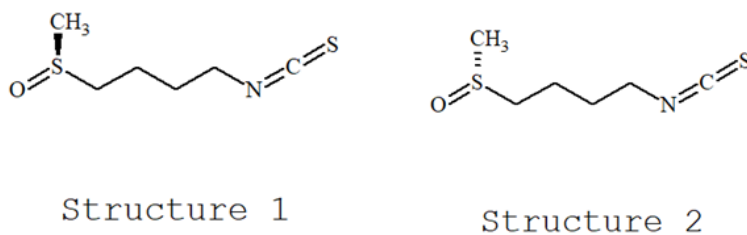


Fig.4 R/S forms of sulforaphane

R,S-Sulforaphane is a synthetic isothiocyanate while R form of Sulforaphane is the naturally-occurring isomer, found in broccoli (Fig.4). R-Sulforaphane is known for its anticancer chemotherapeutic, and chemopreventive, neuromodulatory, anti-inflammatory, antioxidative, neuroprotective, activities. Mirror images of 3D optimized forms of Sulforaphane as indicated by 3D Viewer of Chems sketch is given in Fig.5.

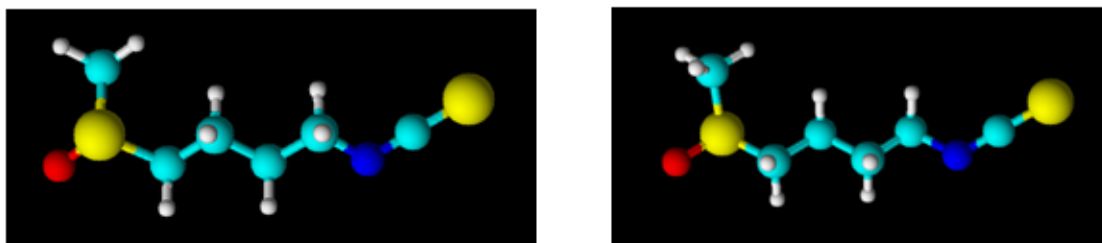


Fig. 5 mirror images of 3D optimized forms of sulforaphane

Hypothetical Study of Sulforaphane using Chemicalize Software

Basic properties of Sulforaphane

The structure of Sulforaphane is drawn as the input and from the data ^{16,17} given (Table 3) it is clearly evident that the formula of Sulforaphane is $C_6H_{11}NOS_2$ and its composition is C=40.65%, H=6.25%, N=7.90%, S (36.17%). The molar mass of Sulforaphane (SFN) is 177.28 g/mol and its exact mass is 177.028206326 Da.

Table 3. properties of sulforaphane as determined by chemicalize software

Input	Sulforaphane
Molar mass	177.28 g/mol
Exact mass	177.028206326 Da
Formula	$C_6H_{11}NOS_2$
Composition	C (40.65%), H (6.25%), N (7.90%), O (9.02%), S (36.17%)

Structural Properties of Sulforaphane

The evaluation of various topology-related characteristics, hydrogen bonding, and other physical properties is done by the Structural calculations.

Data of structural properties of Sulforaphane (SFN) were presented in Table.4. The atom count of 21 of Sulforaphane is in agreement with the number of atoms as given in chemical formula of $C_6H_{11}NOS_2$

In this there are 6 carbons , 1 nitrogen, 1 oxygen and 2 sulphurs which are the heavy atoms and the sum of these is in agreement with the total heavy atom count of 10 atoms(fig 1&2). There is one asymmetric atom and Sulforaphane has five rotatable bonds¹⁸⁻²⁰. The topological polar surface area^{21,22} of Sulforaphane is 29.43 Å². Molar refractivity of Sulforaphane is indicated to be 49.57 cm³/mol.

Table 4. structural properties of Sulforaphane as determined by Chemicalize

Atom count	21
Heavy atom count	10
Asymmetric atom count	1
Rotatable bond count	5
Ring count	0
Aromatic ring count	0
Hetero ring count	0
FSP3	0.83
Hydrogen bond donor count	0
Hydrogen bond acceptor count	2
Formal charge	0
Topological polar surface area	29.43 Å²
Polarizability	19.27 Å³
Molar refractivity	49.57 cm³/mol

Names and Identifiers of Sulforaphane

The following names of Sulforaphane(SFN) were given by the chemicalize software. other details like SMILES, InChI, InChIKey ,CAS Registry numbers of Sulforaphane were also obtained(Table 5)

The name of the compound according to the International Union of Pure and Applied Chemistry nomenclature and the commonly used trivial or traditional name is also shown

Table 5. names and identifiers of sulforaphane given by chemicalize software

IUPAC name	1-isothiocyanato-4-methanesulfinylbutane
Traditional name	sulforaphane
Common names	(+/-)-sulforaphane; DL-sulforaphane; SFN; sulforafan; sulforaphane; sulforathane
SMILES	CS(=O)CCCCN=C=S
InChI	InChI=1/C6H11NOS2/c1-10(8)5-3-2-4-7-6-9/h2-5H2,1H3
InChIKey	SUVMJBTUFCVSAD-UHFFFAOYNA-N

pKa of Sulforaphane

pKa is the measure of the acid dissociation constant given as $pK_a = -\log_{10}(K)$ and it is a measure of the strength of an acid in solution quantitatively²³⁻²⁷. In chemicalize the pKa values of Sulforaphane is found to be 0.87 thereby indicating its strong basic nature (Fig 6.). This is attributed to the dissociation of protons of -NH group.

$$pK_a = -\log_{10}(K)$$

$$pK_a = pH + \log_{10}\left(\frac{[AH]}{[A^-]}\right)$$

$$\Rightarrow pK_a = pH + \log_{10}\frac{[\text{conjugated acid}]}{[\text{conjugated base}]}$$

$$pK_a = pH + \log_{10}\left(\frac{[RNH_3^+]}{[RNH_2]}\right)$$

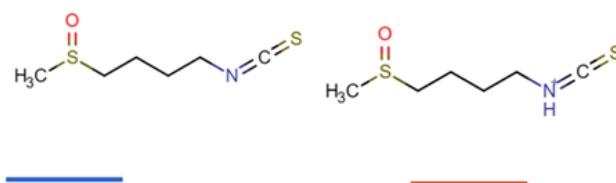
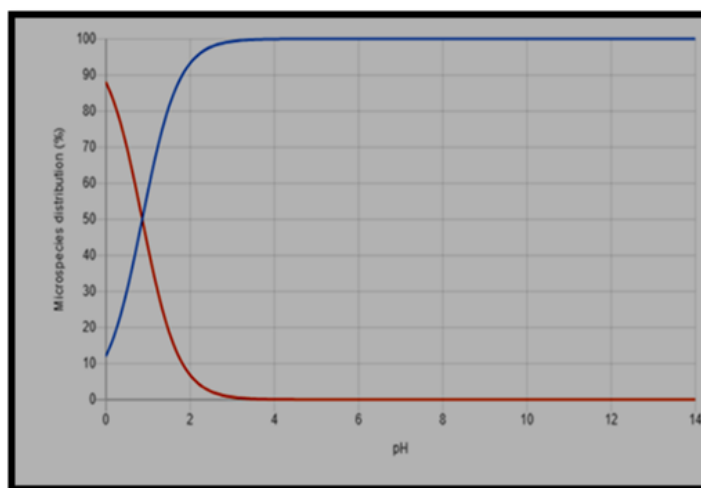


Fig.6 distribution of pH for the different microspecies of sulforaphane as given by chemicalize software

Isoelectric Point of Sulforaphane

The isoelectric point is the pH at which a particular molecule or surface carries no net electrical charge. The gross charge distribution of a molecule as a function of pH is calculated as well.

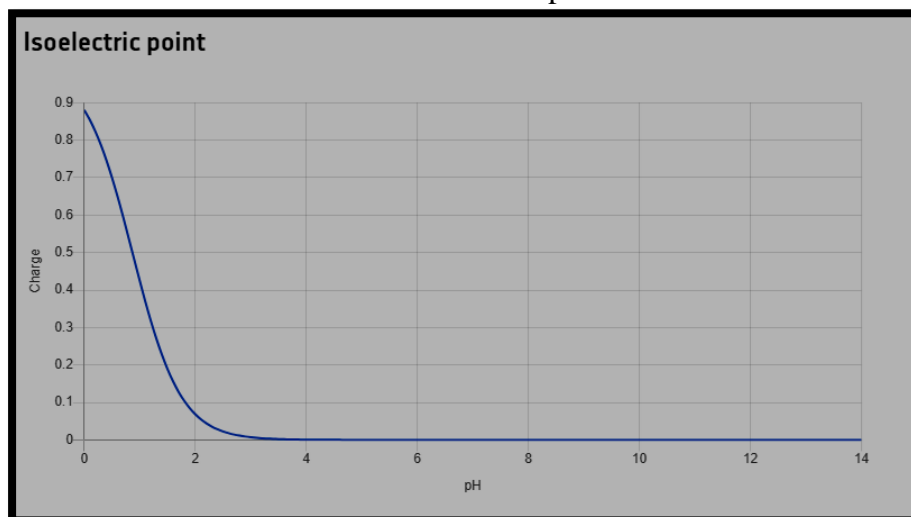


Fig.7 Distribution of charge with pH of Sulforaphane as given by chemicalize software

Table.6 data of distribution of charge with pH of Sulforaphane as given by chemicalize software

pH	Charge
1.7	0.13
4.6	0
6.5	0
7.4	0
8	0

The distribution of charge with pH of Sulforaphane(SFN) is graphically depicted in the fig7. and the corresponding data is given in the Table.6. From the above graph (Fig.7) it is evident that Sulforaphane is electrically neutral with zero electric charge within the pH range of 4.6 to 8 indicating the isoelectric point^{28,29}

log P and log D of Sulforaphane

logP

The partition coefficient is a ratio of concentrations of an un-ionized compound in the two phases of immiscible solvents (water and n-octanol) at equilibrium. logP is the 10-base logarithmic measure of the coefficient.

$$\log P_{oct/wat} = \log \left(\frac{[solute]_{octanol}}{[solute]_{water}^{un-ionized}} \right)$$

logD

Compounds having ionizable groups exist in solution as a mixture of different ionic forms. The ionization of those groups, thus the ratio of the ionic forms depends on the pH. Since logP describes the hydrophobicity of one form only, the apparent logP value can be different. The octanol-water distribution coefficient, logD represents the compounds at any pH value.

$$\log D_{oct/wat} = \log \left(\frac{[solute]_{octanol}}{[solute]_{water}^{ionized} + [solute]_{water}^{neutral}} \right)$$

The hydrophilic-lipophilic balance number (HLB number) measures the degree of a molecule being hydrophilic or lipophilic. This number is calculated based on identifying various hydrophil and lipophil regions in the molecule. This number is a commonly used descriptor in any workflow in which lipid based delivery can be an option (e.g. lipid-based drug delivery, cosmetics). HLB number of Sulforaphane is 10.77

logP is the octanol-water partition for the neutral (un-ionized) form of the compound. logP value of Sulforaphane³⁰⁻³² is found to be 0.22. log D is a log of partition of a chemical compound between the lipid and aqueous phases. The following figure shows the variation of the log D value of Sulforaphane with pH. It is observed that the log D value is same being 0.22 within the pH range of 4.6 to 8 and further log D value increases as the pH increases. (Fig 8 & Table 7). The column and the line graph showing variation of log D with pH is given in the figure 9.

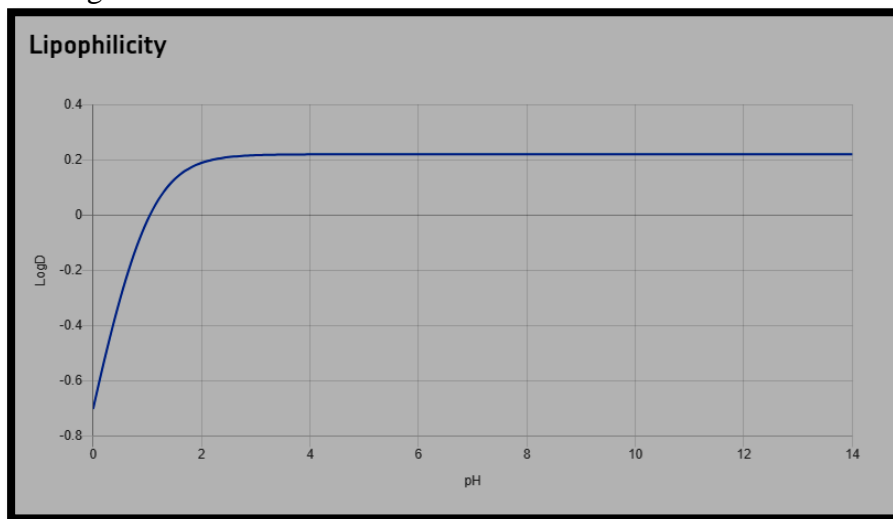


Fig.8 distribution of log D with pH of sulforaphane as given by chemicalize software

Table.7 data of distribution of log D with pH of sulforaphane

pH	log D
1.7	0.16
4.6	0.22
6.5	0.22
7.4	0.22
8	0.22

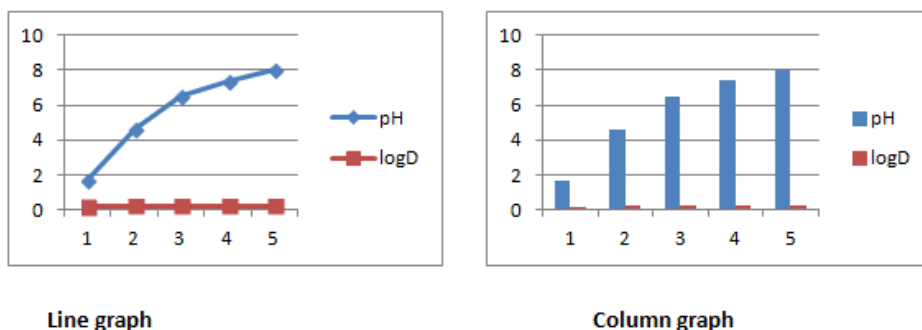


Fig.9 distribution of log D with pH as given by chemicalize software

Solubility of Sulforaphane (log S)

Solubility is a chemical property referring to the ability for a given substance, the solute, to dissolve in a solvent. $\log S$ is the 10-based logarithm of the solubility measured in mol/l.

The following graph shows the distribution of $\log S$ with pH (Fig.10) and the data (Table.8) indicates that Sulforaphane³³⁻³⁶ is of High solubility category with Intrinsic solubility of -1.313. The column and the line graph showing variation of Solubility of Sulforaphane ($\log S$) with pH is given in the figure 11.

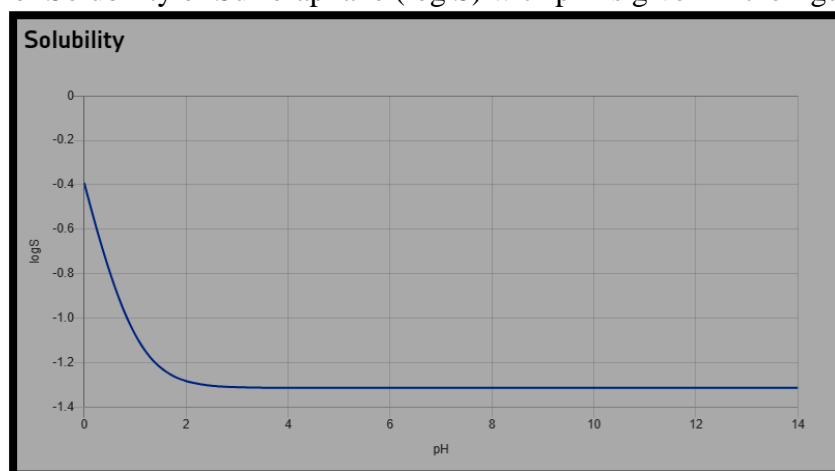


Fig.10 distribution of $\log S$ with pH of sulforaphane as given by chemicalize software

Table.8 data of Distribution of $\log S$ with pH of sulforaphane as given by chemicalize software

pH	Solubility [logS]
1.7	-1.25
4.6	-1.31
6.5	-1.31
7.4	-1.31
8	-1.31

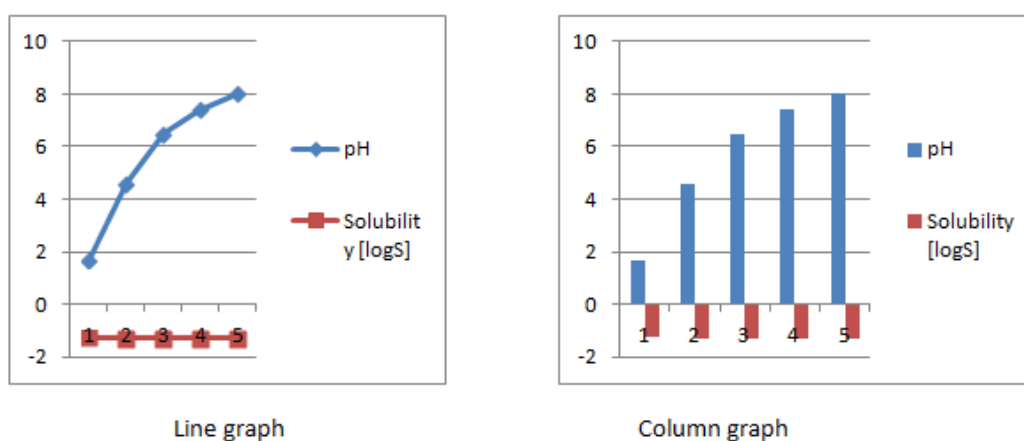


Fig.11 distribution of $\log S$ with pH of sulforaphane as given by chemicalize software

Geometry of Sulforaphane

By using the chemicalize software the following information of vanderwaals volume, surface area ,projection area projection radius of Sulforaphane were obtained³⁷.

Table. 9 data of of volume, surface area ,projection area and projection radius of sulforaphane as given by chemicalize software

Van der Waals volume	158.99 Å³
Van der Waals surface area	267.14 Å²
Solvent accessible surface area	395.44 Å²
Topological polar surface area	29.43 Å²
Minimum projection area	24.4 Å²
Maximum projection area	58.03 Å²
Minimum projection radius	3.2 Å
Maximum projection radius	6.86 Å

H-NMR Spectrum of Sulforaphane

NMR spectra for standard organic molecules is predicted by the NMR Predictor in ChemAxon.A mixed HOSE and linear model based on topological description scheme is used for estimating the chemical shifts^{38,39}. This estimation is done in relation to the chemical shift of tetra methylsilane (TMS = 0ppm)H-NMR spectrum of Sulforaphane(SFN) is given in the figure 12.

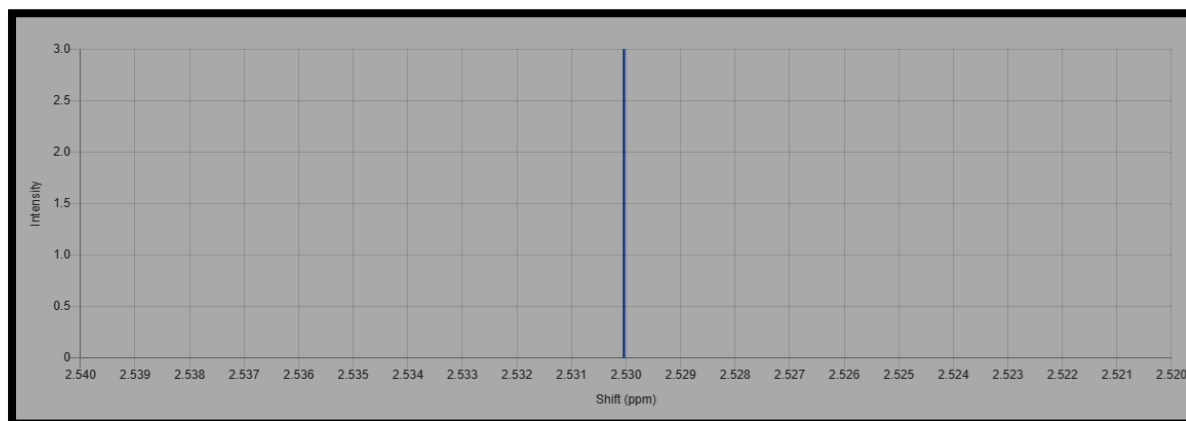
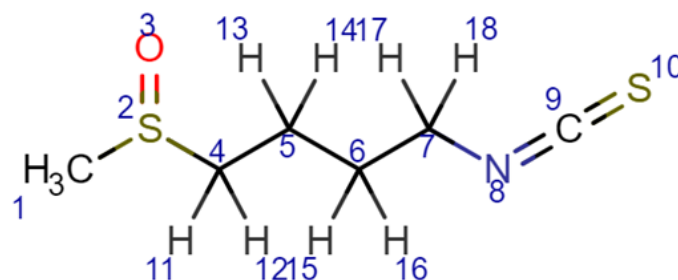


Fig.12 1HNMR spectrum of sulforaphane as given by chemicalize software

Table 10. shifts caused by the protons of sulforaphane and the intensity and quality for each shift and corresponding protons as given by chemicalize software



Atoms	Shift	Intensity	Multiplet	Quality
15	1.870 ppm	1	n	medium
13	1.899 ppm	1	p	medium
16	2.098 ppm	1	n	medium
14	2.261 ppm	1	p	medium
11	2.290 ppm	1	t	medium
1, 1, 1	2.530 ppm	3	s	good
12	3.010 ppm	1	t	medium
17	3.330 ppm	1	t	medium
18	3.726 ppm	1	t	medium

The above table 10 shows the shifts caused by the protons of Sulforaphane and it also indicates the intensity and quality for each shift. The shift observed at 2.530 ppm corresponds to protons of methyl group.

Conclusions

Structural and physicochemical aspects of Sulforaphane is well understood by the information provided by chemsketch study. Different styles of 3D representation of structure, mirror images and R/S forms of Sulforaphane were well visualized by applying ACD/3D Viewer integrated with ACD/ChemSketch

As indicated by data of chemicalize software from pKa values and ¹HNMR spectral data it is understood that Sulforaphane is of strongly basic nature having one dissociable proton. Graphical interpretation showing distribution of log D, log S, solubility in mg/L with pH of Sulforaphane enabled the study of variation of these properties with pH. Geometrical studies of Sulforaphane done using chemicalise software provided the data of properties like vanderwaals area, vanderwaals volume, projection area projection radius.

References

1. Sulforaphane glucosinolate. Monograph. Altern Med Rev. 2010 Dec;15(4):352-60. PMID: 21194251.
2. Ullah MF. Sulforaphane (SFN): An Isothiocyanate in a Cancer Chemoprevention Paradigm. Medicines (Basel). 2015 Jul 17;2(3):141-156. doi: 10.3390/medicines2030141. PMID: 28930206; PMCID: PMC5456215.
3. Su X, Jiang X, Meng L, Dong X, Shen Y, Xin Y. Anticancer Activity of Sulforaphane: The Epigenetic Mechanisms and the Nrf2 Signaling Pathway. Oxid Med Cell Longev. 2018 Jun 6;2018:5438179. doi: 10.1155/2018/5438179. PMID: 29977456; PMCID: PMC6011061.
4. Clarke JD, Dashwood RH, Ho E. Multi-targeted prevention of cancer by sulforaphane. Cancer Lett. 2008 Oct 8;269(2):291-304. doi: 10.1016/j.canlet.2008.04.018. Epub 2008 May 27. PMID: 18504070; PMCID: PMC2579766.

5. Schepici G, Bramanti P, Mazzon E. Efficacy of Sulforaphane in Neurodegenerative Diseases. *Int J Mol Sci.* 2020 Nov 16;21(22):8637. doi: 10.3390/ijms21228637. PMID: 33207780; PMCID: PMC7698208.
6. Huang C, Wu J, Chen D, Jin J, Wu Y, Chen Z. Effects of sulforaphane in the central nervous system. *Eur J Pharmacol.* 2019 Jun 15;853:153-168. doi: 10.1016/j.ejphar.2019.03.010. Epub 2019 Mar 8. PMID: 30858063.
7. Alessio Alfieri ^a, Salil Srivastava ^a, Richard C.M. Siow ^a, Diana Cash ^b, Michel Modo ^c, Michael R. Duchon ^d, Paul A. Fraser ^a, Steven C.R. Williams ^b, Giovanni E. Mann, Sulforaphane preconditioning of the Nrf2/HO-1 defense pathway protects the cerebral vasculature against blood-brain barrier disruption and neurological deficits in stroke, <https://doi.org/10.1016/j.freeradbiomed.2013.08.190>
8. Conzatti A, Fróes FC, Schweigert Perry ID, Souza CG. Clinical and molecular evidence of the consumption of broccoli, glucoraphanin and sulforaphane in humans. *Nutr Hosp.* 2014 Nov 30;31(2):559-69. doi: 10.3305/nh.2015.31.2.7685. PMID: 25617536.
9. ACD Labs, Free chemistry software & Apps, <https://www.acdlabs.com/resources/free-chemistry-software-apps/>
10. Utilizando ChemsSketch". Retrieved 21 August 2014.
11. ACD/ChemSketch Freeware, version 11 (2006) Advanced Chemistry Development Inc., Toronto, ON, Canada, www.acdlabs.com.
12. International Union of Pure and Applied Chemistry, Organic Chemistry Division Commission on Nomenclature of Organic Chemistry, Nomenclature of Organic Chemistry, Sections A, B, C, D, E, F, and H, 1979 Edition, J. Rigaudy and S. P. Klesney, eds., Pergamon Press, Oxford, 1979, (Sections A, B, C, D, E, and F are available).
13. International Union of Pure and Applied Chemistry, Organic Chemistry Division, Commission on Nomenclature of Organic Chemistry (III.1), A Guide to IUPAC Nomenclature of Organic Compounds (Recommendations 1993), R. Panico, W.H. Powell and Jean-Claude Richer, eds., Blackwell Scientific Publications, Oxford, 1993.
14. "SMILES Tutorial: What is SMILES?". U.S. Environmental Protection Agency. Retrieved 2012-09-23.
15. National Center for Biotechnology Information (NCBI). PubChem Compound. (accessed May 12, 2012) PubChem Compound CID=183413 (Cephalostatin-1).
16. G. Audi, A.H. Wapstra, The 1993 update to the atomic mass evaluation, *Nuclear Physics A*, Vol. 595, Issue 4, pp. 409- 480, 1995.
17. Trepalin, S.V., Bessonov, Y.E., Fel'dman, B.S. *et al.* The Structural Chemical Database of the All-Russian Institute for Scientific and Technical Information, Russian Academy of Sciences. An Autonomous System for Structural Searches. *Autom. Doc. Math. Linguist.* **52**, 297–305 (2018). <https://doi.org/10.3103/S0005105518060055>
18. Molecules from the Minkowski space: an approach to building 3D molecular structures, December 2003, *Journal of Molecular Structure THEOCHEM* s 666–667(6C):51–59 DOI: [10.1016/j.theochem.2003.08.013](https://doi.org/10.1016/j.theochem.2003.08.013)
19. Bender, B.J., Gahbauer, S., Luttsen, A. *et al.* A practical guide to large-scale docking. *Nat Protoc* **16**, 4799–4832 (2021). <https://doi.org/10.1038/s41596-021-00597-z>
20. ChemAxon poster: Advanced automatic generation of 3D molecular structures
21. Ferrara P, Apostolakis J, Caflisch A. Evaluation of a fast implicit solvent model for molecular dynamics simulations. *Proteins.* 2002 Jan 1;46(1):24-33. doi: 10.1002/prot.10001. PMID: 11746700.
22. Norma Flores-Holguín¹, Juan Frau², Daniel Glossman-Mitnik, Computational Chemistry and Molecular Modeling Techniques for the Study of Micropeptin EI-964: Insights into Its Chemical Reactivity and Potential Pharmaceutical Properties, *Computational Molecular Bioscience*, Volume 13, Number 3, September 2023, DOI: 10.4236/cmb.2023.133003
23. Theoretical Determination of the pK_a Values of Betalamic Acid Related to the Free Radical Scavenger Capacity: Comparison Between Empirical and Quantum Chemical Methods, Marco Tutone, Antonino Lauria, Anna Maria Almerico, July 2015, *Interdisciplinary Sciences Computational Life Sciences* 8(2)

DOI: [10.1007/s12539-015-0101-3](https://doi.org/10.1007/s12539-015-0101-3)

24. Calculating pKa values of small and large molecules, J.Szegezdi and F.Csizmadia , American Chemical Society Spring meeting ,March 25-29th,2007
25. Epik: A software program for pKa prediction and protonation state generation for drug-like molecules,,January 2008,,Journal of Computer-Aided Molecular Design 21(12):681-91
DOI:[10.1007/s10822-007-9133-z](https://doi.org/10.1007/s10822-007-9133-z)
26. Epik version 2.0 (2009) Schrödinger, LLC, New York
27. Determination of acid dissociation constants (pKa) of cephalosporin antibiotics: Computational and experimental approaches,Chemosphere, Alyson R. Ribeiro, Torsten C. Schmidt,Volume 169, 2017,Pages 524-533, <https://doi.org/10.1016/j.chemosphere.2016.11.097>.
28. Calculation of the isoelectric points of native proteins with spreading of pKa values,G Henriksson¹, A K Englund, G Johansson, P Lundahl, Electrophoresis , 1995 Aug;16(8):1377-80,doi: 10.1002/elps.11501601227
29. pIChemiSt — Free Tool for the Calculation of Isoelectric Points of Modified Peptides, Andrey I Frolov , Sunay V Chankeshwara, Zeyed Abdulkarim , Journal of Chemical information and Modelling, 2023 Jan 9;63(1):187-196. doi: 10.1021/acs.jcim.2c01261. Epub 2022 Dec 27.
30. Bouchard G., Carrupt P.A., Testa B., Gobry V., Girault H.H. Pharmaceutical Research 18 (2001) 702-708. <https://doi.org/10.1023/A>
31. Bouchard G, Pagliara A, Carrupt PA, et al. Theoretical and experimental exploration of the lipophilicity of zwitterionic drugs in the 1,2-dichloroethane/water system. Pharmaceutical Research. 2002 Aug;19(8):1150-1159. DOI: 10.1023/a:1019846125723. PMID: 12240941.
32. Işık, M., Bergazin, T.D., Fox, T. *et al.* Assessing the accuracy of octanol–water partition coefficient predictions in the SAMPL6 Part II log *P* Challenge. *J Comput Aided Mol Des* **34**, 335–370 (2020). <https://doi.org/10.1007/s10822-020-00295-0>
33. Völgyi, G.; Baka, E. *et al.* Study of pH-dependent solubility of organic basis. Revisit of the Henderson-Hasselbalch relationship, *Analytica Chimica Acta*, 2010 , 673, 40-46
34. Avdeef, A. *et al.* Equilibrium solubility measurement of ionizable drugs - consensus recommendations for improving data quality, *ADMET & DMPK* 4(2), 2016 , 117-178
35. Shoghi, E.; Fuguet, E.; Bosch, E.; Rafols, C. Solubility-pH profiles of some acidic, basic and amphoteric drugs, *European Journal of Pharmaceutical Sciences* **2013** , 48, 291-300
36. Alex Avdeef ,Suggested Improvements for Measurement of Equilibrium Solubility-pH of Ionizable Drugs,July 2015,ADMET & DMPK 3(2):84-109,DOI:[10.5599/admet.3.2.193](https://doi.org/10.5599/admet.3.2.193)
37. Chemaxon article: Molecules from the Minkowski space: an approach to building 3D molecular structures
38. J Org Chem. 1997 Oct 17;62(21):7512-7515. doi: 10.1021/jo971176v. Authors. Hugo E. Gottlieb , Vadim Kotlyar, Abraham Nudelman
39. NMR Chemical Shifts of Common Laboratory Solvents as Trace Impurities Hugo E. Gottlieb, Vadim Kotlyar, and Abraham Nudelman J. Org. Chem., 1997, 62 (21), 7512-7515 • DOI: 10.1021/jo971176v Downloaded from <http://pubs.acs.org> on January 23, 2009



Effect of fill pattern on flexural performance of FDM printed PLA

Sumit Srivastava, D. Saritha & R. Sujithra

To cite this article: Sumit Srivastava, D. Saritha & R. Sujithra (2024) Effect of fill pattern on flexural performance of FDM printed PLA, Materials and Manufacturing Processes, 39:6, 787-796, DOI: [10.1080/10426914.2023.2289674](https://doi.org/10.1080/10426914.2023.2289674)

To link to this article: <https://doi.org/10.1080/10426914.2023.2289674>



Published online: 04 Dec 2023.



Submit your article to this journal [↗](#)



Article views: 144



View related articles [↗](#)



View Crossmark data [↗](#)



Effect of fill pattern on flexural performance of FDM printed PLA

Sumit Srivastava^a, D. Saritha^b, and R. Sujithra^a

^aDepartment of Applied Mechanics, Motilal Nehru National Institute of Technology Allahabad, Prayagraj, India; ^bDepartment of Chemistry, Chaitanya Bharathi Institute of Technology, Hyderabad, India

ABSTRACT

In most biomedical devices, such as fracture fixation devices and medical tools, the printed part is subjected to complex loadings that involve large deflections instead of large strains. Among various FDM tool path parameters, the fill pattern has a critical role in controlling voids and raster bonding. This work highlights the flexural performance of the PLA-printed part based on various fill patterns, such as concentric, linear, Hilbert, raster angle 45°, alternate pattern (0°/45°), and concentric pattern with holes resembling bone plate. Based on deposition paths, the dimensional changes and interlayer adhesion were analyzed before and after annealing. The flexural performance was evaluated using quasi-static three-point and four-point bend tests and dynamic flexural tests under temperature sweep. The annealed samples exhibit improved flexural strength regardless of infill pattern and loading conditions, with the concentric pattern showing better performance in both static and dynamic tests.

ARTICLE HISTORY

Received 30 May 2023
Accepted 9 October 2023

KEYWORDS

PLA; infill; FDM; annealing; shrinkage; crystallinity; quasi-static; dynamic; flexural

Introduction

Fused deposition modeling (FDM) is a well-known fabrication technique for manufacturing customized products as it offers no molding cost, waste minimization, and reduces the supply chain process [1–3]. Among many thermoplastics, PLA is most suitable for the biomedical industry due to its biocompatible characteristics, and it can print parts with dimensional stability, nominal warping, and pleasing esthetics [4]. The FDM technique constructs parts by a layer-wise approach; in each layer, the outer boundary, known as the shell, is printed first, then the inside area is filled by a specific fill pattern. However, the layer-wise building approach imparts anisotropy to the manufactured parts, resulting in reduced mechanical properties compared to conventional plastic molding techniques [5]. The non-uniform heat transfer in the solidification process results in an inadequate merging of raster and layers, leading to partial necking and inter-filament voids [6]. These drawbacks can be controlled by optimizing the tool path and temperature parameters, which include layer resolution, raster angle, build orientation, extrusion speed, contour width, extrusion temperature, and bed temperature [7, 8]. Several studies were reported on improving the mechanical behavior of PLA by optimizing the FDM tool path parameters. A better interlayer strength [9] and a reduction in porosity [10, 11] can be achieved by smaller layer resolution, a higher fill rate, and optimal filament extrusion temperature and printing speed. However, the ductility reduces by increasing the layer resolution and feed rate [12]. The PLA part strength can also be enhanced by increasing the extrusion temperature from 200 to 230°C but showed a decline in strength beyond 230°C [13]. Build orientation [14] and the number of contours at the boundary [15] also had an impact on the mechanical strength of PLA samples. The tool path parameters such as layer

thickness, raster width, air gap, and contours at the boundary significantly influenced the dynamic and rheological properties [16].

Among many parameters, the fill pattern is the critical parameter that affects the part performance, as it controls the void content and fusion between the raster [17]. FDM provides a variety of infill patterns, including lines, rectilinear patterns, triangles, concentric patterns, cubic, octet, quarter cubic, zigzag patterns, crosses, triangular patterns, octagonal spiral patterns, Hilbert curves, honeycomb patterns, and Archimedean chords [18]. The infill pattern with a short deposition path promotes the fusion of raster due to higher heat transfer than the long deposition path [19]. PLA is commonly utilized in orthopedic fracture fixation devices, joint implants, and various medical equipment such as needle drivers, hemostats, forceps, surgical retractors, and scalpel handles [20, 21]. FDM-printed PLA components have been tested under flexural loading mode for all the above-specified biomedical applications to withstand forces during service. Depending upon the short and long deposition path, the printed part has variation in the thermal history that ultimately influences the flexural strength. Apart from tool path parameters, annealing is the most common heat treatment method that enhances bonding strength by stimulating the interdiffusion between the neighboring raster and layers, and relieves residual thermal stresses of the printed part. Hence, it is necessary to analyze the various fill patterns based on quasi-static flexural performance under 3-point and 4-point bending before and after annealing. Further, the deposition path of various infill patterns and annealing process will influence the dimensional changes and interlayer adhesion. As the printed part can also be exposed to

dynamic operating conditions during its service life, it is also necessary to analyze the dynamic characteristics of various infill patterns by considering the effect of annealing.

Few authors reported on the effect of fill pattern based on the mechanical characteristics of printed PLA parts. Akhouni et al. reported that the concentric pattern with 20%, 50%, and 100% infill percentages and the Hilbert pattern with 100% infill density provides the most desired tensile and flexural properties compared to rectilinear and honeycomb patterns [19]. Gomez-Gras et al. reported that the honeycomb pattern with 75% fill density has higher fatigue life than the rectilinear pattern, as the voids in the honeycomb pattern slow down the crack propagation [22]. The PLA sample with a triangular pattern exhibits higher energy absorption in the low-velocity impact test due to adequate raster bonding with more contact layers and fewer voids than the grid, tri-hexagon, and quarter cubic infill patterns [23]. The honeycomb and gyroid pattern with 100%, 70%, 50%, and 25% shows better-bending resistance than the grid pattern [24]. The 45°/−45° raster orientation shows an anisotropic behavior with higher fracture strength than 0°/90°, 15°/−75°, and 30°/−60° raster angles, as the alignment of raster orientation was orthogonal to the crack plane [25]. Loading direction and raster angle also affect the tensile strength, as the raster angle above and below 45° shows intralayer and interlayer failure [26–28]. Hence, this directs that the mode of loading should be taken into consideration while selecting the fill pattern.

Szust et al. reported that PLA samples annealed at 60°C for 1 h increased their tensile strength by 24% and reduced their modulus by 7%. In comparison, annealing at 80°C for 1 h resulted in a 10% decrease in modulus with no discernible change in tensile strength [29]. However, Song et al. observed that annealing PLA at 60°C (just below T_g) with a dwelling time of 5 h shows no effect on crystallinity but reduces 30% of its tensile strength [10]. Reis et al. reported that annealing at 80°C shows better flexural strength and modulus due to smaller spherulite size other than 90°C, 110°C, and 119°C, but annealing at 90°C shows a higher crystallinity [30]. Similarly, Wach et al. observed a maximum crystallinity with no cold crystallization peak when annealed at 85°C for 70 min and 95°C for 15 min, which enhances the flexural strength by 11–17% with no significant change in the modulus [31]. Annealing PLA below the T_{cc} (cold crystallization temperature) at 90°C considerably raises the strength, modulus, and failure strain compared to annealing above T_{cc} . An increase in annealing time from 30 to 480 min at 90°C imparts a minor increase in tensile strength from 11 to 17% with no significant change in the modulus [32]. It is observed that better performance could be achieved by annealing PLA between the glass transition and cold crystallization temperatures. Apart from mechanical properties, the annealing process significantly influences geometric deformation. Thus, the annealing temperature, dwelling time, and cooling rate affect the mechanical properties and part-dimensional stability.

The aforementioned literature review indicates that no comparison studies have been reported to comprehend the influence of fill deposition paths on the dimensional changes, raster adhesion, and mechanical performance of the printing part before and after annealing. It is well known that the infill pattern has the most desirable role during the part's service life, as the filament-based fused deposition process leads to partial bonding

of the raster. Therefore, this study aims to investigate how the deposition path influences the thermal history of the printed part, which ultimately affects the raster adhesion and mechanical performance of the printed part. In this work, the author analyzes various infill patterns such as concentric, linear, Hilbert, raster angle 45°, alternate pattern (0°/45°), and concentric pattern with holes similar to bone plates with screw holes based on short, long, and combinations of both deposition paths. The six different infill patterns are experimentally investigated to assess the dimensional changes, interlayer adhesion, degree of crystallinity, quasi-static three-point and four-point flexural tests, and dynamic tests under temperature sweep by considering the effect of annealing. This study will guide the biomedical printing industry in choosing a suitable infill pattern for attaining higher flexural strength in the printed part.

Materials and methods

The PLA samples for FDM printing are modeled using SolidWorks, and their stereolithography file is imported to ideaMaker slicing software for converting 3D models into G-codes that provide the tool path instructions for the 3D printer. FDM printer (Creality CR-10S) with a build capacity of $300 \times 300 \times 400 \text{ mm}^3$ is used to fabricate the PLA samples using a filament of 1.75 mm diameter (Solid Space Technology Ltd.). The rectangular specimens are printed with a dimension of $127 \times 12.7 \times 3.2 \text{ mm}^3$ for quasi-static and $60 \times 10 \times 2 \text{ mm}^3$ for dynamic flexural test. Table 1 shows the FDM tool path parameters for PLA. Six different infill patterns with 100% fill density are chosen to print the samples for the flexural test, as shown in Fig. 1. The raster angle is specified by the movement of the nozzle tool path with reference to the X-axis of the print platform that influences the filament adhesion and bonding. The concentric infill pattern (sample A) preserves the outer shell of the sample, and the raster needs to travel a long distance to fuse with the adjacent raster. The linear infill pattern (sample B) prints longitudinally with a raster angle 0°. Both concentric and linear pattern has a long deposition path compared to other fill patterns. Hilbert (sample C) is a continuous fractal space-filling curve with the shortest deposition path that encourages better interfacial contact of nearby raster only at 100% infill density. For raster angle 45° (sample D), the tool path is inclined at 45° with reference to the X-axis of the build platform, and it has the shortest deposition path to fuse with adjacent raster (by considering the rectangular sample dimension). In the alternate fill pattern of 0°/45° (sample E), the layers are printed with an alternating sequence of raster angle 0° (long deposition path) and raster angle 45° (short

Table 1. PLA print parameters.

Parameters	Value
Nozzle Temperature	225°C
Layer height	0.2 mm
Infill density	100%
Print Speed	45 mm/s
Bed temperature	55°C
Number of shells at the boundary	2
Raster width	0.063 mm
Contour width	0.6 mm
Flow rate	100%

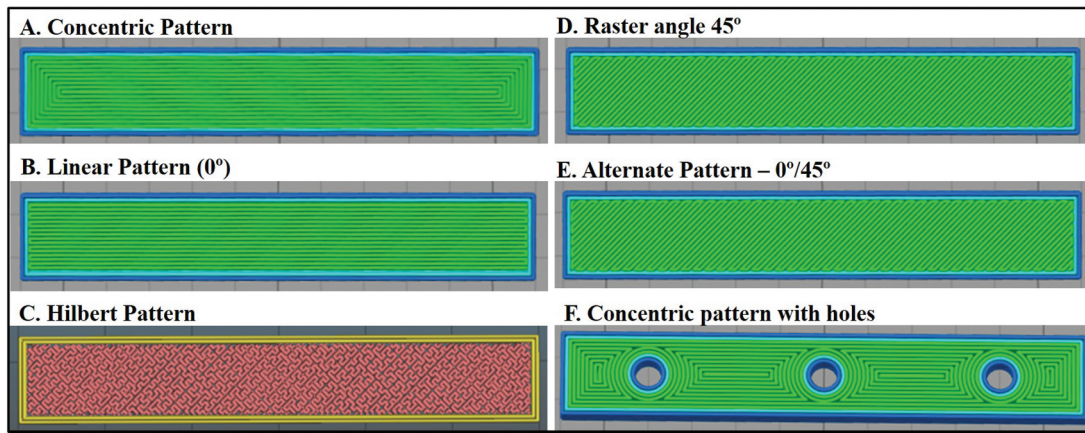


Figure 1. Schematic diagram of rectangular samples with different infill patterns.

deposition path). Sample (F) is printed with holes at equal distances, five holes for flexural and three holes for DMA samples based on the length of the specimen. The concentric pattern is chosen to print the sample with holes by considering the edges and holes as the two shell features, as it avoids the gap between the raster. It combines the short deposition path near the holes and the long deposition path near the edges of every layer. Figure 2 shows the printed flexural and DMA samples.

The layer-wise fabrication process in FDM generates residual stress in the printed part due to repetitive heating and cooling of successive layers that can be relieved by the annealing process. In this work, printed PLA samples are annealed at 90°C (below cold crystallization and above glass transition temperature) for 15 min in a hot air oven, and dimensional changes are measured. The pre- and post-annealing process of PLA samples are examined using scanning electron microscopy (SEM) images to analyze the interlayer bonding of various infill patterns. The cross-sectional surface of the sample was sputter coated with platinum of 10 nm thickness for conductivity. The JSM-IT800 scanning electron microscope is operated at low vacuum pressure, and the images are captured at an accelerating voltage of 5 kV. DSC is carried out using

a Universal V4 5A TA instrument according to ASTM D3418 to calculate the crystallinity of printed PLA samples before and after annealing based on the first heating cycle. The printed PLA of approximately 5–10 mg is placed in the sample pan, and aluminum as reference material in another pan. The heat flow difference between the reference and the PLA sample is monitored by ramping the temperature from 30°C to 250°C at 10°C/min.

The three-point and four-point flexural test is performed on a BISS universal testing machine with a load capacity of 25 kN. The sample is placed on the support span by maintaining the support span-to-depth ratio of 16:1. For four-point bending, the distance between the loading points is one-third of the support span, as shown in Fig. 3. The displacement of the loading nose is set at 1.5 mm/min. The sample is deflected till the fracture or 5% of strain is reached. The flexural stress, flexural strain, and flexural modulus for three-point and four-point bending are calculated as per the ASTM D790 and ASTM D6272. For dynamic testing, the PLA sample is subjected to cyclic deformation to measure the viscoelastic response by evaluating the stored and loss energy as a function of temperature in accordance with ASTM D5063. The temperature sweep test is carried out on DMA 6000

Three-point and four-point bend samples



DMA samples



Figure 2. PLA printed samples with different infill patterns.

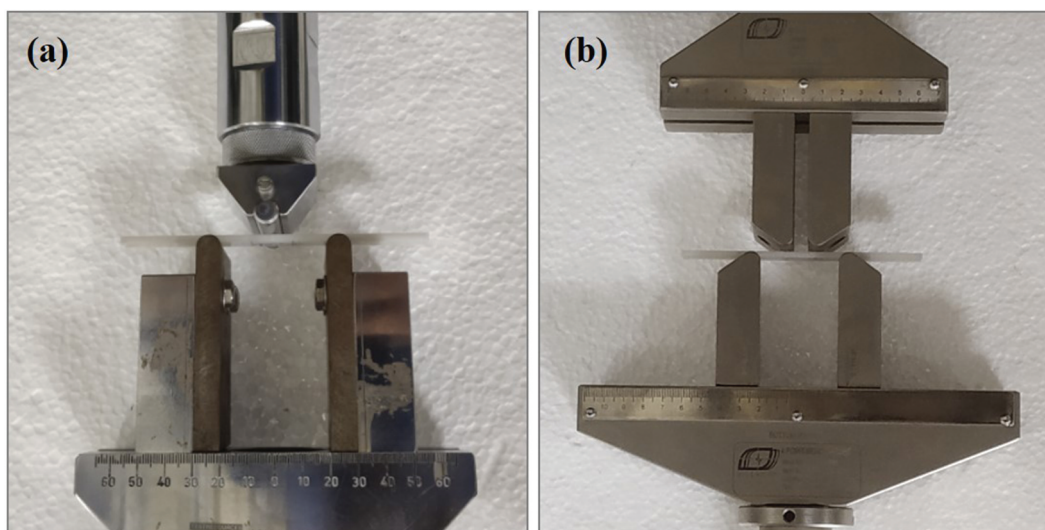


Figure 3. Quasi-static (a) three-point and (b) four-point flexural test.

Hitachi by ramping the temperature from 30 to 90°C at a heating rate of 3°C/min and dynamic strain of 1% at the 1 Hz frequency.

Results and discussion

Dimensional changes

The PLA sample before and after annealing is shown in Fig. 4. Table 2 represents the average dimensional change in the length, width, and thickness of the samples after printing with respect to design dimensions and after annealing with respect to printed sample dimensions. After printing, it is observed that the average dimensional change in length and width shrinks from 0.5% to 1%, and expansion in thickness varies from 2% to 7%, as shown in Table 2. The concentric pattern has the longest deposition path, resulting in a minor expansion in thickness compared to other patterns. The linear pattern shows a slightly higher change in thickness than concentric, as the fusing occurs in a short time at one side compared to the other side (non-uniform heat transfer). But, the concentric pattern with holes has higher expansion in the thickness direction, as the raster near the holes has the shortest deposition path, which leads to shrinkage in the hole diameter of about 5%. All other patterns result in moderate shrinkage. Due to convection heat transfer, the raster with a long deposition path partially solidifies before it comes in contact with the adjacent raster, resulting in lower dimensional change after printing. For the raster with a short deposition path, conduction occurs with the adjacent raster, which helps to form neck growth and diffusion, resulting in better adhesion, and the development of contact stress leads to more shrinkage after printing. Similarly, Akhouni et al. also reported that dimensional changes in samples during printing was dominated due to interfacial fusion by conduction heat transfer compared to convection [19].

The annealed PLA samples are shown in Fig. 4; dimensional changes were observed without excessive geometric distortion due to a shorter annealing time of 15 min. After annealing, the concentric pattern showed the highest shrinkage, whereas the

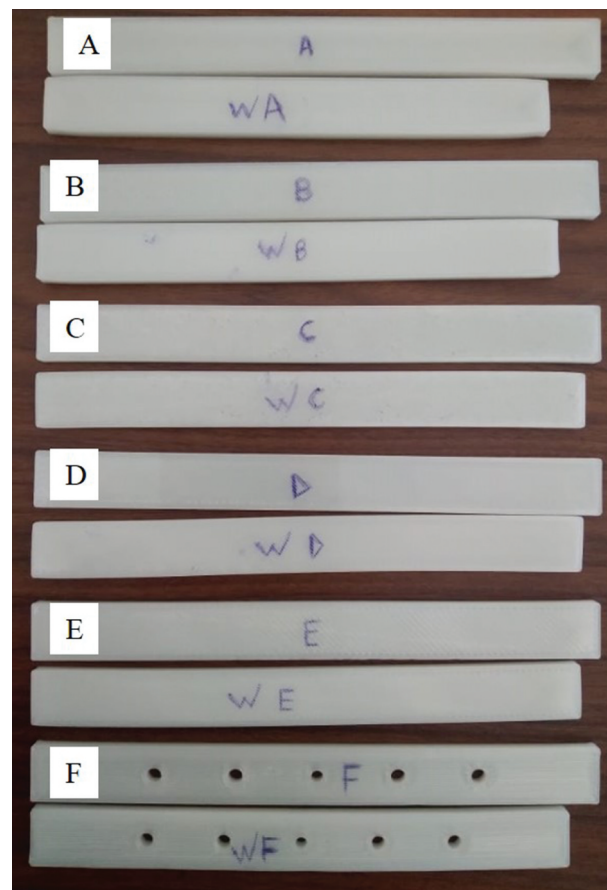


Figure 4. PLA samples before and after annealing (A, B, C, D, E, F represents infill patterns).

Hilbert pattern showed minor shrinkage in the longitudinal direction. Similarly, the concentric pattern shows a significant change in thickness of about 7%, and the Hilbert pattern showed a lesser expansion of about 0.6%. In the transverse direction, a similar amount of shrinkage is observed in Hilbert, raster angle 45°, and alternate pattern (0°/45°), whereas other patterns showed slight expansion in the post-annealing

Table 2. Average change in dimensions before and after annealing.

Infill pattern	After printing			After annealing		
	Average change in length (%)	Average change in width (%)	Average change in thickness (%)	Average change in length (%)	Average change in width (%)	Average change in thickness (%)
Concentric pattern	-0.51	-0.47	2.18	-9.18	1.89	7.03
Linear pattern	-0.49	-1.02	3.12	-7.66	2.78	6.36
Hilbert pattern	-0.52	-0.55	4.06	-2.86	-1.82	0.60
Raster angle 45°	-0.50	-0.39	3.12	-3.69	-2.05	4.54
Alternate pattern	-0.55	-1.02	4.06	-3.49	-2.14	3.90
Concentric pattern with holes	-0.51	-0.78	6.87	-5.32	0.39	3.50

Table 3. DMA parameters under temperature sweep.

Infill patterns	Maximum storage modulus (MPa)	Maximum loss modulus (MPa)	tan δ peak	T _g (E' curve)	T _g (E'' curve)	T _g (tan δ peak)
Concentric pattern	2914	332	0.320	70	61	56
Linear pattern	2267	300	0.321	67	58	52
Hilbert pattern	2608	368	0.329	70	61	56
Raster angle 45°	2772	380	0.315	67	57	52
Alternate pattern	2455	345	0.330	67	58	52
Concentric pattern with holes	2424	320	0.321	70	61	56

process. It is observed that the pattern with long (concentric) and short deposition paths (Hilbert) has major and minor changes in dimension after annealing. However, the raster angle 45° has the shortest deposition path with no voids, resulting in slightly higher shrinkage than Hilbert. The alternate pattern (0°/45°) and the concentric pattern with holes have the combination of shortest and longest deposition paths, resulting in moderate shrinkage. But, the concentric pattern with holes shows a 9% shrinkage of hole diameter after annealing due to long deposition at the boundary. Thus, the long deposition path results in higher shrinkage than the short deposition path after annealing.

Scanning electron microscopy

Figure 5 shows the cross-sectional surface morphologies obtained by cutting the FDM-printed samples before and after annealing. After printing, it is observed that the concentric and linear pattern (long deposition path) shows weak interfacial contact or gap between the layers due to the convection heat transfer. Other patterns, with short deposition paths (Hilbert and raster angle 45°) and the combination of long and short depositions path (alternate 0°/45° and the concentric pattern with holes) show better interlayer coalescence after printing. After annealing, it is observed that the shrinkage of individual raster is higher in long deposition path fill pattern than short deposition. This is due to reduced contact stress or weaker interfacial fusion of the fill pattern during printing. Further, all the infill patterns show enhanced interlayer adhesion after annealing. Compared to all other patterns, it is observed that the combined deposition path (alternate pattern and concentric pattern with holes) shows better interlayer adhesion before and after annealing.

Differential scanning calorimetry

The DSC curve for the unannealed and annealed PLA printed samples is shown in Fig. 6. It is observed that both the

unannealed and annealed sample reveals the glass transition temperature at 52°C, cold crystalline peak at 151°C and melting peak at 220°C. The cold crystallization peak is slightly suppressed for annealed samples, and a similar trend was observed by Bhandari et al. [32]. The calculated degree of crystallinity for unannealed samples is nearly zero. This might be attributed to the FDM process, where the polymer quickly solidifies from the extrusion nozzle to bed temperature within a few seconds, leaving inadequate time for the formation of spherulites. Compared to unannealed samples, annealed samples exhibit an extremely low degree of crystallinity of about 1.8% due to a shorter annealing period to minimize excessive warping. Bhandari et al. observed a degree of crystallinity of about 20% when annealed at 90°C for 8 h, but the shrinkage percentage was not reported [32].

Three-point and four-point flexural test

The three-point and four-point flexural stress-strain curves for PLA samples with different infill patterns without and with annealing are shown in Figs. 7 and 9. For both flexural loadings, all the samples showed failure in the outer surface below or at 5% of strain. Annealed samples result in a brittle fracture with decreased flexural strain compared to the unannealed samples for all the infill patterns, irrespective of loading conditions. For the samples without and with annealing, the highest and lowest value of flexural stress under three-point and four-point bending tests is observed for the concentric and Hilbert patterns. The average and standard deviation values of flexural stress and flexural modulus for the three-point and four-point flexural test of PLA samples without and with annealing are shown in Figs. 8 and 10.

Among all the patterns, the annealed sample with alternate pattern (0°/45°) obtains the highest increment in flexural strength and modulus in both three-point and four-point bending. In four-point bending, the load is eventually distributed over the loading spans and helps to avoid premature

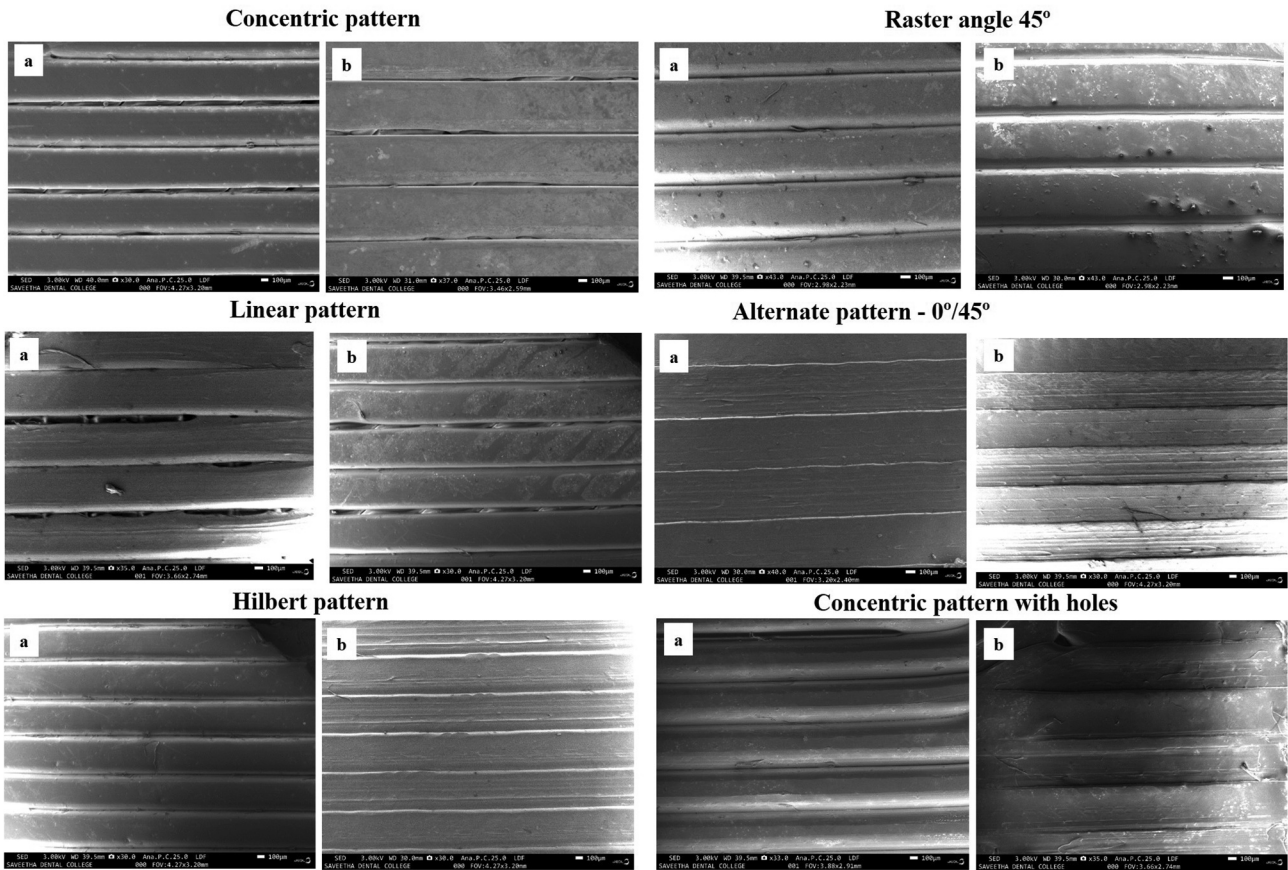


Figure 5. SEM cross-sectional surface images (a) before and (b) after annealing.

failure; thus, it obtains higher flexural strength and modulus than 3-point bending. But the Hilbert pattern shows insignificant change under the 3-point and 4-point flexural tests. Thus, annealing at 90°C for 15 min enhanced the flexural strength and modulus compared to the unannealed sample, irrespective of the fill pattern.

In the concentric pattern, the infill raster is the extension of contours or shells from the boundary and arranged perpendicular to the loading direction, thus resulting in higher flexural strength and modulus irrespective of loading condition and

annealing. The linear pattern has a long raster perpendicular to the loading direction, and the concentric pattern with holes has a long raster at the boundary, resulting in better flexural strength and modulus than other patterns but slightly lower than concentric. The raster angle 45° pattern shows better flexural strength and modulus under a 4-point than three-point bend. In the case of the Hilbert pattern, the presence of void space in the pattern shows minor flexural strength despite loading conditions. However, it obtains a better flexural modulus than the alternate pattern (0°/45°) without annealing.

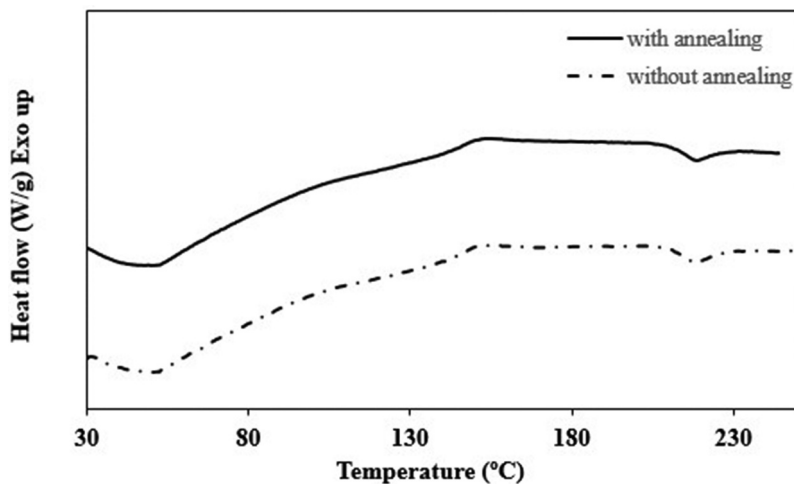


Figure 6. DSC curves for PLA printed samples before and after annealing.

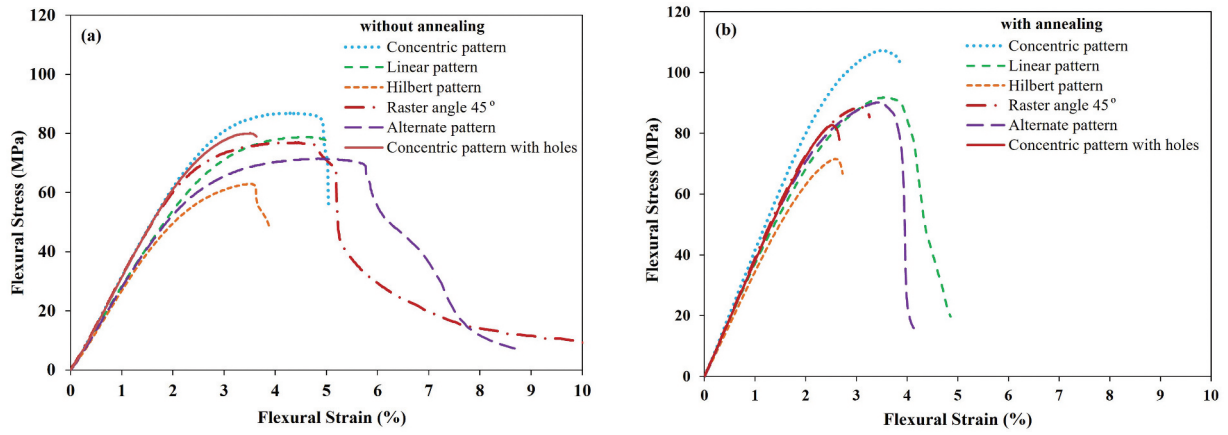


Figure 7. Three-point flexural test (a) without annealing (b) with annealing.

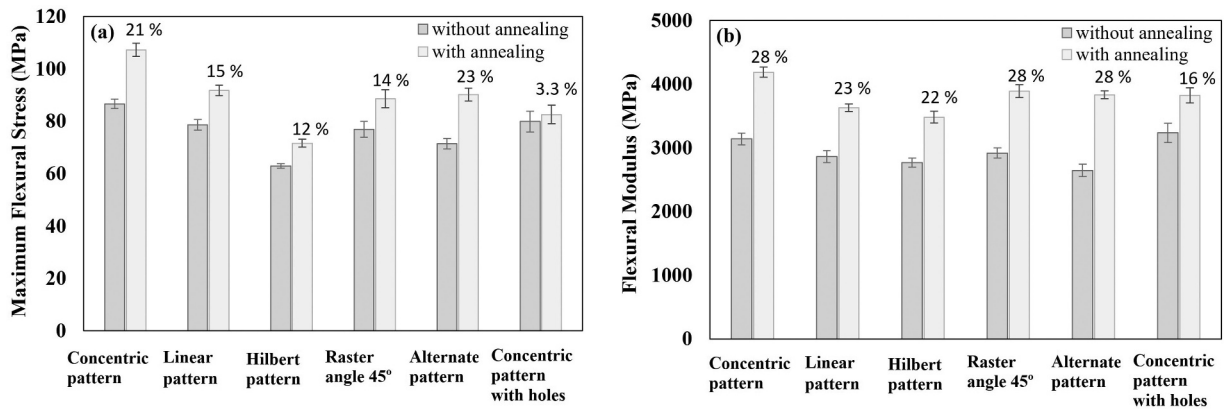


Figure 8. Average and standard deviation of 3-point flexural test (a) flexural stress (b) flexural modulus.

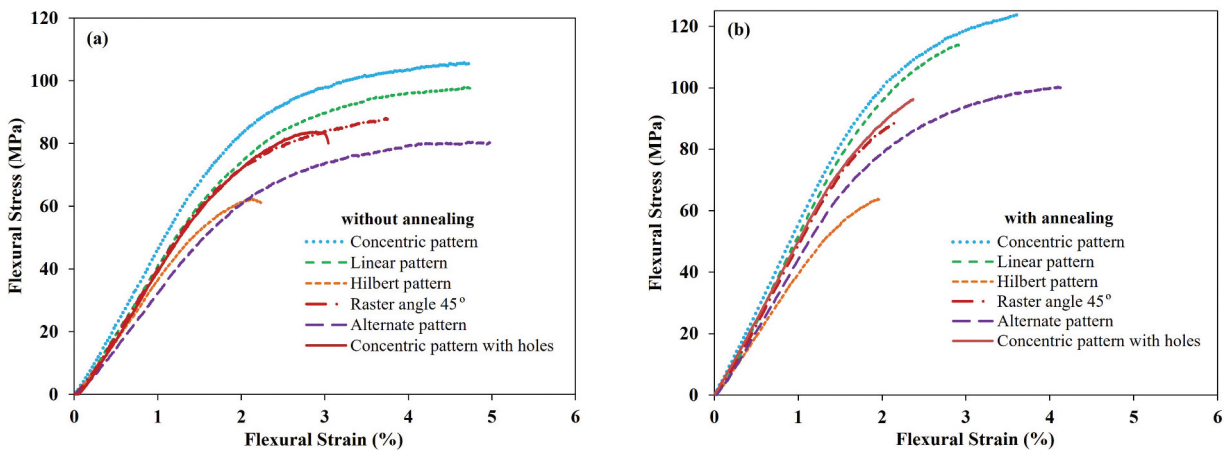


Figure 9. Four-point flexural test (a) without annealing (b) with annealing.

Akhoundi et al. observed higher flexural strength for concentric and Hilbert patterns at 100% fill density than rectilinear and honeycomb patterns under three-point bending [19]. But, the response of the Hilbert pattern under quasi-static loading was controversial to Akhoundi et al., this may be due to the difference in the deposition angle of the Hilbert pattern. Thus, the annealed PLA samples with a long

deposition path show better flexural strength and modulus than the short deposition path.

From the above results, it indicates that the fill deposition path alters the thermal history of the printed part, which ultimately influences the bonding and strength. The long deposition path experiences convection heat transfer, which results in partial solidification before it comes into contact

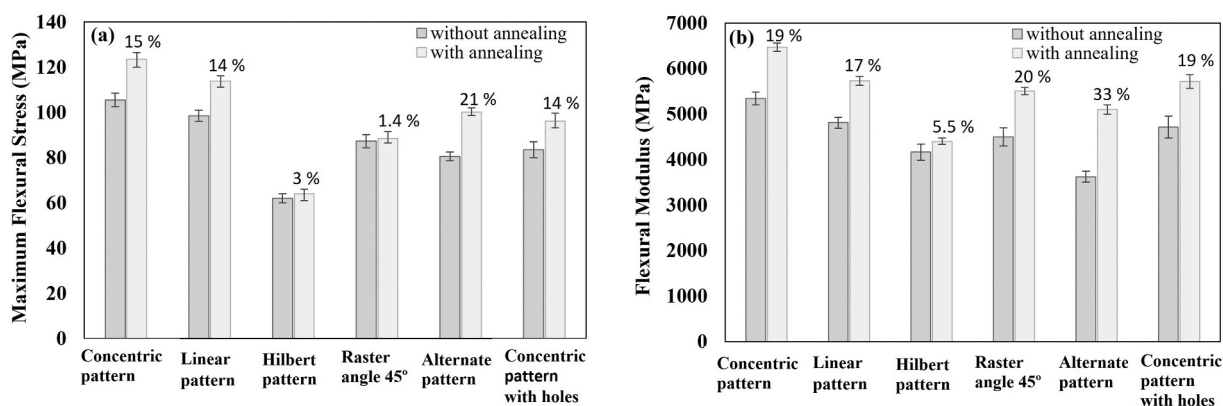


Figure 10. Average and standard deviation of 4-point flexural test (a) flexural stress (b) flexural modulus.

with the adjacent raster and shows weak interfacial contact, as observed in SEM images. In contrast, the short deposition path (Hilbert and raster angle 45°) shows lower flexural strength than long deposition paths even though it experiences conduction heat transfer and shows better interfacial contact. Similarly, the combined short and long deposition path (alternate and concentric pattern with holes) has better interfacial contact before and after annealing but possesses lower flexural strength. It is observed that after annealing, the long deposition path experiences higher shrinkage than the short deposition path. However, Hilbert, raster angle 45, alternate pattern, and concentric pattern with holes show better raster adhesion before and after annealing but result in lower flexural strength than concentric pattern. The main reason is the discontinuity or weaker interface between the infill and the shell or contour boundary. Thus, the concentric fill pattern, which is the extension of the shell, results in higher flexural strength. It is more apparent that the fill pattern and loading direction highly influence flexural performance despite raster adhesion.

Dynamic mechanical analyser

The DMA test is performed for annealed samples, as it obtains higher flexural strength than unannealed samples, irrespective of infill patterns. Figure 11 depicts that the infill pattern significantly influences the dynamic characteristics of FDM-printed PLA samples. Table 3 shows the calculated DMA parameters for various infill patterns. The storage modulus estimates the load-bearing stability at a specific temperature range. As shown in Fig. 11a, all the samples show stable glassy storage modulus plateau at 30°C to 50°C. From 50°C to 65°C, it shows a drastic drop in modulus that specifies the glass transition temperature (T_g), as the sample changes from hard glassy to soft rubbery phase. This indicates that the sample can no longer resist the deformation due to the segmental motion and molecular relaxation. As the temperature increases, the stored energy gradually decreases and thus increases the energy loss, as depicted by the storage and loss modulus curve. Beyond 65°C, the storage modulus decreases further and attains the rubbery plateau from 80°C to 90°C. It is observed that the loss

modulus increases slowly from 30 to 50°C and then significantly increases and attains peak value around 50°C to 65°C and then gradually decreases as shown in Fig. 11b. The $\tan\delta$ curve represents the damping characteristics and depicts a similar behavior of the loss modulus curve as shown in Fig. 11c. The T_g were measured from the onset of the fall in the storage modulus curve, $\tan\delta$ peak and loss modulus curve for different fill patterns. It is noted that the measured glass transition temperature is not consistent; the highest T_g is obtained from the storage modulus curve and the lowest T_g from the $\tan\delta$ curve; hence the T_g can be estimated based on the temperature range. The concentric, Hilbert, and concentric pattern with hole obtains the highest T_g compared to other patterns.

The concentric and linear patterns obtain the highest and lowest glassy storage modulus. During the glassy to a rubbery state transition, the Hilbert and the concentric pattern with holes shows a slight shift in the storage modulus curve than the concentric pattern and thus leads to high T_g as same as the concentric pattern. The raster angle 45°, alternate pattern, and linear pattern show a loss modulus peak at 58°C, with the highest peak for the raster angle 45°. The Hilbert, concentric, and concentric pattern with holes shows a slight shift in the loss modulus curve due to the broadening of relaxations and obtains the peak at 61°C. At 61°C, the highest peak obtains for Hilbert and the lowest for the concentric pattern with holes. A higher loss modulus peak indicates higher energy dissipation and higher mobility. Among all the patterns, raster angle 45° has the highest energy dissipation and indicates higher mobility or a less constrained infill pattern. Wang et al. also observed that PLA samples printed with a raster angle 45° have more tendency to dissipate energy instead of storing it [9].

The raster angle 45°, alternate pattern, and the linear pattern show a $\tan\delta$ peak at 52°C, and Hilbert, concentric, and concentric pattern with holes obtains a peak at 56°C. However, the concentric pattern shows a significant shift in the curve before attaining the $\tan\delta$ peak value compared to other patterns. Similarly, the Hilbert and concentric pattern with holes shows a shift in the $\tan\delta$ curve but less than the concentric pattern. This shift in the $\tan\delta$ curve indicates the lower segmental mobility and constraint flexibility of the infill pattern.

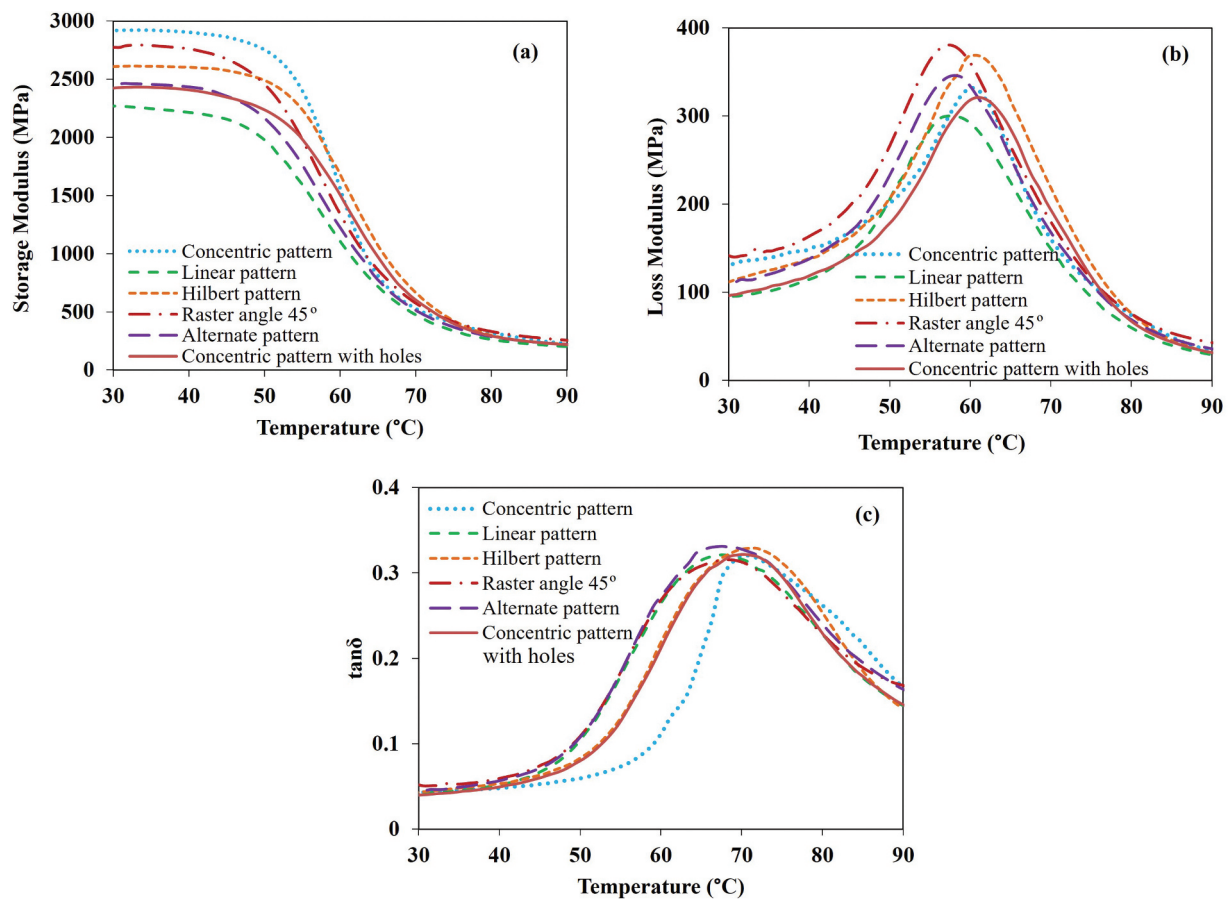


Figure 11. Dynamic flexural test under temperature sweep (a) storage modulus (b) loss modulus (c) loss factor.

Thus, the constrained flexibility of the concentric pattern may be due to the arrangement of the long deposition raster that follows the outer boundary, perpendicular to the loading direction, and higher shrinkage during annealing.

Conclusion

This work investigated FDM-printed PLA samples with various infill patterns based on dimensional changes, raster adhesion, and static and dynamic flexural properties by considering the effect of annealing. The long deposition path (concentric and linear), short deposition path (Hilbert and raster angle 45°), and combination of short and long deposition paths (alternate pattern 0°/45° and concentric pattern with holes) was analyzed, and the following conclusions were drawn:

- The fill pattern greatly influences the amount of shrinkage before and after annealing. After printing, the pattern with a short deposition path results in more shrinkage than the long deposition path. Annealing at 90° C with a dwelling time of 15 min results in less shrinkage for the short deposition path than for the long deposition path.
- SEM micrographs reveal that the shrinkage of individual raster dominates the fusion process due to the shorter annealing time to avoid excessive warpage. Better inter-layer adhesion was observed for the short and combined deposition path patterns before and after annealing.

- The fill path in concentric fill pattern was the extension of the shell and perpendicular to the loading direction; hence, it possesses superior quasi-static and dynamic flexural strength, even though it shows weaker interfacial fusion than other patterns. In other fill patterns, there was a discontinuity or weaker interface between the fill pattern and the shell. Further, it was more evident that the fill pattern and loading direction highly influenced the flexural performance despite raster adhesion.
- Thus, this study will provide guidelines to the biomedical printing industry for selecting fill patterns under flexural loading.

Disclosure statement

No potential conflict of interest was reported by the author(s).

References

- [1] Daminabo, S. C.; Goel, S.; Grammatikos, S. A.; Nezhad, H. Y.; Thakur, V. K. Fused Deposition Modeling Based Additive Manufacturing (3D Printing): Techniques for Polymer Material Systems. *Mater. Today Chem.* 2020, 16, 1002482. DOI: 10.1016/j.mtchem.2020.100248.
- [2] Alizadeh-Osgouei, M.; Li, Y.; Vahid, A.; Ataee, A.; Wen, C. High Strength Porous PLA Gyroid Scaffolds Manufactured via Fused Deposition Modeling for Tissue Engineering Applications. *Smart Mater Med.* 2021, 2, 15–25. DOI: 10.1016/j.smaim.2020.10.003.

- [3] Wu, D.; Spanou, A.; Diez-Escudero, A. P. C.; Persson, C. 3D Printed PLA/HA Composite Structures as Synthetic Trabecular Bone: A Feasibility Study Using Fused Deposition Modeling. *J. Mech. Behav. Biomed. Mater.* **2020**, *103*, 03608. DOI: [10.1016/j.jmbbm.2019.103608](https://doi.org/10.1016/j.jmbbm.2019.103608).
- [4] Sujithra, R.; Saritha, D. Effect of Fill Pattern and Printing Speed on Friction Characteristics of FDM Printed Polylactic Acid Polymer. *Adv. Mater. Technol.* **2022**, *2021*(sup3), 1583–1592. DOI: [10.1080/2374068X.2021.1948707](https://doi.org/10.1080/2374068X.2021.1948707).
- [5] Lay, M.; Thajudin, M. L. N.; Hamid, Z. A. A.; Rusli, A.; Abdullah, M. K.; Shuib, R. K. Comparison of Physical and Mechanical Properties of PLA, ABS and Nylon 6 Fabricated Using Fused Deposition Modeling and Injection Molding. *Compos. B Eng.* **2019**, *176*, 107341. DOI: [10.1016/j.compositesb.2019.107341](https://doi.org/10.1016/j.compositesb.2019.107341).
- [6] Gao, X.; Qi, S.; Kuang, X.; Su, Y.; Li, J.; Wang, D. Fused Filament Fabrication of Polymer Materials: A Review of Interlayer Bond. *Addit. Manuf.* **2021**, *37*, 101658. DOI: [10.1016/j.addma.2020.101658](https://doi.org/10.1016/j.addma.2020.101658).
- [7] Zhang, Y.; Phil, J.; Seung, C.; Moon, K. Effect of Geometry on the Mechanical Response of Additively Manufactured Polymer. *Polym. Test.* **2021**, *100*, 107245. DOI: [10.1016/j.polymertesting.2021.107245](https://doi.org/10.1016/j.polymertesting.2021.107245).
- [8] Popescu, D.; Zapciu, A.; Amza, C.; Baci, F.; Marinescu, R. FDM Process Parameters Influence Over the Mechanical Properties of Polymer Specimens: A Review. *Polym. Test.* **2018**, *69*, 157–166. DOI: [10.1016/j.polymertesting.2018.05.020](https://doi.org/10.1016/j.polymertesting.2018.05.020).
- [9] Wang, S.; Ma, Y.; Deng, Z.; Zhang, S.; Cai, J. Effects of Fused Deposition Modeling Process Parameters on Tensile, Dynamic Mechanical Properties of 3D Printed Polylactic Acid Materials. *Polym. Test.* **2020**, *86*, 106483. DOI: [10.1016/j.polymertesting.2020.106483](https://doi.org/10.1016/j.polymertesting.2020.106483).
- [10] Song, Y.; Li, Y.; Song, W.; Yee, K.; Lee, K.-Y.; Tagarielli, V. L. Measurements of the Mechanical Response of Unidirectional 3D-Printed PLA. *Mater. Des.* **2017**, *123*, 154–164. DOI: [10.1016/j.matdes.2017.03.051](https://doi.org/10.1016/j.matdes.2017.03.051).
- [11] Koch, C.; Hulle, L. V.; Rudolph, N. Investigation of Mechanical Anisotropy of the Fused Filament Fabrication Process via Customized Tool Path Generation. *Addit. Manuf.* **2017**, *16*, 138–145. DOI: [10.1016/j.addma.2017.06.003](https://doi.org/10.1016/j.addma.2017.06.003).
- [12] Chacón, J. M.; Caminero, M. A.; García-Plaza, E.; Núñez, P. J. Additive Manufacturing of PLA Structures Using Fused Deposition Modelling: Effect of Process Parameters on Mechanical Properties and Their Optimal Selection. *Mater. Des.* **2017**, *124*, 143–157. DOI: [10.1016/j.matdes.2017.03.065](https://doi.org/10.1016/j.matdes.2017.03.065).
- [13] Tang, C.; Liu, J.; Yang, Y.; Liu, Y.; Jiang, S.; Hao, W. Effect of Process Parameters on Mechanical Properties of 3D Printed PLA Lattice Structures. *Compos. C.* **2020**, *3*, 100076. DOI: [10.1016/j.jcomc.2020.100076](https://doi.org/10.1016/j.jcomc.2020.100076).
- [14] Azadi, M.; Dadashi, A.; Dezhianian, S.; Kianifar, M.; Torkaman, S.; Chiyani, M. High-Cycle Bending Fatigue Properties of Additive-Manufactured ABS and PLA Polymers Fabricated by Fused Deposition Modeling 3D-Printing. *Forces In Mech.* **2021**, *3*, 100016. DOI: [10.1016/j.finmec.2021.100016](https://doi.org/10.1016/j.finmec.2021.100016).
- [15] Lubomdo, C.; Huneault, M. A. Effect of Infill Patterns on the Mechanical Performance of Lightweight 3D-Printed Cellular PLA Parts. *Mater. Today Commun.* **2018**, *17*, 214–228. DOI: [10.1016/j.mtcomm.2018.09.017](https://doi.org/10.1016/j.mtcomm.2018.09.017).
- [16] Mohamed, O. A.; Masood, S. H.; Bhowmik, J. L. Experimental Investigations of Process Parameters Influence on Rheological Behavior and Dynamic Mechanical Properties of FDM Manufactured Parts. *Mater. Manuf.* **2016**, *31*(15), 1983–1994. DOI: [10.1080/10426914.2015.1127955](https://doi.org/10.1080/10426914.2015.1127955).
- [17] Penumakal, P. K.; Santo, J.; Thomas, A. A Critical Review on the Fused Deposition Modeling of Thermoplastic Polymer Composites. *Compos. B Eng.* **2020**, *201*, 108336. DOI: [10.1016/j.compositesb.2020.108336](https://doi.org/10.1016/j.compositesb.2020.108336).
- [18] Sathies, T.; Senthil, P.; Anoop, M. S. A Review on Advancements in Applications of Fused Deposition Modeling Process. *Rapid Prototyp. J.* **2020**, *26*(4), 669–687. DOI: [10.1108/RPJ-08-2018-0199](https://doi.org/10.1108/RPJ-08-2018-0199).
- [19] Akhoundi, B.; Behraves, A. H. Effect of Filling Pattern on the Tensile and Flexural Mechanical Properties of FDM 3D Printed Products. *Exp. Mech.* **2019**, *59*(6), 883–897. DOI: [10.1007/s11340-018-00467-y](https://doi.org/10.1007/s11340-018-00467-y).
- [20] Rankin, T. M.; Giovinco, N. A.; Cucher, D. J.; Watts, G.; Hurwitz, B.; Armstrong, D. G. Three-Dimensional Printing Surgical Instruments: Are We There Yet. *J. Surg. Res.* **2014**, *189*(2), 193–197. DOI: [10.1016/j.jss.2014.02.020](https://doi.org/10.1016/j.jss.2014.02.020).
- [21] George, M.; Aroom, K. R.; Hawes, H. G.; Gill, B. S.; Love, J. 3D Printed Surgical Instruments: The Design and Fabrication Process. *World J. Surg.* **2017**, *41*, 314–319. DOI: [10.1007/s00268-016-3814-5](https://doi.org/10.1007/s00268-016-3814-5).
- [22] Gomez-Gras, G.; Jerez-Mesa, R.; Travieso-Rodriguez, J. A.; Llumafuentes, J. Fatigue Performance of Fused Filament Fabrication PLA Specimens. *Mater. Des.* **2018**, *140*, 278–285. DOI: [10.1016/j.matdes.2017.11.072](https://doi.org/10.1016/j.matdes.2017.11.072).
- [23] Aloyaydi, B.; Sivasankaran, S.; Mustafa, A. Investigation of Infill Patterns on Mechanical Response of 3D Printed Polylactic Acid. *Polym. Test.* **2020**, *87*, 106557. DOI: [10.1016/j.polymertesting.2020.106557](https://doi.org/10.1016/j.polymertesting.2020.106557).
- [24] Birosz, M. T.; Ledenyák, D.; M, A. Effect of FDM Infill Patterns on Mechanical Properties. *Polym. Test.* **2022**, *113*, 107654. DOI: [10.1016/j.polymertesting.2022.107654](https://doi.org/10.1016/j.polymertesting.2022.107654).
- [25] Ayatollahi, M. R.; Nabavi-Kivi, A.; Bahrami, B.; Yahya, M. Y.; Khosravi, M. R. The Influence of In-Plane Raster Angle on Tensile and Fracture Strengths of 3D-Printed PLA Specimens. *Eng. Fract. Mech.* **2020**, *237*, 107225. DOI: [10.1016/j.engfracmech.2020.107225](https://doi.org/10.1016/j.engfracmech.2020.107225).
- [26] Kiendl, J.; Gao, C. Controlling Toughness and Strength of FDM 3D-Printed PLA Components Through the Raster Layout. *Compos. B Eng.* **2020**, *180*, 107562. DOI: [10.1016/j.compositesb.2019.107562](https://doi.org/10.1016/j.compositesb.2019.107562).
- [27] Yao, T.; Yea, J.; Deng, Z.; Zhang, K.; Ma, Y.; Ouyang, H. Tensile Failure Strength and Separation Angle of FDM 3D Printing PLA Material: Experimental and Theoretical Analyses. *Compos. B Eng.* **2020**, *188*, 107894. DOI: [10.1016/j.compositesb.2020.107894](https://doi.org/10.1016/j.compositesb.2020.107894).
- [28] Zhao, Y.; Chen, Y.; Zhou, Y. Novel Mechanical Models of Tensile Strength and Elastic Property of FDM AM PLA Materials: Experimental and Theoretical Analyses. *Mater. Des.* **2019**, *181*, 108089. DOI: [10.1016/j.matdes.2019.108089](https://doi.org/10.1016/j.matdes.2019.108089).
- [29] Szust, A.; Adamski, G. Using Thermal Annealing and Salt Remelting to Increase Tensile Properties of 3D FDM Prints. *Eng. Fail. Anal.* **2022**, *132*, 105932. DOI: [10.1016/j.engfailanal.2021.105932](https://doi.org/10.1016/j.engfailanal.2021.105932).
- [30] Reis, I. A.; Claro, P. I. C.; Marcomini, A. L.; Mattoso, L. H. C.; Silva, S. P.; Neto, A. R. S. Annealing and Crystallization Kinetics of Poly(lactic Acid) Pieces Obtained by Additive Manufacturing. *Polym. Eng. Sci.* **2021**, *61*(7), 2097–2104. DOI: [10.1002/pen.25737](https://doi.org/10.1002/pen.25737).
- [31] Wach, R. A.; Wolszczak, P.; Adamus-Włodarczyk, A. Enhancement of Mechanical Properties of FDM-PLA Parts via Thermal Annealing. *Macromol. Mater. Eng.* **2018**, *303*(9), 1800169. DOI: [10.1002/mame.201800169](https://doi.org/10.1002/mame.201800169).
- [32] Bhandari, S.; Lopez-Anido, R. A.; Gardner, D. J. Enhancing the Interlayer Tensile Strength of 3D Printed Short Carbon Fiber Reinforced PETG and PLA Composites via Annealing. *Addit. Manuf.* **2019**, *30*, 100922. DOI: [10.1016/j.addma.2019.100922](https://doi.org/10.1016/j.addma.2019.100922).

Development of Biocomposites Using Novel Green Pea Pod Lignin and Hybridised Pod Sheath Fiber-Bamboo Epoxy Composite for Human Prosthetic Application

Journal:	<i>Part L: Journal of Materials: Design and Applications</i>
Manuscript ID	JMDA-23-0703.R1
Manuscript Type:	Original article
Date Submitted by the Author:	n/a
Complete List of Authors:	R, Sujithra; Motilal Nehru National Institute of Technology, D, Saritha; Chaitanya Bharathi Institute of Technology Proddatur
Keywords:	Polymer Matrix Composites < Composites < Materials by Type, Bioactive Composites < Biomaterials (also Medical Biomaterials), Biodegradable Materials < Biomaterials (also Medical Biomaterials), Polymers < Materials by Type, Superplasticity < Materials: Mechanical Properties/ Strength, Materials Testing
Abstract:	<p>In this research epoxy based biocomposites were developed using novel green pea pod lignin (GPL) and hybridised pod sheath fiber-bamboo epoxy composite for human prosthetic applications. The outcomes of this investigation demonstrate that the inclusion of lignin, up to 1.0 vol. %, yields a tensile strength of 159 MPa, flexural strength of 202 MPa, inter-laminar shear strength of 28.6 MPa and Izod impact toughness of 5.93 J. In terms of wear resistance, the composite designation with 2.0 vol. % of lignin exhibited lower wear loss of 0.01 g and 0.38 of coefficient of friction. Both the mechanical and wear results are statistically significant with 'P < 0.05), confirmed by analysis of variance (ANOVA). Additionally, the highest fatigue life counts were recorded for composite with 1 vol. % of lignin with counts of 34,632 cycles for 30% of the ultimate tensile strength. Furthermore, the addition of lignin up to 2.0 vol. % resulted in the lowest contact angle of 82° and water absorption percentage of 0.16%. Scanning electron microscopy (SEM) analysis indicated that the incorporation of surface-treated fibers and lignin uniformly dispersed and adhered more. Based on these findings, it is evident that the composite containing 40 vol. % of sheath/bamboo hybridized fiber with 1.0 vol. % of lignin in the epoxy matrix represents the most favourable outcome for prosthetic applications.</p>

SCHOLARONE™
Manuscripts

Development of Biocomposites Using Novel Green Pea Pod Lignin and Hybridised Pod Sheath Fiber-Bamboo Epoxy Composite for Human Prosthetic Application

Sujithra R^a, and Saritha D^{b*}

^aDepartment of applied mechanics, Motilal Nehru National Institute of Technology, Allhabad, prayagraj, UP,211004,India

^bDepartment of Chemistry, Chaitanya Bharathi Institute of Technology, Hyderabad, Telangana, Gandipet, 500075, India

*dsarithamnnit@hotmail.com

Abstract

In this research epoxy based biocomposites were developed using novel green pea pod lignin (GPL) and hybridised pod sheath fiber-bamboo epoxy composite for human prosthetic applications. The outcomes of this investigation demonstrate that the inclusion of lignin, up to 1.0 vol. %, yields a tensile strength of 159 MPa, flexural strength of 202 MPa, inter-laminar shear strength of 28.6 MPa and Izod impact toughness of 5.93 J. In terms of wear resistance, the composite designation with 2.0 vol. % of lignin exhibited lower wear loss of 0.01 g and 0.38 of coefficient of friction. Both the mechanical and wear results are statistically significant with 'P < 0.05), confirmed by analysis of variance (ANOVA). Additionally, the highest fatigue life counts were recorded for composite with 1 vol. % of lignin with counts of 34,632 cycles for 30% of the ultimate tensile strength. Furthermore, the addition of lignin up to 2.0 vol. % resulted in the lowest contact angle of 82° and water absorption percentage of 0.16%. Scanning electron microscopy (SEM) analysis indicated that the incorporation of surface-treated fibers and lignin uniformly dispersed and adhered more. Based on these findings, it is evident that the composite containing 40 vol. % of sheath/bamboo hybridized fiber with 1.0 vol. % of lignin in the epoxy matrix represents the most favourable outcome for prosthetic applications.

Keywords: Hybrid composite; Lignin; Fibre; Wear; Mechanical properties; Hydrophobicity

1 Introduction

The manufacture of synthetic petroleum-based products as well as glass, carbon, aramid and other synthetic fibers emits a huge volume of carbon emissions gases into the environment

[1]. Recent decades, it has been thought that using ecologically sustainable low carbon materials would lessen the global damage by petroleum-based products. These products will be biodegradable, recyclable, and eco-friendly. Completely green composites are a form of biocomposite made using biofibers and resins that come from sustainable agro waste and natural resources inputs [2]. This form of composites is degraded and decomposed without affecting the environmental ecosystems at the end of its useful lifespan. In the creation of biocomposites, various types of plant-based fiber like flax, abaca, jute, bamboo sisal, aloe vera, hemp, pineapple and kenaf have been employed commonly [3]. Natural fibers have a superior property such as a higher strength to weight ratio, corrosion resistances, high fracture toughness, recyclability, and are sustainable, giving them distinct benefits over other materials [4]. Because they are more environmentally friendly and perform better mechanically, polymer biocomposites made from natural fibers have gained the interest of researchers and scientists. Producing biocomposites from renewable sources is a difficult operation that requires metals, polymers, and ceramics [5]. Due to the biocompatibility of such biocomposites it already has been utilized as drug, antibiotics and gene delivery, tissue engineering, orthopaedics, as well as in aesthetic orthodontics applications. Acceptance by the human body is the most important prerequisite for materials to be employed as prosthetics. Biocomposites has the ability to substitute damaged or deteriorated organs or tissues, or act as a framework for their regeneration, increasing the quality of life of sufferer [6].

Egoh et al [7] examined the application of bamboo in the latest decades with a focus on orthopaedics and prosthetic remediation. The author noted that creating artificial limbs to help people make up for the loss of a limb has been a practice dating back to the ancient Egyptians and French surgeon Ambroise Pare. In this study, applications of bamboo fiber such as the bamboo endoskeleton patellar-tendon-bearing prosthesis and the bamboo above-knee prosthesis with coco-nut knee joint were reviewed. However, Kulandaivel et al [8] investigated the extraction and characterization of unique natural cellulose-based fibers of pigeon pea plant. Additional decomposition between the temperature ranges of 250°C and 400°C, with a very noticeable peak at 358°C, demonstrates that cellulose degradation is responsible for a significant mass loss of roughly 52.3%. Similar research was conducted by Bhiri et al. [9] on the extraction and physicochemical characterization of pea by-products for the purpose of isolating cellulosic microbes. Thermogravimetric analysis indicated the superior thermal stability of cellulosic

1
2
3 microfibers compared to the pure material. However, green pea sheath is abundantly available
4 worldwide and fiber extraction is also cheaper. But this fiber has lesser strength as compared to
5 other natural fiber hence the inbound hybridization was done with bamboo fiber. This
6 hybridization provides new chances to expand the functionality of such fiber materials,
7 especially in advanced applications, by enhancing the toughness or impact-resistance. In
8 addition, hybridization of fibers offers greater design flexibility than non-hybrid
9 fiber composites, which results in a collaborative effect that isn't possible with any particular
10 material by alone. The choice of the fibers, a good fiber combination, and their interaction in the
11 hybrid system are just a few ways to produce the synergetic effect [10].
12
13
14
15
16
17
18

19 In the domain of particulate strengthening, various substances like cellulose, lignin,
20 bagasse powder, biosilica, biochar and silica fume are commonly used in polymer composite
21 applications [11]. These particulates are different in nature starting from metallic to ceramics and
22 possess their unique advantages. Among various types there are particulates they are in the class
23 of biopolymer too. In these biopolymers, lignin stands out as highly functional biopolymer with
24 extensive applications in composite technology [12]. This lignin has advantages such as
25 improved cross-linking density and reinforcing ability of the base polymer due to its long,
26 continuous chain structure and ability to make interpenetrating polymer networks [13]. Thus, it is
27 suitable in creating high load bearing structural composites for prosthetic and medical
28 applications where high degree of eco-friendly material application is required. Khan et al [14]
29 published their research finding on human prosthetic leg material, which is made of ABS-
30 biocarbon derived from abaca bracts. According to author the addition of biocarbon into the bare
31 ABS improved the load bearing ability as well as structural rigidity. Similarly, Alshahrani et al
32 [15] revealed the effectiveness of adding grape stalk derived lignin as strengthening material for
33 bamboo fiber reinforced polyester composite, which is aimed as human prosthetic leg and limb
34 material. Author claimed that the addition of grape stalk lignin into the polyester significantly
35 improved the tensile, flexural, wear and thermal degradation stability. Thus it is clear that the
36 addition lignin into the polymer could improve their functional and load bearing competency in
37 the prosthetic applications.
38
39
40
41
42
43
44
45
46
47
48
49
50
51

52
53 Consequently, this study aims to explore the preparation of lignin extracted from green
54 pea pods and its impact on epoxy composites. It also recognized a significant gap in natural fiber
55
56
57

1
2
3 composites, particularly in the hybridization of bamboo fibers with pod sheath fibers in epoxy
4 composites. Therefore, the research endeavor sought to create biocomposites by incorporating
5 green pea pod lignin and hybridizing pod sheath fibers with bamboo in epoxy composites. The
6 primary focus of this investigation revolved around assessing the mechanical, wear, and fatigue
7 properties of these composites. To achieve this, composite laminates were meticulously crafted
8 using the hand layup process and subsequently subjected to comprehensive characterization
9 following the relevant ASTM standards. The ultimate goal is to produce mechanically robust and
10 wear-resistant composites, potentially suitable for applications in human prosthetics.
11
12
13
14
15
16

17 **2 Experimental investigations:**

18 **2.1 Materials**

19
20
21
22 In this study, an Araldite LY556 epoxy resin which having a density of 1.18 g/cm³ and a
23 molecular mass of 190,1 g/mol was utilized. TETA HY951, a curing agent having a density of
24 1.04 g/cm³, is used to cure composites. Similarly, bamboo fibers with a density of 1.45 g/cm³
25 were acquired from the Metro Composites Research and Training Institute in Chennai, India.
26 Green pea pods gathered from nearby farms were used to manufacture the pea sheath fiber and
27 green pea pod lignin. This green sheath fiber has a density of 1.1g/cc, is 50-70 mm long, and has
28 a diameter of 180-220 μm. It also consist nearly 40-55% cellulose, 18% holocellulose, and 1.8%
29 lignin. Sigma Aldrich in the United States provided the silane surface modification 3-
30 Aminopropyltrimethoxysilane (APTMS). Additional components, such as ethanol, NaOH having
31 concentration of 1 N, acetic acid, and distilled water, are obtained from Merck India.
32
33
34
35
36
37
38
39

40 **2.2 Fiber Extraction**

41
42
43 The fibers were manufactured according to earlier research [16]. This study utilized
44 retting and manual shredding to produce the fibers from the green pods. The green pea sheath
45 was acquired from surrounding fields and washed three to four times to remove any traces of dirt
46 and foreign debris. The cleansed sheaths were then immersed in water for 72 h to ensure their
47 thorough decomposition. After draining and combing the fleshy materials, the existing fibers are
48 separated. To eliminate the acquired water molecules, the separated fibers and water was
49 repeatedly rinsed and then dried in the sun. Figure 1 depicts the procedure for preparing fiber
50 from green pea sheath with a SEM image of the resulting fiber. The surface of this fiber was
51
52
53
54
55
56
57
58
59
60

further treated with a base (1N concentration of NaOH) using a simple immersion procedure. After 10 minutes of immersion in a 1 N base solution, the fiber was drained. The extracted fiber, which had undergone surface treatment, was subsequently subjected to drying in an oven to eliminate any residual moisture before proceeding with further processing. [17].

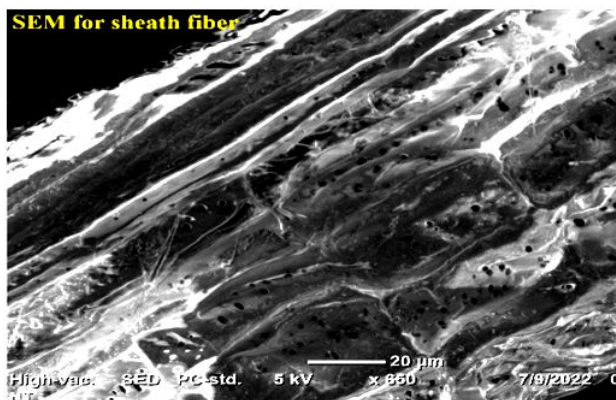
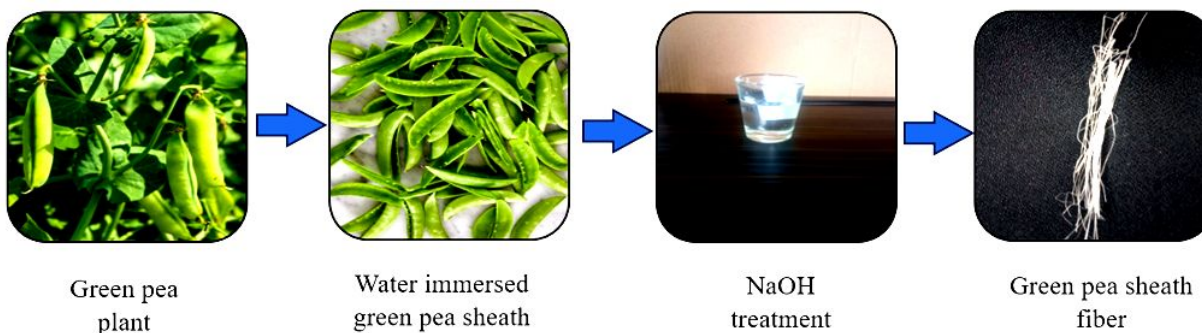


Figure 1 Green pea sheath fiber preparation and SEM images of fiber

2.3 Lignin Preparation

The lignin preparation process began with the acquisition of green pea pods from a local farmer. These pods were initially cleaned with tap water and left to sun-dry for a period of 48 hours to ensure the removal of any residual moisture. Once thoroughly dried, the green pea pods were further processed by grinding them into pellets using a crusher. In the first step of lignin extraction, 2 g of the powdered green pea pods were combined with 12 mm of H_2SO_4 and 3 mm of distilled water in a beaker, as described in reference [18]. The mixture was constantly stirred for three hours using a hot plate magnetic stirrer, maintaining a temperature of approximately 25°C by placing the beaker in an ice water bath. After this three-hour stirring period, the mixture

was filtered through filter paper and allowed to air-dry for duration of twenty-four hours. Subsequently, in the second phase of the process, a similar solution was created using the dried powdered material and stirred for two hours at room temperature with the assistance of a magnetic stirrer. After two hours of stirring, the solution was filtered using distilled water until the pH of the drained water reached 7.0. The filtered material was then dried. For a visual representation of the lignin preparation process, including SEM (Scanning Electron Microscope) and XRD (X-Ray Diffraction) analyses please refer to Figure 2.

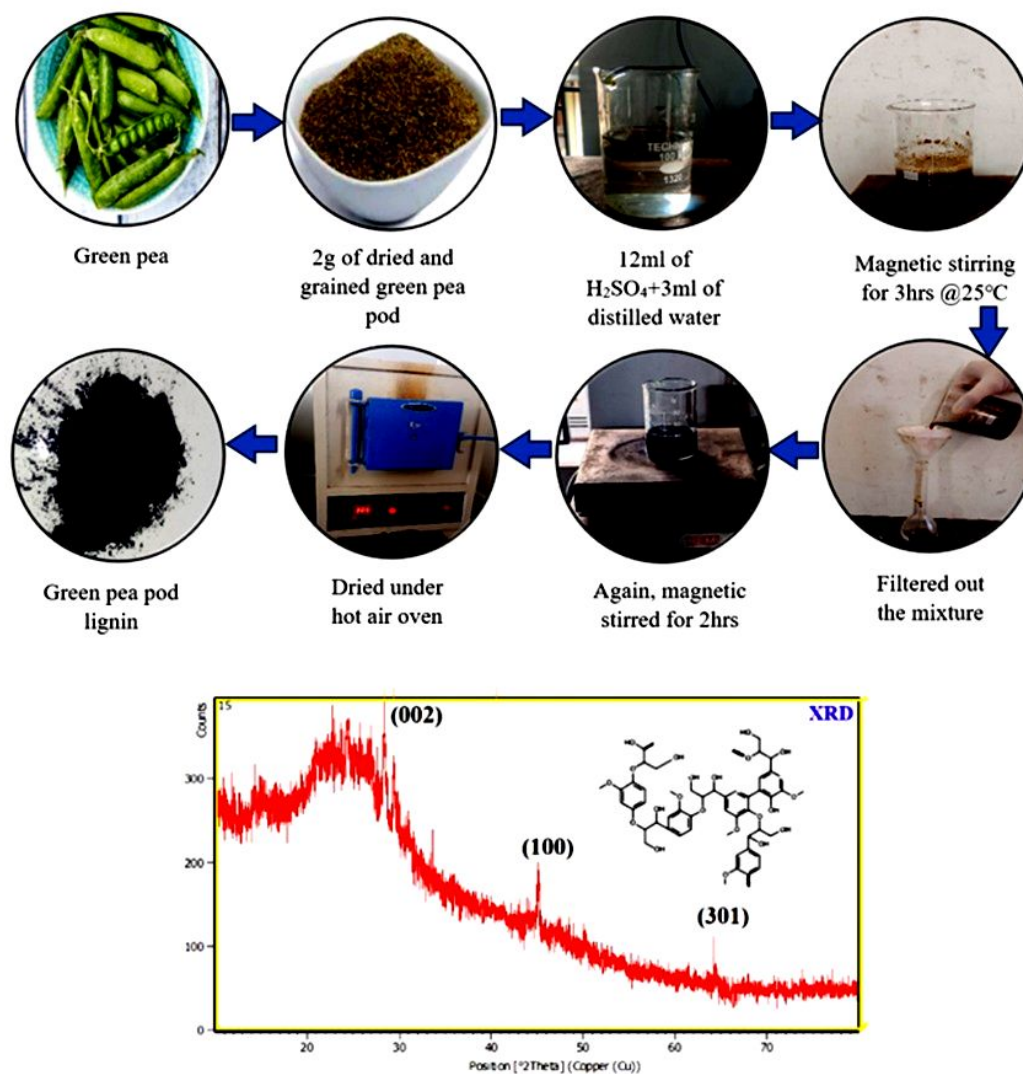


Figure 2 Lignin preparation from green pea plant with XRD

Powder X-ray diffractors were utilized for the x-ray diffraction (Match phase analyser, Germany). Most of those exhibit a peak at 22.6° (2θ), which is reflective of type I crystalline cellulose (belongs to the 002 plane), and a second peak at 34.5° (2θ), which corresponds to either the 100 or 301 planes. Lignin molecules are randomly orientated and tend to generate intermolecular and intramolecular hydrogen bridges. Lignin has a highly crystalline packing density and may contain up to 80% crystalline zones [19].

2.4 Hybridized Bamboo-pea sheath fibre woven mat making

The prepared sheath fibres are blended with bamboo long fibre at 25 vol. % via manual twisting and rolling process. Natural cassava glue is marginally applied to make a tight bond between base fibre (bamboo) and secondary fibre (sheath pea fibre). Since the sheath fibre is low strength, it can be blended along with high strength fibre and make use of woven mat with different weaving styles. In this the 25:75 vol. % sheath and bamboo fibre yarns are further subjected to weaving using hand looming machine. Both the weft and warp are engaged with hybridized fibre of sheath and bamboo with the weaving style of in-plane interplay. The weaving process produced an outcome of 1m/h with a GSM of 200. Figure 3 shows the hybridized fibre mat made using sheath pea fibre and bamboo.

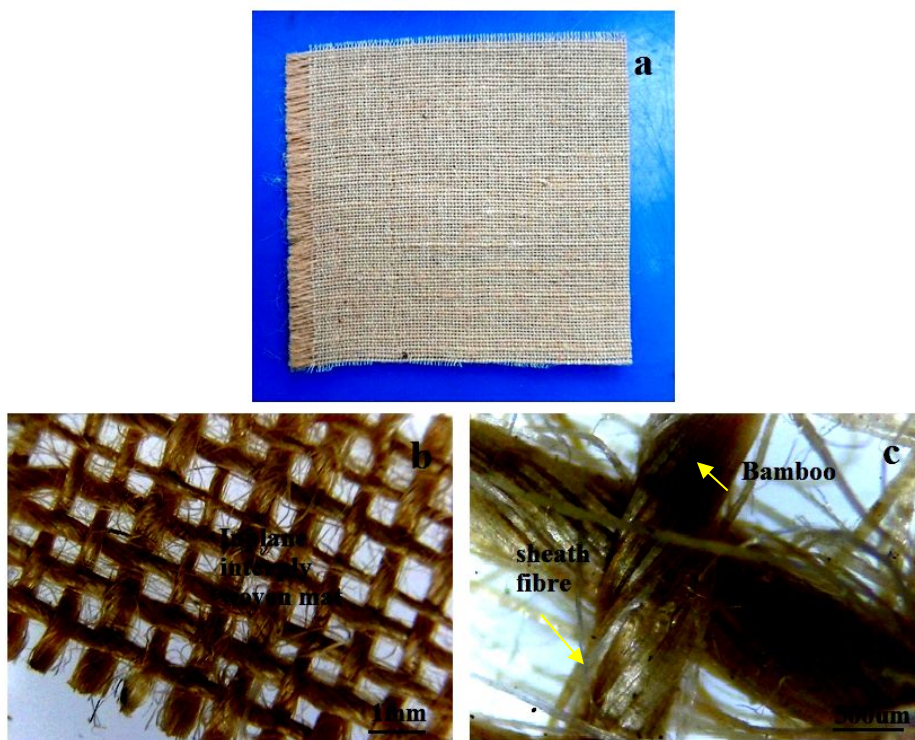


Figure 3 views of hybridised fibre of pea sheath fibre and bamboo (a) photographic, (b) optical microscope image with interplay arrangement and (c) fibre yarns of both sheath fibre and bamboo

2.5 Silane Surface Treatment

The surface treatment of hybridized fiber and lignin was performed with a silane coupling agent via acid hydrolysis process for better adhesion properties with resin. In this an aqueous solution was prepared using 95 % of ethanol and 5% of water. After thorough mix up, the silane substance of 4 wt. % was added into the admixture as drop by drop. The resulted solution was then stirred thoroughly using ultrasonicator for 10 min ensured the silane is completely dissolved in the aqueous solution. Meanwhile the pH of the solution is adjusted to 4.5 using acetic acid for better hydrolysis. The fibre and particle are then immersed in the silane solution and soaked for 10 min and then separated and dried in a hot air oven for 10 min to form condensed Si-O-Si structure [20].

2.6 Composite Fabrication

In this study, the fabrication of composites involved a manual process known as hand layup technique. Initially, a mold was prepared by cleaning and applying a generous coat of wax to the desired surface. This wax coating served the purpose of facilitating the easy removal of the final product from the mold. A homogeneous solution was prepared by mixing epoxy resin and the surface-treated green pea pod lignin with the assistance of a magnetic stirrer. Once the solution achieved uniformity, a hardener was added and thorough stirring ensured proper mixing. After the mixture was well-prepared, it underwent a degasification process to remove any trapped air or bubbles. The degassed resin was poured into the prepared mold, and layers of fiber mat were placed one by one on top of it. The composite was allowed to cure at room temperature. Subsequently, it underwent a post-curing process for 48 h at a temperature of 120°C [21]. Table 1 provides details of the composite designations for different combinations used in the study.

Table 1 Composite designation for various hybrid epoxy composites

Composite designation	Resin (vol.%)	Bamboo-pea sheath fibre	Lignin macromolecule
-----------------------	---------------	-------------------------	----------------------

		(vol.%)	(vol.%)
E	100	-	-
EP	60	40	-
EPL1	59.5	40	0.5
EPL2	59	40	1.0
EPL3	58	40	2.0

3 Characterizations

Upon completion of the curing process, a thorough visual inspection was conducted to detect any surface defects or imperfections. To obtain acceptable ASTM test specimens from the cured composite plates, an abrasive water jet machine (Maxiem water jets, 1515, KENT) was used [22]. The hybridized epoxy composites underwent mechanical tests in accordance with ASTM standards. Tensile strength testing followed the ASTM D-3039 standard (175 x 25 x 3 mm), while flexural strength was assessed using ASTM D-790 (125 x 13 x 3 mm) specifications. Inter-Laminar Shear Strength (ILSS) was evaluated in compliance with ASTM D-2344 (30 x 9 x 3 mm). All these mechanical tests were performed using a universal testing machine (INSTRON 4355, UK) with a cross-head speed of 1.5 mm/min. In addition, Izod impact testing was carried out in line with ASTM D-256 (125 x 13 x 3 mm) standards, utilizing a mini-impact tester from Krystal Equipment, India, Pvt. Ltd., which had a measuring capacity of 20 J. Similarly, wear properties of the epoxy resin hybrid composite was evaluated using a pin-on-disc test setup with a track diameter of 150 mm, disc speed of 500 rpm and a load of 5 N. Wear resistance was assessed using 3 mm thick by 5 mm wide flat specimens. Similarly, the fatigue behavior was examined with a tension-tension fatigue machine (MTS Landmark 370 load frame, United States), subjecting dumbbell-shaped specimens to ASTM D 3479. The sample measures a length of 150mm, width of 20mm, span length of 110mm, span width of 10mm, span radius of 60mm and thickness of 3 mm. The testing process incorporated specific parameters: a loading frequency of 5 Hz, a stress ratio of 0.1, a maximum load of 1.28 kN (30% of the ultimate tensile load, as 60% and 90% of UTS), an elastic modulus of 6.00 GPa, and a controlled environment at 23°C. Each test was repeated with 5 uniformly shaped specimens, and the average values were calculated. Furthermore, a sessile drop contact angle meter (HO-IAD-CAM-01, India) was used

1
2
3 to assess the hydrophobicity of composites. It has manual dispensing with camera interface for
4 measuring contact angle of liquids on solid surfaces. The surface over which contact angle is to
5 be measured is held in horizontal position to find out contact angle using sessile drop method.
6

7
8 Similarly, water absorption % of composites was accessed via water immersion method in
9 according to ASTM D 570. Square shaped specimens of 60 mm were immersed in water for 24 h
10 and the difference in weight was converted as % of water uptake. Finally, a field-emission CARL
11 ZEISS Supra-55 scanning electron microscope from Germany was employed to examine the
12 surface morphology of the composites. Prior to scanning, the broken surfaces of the samples
13 were coated with a layer of gold for analysis.
14
15
16
17
18

19 **4 Results and Discussion:**

20 **4.1 Mechanical Properties**

21
22
23
24 In Figure 4, the mechanical properties of the hybridized epoxy resin composites are
25 illustrated. Composite designation "E" exhibits lower mechanical values, approximately 62 MPa
26 for tensile strength, 2.168 GPa for tensile modulus, 96 MPa for flexural strength, 3.824 GPa for
27 flexural modulus, 0.36 J for Izod impact, and an 86 Shore-D hardness. These values reflect the
28 poor strength of pure epoxy composites, attributed to the uneven load distribution and the brittle
29 nature of the material [23]. However, the introduction of 40 vol. % of hybridized bamboo fiber
30 and green pea sheath fibers in pure epoxy composites significantly enhances the mechanical
31 properties. Tensile strength, tensile modulus, flexural strength, flexural modulus, inter-laminar
32 shear strength (ILSS), Izod impact, and hardness all increase to around 128 MPa, 5.38 GPa, 152
33 MPa, 6.08 GPa, 24.7 MPa, 3.71 J, and 87 Shore-D for composite designation "EP." This
34 improvement is attributed to the ability of hybridized sheath and bamboo fibers to evenly
35 distribute applied loads throughout the matrix, resulting in enhanced properties. The presence of
36 high-cellulose bamboo fiber in combination with pea sheath fiber further strengthens the
37 composite [24].
38
39
40
41
42
43
44
45
46
47
48

49 Additionally, the incorporation of green pea lignin particles at 0.5%, 1.0%, and 2.0% by
50 volume improves the mechanical properties for composite designations "EPL1," "EPL2," and
51 "EPL3." The composite "EPL2" with 1.0% lignin and 40% hybridized pod sheath/bamboo fiber
52 exhibits the highest mechanical properties, with values of approximately 159 MPa for tensile
53 strength, 6.21 GPa for tensile modulus, 202 MPa for flexural strength, 6.86 GPa for flexural
54
55
56
57
58
59
60

modulus, 28.6 MPa for ILSS, and 5.93 J for Izod impact. This enhancement is attributed to improved adhesion and reduced cross-linking density in the epoxy matrix [25]. However, further incorporation of lignin particles up to 2.0% by volume decreases the mechanical properties for composite designation "EPL3" due to cluster formation. On the other hand, an increase in hardness values is observed, reaching about 91 Shore-D. This increase is a result of the rigid lignin particles being incorporated into the epoxy matrix, altering the crosslink structures and making the composite harder and more brittle.

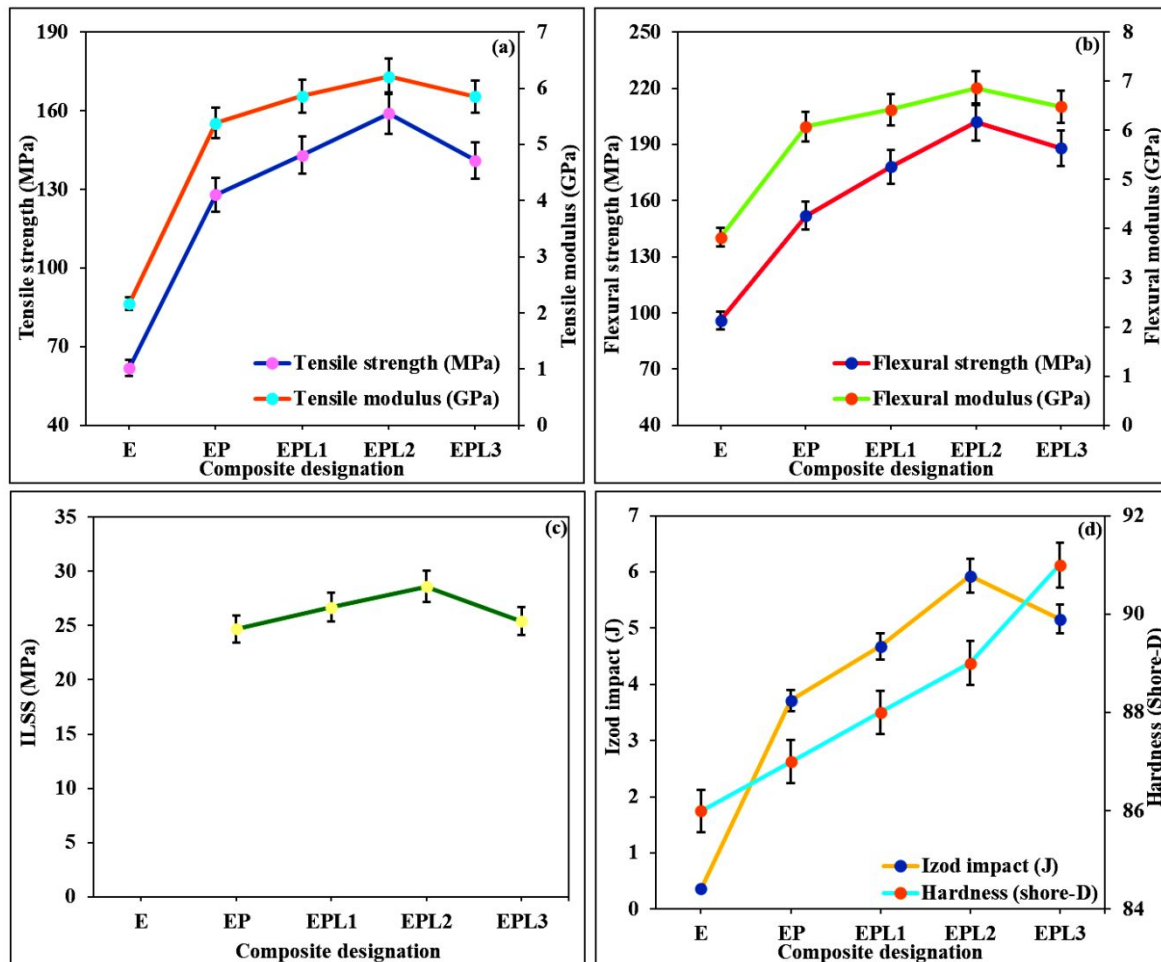


Figure 4 Mechanical properties for various composite designations (a) tensile, (b) flexural, (c) ILSS and (d) Izod and hardness

Table 2 presents the statistical analysis results (ANOVA) for the mechanical properties of different composites. The analysis included the use of appropriate statistical tests to assess the significance of differences. The results indicate significant variations in the mechanical

properties among the composites ($p < 0.05$). The obtained p-value is 0.0000000000002892, thus the null hypothesis is rejected and the results obtained are statically significant. Moreover the patterns are varying without any random case.

Table 2 ANOVA for mechanical properties

Source	DF	Sum of square	Mean square	F Statistic	P-value
Groups (within groups)	6	131986.6357	21997.7726	46.3385	2.892E-13
Error (within groups)	28	13292.1237	474.7187		
Total	34	145278.7593	4272.9047		

Figure 5 (a-d) demonstrates the SEM fractograph of tensile tested composites. Figure 5 (a) and (b) shows the SEM fractograph of composite EP. It represents the adhesion improved fiber in the fracture zone with matrix. The fibre has the remains of matrix, which confirms how better the fibre is adhered with resin during the curing process. This improvement is due to the surface treatment on hybridized bamboo/sheath fiber, which contains NH_2 functional group on their surface [26]. However, further inclusion of lignin shows the toughness improved matrix as well as debonding of sheath fiber as represented in Figure 5 (c) for composite designation EPL2. As well as due to the improved toughness this composite designation shows waviness pattern on fractured surface as observed in Figure 5 (d). Moreover, lignin up to the 1.0 vol. % shows highly reacted phase of fiber and matrix is observed for composite designation EPL2 with lignin toughened matrix as illustrated in Figure 5 (e) and (f). The Figure 5 (e) shows the fiber marks after fracture and lignin reached matrix for composite designation ELP2.

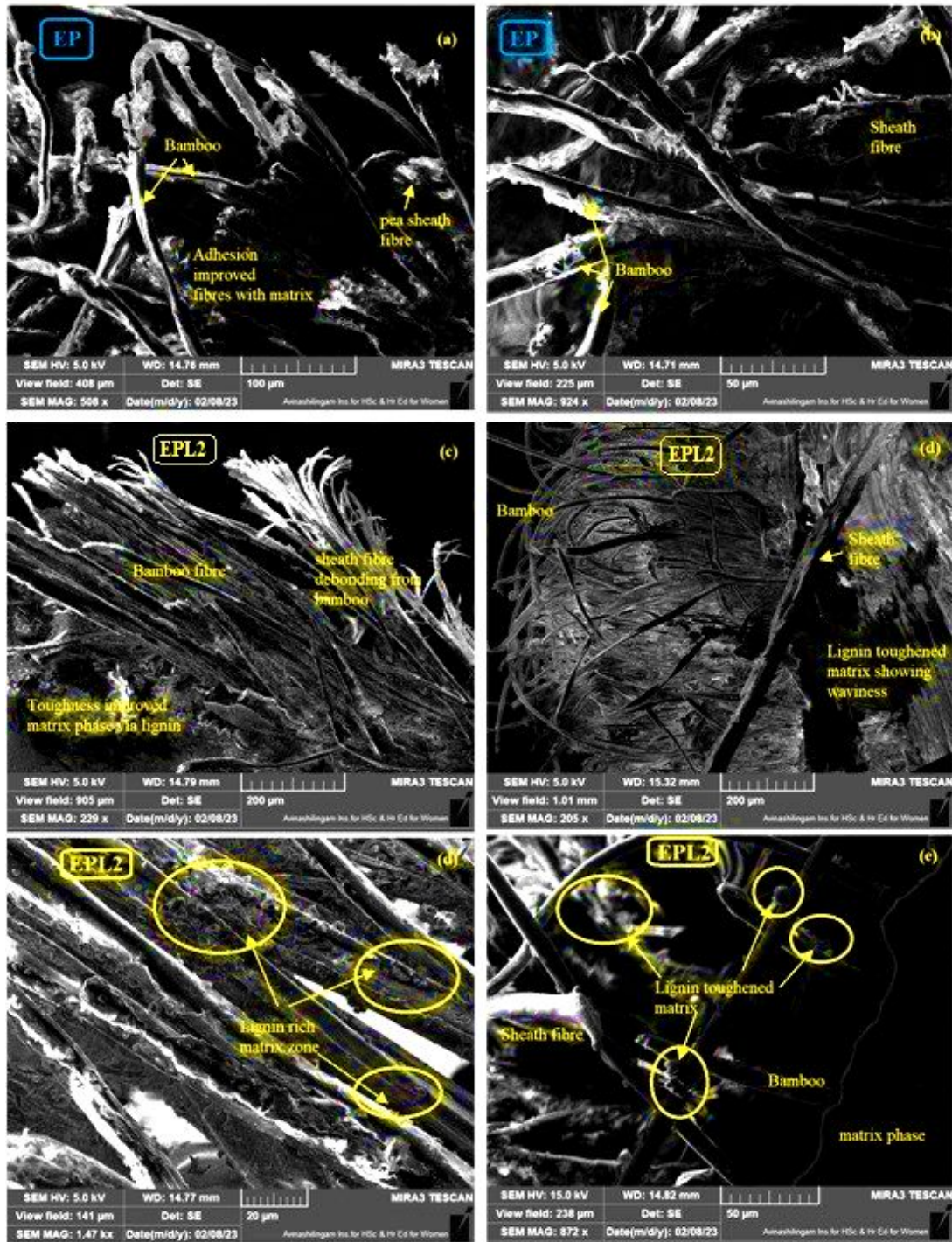


Figure 5 SEM fractography for fractured samples of tensile test

4.2 Wear properties

In Figure 6, the wear properties of pure epoxy and its various composite combinations are depicted. Pure epoxy exhibits lower wear resistance values compared to the other composite

designations, with approximately 0.05 g for wear loss and a coefficient of friction (COF) of 0.57. This reduced wear resistance can be attributed to the softness of epoxy molecules, making them susceptible to wearing on the abrasive disk [27]. However, the inclusion of 40 vol. % of bamboo and sheath fiber significantly reduces the wear values for the composite designation "EP" to around 0.02 g of wear loss and a COF of 0.48. The incorporation of surface-treated fibers enhances the bonding mechanism between the fibers and the matrix, resulting in a stronger grip on the epoxy molecules and reducing direct contact with the wear disk. Similarly, the further addition of green pea pod lignin at 0.5%, 1.0%, and 2.0% by volume improves the wear resistance for composite designations "EPL1," "EPL2," and "EPL3," respectively. Among all the composite designations, the highest wear resistance is observed in composite designation "EPL3," with approximately 0.01 g of wear loss and a COF of 0.38. This improved wear resistance is attributed to the surface treatment of the lignin, which enhances adhesion and the crystalline nature of the lignin particles, reducing the abrasion wear phenomenon. These lignin particles are naturally harder, providing resistance to wear and reducing the likelihood of three-body abrasion [28].

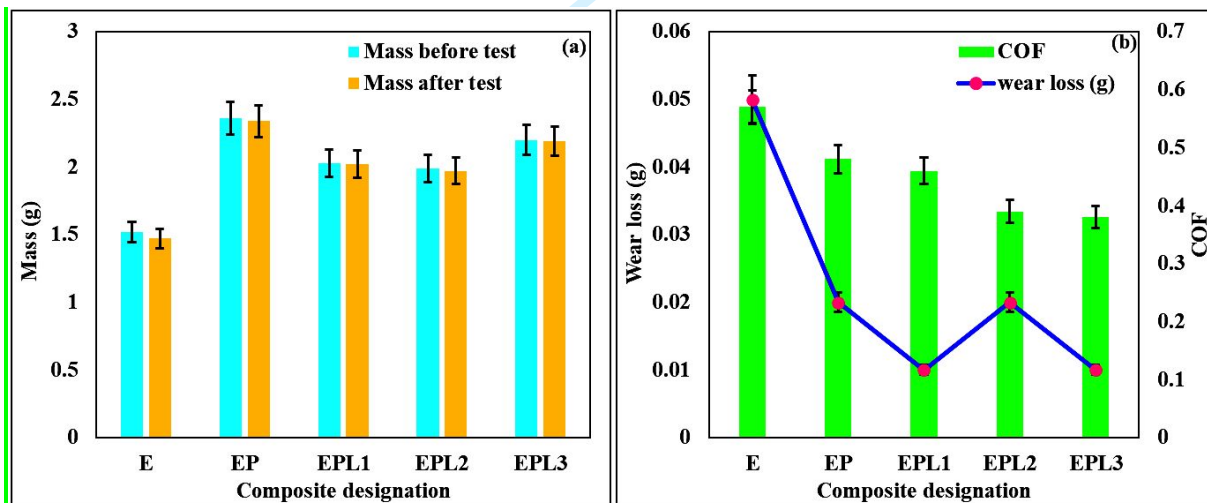


Figure 6 Wear properties for various composite designation (a) mass loss and (b) wear loss and COF

Table 3 presents the statistical analysis results (ANOVA) for the wear properties of different composites. The results indicate significant variations in the wear properties such as wear loss, coefficient of friction and sp. wear rate among the composites ($p < 0.05$). The obtained

p-value is 7.602E-10, thus the null hypothesis is rejected and the results obtained are statically significant. The patterns are varying without any random case.

Table 3 ANOVA for mechanical properties

Source	DF	Sum of square	Mean square	F Statistic	P-value
Groups (within groups)	3	16.5957	5.5319	79.9328	7.602E-10
Error (within groups)	16	1.1073	0.06921		
Total	19	17.703	0.9317		

4.3 Fatigue behaviour

Figure 7 provides insights into the fatigue life counts of pure epoxy and its various composite combinations. The composite designation "E" exhibits lower fatigue life counts, approximately 2208, 1471, and 1063 for 30%, 60%, and 90% of the ultimate tensile strength (UTS). This reduced fatigue life in the "E" composite is attributed to the brittle nature of pure epoxy. Under repetitive loads, the molecular chains in cured epoxy undergo significant stretching, accumulating residual stress. These accumulated stresses subsequently lead to the rapid propagation of microcracks, resulting in deformation [29]. The inclusion of 40 vol. % of surface-treated bamboo and sheath fibers in the composite designation "EP" significantly improves fatigue life counts, reaching approximately 26181, 22871, and 16308 for 30%, 60%, and 90% of UTS, respectively. The enhanced adhesion of fibers to the matrix, facilitated by the Si-O-Si bond established through silane surface treatment, plays a crucial role in this improvement. Additionally, the combination of green pea sheath microfibrils and bamboo fibers effectively transfers applied loads and enhances the matrix's resilience [30].

Moreover, the incorporation of green pea pod lignin particles at 0.5%, 1.0%, and 2.0% by volume further increases the fatigue life counts for composite designations "EPL1," "EPL2," and "EPL3," respectively. Among all the composite designations, the highest fatigue life counts are observed in composite designation "EPL2," with approximately 34632, 29671, and 24275 for 30%, 60%, and 90% of UTS, respectively. The addition of lignin in fiber-reinforced epoxy

composites hinders the formation of microcracks by improving surface bonding. As a result, the storage of plastic strain decreases with each loading cycle, leading to the observed increase in fatigue life counts. However, a slight decrease in fatigue life counts for composite designation "EPL3" occurs with a further increase in lignin volume percentage, likely due to particle agglomeration in the matrix [31].

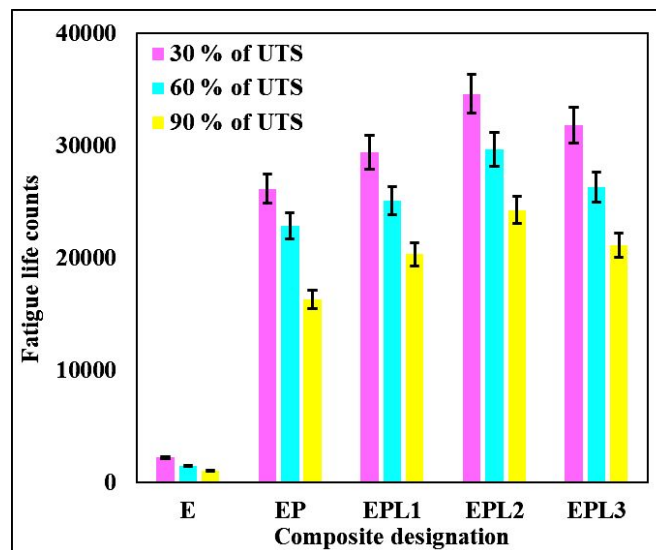


Figure 7 Fatigue life counts for various composite designations

4.4 Hydrophobic Behaviour (Immersion and Contact angle)

Figure 8 illustrates the hydrophobic behavior of pure epoxy and its composite combinations. The composite designation "E" exhibits higher contact angle values of about 102° and lower water absorption percentage of 0.24%. This is attributed to the pure epoxy content in this composite, which exhibits a water-repelling effect on OH molecules [32]. However, the inclusion of 40 vol. % sheath/bamboo fibers in the composite designation "EP" results in slightly increased water absorption values, approximately 0.34%, and a decreased contact angle of about 92° . This increase in water absorption can be attributed to the addition of natural fibers that are inherently hydrophilic. On the other hand, the addition of green pea pod lignin at 0.5%, 1.0%, and 3.0% by volume gradually reduces water absorption and contact angles for composite designations "EPL1," "EPL2," and "EPL3," respectively. Among all the composite designations, the lowest contact angle and water absorption percentage are noted for composite designation "EPL3," with values of about 82° and 0.16%, respectively. This reduction in values is due to the

increased lignin content, which raises the surface energy of the entire composite [33]. However, it's important to note that all composite designations maintain contact angles above 70°, indicating that the addition of natural fibers and green pea pod lignin particles does not make the composite more hydrophilic; instead, it retains its hydrophobic characteristics.

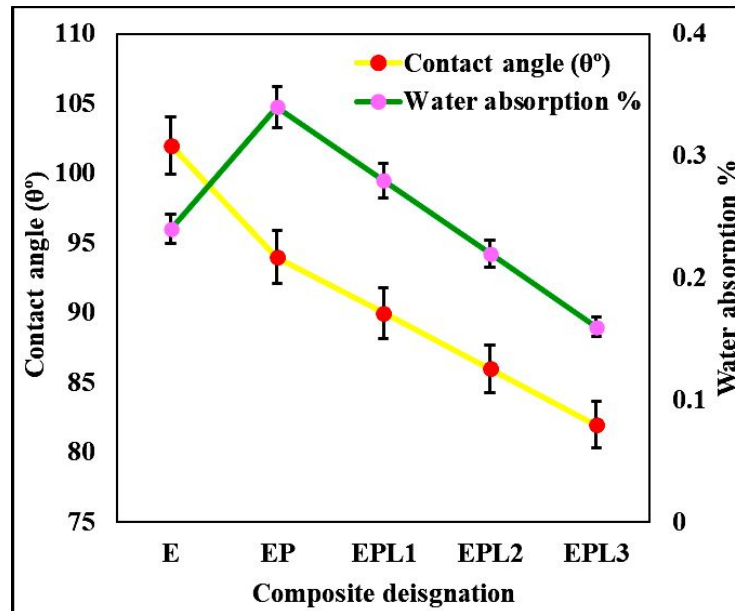


Figure 8 Water up take of various composite designations

5 Conclusions

This study aims to develop epoxy based biocomposites by incorporating green pea pod lignin and hybridized pod sheath fiber-bamboo. The conclusion attained by the results of this research is as follows.

- i. Incorporating 40 vol. % of sheath/bamboo hybridized fiber and 1 vol. % of lignin into pure epoxy yielded 159 MPa of tensile strength, 6.21 GPa of tensile modulus, 202 MPa of flexural strength, 6.86 GPa of flexural modulus, 28.6 MPa of ILSS and 5.93 J of Izod impact. Moreover according to the ANOVA the obtained results are significant with $P < 0.05$.
- ii. In terms of wear resistance, composite designation "EPL3" exhibited the best performance, with values of 0.01 g for wear loss and a coefficient of friction (COF) of 0.38 after the addition of 2.0 vol. % of lignin. The ANOVA confirms that the results are significant with $P < 0.05$.

- 1
2
3
4
5
6
7
8
9
10
11
12
13
14
15
16
17
18
19
20
21
22
23
24
25
26
27
28
- iii. The highest fatigue life counts were observed in composite designation "EPL2," with values of approximately 34,632 cycles for 30% of UTS, 29,671 cycles for 60% of UTS, and 24,275 cycles for 90% of UTS.
 - iv. Additionally, composite designation "EPL3" demonstrated the lowest contact angle of 82° with a water absorption % of 0.16, emphasizing its hydrophobic nature.
 - v. Scanning electron microscopy (SEM) analysis indicated that the addition of surface-treated fibers and lignin particles led to uniform distribution and improved bonding mechanisms in the composites.
 - vi. Based on these findings, it is evident that the fibre hybridization fetched useful mechanical properties as well as created a path for utilizing the novel fibres for sustainable material production. It is concluded that the composite designation "EPL2" is a preferable material composition choice for prosthetic applications due to its superior properties.

Declarations

Ethical approval - Not applicable

Competing interest - The authors declare no competing interests

Authors' contribution –

Sujithra R and Saritha - Involved in experimental research work

Funding – Not applicable

Availability of data and materials - All data within the manuscript. No more additional data is available.

References

- [1] Thiagamani, S. M. K., et al, (2023). Heliyon, 9(7). <https://doi.org/10.1016/j.heliyon.2023.e17760>
- [2] Jeyaguru, S., et al, (2024). Composites Part A: Applied Science and Manufacturing, 176, 107845. <https://doi.org/10.1016/j.compositesa.2023.107845>

[3] Mirzamohammadi, S., et al (2023). *Advanced Engineering Materials*, 25(12), 2201791. <https://doi.org/10.1002/adem.202201791>

[4] Yoganandam et al. *Adv. Mater. Sci. Eng.* 2021;2021:2491489. doi: 10.1155/2021/2491489.

[5] Maiti et al. *Adv. Sustainable Syst.* 2022, 6, 2200258. <https://doi.org/10.1002/adsu.202200258>

[6] Spalek et al. *Int J Mol Sci.* vol. 23,5 2575. 25 Feb. 2022, doi:10.3390/ijms23052575

[7] Egoh et al. *Materials Sciences and Applications*, 11, 2020 415-430. doi: 10.4236/msa.2020.117028.

[8] Kulandaivel et al. *Journal of Natural Fibers*. 17. 1-11. 10.1080/15440478.2018.1534184.

[9] BHIRI et al. *Research and Technology Center of Energy*: (2022).<https://orcid.org/0000-0001-7099-9962>

[10] J. Shesan et al. *IntechOpen*, Dec. 2019. Crossref, doi:10.5772/intechopen.84753.

[11] Ajala et al. *Bioresour. Bioprocess.* 8, 87 (2021). <https://doi.org/10.1186/s40643-021-00440-z>

[12] Sigit et al. *Bioactive Materials*, (2022), -. doi:10.1016/j.bioactmat.2021.06.023

[13] Spiridon et al. *Environmental Chemistry Letters*. (2020) 18. 10.1007/s10311-020-00981-3.

[14] Khan, M.K.A., Alshahrani, H. & Arun Prakash, V. *Biomass Conv. Bioref.* (2023). <https://doi.org/10.1007/s13399-023-05196-4>

[15] Alshahrani, H., & Prakash, V. A. (2022). *International Journal of Biological Macromolecules*, 223, 851-859.

[16] Jayabalakrishnan et al. *Biomass Conv. Bioref.* (2022). <https://doi.org/10.1007/s13399-022-03555-1>

[17] Sathees et al. *Fibers Polym* **22**, 1675–1683 (2021). <https://doi.org/10.1007/s12221-021-0910-4>

[18] Taleb et al. *Sci Rep* **10**, 11048 (2020). <https://doi.org/10.1038/s41598-020-68047-6>

[19] Yan et al. *Front. Chem. Sci. Eng.* (2023). <https://doi.org/10.1007/s11705-022-2237-0>

[20] Rajadurai, A. (2016). *Applied surface science*, 384, 99-106. <https://doi.org/10.1016/j.apsusc.2016.04.185>

[21] Jayabalakrishnan et al. *Polym. Compos.* 2021, 1. <https://doi.org/10.1002/pc.26393>

[22] Sathees et al. *Fibers Polym* **21**, 1508–1514 (2020). <https://doi.org/10.1007/s12221-020-9853-4>

1
2
3 [23] Arun et al. *Int J Plast Technol* 23:207–217. 2019, [https://doi.org/10.1007/s12588-019-](https://doi.org/10.1007/s12588-019-09251-6)
4 09251-6
5

6 [24] Mirzamohammadi, S., et al, (2023). *Proceedings of the Institution of Mechanical Engineers,*
7 *Part C: Journal of Mechanical Engineering Science*, 237(8), 1877-1886.
8 <https://doi.org/10.1177/09544062221134223>
9

10
11
12 [25] Ramesh et al. Singapore. 2021, https://doi.org/10.1007/978-981-15-9643-8_2
13

14 [26] Praveenkumara et al. *Journal of Natural Fibers*, 19:11, 4132-
15 4147, DOI: [10.1080/15440478.2020.1854145](https://doi.org/10.1080/15440478.2020.1854145)
16

17 [27] M. Hamdan et al. *Polym. Compos.* 2019, 27, 096739111984755.
18 <https://doi.org/10.1177/0967391119847552>
19

20 [28] S, Mahalingam et al. *Transactions of FAMENA*, vol. 47, no. 1, 2023, pp. 1-12.
21 <https://doi.org/10.21278/TOF.471048622>. Accessed 15 Mar. 2023.
22
23

24 [29] Pulikkalparambil et al. *Biomass Conv. Bioref.* (2023). [https://doi.org/10.1007/s13399-023-](https://doi.org/10.1007/s13399-023-03811-y)
25 03811-y
26

27 [30] Kaliappan et al. *Polym. Compos.* 2023, 1. <https://doi.org/10.1002/pc.27228>
28

29 [31] Khan et al. *Adv. Fiber Mater.* 4, 683–704 (2022). [https://doi.org/10.1007/s42765-022-](https://doi.org/10.1007/s42765-022-00143-w)
30 00143-w
31

32 [32] Thiyagu et al. *Biomass Conv. Bioref.* (2021). <https://doi.org/10.1007/s13399-021-01941-9>
33

34 [33] Sumesh et al. *J Ind Text* 2020. <https://doi.org/10.1177/1528083720971344>.
35
36
37
38
39
40
41
42
43
44
45
46
47
48
49
50
51
52
53
54
55
56
57
58
59
60

Advanced copper-based electrocatalysts for the electrochemical reduction of carbon dioxide to valuable fuels: Recent advances

Dhruv Gollapudi ^a, Lingala Eswaraditya Reddy ^a, Gaurav Mahnot Jain ^a, Sravya Kolluru ^a, Gubbala V. Ramesh ^b  

Show more 

 Share  Cite

<https://doi.org/10.1016/j.matpr.2024.04.086> 

[Get rights and content](#) 

Abstract

The growing worldwide dependence on fossil fuels and the subsequent release of CO₂ emissions pose substantial environmental challenges. The purpose of this review is to examine the process of electrochemical carbon reduction (ECR) and specifically investigate the use of copper-based electrocatalysts for the conversion of CO₂ into chemically valuable substances. The synthetic methods employed for these catalysts are analyzed, along with their impact on product selectivity and the potential advantages they present. The focus of our research lies in the exploration of alloy electrocatalysts, specifically those composed of Cu-Au, Cu-Pd, and CuNi combinations. These particular combinations have demonstrated improved efficiency and selectivity in the reduction of CO₂. This paper aims to assist in the design of high-performance copper catalysts and the optimization of ECR processes by providing insights into the structure–function relationships and intermediate modulation.

Introduction

Our reliance on fossil fuels is escalating energy and environmental issues, evidenced by the yearly increase of atmospheric CO₂ levels by approximately 2 parts per million. This has grave implications, including the gradual collapse of our world's most delicate ecosystems [1]. As a result, immense effort has been made in recent years to curb and ultimately cut these emissions. However, reducing emissions isn't a simple task. It is crucial for our survival, holds immense scientific significance, but proves economically challenging [2]. The battle against the damaging effects of CO₂ emissions is complex, especially since currently available technologies are heavily dependent on fossil fuels. This dependence on fossil fuels is a critical hurdle. To address this, the reversal of the carbon cycle, which involves capturing and using CO₂, has gained traction. This strategy presents an attractive solution for managing energy and environmental crises simultaneously. In the long term, it could be key to achieving green and sustainable development. One promising method for managing CO₂ levels involves converting atmospheric CO₂ into valuable fuels and chemicals through carbon sequestration. Various methods have been studied for this purpose, including chemical, photochemical, biological, and electrocatalytic processes [3], [4]. The schematic design in Fig. 1 illustrates the several approaches used in the reduction of CO₂. Biological CO₂ reduction typically involves using rapidly growing biomass to replace traditional chemical processes for fuel and chemical production. However, chemical reactions often involve high energy–density species like H₂. These reactions require significant energy inputs and operate under high temperature and pressure settings [4]. Photochemical and ECR are among the most cost-effective strategies for managing and converting CO₂. ECR powered by renewable energy, offers distinct advantages over photochemical CO₂ reduction. This includes milder operating conditions, high energy efficiency, and superior product selectivity. In theory, ECR could allow to produce high-value items with varied potential applications. However, there remain substantial challenges before ECR becomes a mature technology. The current limitations include factors such as energy efficiency, product selection, achieving optimum yield, and overall financial advantages.

Multiple proton/electron transfer processes are required for the ECR into high-value-added compounds. This heterogeneity in

reaction pathways and product production processes during CO₂ reduction reaction (CO₂RR) [5], [6] is indicative of the process's complexity. These two properties have an intriguing link to the electronic properties of the materials at play. The only metal-based catalysts shown to be successful in converting CO₂ into C₂+products, copper (Cu)-based CO₂RR electrocatalysts, which exhibit modest adsorption towards the *CO intermediate. They also favour C–C coupling, which suggests an inclination to produce high carbon fuels at a lower potential [7], [8]. However, the absence of a selective route in the CO₂RR results in Cu-based electrocatalysts exhibiting a wide array of products, limited selectivity, and poor Faraday efficiency. Extensive research has been conducted on the optimisation of Cu-based catalyst shapes, sizes, and supporting substrates to optimise their performance. [9], [10]. Significant attention has been paid to the development of ECR using bimetallic Cu-based catalysts. The electronic structure of Cu can be altered by including another metal into Cu. As a result, the overall performance is enhanced and selectivity towards the target intermediates is increased [11], [12]. Understanding the electronic structure of these bimetallic electrocatalysts for CO₂RR is useful because they have good conductivity and adsorption. This is especially significant since the CO₂RR performance of materials based on Cu might vary depending on the metals that are integrated into such materials. Unlocking these rules may allow for the development of practical electrocatalysts. Changing the electronic structure of catalysts is a powerful method for increasing their activity. The electrical conductivity and adsorption strength of particular intermediates may be precisely controlled by manipulating their structure. In turn, this improves the catalysts' overall activity and selectivity. Through processes including heterostructure development, defect engineering, and surface alteration, adding other metals to Cu can improve their conductivity and adsorption capabilities. As a result, the electronic characteristics are optimised by this procedure, leading to superior catalytic activity and selectivity in the CO₂RR.

This concise review is intended to provide an insightful and timely assessment of strategic structural engineering and intermediate modulation, both of which are governed by synthetic methodologies. The ultimate objective is to simplify the production of effective Cu catalysts for simple, highly selective ECR. This article explores the use of copper and its derivatives as electrocatalysts for ECR, analysing the various synthetic approaches and their effects on product selectivity. By deciphering the complexity of structure–function associations and intermediate modulation, we hope to set the groundwork for the rational development of Cu catalysts, thereby optimising the selectivity and efficiency of ECR.

Section snippets

Cu-based electrocatalysts

Copper (Cu) plays a pivotal part in this process ECR, which converts carbon dioxide (CO₂) into valuable multi-carbon compounds. But Cu catalysts have problems with stability and selectivity. The importance of effective catalysts in ECR has been the focus. Researchers anticipated the optimal conditions for producing high-performance Cu catalysts by employing Design of experiments and response surface approaches. Cheng et al. discovered that by altering the evaporation conditions, especially the ...

Cu–Au

In order to optimise their performance in ECR, Huang et al. [19] directed their attention on the development of nanostructures composed of gradient alloy of gold and copper (AuCu-g). The researchers fabricated AuCu-g catalysts using a solvothermal approach, resulting in a surface composition that is mostly Cu-rich and a core composition that is predominantly Au-rich. The catalyst's performance was remarkable, as it consistently produced large amounts of C₂H₄ with a notable FE of over 20% at a ...

Conclusion

The substantial potential of copper-based catalysts in furthering carbon sequestration endeavours is emphasised in this review. By virtue of its distinctive electronic characteristics and its malleability via alloying, copper offers advantageous opportunities to improve product selectivity and energy efficiency. Despite the persistent challenges associated with catalyst stability and economic viability, continuous progress in the fields of material science and electrochemistry is progressively ...

CRedit authorship contribution statement

Dhruv Gollapudi: Writing – original draft, Visualization, Investigation, Formal analysis. **Lingala Eswaraditya Reddy:** . **Gaurav Mahnot Jain:** Resources, Investigation, Data curation. **Sravya Kolluru:** Resources, Investigation, Data curation. **Gubbala V. Ramesh:** Writing – review & editing, Visualization, Supervision, Formal analysis, Conceptualization. ...

Declaration of competing interest

The authors declare that they have no known competing financial interests or personal relationships that could have appeared to influence the work reported in this paper. ...

[Recommended articles](#)

Reference (41)

J. Cheng *et al.*

[Design of experiments unravels insights into selective ethylene or methane production on evaporated Cu catalysts](#)

Journal of Energy Chemistry (2022)

J. Huang *et al.*

[Bimetallic Au-Cu gradient alloy for electrochemical CO₂ reduction into C₂H₄ at low overpotential](#)

J. Catal. (2022)

L. Zhu *et al.*

[Tuning the intermediate reaction barriers by a CuPd catalyst to improve the selectivity of CO₂ electroreduction to C₂ products](#)

Chin. J. Catal. (2021)

Z.F. Yan *et al.*

[Renewable electricity storage using electrolysis](#)

PNAS (2020)

S.C. Peter

[Reduction of CO₂ to chemicals and fuels: a solution to global warming and energy crisis](#)

ACS Energy Lett. (2018)

G. Glensk *et al.*

[Economics of converting renewable power to hydrogen](#)

Nat. Energy (2019)

Z.P. Cano *et al.*

[Batteries and fuel cells for emerging electric vehicle markets](#)

Nat. Energy (2018)

Y. Xue *et al.*

[Catalyst design for electrochemical reduction of CO₂ to multicarbon products](#)

Small Methods (2021)

L. Kuo *et al.*

[Toward efficient catalysts for electrochemical CO₂ conversion to C₂ products](#)

Curr. Opin. Electrochem. (2021)

S. Popovic *et al.*

[Stability and degradation mechanisms of copper-based catalysts for electrochemical CO₂ reduction](#)

Angew. Chem. Int. Ed. Engl. (2020)



[View more references](#)

Cited by (0)

[View full text](#)



All content on this site: Copyright © 2025 Elsevier B.V., its licensors, and contributors. All rights are reserved, including those for text and data mining, AI training, and similar technologies. For all open access content, the Creative Commons licensing terms apply.





Nanoarchitectonics of cathode electrocatalyst based on CoMn_2O_4 and graphene nanocomposite for fuel cell applications

Maidhily Manikandan¹ · Ch. G. Chandaluri² · Hideki Abe^{1,3,4} · Gubbala V. Ramesh⁵

Received: 24 March 2023 / Accepted: 20 July 2023 / Published online: 3 August 2023
© King Abdulaziz City for Science and Technology 2023

Abstract

We report the development of a novel electrocatalyst composed of nanoarchitectured spinel cobalt manganese oxide and graphene for the oxygen reduction reaction (ORR). A combination of co-precipitation and hydrothermal methods achieved the unique nanoarchitecture of the electrocatalyst. The formation of CoMn_2O_4 electrocatalyst was confirmed by X-ray diffraction, transmission electron microscopy, and other spectroscopic and microscopic techniques. In addition to synthesizing Co_xO_y and Mn_xO_y as control electrocatalysts, we created a physical mixture of CoMn_2O_4 and graphene to investigate the impact of their interface on electrocatalytic activity. Our findings indicate that CoMn_2O_4 /graphene exhibits improved ORR activity, stability, and methanol tolerance in an alkaline medium. This enhancement can be attributed to the synergistic effect and strong interface interaction between CoMn_2O_4 and graphene. This study demonstrates the potential of the proposed electrocatalyst as a cost-effective and eco-friendly alternative for oxygen reduction in fuel cells applications.

Keywords CoMn_2O_4 · Oxygen Reduction Reaction · Graphene · Cathode Electrocatalyst · Spinel Oxide · Nanoarchitectonics

Introduction

Nanoarchitectonics is the process of designing and assembling molecular/nano units to produce useful materials, and it incorporates a wide range of methods, including atom/molecular-level modification, chemical transformations, self-assembly, micro/nano-fabrication, and biological

processes. (Ariga and Shrestha 2020) The idea of nanoarchitectonics was first put forward by Masakazu Aono, (Ariga et al. 2012; Weiss 2007) who envisioned the creation of functional materials using the following principles: (i) assembling nanometer-scale structures (nanounits) to construct functional materials and systems, Despite certain inherent uncertainty; (ii) These formations may exhibit unique qualities that are distinct from those of their constituent nanounits, with the potential for interactions that create new functionalities; (iii) a large number of nanounits can be assembled to produce unexpected functionalities; (iv) These manufacturing techniques necessitate novel theories and computational techniques. (Ariga et al. 2015) Because the principles of nanoarchitectonics are general and can be applied to many materials systems, this concept has wide-ranging potential for research. This concept was adopted by researchers, who subsequently created a variety of catalysts with diverse applications. (Liu et al. 2020; Ariga and Yamauchi 2020; Maji et al. 2019).

The twenty-first century has seen a significant amount of time and effort dedicated by numerous researchers to the study and development of technologies aimed at enabling the production and transfer of energy, including but not limited to fuel cells and batteries. These efforts have been driven

✉ Hideki Abe
ABE.Hideki@nims.go.jp

✉ Gubbala V. Ramesh
venkataramesh_chm@cbit.ac.in

¹ National Institute for Materials Science, 1-2-1 Sengen, Tsukuba, Ibaraki 305-0047, Japan

² Faculty of Chemistry, Humanities and Sciences Division, Indian Institute of Petroleum and Energy, Visakhapatnam, India

³ CREST, JST, 4-1-8 Honcho, Kawaguchi, Saitama 332-0012, Japan

⁴ Graduate School of Science and Technology, Saitama University, 255 Shimoookubo, Saitama 338-8570, Japan

⁵ Department of Chemistry, Chaitanya Bharathi Institute of Technology (A), Gandipet, Hyderabad, Telangana 500075, India

by a desire to harness the potential of these technologies to address pressing energy-related issues facing society. (Monama et al. 2022; Abbas et al. 2020) Due to their potential for high efficiency, the electrochemical conversion of oxygen to water in aqueous media (oxygen reduction reaction, ORR) and its reciprocal reaction, water to oxygen (oxygen evolution reaction, OER), have received considerable attention. (Liu et al. 2021; Kinoshita 1992) Platinum (Pt) is a costly component used in proton exchange membrane fuel cells (PEMFC) that cannot be readily modified due to the slower rate of ORR in acidic medium compared to alkaline medium. This allows for the use of non-platinum catalyst materials for ORR in alkaline state. High cost, poor tolerance to methanol, and restricted availability have all worked against the widespread use of platinum group metals as catalysts for the ORR. Since Pt-based metals are used as electrocatalysts, these constraints have slowed the widespread adoption of low-temperature fuel cells. (Debe 2012) Thus, in order to get around these problems, scientists have been looking for low-cost alternatives to ORR with activity comparable to Pt/C. (Jeon et al. 2012) However, designing such electrocatalysts that are also economically viable, abundant, and non-precious is a significant challenge.

A variety of inorganic materials have been studied for their potential as electrocatalysts, with perovskite materials emerging as a promising candidate due to their unique electronic and structural properties. Researchers have extensively investigated the electrocatalytic properties of perovskite materials for ORR, with promising results. (Carbonio et al. 1988; Jörissen 2006) Perovskites are susceptible to deterioration during cathodic operation, despite their promising peroxide-degrading ability, in addition to perovskites, spinel-structured metal oxides have also been discovered to be effective for ORR. (Kaur and Singh 2020) Electrocatalytic activity, corrosion resistance, and cost effectiveness are the most important criteria to consider when choosing an electrocatalyst. It is well known that spinel oxides containing Mg, Cd, Fe, Co, and/or Mn are efficient. (Dosaev et al. 2022; Yang et al. 2019) Due to their numerous valences, low cost, and widespread availability, spinel oxides containing cobalt and/or manganese are especially appealing among these materials. (Lankauf et al. 2020; Cheng et al. 2010) Cobalt and manganese oxides have shown improved electrocatalytic activity for ORR because of their thermal stability and reduced resistance. Spinel oxides of cobalt and manganese, such as Co_3O_4 and Mn_3O_4 , have high ORR activity on their own. (He et al. 2016; Li et al. 2015) However, partial substitution with other metals increases ORR activity in alkaline solutions by varying the ratio of cations between tetrahedral and octahedral sites (Restovic et al. 2002).

It has been shown that manganese oxides with cobalt added increase the electrocatalytic activity of the OER and ORR. (Chen et al. 2011; Prabu et al. 2014) The

electrocatalytic efficiency of materials used for oxygen-related reactions, such as ORR, is dependent on the electrochemical surface area available at the interface between oxygen, the catalyst, and the medium of electrolyte for reactions to occur. Consequently, the size and shape of these nanoparticles and electrochemical surface area of these materials are critical factors that have a significant impact on their electrocatalytic efficacy. However, the bigger, low-surface-area particles produced by conventional ceramic processes tend to be spinel oxides. However, conventional ceramic processes result in bigger and low-surface area spinel oxide particles. Careful synthesis of spinel metal oxides under precise conditions is essential for achieving desired properties such as required nanoparticles size, shape with huge electrochemical surface area. This requires attention to various factors, including the choice of starting materials, reaction conditions, and calcination temperature. (Olowoyo and Kriek 2022) Given the excellent conductivity of the carbon nanomaterials, the combination of spinel oxide and carbon nanomaterials increases electrocatalytic activity and enhances mechanical stability and durability, making them an attractive option for fuel cell and energy storage applications. (Feng et al. 2012).

Numerous studies have focused on the fabrication of CoMn_2O_4 nanoparticles (NPs) in conjunction with graphene oxides, reduced graphene oxides, etc. Du et al. synthesized CoMn_2O_4 nanodots (less than 3 nm) monodispersed on reduced graphene oxide (rGO). This composite demonstrated a 20 mV higher ORR half-wave potential, double the kinetic current, and superior catalytic durability compared to carbon-supported platinum nanoparticles. (Jing et al. 2015) Another hybrid nanostructures of CoMn_2O_4 mesoporous nanosheets and 3D rGO, supported by nickel foam, to enhance supercapacitor performance reported by Zhang and coworkers. (Zhang et al. 2019) These nanostructures, with controlled morphologies and electronic properties, induce interface charge separation and a built-in electric field, improving charge transfer kinetics and operation voltage. An all-solid-state supercapacitor, constructed using this heterostructure, exhibited exceptional energy density and excellent cycling stability. CoMn_2O_4 nanoparticles grown on graphene oxide sheets (CMOG) and their bifunctional catalytic activity were reported by Wang et al. The CMOG has a notable catalytic effect on both ORR and OER. Despite a high discharge capacity, the carbon air electrode based on CMOG experiences rapid capacity degradation. (Wang et al. 2011) Shi and colleagues created controlled-size quantum dots (QDs) using spinel CoMn_2O_4 , a multivalent transition metal oxide. They created QDs using a combination hot-injection and heat-up method, changing the reaction temperature to regulate the size. The QDs were supported on carbon nanotubes (CNTs) utilising solvent separation while retaining their inherent characteristics. The electrochemical

investigation revealed a substantial size dependency in ORR/OER catalytic performance. (Shi et al. 2017) In the literature, graphene derivatives are often referred to as graphene. The electrical conductivity of graphene and its derivatives, graphene oxide (GO) and reduced graphene oxide (rGO), varies and is crucial for electrochemistry. With a delocalized π -electron system, pure graphene facilitates quick electron transport and provides higher electrical conductivity. However, GO, which was created by adding oxygen-functional groups to graphene, is an insulating substance with low electrical conductivity. By eliminating certain oxygen groups, the reduction process of GO to rGO somewhat recovers its conductivity, although it remains less conductive than pure graphite (graphene). (Guex et al. 2017) The high conductivity of pure graphene makes it a more effective support material for electrochemical processes like ORR than GO and rGO.

The aim of this study is to investigate the feasibility of augmenting the electrical conductivity and reactive sites by combining graphene with spinel metal oxides. We present a simple hydrothermal method for synthesizing a nanoarchitectonics guided mesoporous hybrid $\text{CoMn}_2\text{O}_4/\text{graphene}$ nanostructure for ORR in an alkaline environment. Electronic structure and chemical composition of the synthesized hybrid catalyst was characterized hard X-ray photoelectron spectroscopy (HAXPES). Our focus is on enhancing the conductivity of CoMn_2O_4 by modifying its surface structure with carbonaceous graphene with a large surface area. Compared to Pt/C, the hybrid nanostructure exhibited improved electrochemical properties, such as a more favourable onset potential and decreased impedance. These results suggest enhanced charge transfer at the interface and methanol resistance. The $\text{CoMn}_2\text{O}_4/\text{G}$ nanostructure also showed long-term stability, making it a Potential substitute to commercial electrocatalysts.

Materials and methods

Materials

Cobalt chloride (CoCl_2 , 97%, Sigma-Aldrich), potassium permanganate (KMnO_4 , $\geq 99.0\%$, Sigma Aldrich, ACS reagent), ethylene glycol (anhydrous, 99.8%, Sigma Aldrich), graphene (Toyotsu-chemiplas, Japan).

Synthesis of $\text{CoMn}_2\text{O}_4/\text{Graphene}$

Hydrothermal method was used for this synthesis. Required amount of cobalt chloride (CoCl_2) and potassium permanganate (KMnO_4) was added to ethylene glycol in a 1:3 molar ratio in an Teflon lined autoclave, subsequent to the addition of 100 mg of graphene powder. The resultant solution

was stirred for 30 min and annealed at 180 °C for 12 h in a preheated electric oven and cooled to naturally. The precipitate was centrifuged, rinsed multiple times with Milli-Q water and ethanol, and then desiccated under vacuum prior to being annealed in air at 300 °C for 2 h. The same method was also used to create $\text{Co}_x\text{O}_y/\text{G}$, $\text{Mn}_x\text{O}_y/\text{G}$, and CoMn_2O_4 without graphene as a control. The physical external mixture of CoMn_2O_4 and graphene ($\text{CoMn}_2\text{O}_4 + \text{graphene}$) also prepared for another control. Various analytical techniques, including pXRD, SEM, TEM, and HXPES, were used to characterize all synthesized materials. Our previous works contain detailed discussions on these methods. (Kodiyath et al. 2020; Ramesh et al. 2014a, 2014b).

Electrode preparation

Catalytic ink was prepared by mixing 0.875 mL water, 0.220 mL of 2-propanol and 0.002 mL of Nafion (Aldrich) solution containing 5% lower aliphatic alcohols in a glass vial. To the above solution 0.045 g of the catalyst was added and sonicated the resultant mixture. A specific quantity of ink was applied onto a glassy carbon electrode with 5 mm diameter via micro-pipette and subsequently dried in air at 60 °C. The weight of the electrocatalyst present on top of the electrode was 0.125 mg. All electrochemical tests were conducted using 0.1 M aqueous KOH.

Results and discussions

pXRD analysis

Figure 1 shows the crystallographic structures of the synthesized $\text{CoMn}_2\text{O}_4/\text{G}$ sample after thermal annealing at 300 °C for 2 h. The presence of graphene is indicated by the peak at 25°. The formation of a $\text{CoMn}_2\text{O}_4/\text{G}$ hybrid nanostructure is confirmed by the presence of crystalline peaks

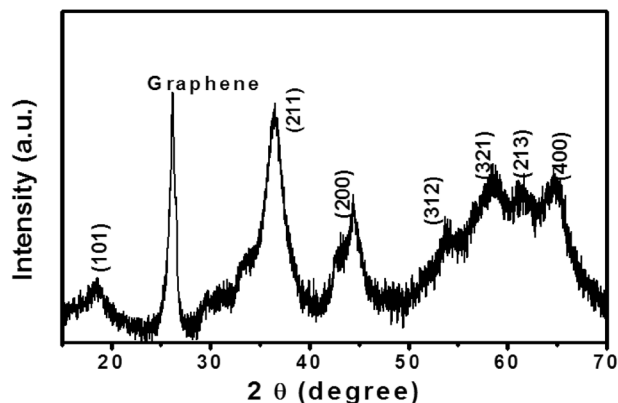


Fig. 1 pXRD profile for $\text{CoMn}_2\text{O}_4/\text{G}$ after heating 300°C for 2 h

at 39.75° , indicating a tetragonal crystal system and a space group of I41/amd. (JCPDS No. 77–0471) (Jung et al. 2015).

SEM analysis

We used pure graphene flakes as a material to create hybrid nanostructures with CoMn_2O_4 . Graphene, a two-dimensional carbon-based material, is known for its excellent electrical conductivity and large surface area, these properties are attractive for various applications, including energy storage and conversion. The method we used to combine graphene with CoMn_2O_4 was a hydrothermal synthesis, which allows the growth of CoMn_2O_4 particles on the surface of the graphene flakes. The resulting structure is a flower-like shape, where the CoMn_2O_4 particles are on the nanometer scale, and embedded on the surface of the graphene. Crystal growth mechanisms and unusual interactions during the hydrothermal process are mostly responsible for the formation of flower-like structures in CoMn_2O_4 -graphene nanocomposites. Precursors CoCl_2 and KMnO_4 react in a hydrothermal environment to produce CoMn_2O_4 nuclei, which serve as the primary building blocks. Over time, the system moves towards a lower surface energy state as smaller particles dissolve and redeposit onto bigger ones, a phenomenon known as Ostwald ripening. This allows for the development of larger, flower-like structures. CoMn_2O_4 uses the graphene powder present in the combination as a 2D growth template. The adsorption of precursors or nuclei onto its enormous surface area promotes preferential development of CoMn_2O_4 along certain planes, leading to its characteristic flower-like shape. The presence of ethylene glycol, which serves as a moderate reducing agent and induces anisotropic growth, affects the rate of growth of distinct crystal faces of CoMn_2O_4 . The flower-like CoMn_2O_4 structures on graphene are shaped in the final step by a two-stage annealing process, with the first stage occurring in an electric oven to generate the initial structure and the second stage occurring in air to perhaps improve crystallinity and stability. Figure 2 displays

graphene flake images at low and high magnification. Flower-like structures of hybrid $\text{CoMn}_2\text{O}_4/\text{G}$ are disclosed in the SEM images, as shown in Fig. 3 at various magnifications. This hybrid structure can enhance the conductivity, stability and electrocatalytic activity of the CoMn_2O_4 particles, making it a promising candidate for ORR.

TEM analysis

Figure 4A–D depicts TEM images with varying magnifications that demonstrate a tight interaction between graphene flakes and small CoMn_2O_4 particles with a narrow distribution of 5–8 nm. The TEM analysis revealed that the hybrid structure is homogeneous, with no graphene-free nanoparticles or clumps of CoMn_2O_4 observed. The controlled thermal annealing process allowed the CoMn_2O_4 nanoparticles to strongly bind to the surface of the graphene flakes, resulting in a hybrid nanostructure of $\text{CoMn}_2\text{O}_4/\text{G}$. HR-TEM and FFT image analysis further suggests the formation of desirable nanoparticles. (Fig. 4E, F). This hybrid structure preserves the nano-scale nature of the CoMn_2O_4 particles, which is important for its electrocatalytic activity.

BET surface area measurements

Figure 5 shows the $\text{CoMn}_2\text{O}_4/\text{G}$ N_2 adsorption–desorption isotherms. These isotherms are a representation of the amount of gas adsorbed onto a material with respective of relative pressure. The BET technique, which stands for Brunauer–Emmett–Teller, was used to determine the specific surface area of the $\text{CoMn}_2\text{O}_4/\text{G}$ hybrid, which was found to be $375 \text{ m}^2 \cdot \text{g}^{-1}$. The BJH technique, also known as Barrett–Joyner–Halenda, was used to determine the average pore size distribution of the material, which was found to have a pore width of 5–15 nm.

This hybrid material has a mesoporous nanostructure, meaning that the pores are in the range of 2 – 50 nm. The electrocatalyst high BET surface area can be attributed to

Fig. 2 SEM images of graphene flakes (A) low and (B) high magnifications

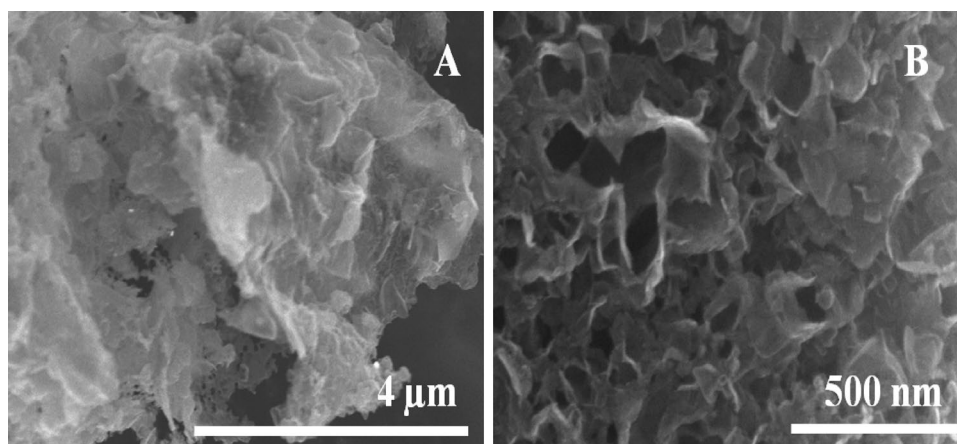


Fig. 3 (A–D) shows different magnification SEM images of $\text{CoMn}_2\text{O}_4/\text{G}$ hybrid material

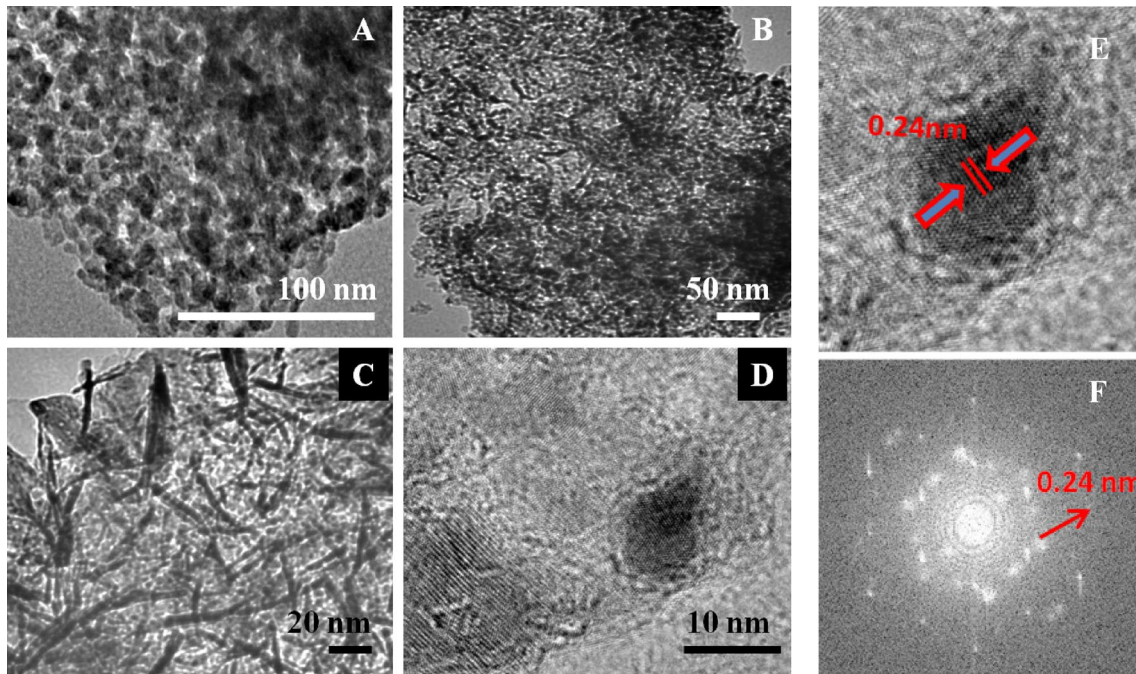
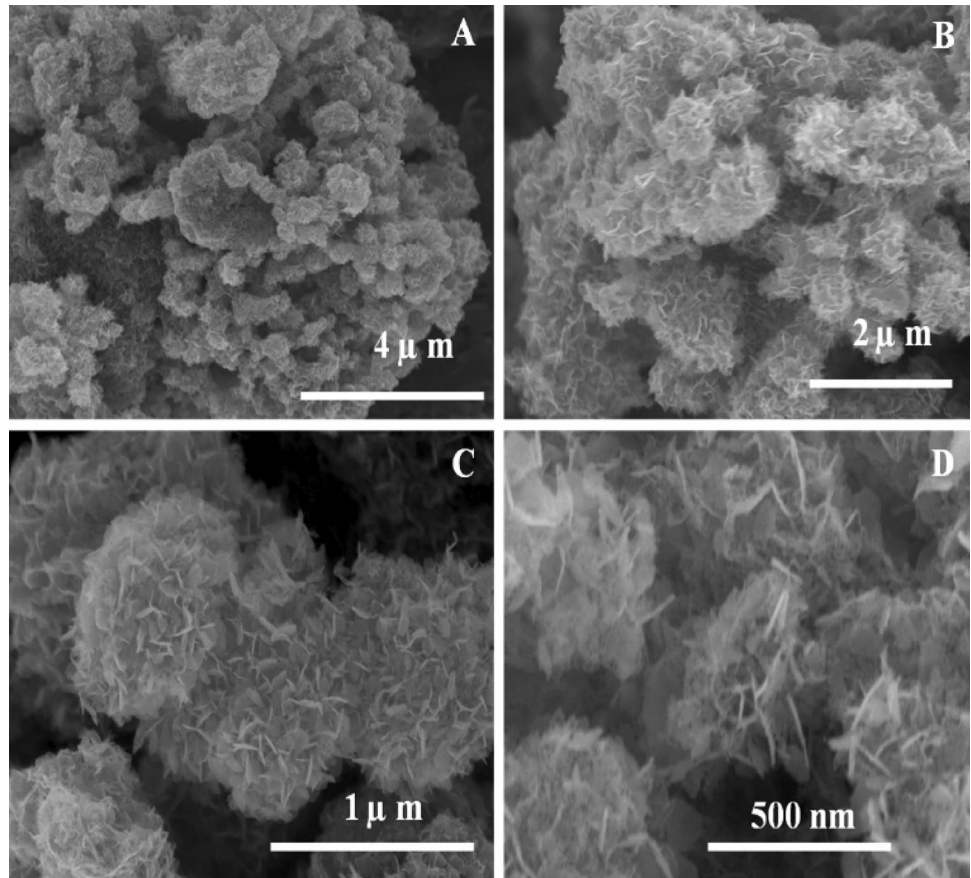


Fig. 4 (A–D) TEM images with varying magnifications, (E) HR-TEM image and (F) Fast Fourier transform FFT image of the hybrid $\text{CoMn}_2\text{O}_4/\text{G}$

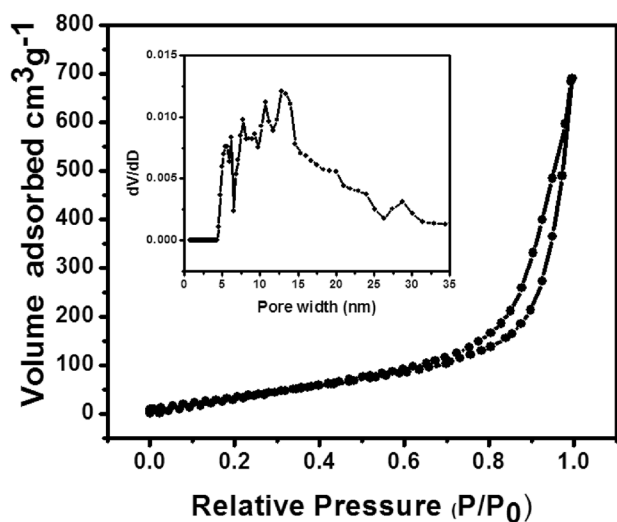


Fig. 5 BET surface area analysis for CoMn₂O₄/G (inset shows pore size distribution)

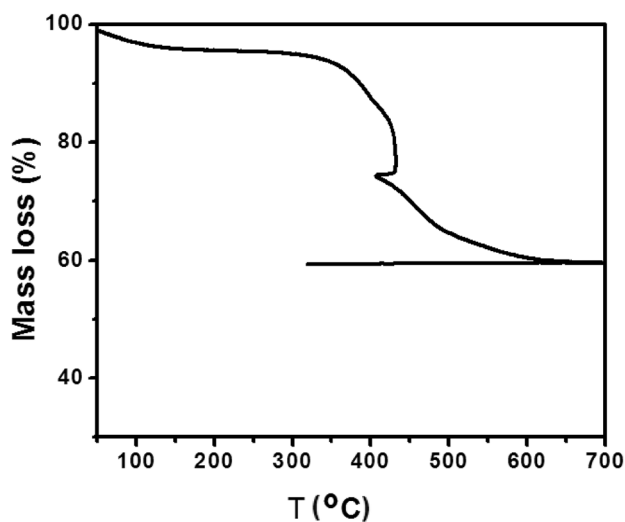


Fig. 6 TGA analysis of CoMn₂O₄/G

its mesoporous characteristic. In catalytic reactions, a larger surface area is essential because it increases the number of active sites available for the reaction to occur. Additionally, the mesoporous structure also increases the stability of the catalyst as it allows for better control of the reaction environment. The high BET surface area and mesoporous nanostructure of CoMn₂O₄/G make it a very attractive material for catalytic reactions such as oxygen reduction reactions.

Thermogravimetric analysis (TGA)

TGA was used to identify the percentage of graphene in the CoMn₂O₄/G hybrid electrocatalyst, as shown in Fig. 6. The

TGA involved heating the substance in a regulated environment (usually air) and then determining the percentage of weight loss at different temperatures.

As the temperature increases, the absorbed water evaporates, and the gravimetric curves reveal a loss of mass between 80 and 150 °C. This corresponds to the evaporation of water that was adsorbed on the surface of the material. The second loss of mass between 350 and 600 °C is due to the burning of graphene. This process causes the graphene to break down into its individual carbon atoms, which leads to a reduction in mass.

The thermogravimetric study suggests that graphene makes up around 38% of the material, this means that the CoMn₂O₄/G hybrid is composed of 38% graphene and 62% CoMn₂O₄. The TGA results suggested that the synthesis of CoMn₂O₄/G hybrid was successful and creating a homogeneous hybrid material. The percentage of graphene in the hybrid material is important because it affects the properties of the material, such as electrical conductivity and stability.

Hard X-ray photoelectron spectroscopy (HAXPES)

HAXPES has emerged as a powerful technique for studying the electronic structure and chemical composition of solid surfaces and interfaces. Recent advances have made HAXPES a potent tool. Compared to standard X-ray photoelectron spectroscopy (XPS), HAXPES's use of higher-energy X-rays (over 2 keV) allows for greater probing depths and increased sensitivity to buried layers. At BL15XU at SPring-8 in Japan, HXAPES was conducted using an X-ray with a photon energy of 5.95 keV. (Hideki et al. 2015) There are several benefits that HAXPES has over regular XPS. HAXPES is well suited for investigating subsurface layers and interfaces because of the increased bulk sensitivity made possible by the higher X-ray energy employed. Improved chemical-state specificity is another way in which HAXPES aids in penetrating analyses of complicated materials. When compared to XPS, it has less of an impact on measurements due to surface charging effects, making it easier to understand results.

The photoelectron peaks in the survey spectrum (Fig. 7) for carbon, oxygen, cobalt, and manganese reveal that these elements are present in the hybrid nanostructure without any extraneous contaminants. The peaks for these elements can be identified by their unique binding energy values, which correspond to the energy required to remove an electron from a specific element. The HAXPES technique also allows us to determine the oxidation states of metal atoms, which is important to understand the electrocatalytic properties. The existence of these elements in their expected oxidation states and ratios indicates that the synthesis method used to create the CoMn₂O₄/G hybrid was successful in incorporating

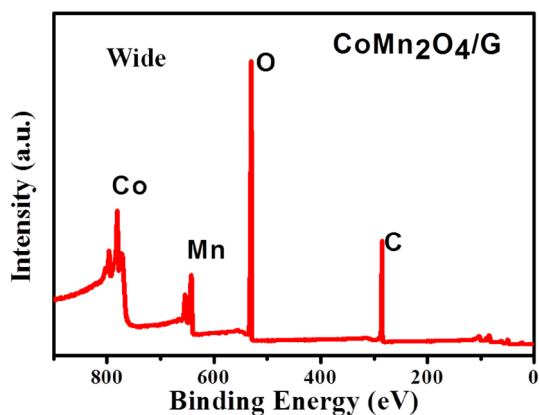


Fig. 7 Spectral survey of $\text{CoMn}_2\text{O}_4/\text{G}$

the metal ions in the material without any extraneous contaminants. This is important because the presence of impurities can affect the properties of the material and its performance as a catalyst in electrochemical reactions.

Figure 8A shows that the Co 2p region displayed two peaks, one at 780.1 eV corresponding to the Co $2p_{3/2}$, and the other at 795.5 eV corresponding to the Co $2p_{1/2}$. New shoulder peaks at 786.1 and 802.7 eV were seen, suggesting the existence of Co^{+2} ion. (McIntyre et al. 1990; Zhang et al. 2006) The peak separation value (Co $2p_{1/2}$ - $2p_{3/2}$) is quite close to 16.0 eV, further confirming the divalent nature of cobalt. (Frost et al. 1972) The existence of both the oxidation states (+2, +3) of cobalt are showed in Fig. 8B. (Garg et al. 2015) Fig. 8C illustrates the Mn 2p spectrum, which exhibits two distinct peaks at 641.7 and 653.3 eV. These peaks correspond to the Mn $2p_{3/2}$ and Mn $2p_{1/2}$ electrons. These peaks are separated by a spin-orbit splitting energy of 11.6 eV, which is a characteristic feature of Mn 2p spectra. These peaks are indicative of the presence of Mn in its trivalent form, which agrees with values reported in previous research. (Carver et al. 1972) Fig. 8D illustrates the presence of both oxidation states (+2 and +3) of Mn. The O 1s spectrum (Fig. 8F) exhibits two peaks, one at a binding energy of 529.9 eV and another at 531.4 eV. The peak at 529.9 eV is indicative of the presence of oxide ions. This peak is relatively large, suggesting that there is a significant amount of oxide ions in the sample. The smaller peak at 531.4 eV is attributed to OH^- and/or absorbed H_2O . (Tan et al. 1991) Based on the obtained HXPS data, it can be inferred that the material under investigation has formed $\text{Co}^{2+}\text{Mn}^{3+}_2\text{O}_4$. Additionally, peak at 284.6 eV in the C1s spectrum (Fig. 8E), which is associated with carbon, provides evidence for the existence of graphene in the hybrid composite electrocatalyst.

Electrochemical analysis

Oxygen reduction reaction activity

Figure 9A shows the CV polarization curves, illustrating a higher current in an oxygen environment in comparison to an argon environment. Figure 9B presents a comparison of ORR activity of various nanostructures, as measured by RDE. The graph compares the oxygen diffusion limiting currents at 2400 rpm obtained for $\text{CoMn}_2\text{O}_4/\text{G}$, graphene, $\text{CoMn}_2\text{O}_4 + \text{G}$ (physical mixture), $\text{Co}_x\text{O}_y/\text{G}$, $\text{Mn}_x\text{O}_y/\text{G}$, and CoMn_2O_4 . The $\text{CoMn}_2\text{O}_4/\text{G}$ hybrid nanostructure had the highest ORR onset potential at -0.028 V, compared to $\text{CoMn}_2\text{O}_4 + \text{G}$ (-0.060 V) and CoMn_2O_4 without graphene (-0.206 V). The $\text{CoMn}_2\text{O}_4/\text{G}$ hybrid had a current density of $9.11 \text{ mA}/\text{cm}^2$, while $\text{Co}_x\text{O}_y/\text{G}$ had a lower onset potential of -0.089 V but a similar limiting current. The ORR activities of graphene and CoMn_2O_4 were low. The $\text{CoMn}_2\text{O}_4/\text{G}$ hybrid had a more positively shifted ORR half wave potential, similar to that of the Pt/C catalyst. The catalytic properties of $\text{Co}_x\text{O}_y/\text{G}$ and $\text{Mn}_x\text{O}_y/\text{G}$ were also analyzed. The high-surface-area graphene present in the CoMn_2O_4 nanostructure is likely responsible for the increased activity observed for the ORR onset potential, half-wave potential, and cathodic limiting current. The reaction kinetics during the ORR process were also analyzed using different Rotating Disc Electrode (RDE) rotation rates (Figs. 10 and 11). As the rotation speed increased, the limiting current also increased.

The Koutecky-Levich (K-L) plots for each compound are shown in Figs. 12 and 13, displaying the inverse current (I^{-1}) against the inverse square root of rotation speed ($\omega^{-1/2}$). The number of electrons (n) contributing to the ORR can be found by examining the slope of the K-L curve, which is in turn determined by the K-L equation. It was determined that the number of electrons in the $\text{CoMn}_2\text{O}_4/\text{G}$ hybrid catalyst is 4.01 (analyzed in the range of -0.75 – -0.9 V). Whereas for graphene the number of electrons equal to 1.9, indicating that the ORR is primarily driven by a $2 e^-$ process. This suggests that partial oxidation of O_2 occurs, leading to the formation of undesired H_2O_2 .

Additionally, the number of electrons transported in the control samples were determined to be 3.4, 3.2, 3.4, and 3.6 for CoMn_2O_4 , $\text{CoMn}_2\text{O}_4 + \text{G}$, $\text{Co}_x\text{O}_y/\text{G}$, and $\text{Mn}_x\text{O}_y/\text{G}$, respectively. Compared to other metal oxides, the $\text{CoMn}_2\text{O}_4/\text{G}$ hybrid compound had better ORR activity and electron transfer mechanism. In terms of both onset potential and limiting current density, the electrocatalytic performance of the hybrid CoMn_2O_4 and graphene ($\text{CoMn}_2\text{O}_4/\text{G}$) nanostructure has shown to be comparable to that of the commonly used Pt/C catalyst. This

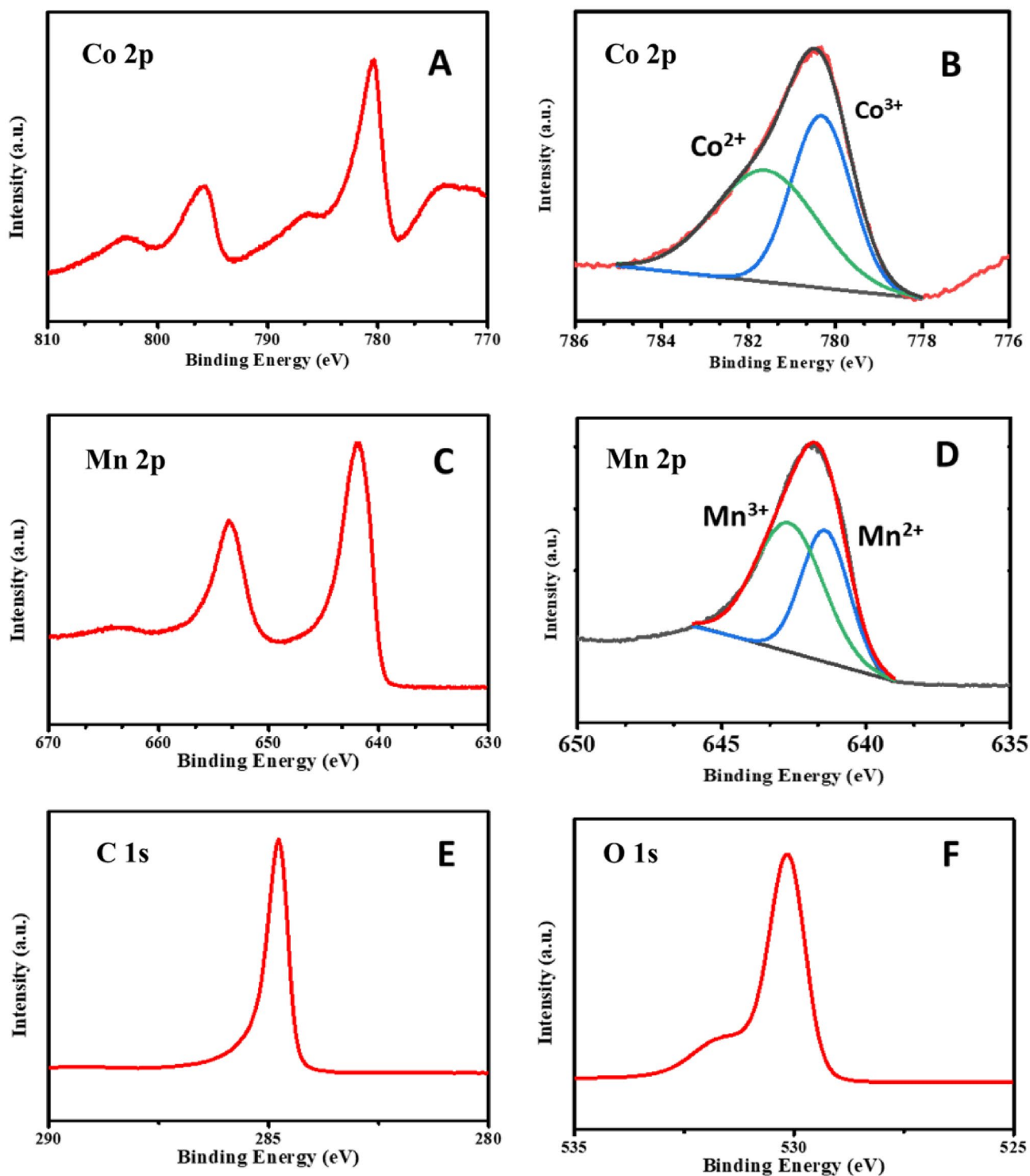


Fig. 8 HAXPES spectra of in the regions of (A, B) Cobalt (C, D) Manganese (E) Carbon and (F) Oxygen

impressive performance of the $\text{CoMn}_2\text{O}_4/\text{G}$ hybrid can be attributed to several factors. Firstly, the material has a large surface area due to the presence of the mesoporous CoMn_2O_4 nanoparticles, which allows for more active sites to be available for the electrocatalytic reaction to occur.

Additionally, the mesoporous structure promotes mass transfer of the reactants and products, enhancing the overall catalytic efficiency. Furthermore, the graphene component in the hybrid structure is known to have excellent electrical conductivity, which facilitates efficient charge

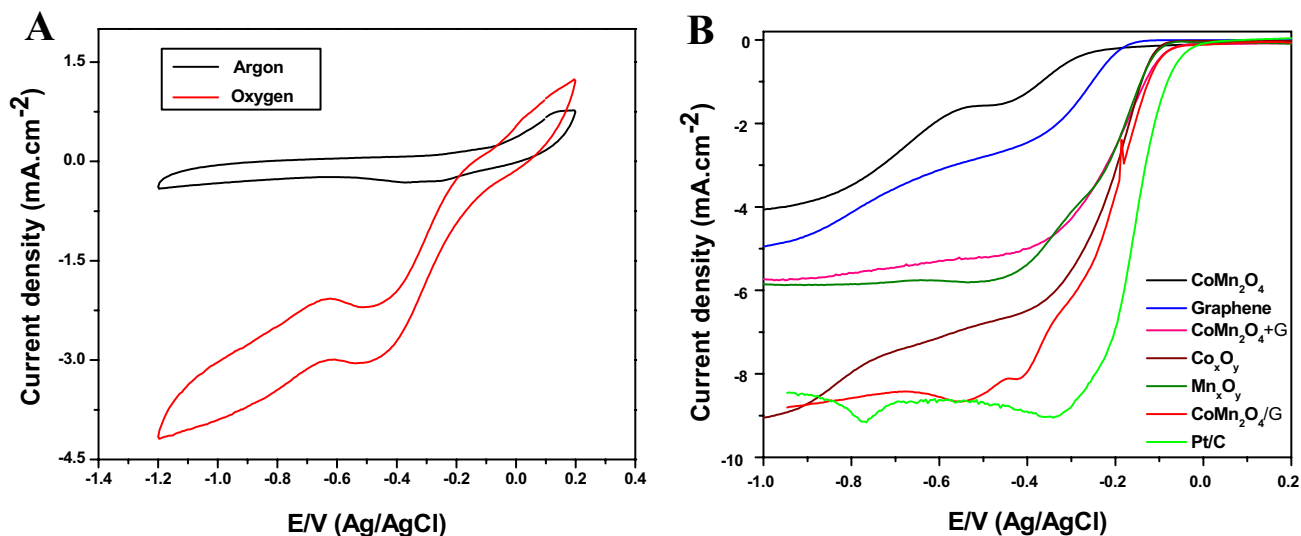


Fig. 9 (A) CV polarization curves for CoMn₂O₄/G (B) ORR polarization curves of CoMn₂O₄, Graphene, CoMn₂O₄+G, CoxOy/G, Mn_xO_y/G, CoMn₂O₄/G and Pt/C

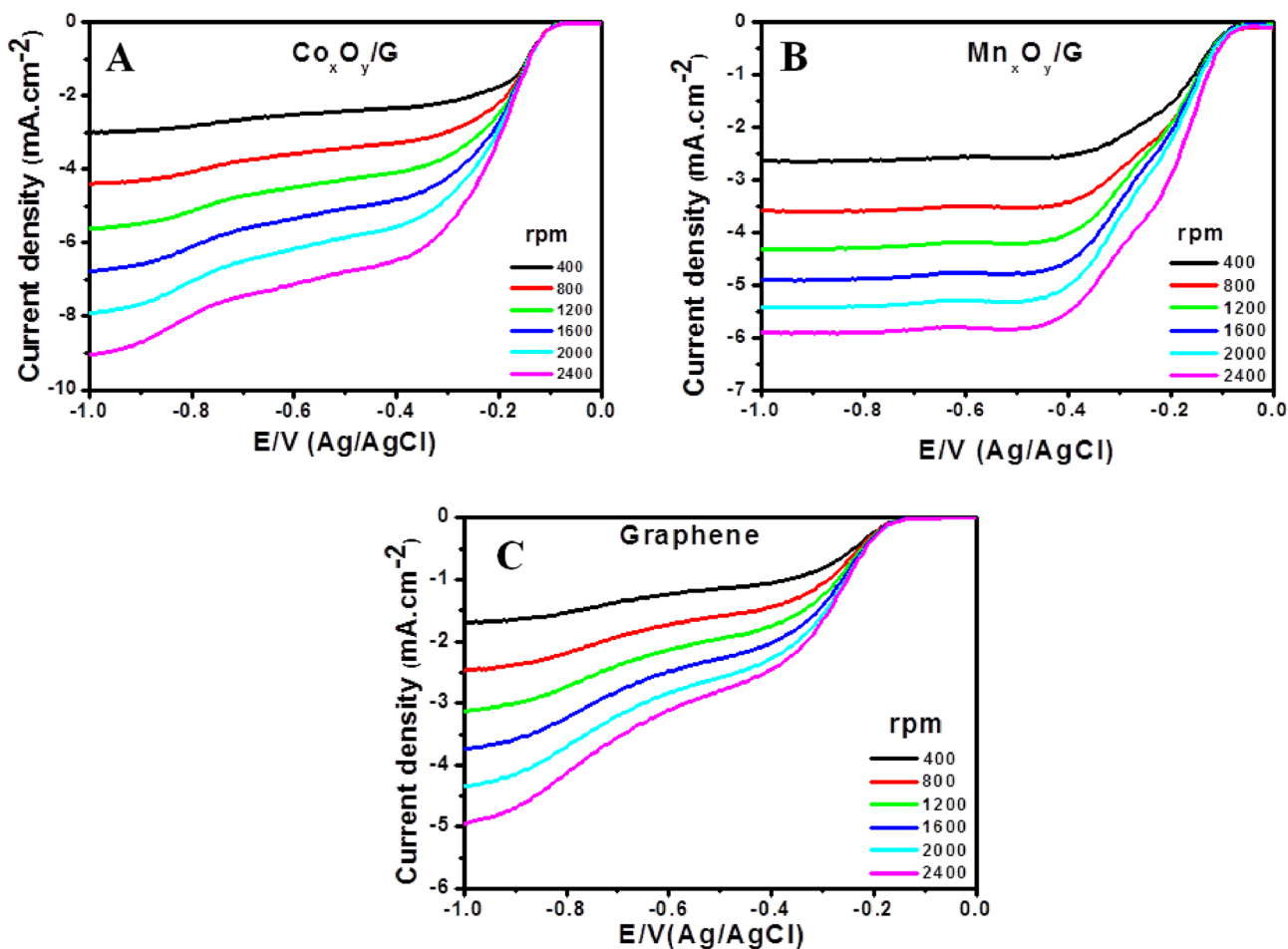


Fig. 10 ORR polarization curves of (A) CoMn₂O₄/G, (B) CoMn₂O₄+G and (C) CoMn₂O₄ at different rotation rates

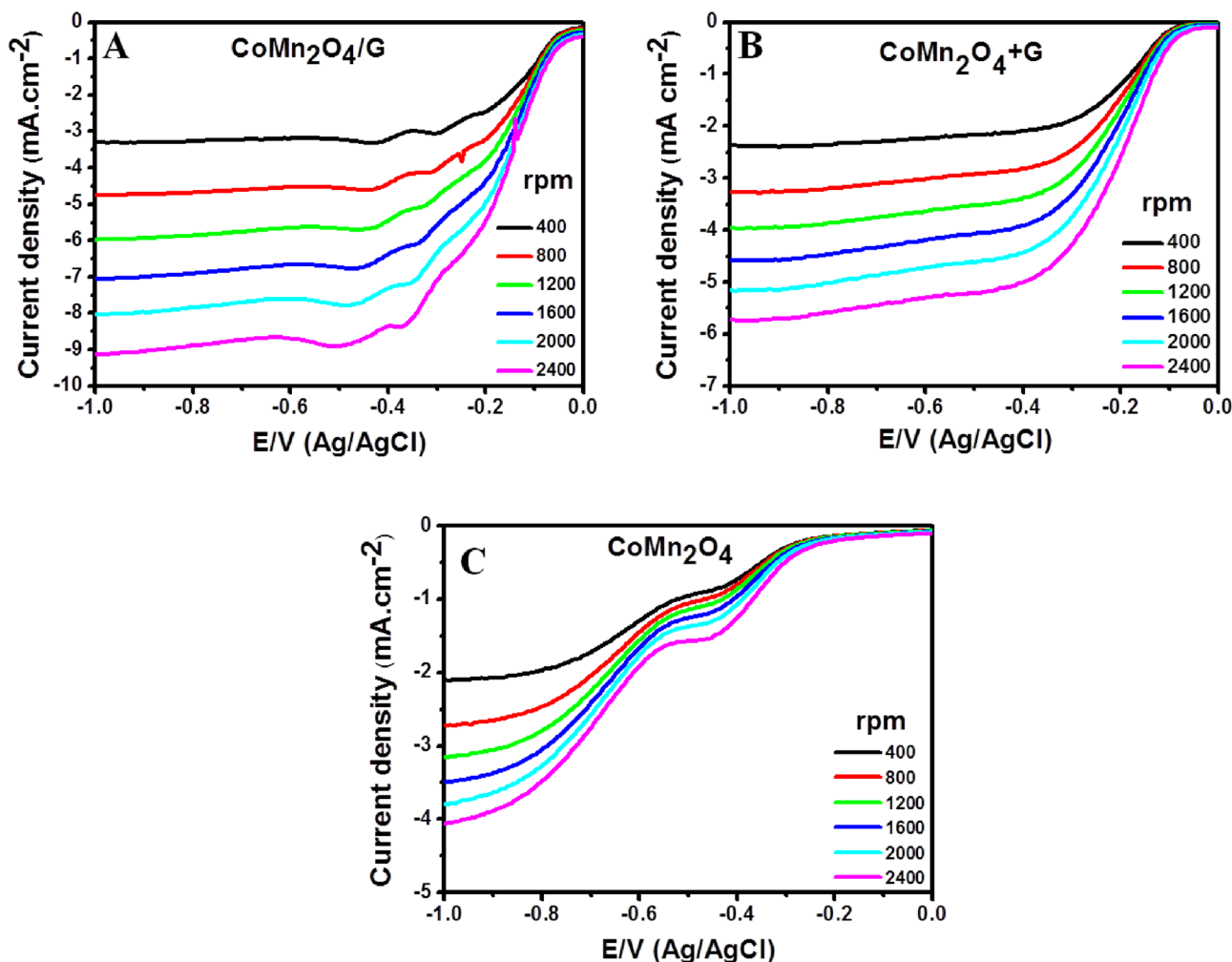


Fig. 11 ORR polarization curves of (A) Co_xO_y/G, (B) Mn_xO_y/G and (C) Graphene

transfer during the electrocatalytic process. The strong contact effect between CoMn₂O₄ and graphene further enhances this property, resulting in improved catalytic performance.

Chronoamperometry analysis

In the context of ORR, electrocatalysts must possess high selectivity and stability. To assess these properties, the chronoamperometric responses of both CoMn₂O₄/G and Pt/C catalysts were compared. The potential was fixed at -0.5 V. (Fig. 14) The Pt/C electrocatalyst experienced a significant decrease in amperometric current due to methanol oxidation on its surface, while the CoMn₂O₄/G hybrid catalyst showed no significant change in current, indicating higher tolerance towards methanol. The CoMn₂O₄/G hybrid electrocatalyst exhibited enhanced methanol tolerance and stability. During a 10000 s durability test, the hybrid structure displayed only a 5% reduction in relative current (I/I_0),

in contrast to a 15% reduction observed for Pt/C. Thus, the CoMn₂O₄/G hybrid nanostructure has the potential to serve as an efficient electrocatalyst for ORR in fuel cell applications.

Electrochemical impedance spectroscopy analysis

The Electrochemical Impedance Spectroscopy (EIS) data for the CoMn₂O₄+G, Pt/C, and CoMn₂O₄/G samples indicate distinct differences in their electrochemical behavior. A systematic examination of the relationship between the real part of the impedance [$\text{Re}(Z)$] and the negative natural logarithm of the modulus of the impedance [$-\ln|Z|$] offers insights into their resistive and capacitive properties. Figure 15 illustrate the electrochemical impedance spectra (EIS) of the samples conducted O₂-saturated 0.1 M KOH at a potential of -0.1 V versus Ag/AgCl. CoMn₂O₄+G sample demonstrates a considerable increase in both $\text{Re}(Z)$ and $-\ln|Z|$, suggesting an increase in both the resistive and

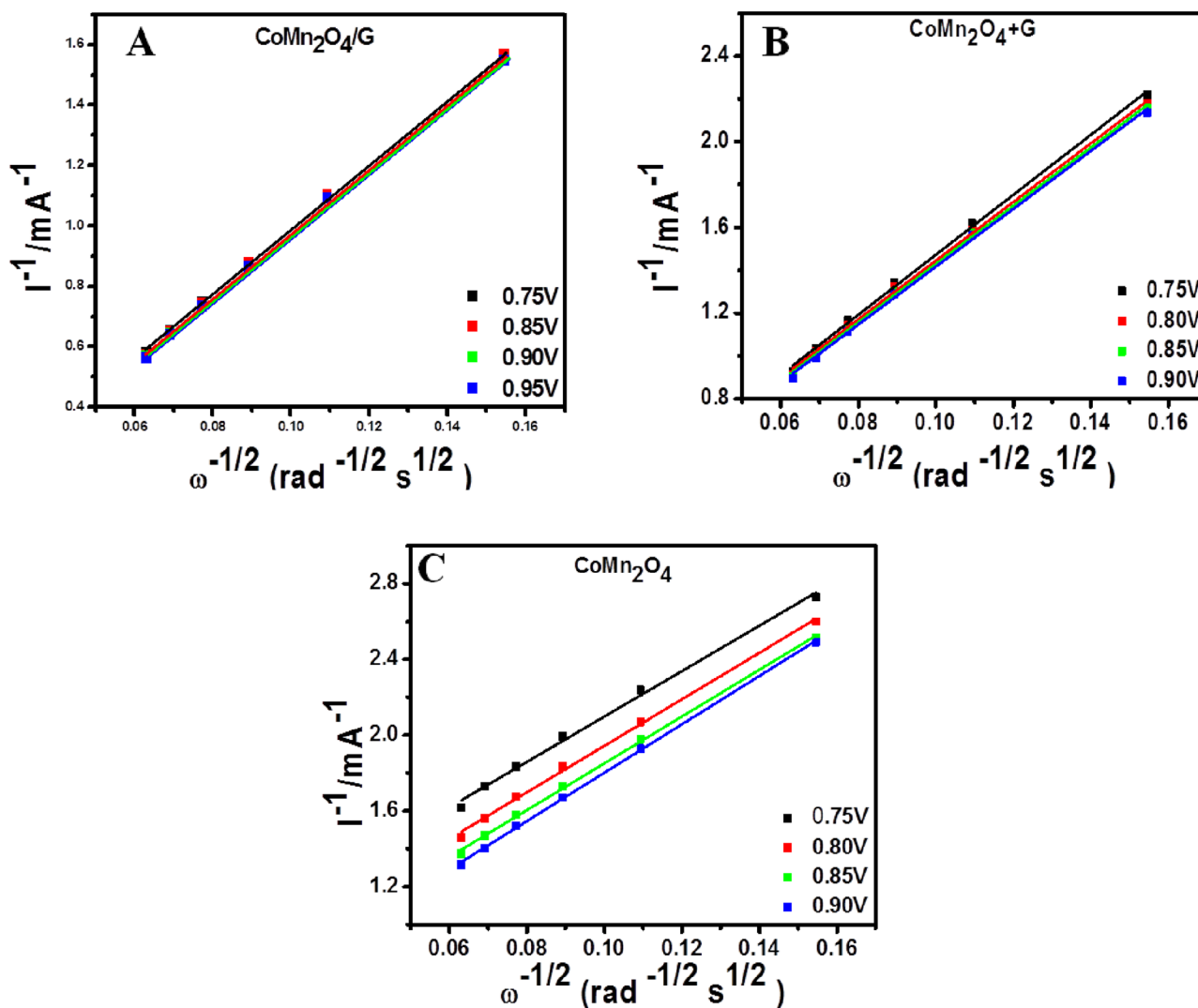


Fig. 12 Koutecky-Levich plots obtained for (A) $\text{CoMn}_2\text{O}_4/\text{G}$, (B) $\text{CoMn}_2\text{O}_4+\text{G}$ and (C) CoMn_2O_4

capacitive elements of the impedance. This increment indicates an elevation in both the charge transfer resistance and the diffusion limitations as the frequency reduces. Consequently, the electrochemical performance might be compromised due to these factors. Conversely, the Pt/C sample, although showing an increasing trend in both $\text{Re}(Z)$ and $-\ln|Z|$ as the frequency reduces, exhibits lower overall impedance values in comparison to the $\text{CoMn}_2\text{O}_4/\text{G}$ sample. This suggests that Pt/C, despite facing increasing charge transfer resistance and diffusion limitations at lower frequencies, demonstrates superior electrochemical performance, possibly due to the inherently lower resistances in the material. In contrast, the $\text{CoMn}_2\text{O}_4/\text{G}$ sample stands out with the smallest $\text{Re}(Z)$ and $-\ln|Z|$ values among all the samples, indicating the lowest overall impedance. Such low impedance suggests superior electrochemical performance, presumably due to reduced resistances, which may be attributed to enhanced

electron transfer and reduced diffusion limitations. Overall, each sample demonstrates unique electrochemical characteristics, which could be attributed to their compositional and structural differences. While all the samples show an increasing trend in impedance with reducing frequency, the $\text{CoMn}_2\text{O}_4/\text{G}$ sample shows promise due to its lowest overall impedance.

Conclusions

The $\text{CoMn}_2\text{O}_4/\text{G}$ hybrid nanoarchitectonics electrocatalyst was produced using hydrothermal synthesis followed by air annealing. This method allows for precise control over the structure of the hybrid material and the strength of the interaction between the spinel oxide and graphene. As a result, the produced $\text{CoMn}_2\text{O}_4/\text{G}$ hybrid nanostructure

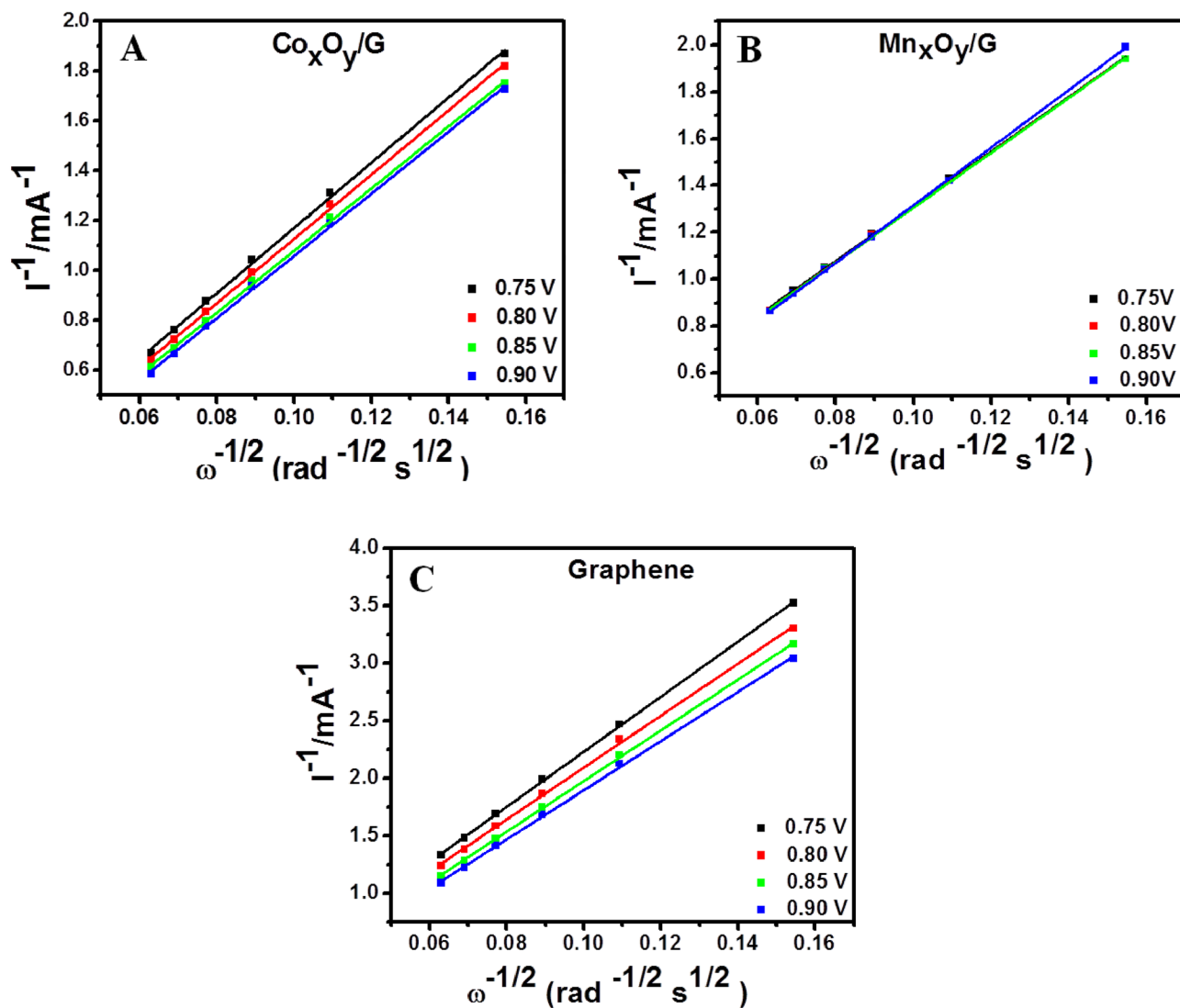


Fig. 13 Koutecky-Levich plots obtained for (A) $\text{Co}_x\text{O}_y/\text{G}$ (B) $\text{Mn}_x\text{O}_y/\text{G}$ and (C) Graphene

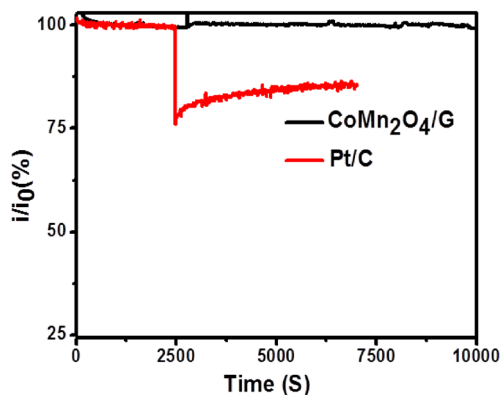


Fig. 14 The chronoamperometric responses of the $\text{CoMn}_2\text{O}_4/\text{G}$ and Pt/C

displayed extraordinary electrocatalytic activity towards ORR, so this material could be a potential electrocatalyst for alkaline fuel cell (AFC) application. The oxygen reduction process in $\text{CoMn}_2\text{O}_4/\text{G}$ takes place through a four-electron transfer, as shown by the electron transfer number of 4.01. Furthermore, the $\text{CoMn}_2\text{O}_4/\text{G}$ electrocatalyst is more durable and displays more selectivity towards methanol than the Pt/C electrocatalyst. $\text{CoMn}_2\text{O}_4/\text{G}$ is a potential catalyst for ORR that is both inexpensive and efficient, making it a promising alternative to noble metal-based catalysts for use in various applications. The study provides a practical strategy for designing and synthesizing hybrid materials, which can be expanded to generate similar materials for a wide range of energy-related applications.

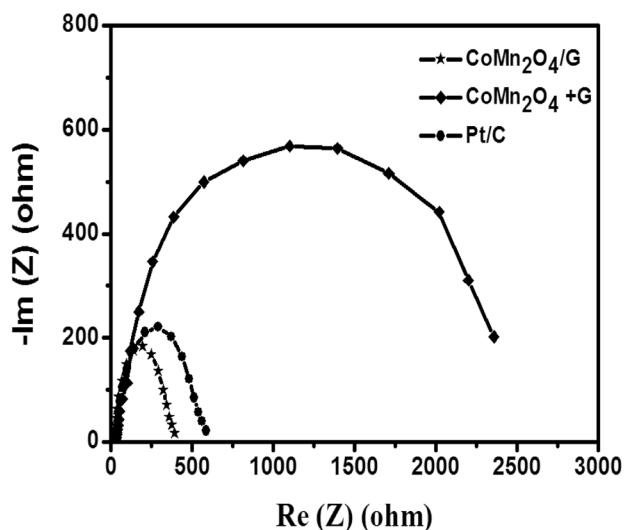


Fig. 15 Impedance spectra of $\text{CoMn}_2\text{O}_4/\text{G}$, $\text{CoMn}_2\text{O}_4+\text{G}$, and Pt/C were examined by spectroscopy in O_2 -saturated 0.1 M KOH at -0.1 V (Vs Ag/AgCl) and $50 \text{ mg}\cdot\text{cm}^{-2}$ of catalytic loading and rotation was at 2025 rpm

Declarations

Conflict of interest The authors declare no conflict of interest.

References

- Abbas Q, Mirzaeian M, Hunt MRC, Hall P, Raza R (2020) Current state and future prospects for electrochemical energy storage and conversion systems. *Energies* 13(21):5847. <https://doi.org/10.3390/en13215847>
- Ariga K, Shrestha LK (2020) Fullerene nanoarchitectonics with shape-shifting. *Materials* 13(10):2280. <https://doi.org/10.3390/ma13102280>
- Ariga K, Yamauchi Y (2020) Nanoarchitectonics from atom to life. *Chem Asian J* 15(6):718–728. <https://doi.org/10.1002/asia.202001016>
- Ariga K, Ji Q, Hill J et al (2012) Forming nanomaterials as layered functional structures toward materials nanoarchitectonics. *NPG Asia Mater* 4:e17. <https://doi.org/10.1038/am.2012.30>
- Ariga K, Ji Q, Nakanishi W, Hill JP, Aono M (2015) Nanoarchitectonics: a new materials horizon for nanotechnology. *Mater Horiz* 2(4):406–413. <https://doi.org/10.1039/c5mh00012b>
- Carbonio RE, Fierro C, Tryk D, Scherson D, Yeager E (1988) Perovskite-type oxides: oxygen electrocatalysis and bulk structure. *J Power Sources* 22(3–4):387–398. [https://doi.org/10.1016/0378-7753\(88\)80032-6](https://doi.org/10.1016/0378-7753(88)80032-6)
- Carver JC, Schweitzer GK, Carlson TA (1972) Use of X-Ray photoelectron spectroscopy to study bonding in Cr, Mn, Fe, and Co compounds. *J Chem Phys* 57(2):973–982. <https://doi.org/10.1063/1.1678348>
- Chen Z, Higgins D, Aiping Yu, Zhang L, Zhang J (2011) A review on non-precious metal electrocatalysts for PEM fuel cells. *Energy Environ Sci* 4(9):3167. <https://doi.org/10.1039/c0ee00558d>
- Cheng F, Shen J, Peng Bo, Pan Y, Tao Z, Chen J (2010) Rapid room-temperature synthesis of nanocrystalline spinels as oxygen reduction and evolution electrocatalysts. *Nat Chem* 3(1):79–84. <https://doi.org/10.1038/nchem.931>
- Debe MK (2012) Electrocatalyst approaches and challenges for automotive fuel cells. *Nature* 486(7401):43–51. <https://doi.org/10.1038/nature11115>
- Dosaev KA, Istomin SYa, Strebkov DA, Tsirlina GA, Antipov EV, Savinova ER (2022) AMn_2O_4 spinels (A - Li, Mg, Mn, Cd) as ORR catalysts: the role of Mn coordination and oxidation state in the catalytic activity and their propensity to degradation. *Electrochimica Acta* 428:140923. <https://doi.org/10.1016/j.electacta.2022.140923>
- Feng Ju, Liang Y, Wang H, Li Y, Zhang Bo, Zhou J, Wang J, Regier T, Dai H (2012) Engineering manganese oxide/nanocarbon hybrid materials for oxygen reduction electrocatalysis. *Nano Res* 5(10):718–725. <https://doi.org/10.1007/s12274-012-0256-8>
- Frost DC, McDowell CA, Woolsey IS (1972) Evidence for multiplet splitting of 2p photoelectron lines of transition metal complexes. *Chem Phys Lett* 17(3):320–323. [https://doi.org/10.1016/0009-2614\(72\)87086-6](https://doi.org/10.1016/0009-2614(72)87086-6)
- Garg N, Mishra M, Govind G, Ganguli AK (2015) Electrochemical and magnetic properties of nanostructured CoMn_2O_4 and Co_2MnO_4 . *RSC Adv* 5:84988–84998. <https://doi.org/10.1039/C5RA16937B>
- Guex LG, Sacchi B, Peuvot KF, Andersson RL, Pourrahimi AM, Ström V, Farris S, Olsson RT (2017) Experimental review: chemical reduction of graphene oxide (GO) to reduced graphene oxide (rGO) by aqueous chemistry. *Nanoscale* 9:9562–9571
- He X, Yin F, Yuan S, Liu N, Huang X (2016) Hybrid spinel oxides/N-doped reduced graphene oxide as Highly-active bifunctional electrocatalysts for oxygen reduction/evolution reactions. *Chem Electro Chem* 3(7):1107–1115. <https://doi.org/10.1002/celec.20160061>
- Hideki A, Hideki Y, Umezawa Naoto X, Ya SG, Ramesh GV, Tanabe T, Rajesh K, Shigenori U, Nobuaki S, Yoko Y-M, Masahiko S, Takahisa O, Futoshi M, Takayuki K (2015) Correlation between the surface electronic structure and CO-oxidation activity of Pt alloys. *Phys Chem Chem Phys* 17:4879–4887. <https://doi.org/10.1039/C4CP03406F>
- Jeon I-Y, Choi H-J, Jung S-M, Seo J-M, Kim M-J, Dai L, Baek J-B (2012) Large-scale production of edge-selectively functionalized graphene nanoplatelets via ball milling and their use as metal-free electrocatalysts for oxygen reduction reaction. *J Am Chem Soc* 135(4):1386–1393. <https://doi.org/10.1021/ja3091643>
- Jing Du, Chen C, Cheng F, Chen J (2015) Rapid synthesis and efficient electrocatalytic oxygen reduction/evolution reaction of CoMn_2O_4 nanodots supported on graphene. *Inorg Chem* 54(11):5467–5474. <https://doi.org/10.1021/acs.inorgchem.5b00518>
- Jörissen L (2006) Bifunctional oxygen/air electrodes. *J Power Sour* 155(1):23–32. <https://doi.org/10.1016/j.jpowsour.2005.07.038>
- Jung K-N, Hwang SM, Park M-S, Kim KJ, Kim J-G, Dou SX, Kim JH, Lee J-W (2015) One-dimensional manganese-cobalt oxide nanofibres as bi-functional cathode catalysts for rechargeable metal-air batteries. *Sci Rep* 5:1. <https://doi.org/10.1038/srep07665>
- Kaur P, Singh K (2020) Review of perovskite-structure related cathode materials for solid oxide fuel cells. *Ceram Int* 46(5):5521–5535. <https://doi.org/10.1016/j.ceramint.2019.11.066>
- K Kinoshita I (1992) *Electrochemical Oxygen Technology*. Wiley-Interscience. ISBN: 978-0-471-57043-1. <https://www.wiley.com/en-us/Electrochemical+Oxygen+Technology-p-9780471570431>
- Kodiyath R, Ramesh GV, Manikandan M, Ueda S, Fujita T, Abe H (2020) Intermetallic Pd_3X (X = Ti and Zr) nanocrystals for electro-oxidation of alcohols and formic acid in alkaline and acidic media. *Sci Technol Adv Mater* 21(1):573–583. <https://doi.org/10.1080/14686996.2020.1789437>

- Lankauf K, Cysewska K, Karczewski J, Mielewczyk-Gryń A, Górnicka K, Cempura G, Chen M, Jasiński P, Molin S (2020) $\text{Mn}_x\text{Co}_{3-x}\text{O}_4$ spinel oxides as efficient oxygen evolution reaction catalysts in alkaline media. *Int J Hydrogen Energy* 45(29):14867–14879. <https://doi.org/10.1016/j.ijhydene.2020.03.188>
- Li C, Han X, Cheng F, Yuxiang Hu, Chen C, Chen J (2015) Phase and composition controllable synthesis of cobalt manganese spinel nanoparticles towards efficient oxygen electrocatalysis. *Nat Commun* 6:1. <https://doi.org/10.1038/ncomms8345>
- Liu J, Zhou H, Yang W, Ariga K (2020) Soft nanoarchitectonics for enantioselective biosensing. *Acc Chem Res* 53(3):644–653. <https://doi.org/10.1021/acs.accounts.9b00612>
- Liu Y, Zhou D, Deng T, He G, Chen A, Sun X, Yang Y, Miao P (2021) research progress of oxygen evolution reaction catalysts for electrochemical water splitting. *Chemsuschem* 14(24):5359–5383. <https://doi.org/10.1002/cssc.202101898>
- Maji S, Shrestha LK, Ariga K (2019) Nanoarchitectonics for nanocarbon assembly and composite. *J Inorg Organomet Polym Mater* 30(1):42–55. <https://doi.org/10.1007/s10904-019-01294-x>
- McIntyre NS, Johnston DD, Coatsworth LL, Davidson RD, Brown JR (1990) X-ray photoelectron spectroscopic studies of thin film oxides of cobalt and molybdenum. *Surf Interface Anal* 15(4):265–272. <https://doi.org/10.1002/sia.740150406>
- Monama GR, Ramohlola KE, Iwuoha EI, Modibane KD (2022) Progress on perovskite materials for energy application. *Results Chem* 4:100321. <https://doi.org/10.1016/j.rechem.2022.100321>
- Olowoyo JO, Kriek RJ (2022) Recent progress on bimetallic-based spinels as electrocatalysts for the oxygen evolution reaction. *Small* 18(41):2203125. <https://doi.org/10.1002/smll.202203125>
- Prabu M, Ramakrishnan P, Shanmugam S (2014) CoMn_2O_4 nanoparticles anchored on nitrogen-doped graphene nanosheets as bifunctional electrocatalyst for rechargeable zinc–air battery. *Electrochem Commun* 41:59–63. <https://doi.org/10.1016/j.elecom.2014.01.027>
- Ramesh GV, Kodiyath R, Tanabe T, Manikandan M, Fujita T, Matsumoto F, Ishihara S, Ueda S, Yamashita Y, Ariga K, Abe H (2014a) NbPt_3 intermetallic nanoparticles: highly stable and CO-Tolerant electrocatalyst for fuel oxidation. *Chem Electro Chem* 1(4):728–732. <https://doi.org/10.1002/celec.201300240>
- Ramesh GV, Kodiyath R, Tanabe T, Manikandan M, Fujita T, Umezawa N, Ueda S, Ishihara S, Ariga K, Abe H (2014b) Stimulation of electro-oxidation catalysis by bulk-structural transformation in intermetallic ZrPt_3 nanoparticles. *ACS Appl Mater Interfaces* 6(18):16124–16130. <https://doi.org/10.1021/am504147q>
- Restovic A, Ríos E, Barbato S, Ortiz J, Gautier JL (2002) Oxygen reduction in alkaline medium at thin $\text{Mn}_x\text{Co}_{3-x}\text{O}_4$ ($0 \leq x \leq 1$) spinel films prepared by spray pyrolysis. Effect of oxide cation composition on the reaction kinetics. *J Electroanalytical Chem* 522(2):141–151. [https://doi.org/10.1016/s0022-0728\(02\)00639-3](https://doi.org/10.1016/s0022-0728(02)00639-3)
- Shi J, Lei K, Sun W et al (2017) Synthesis of size-controlled CoMn_2O_4 quantum dots supported on carbon nanotubes for electrocatalytic oxygen reduction/evolution. *Nano Res* 10:3836–3847. <https://doi.org/10.1007/s12274-017-1597-0>
- Tan BJ, Klabunde KJ, Sherwood PMA (1991) XPS studies of solvated metal atom dispersed (SMAD) catalysts. Evidence for layered cobalt-manganese particles on alumina and silica. *J Am Chem Soc* 113(3):855–861. <https://doi.org/10.1021/ja00003a019>
- Wang L, Zhao X, Yuhao L, Maowen X, Zhang D, Ruoff RS, Stevenson KJ, Goodenough JB (2011) CoMn_2O_4 spinel nanoparticles grown on graphene as bifunctional catalyst for lithium-air batteries. *J Electrochem Soc* 158:A1379
- Weiss PS (2007) A conversation with Dr. Masakazu Aono: leader in atomic-scale control and nanomanipulation. *ACS Nano* 1(5):379–383. <https://doi.org/10.1021/nn7004014>
- Yang Y, Xiong Y, Holtz ME, Feng X, Zeng R, Chen G, DiSalvo FJ, Muller DA, Abruña HD (2019) Octahedral spinel electrocatalysts for alkaline fuel cells. *Proc Natl Acad Sci* 116(49):24425–24432. <https://doi.org/10.1073/pnas.1906570116>
- Zhang D, Zhang X, Ni X, Song JiMei, Zheng H (2006) Low-temperature fabrication of MnFe_2O_4 octahedrons: Magnetic and electrochemical properties. *Chem Phys Lett* 426(1–3):120–123. <https://doi.org/10.1016/j.cplett.2006.05.100>
- Zhang C, Zheng B, Huang C, Li Y, Wang J, Tang S, Deng M, Youwei Du (2019) Heterostructural three-dimensional reduced graphene Oxide/ CoMn_2O_4 nanosheets toward a wide-potential window for high-performance supercapacitors. *ACS Appl Energy Mater* 2(7):5219–5230. <https://doi.org/10.1021/acsaeem.9b00904>

Publisher's Note Springer Nature remains neutral with regard to jurisdictional claims in published maps and institutional affiliations.

Springer Nature or its licensor (e.g. a society or other partner) holds exclusive rights to this article under a publishing agreement with the author(s) or other rightsholder(s); author self-archiving of the accepted manuscript version of this article is solely governed by the terms of such publishing agreement and applicable law.

NANOSCALE BISMUTH SELENIDE AS AN EFFICIENT CATALYST FOR SOLVOTHERMAL, AND MICROWAVE-ASSISTED ONE-POT SYNTHESIS OF BIS(INDOLYL)METHANES

M. Shanti^{1,2}, Vijayshekar Pulusu¹, S. Shylaja³, G. Yaku¹ and U. Umesh Kumar^{1,✉}

¹Department of Chemistry, Osmania University, Hyderabad-500 007, T. S. India

²G. Narayanamma Institute of Technology Science, Hyderabad-500 104, T. S. India

³Chaitanya Bharathi Institute of Technology (A), Hyderabad-500075, T.S. India

✉Corresponding Author: utkooor@gmail.com

ABSTRACT

Bi₂Se₃ nanoparticles were synthesized under greenery conditions by using economically viable desktop chemicals such as Bi(NO₃)₃, sodium selenite (Na₂SeO₃), EDTA, and L-Ascorbic acid. Prepared Bi₂Se₃ nanoparticles were characterized by UV-Vis Spectrophotometer, X-ray Diffraction, X-ray photoelectron spectroscopy (XPS), and Scanning electron microscopy. A prepared nanocatalyst is found to work efficiently for one-pot synthesis of diindolylmethanes from a set of indole and different aldehydes under solvent-free microwave environment and solvothermal conditions. Observed reaction times are enormously decreased when the reactions are conducted under a solvent-free microwave environment.

Keywords: Nano Bismuth Selenide, Catalysis, L-Ascorbic Acid, Indoles, Diindolylmethanes, Solvent-Free Microwave Propagation.

RASAYAN J. Chem., Vol. 16, No. 3, 2023

INTRODUCTION

Recently, interest in the synthesis of Bismuth chalcogenides (Bi₂O₃, Bi₂S₃, Bi₂Se₃, and Bi₂Te₃) has increased dramatically because of their immense importance in the fields of photoelectric and thermoelectric functional materials. Among, them synthesis of Bismuth Selenide (Bi₂Se₃) at nanoscale has received much more attention due to its semiconductor (with a gap of 0.3 eV) and thermoelectric properties.¹ Due to the observation of topologically protected surface states in bismuth selenide.^{3,4} It has been the focus of continuing scientific study by numerous groups.² On the other hand, bis(indolyl) methanes are an important class of heterocyclic compounds derived from indole, which are explored as useful bioactive intermediates in the pharmaceutical industry.⁵⁻¹² The research team of Bubun Banerjee recently released an amazing bibliography on the synthesis of various indolyl methanes such as bis(indolyl), di(bis-indolyl), and tris-indolyl methanes obtained by the reaction of indole with carbonyl compounds (aldehydes and ketones).⁸ In the current study, we have created a greener synthetic technique for the production of "Nano Bismuth Selenide (Bi₂Se₃)" utilizing inexpensive chemicals such as ascorbic acid (vitamin C), Bi(NO₃)₃, EDTA, and sodium selenite (Na₂SeO₃). Under solvothermal and solvent-free conditions, the "Nano (Bi₂Se₃)" thus generated has been investigated as an effective nanocatalyst for one-pot synthesis of bis diindolylmethanes by using various indoles and aromatic aldehydes (Scheme-1).

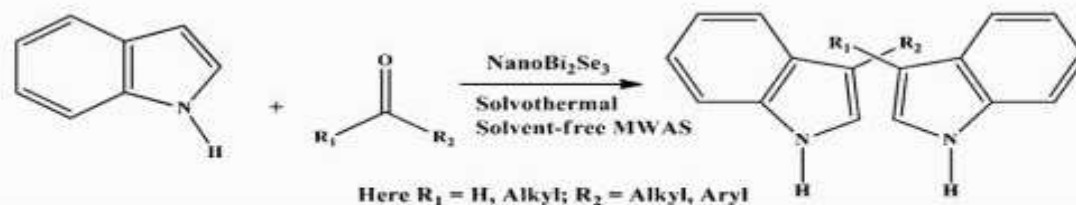
EXPERIMENTAL

Material and Methods

Reagent grade bismuth nitrate (Bi(NO₃)₃), sodium selenite (Na₂SeO₃), ethylene diamine tetra acetate (EDTA), L-Ascorbic acid, potassium hydroxide (KOH), aldehydes, indoles, and necessary solvents were purchased from a local vendor, and used as such which includes Avra (India) and Aldrich(India) chemicals.

Synthesis and Characterization of Bismuth Nanoparticles

In a typical synthesis process, 10mmol of Sodium Selenite (Na_2SeO_3), 6.66mmol $\text{Bi}(\text{NO}_3)_3$, and 0.666g ethylene diamine tetra acetic disodium salt (EDTA) was mixed with 135 mL distilled water in a 250mL R.B flask. After thorough mixing, 1.166g of KOH, and 1.166g of ascorbic acid were added to the contents of the R.B. flask. The flask's contents were heated on a magnetic stirrer for 48 hours at 150 °C while being constantly stirred at a speed of 100 rpm. The dark grey powder that had precipitated was filtered then repeatedly washings were done with distilled water and ethyl alcohol. The as-obtained sample was calcined for approximately 6 hours at 100°C. The sample was then subjected to analysis by various techniques such as ultraviolet-DRS, XRD, SEM, TEM, TGA, DSC, and BET SA-PSD techniques.



Scheme-1: Bismuth Selenide-catalyzed one-pot synthesis of Bis(indolyl)methanes

Synthesis of bis(indolyl)methanes

The reaction done in a reaction vessel; the reactants were mixed (2:1 molar ratio of indole to carbonyl compound) with a prepared Nano- Bi_2Se_3 catalyst. The reaction mixture was then kept at rt (room temperature) in a laboratory microwave oven (Scheme-1 and Table-2). TLC analysis confirms the reaction completion. Once the reaction had been verified to be completed, EtOAc (20 mL) was added to the reaction mixture. Using short-column chromatography, the residue was run down using pet ether-EtOAc (8:2) to produce the pure chemical. The filtrate was concentrated after the solid was removed, and the residue was then treated. After the filtration of the solid, the filtrate was concentrated, and then the residue was processed. Physical and spectroscopic data used to characterize the product were in accordance with literature reports and found to be bisindolylmethane compounds.

Reusability of Catalyst

In the present study, it is quite interesting to see that the yield of products was slightly lower and the catalyst could be recycled more easily. Once the reaction is in the first batch, the catalyst is filtered and treated with ethyl acetate to remove organic traces. After removing ethyl acetate, the obtained catalyst is calcinated in a hot air oven at 100 °C for up to two to three hours. For another batch of experiments, the as-activated catalyst is reused. For reusability of the catalyst similar process is followed up to four to five cycles and related observations were compiled as shown in Table-1, and Fig.-1.

Table-1: Reusability of Catalyst

Cycle	4-nitro benzaldehyde		Benzaldehyde		4-methoxy benzaldehyde	
	R.T (min)	Yield (%)	R.T (min)	Yield (%)	R.T (min)	Yield (%)
First	3.0	77	4.0	80	5.0	78
Second	4.0	76	5.0	79	5.0	77
Third	5.0	75	5.0	78	5.0	76
Fourth	5.0	74	5.0	77	6.0	75
Fifth	6.0	73	6.0	76	6.0	74

Characterization of Bismuth Nanoparticles

X-ray Diffraction (XRD) Studies

The XRD patterns of the Bi_2Se_3 nanostructure prepared in a KOH medium at 150 °C for 48 h, can be seen in Fig.-2. In this pattern, all the diffraction peaks can be steadily indexed to a rhombohedral geometry phase of Bi_2Se_3 (JCPDS:33-0214) preferential growth orientation along the (015) direction. XRD results revealed

that the bismuth selenide nanostructures prepared in a KOH medium exhibit a high tendency of acquiring crystalline nature indicating the high purity of the Bi_2Se_3 samples, and no peaks are formed corresponding to Bi_2O_3 or bismuth selenium oxide ($\text{Bi}_2\text{O}_5\text{Se}$) during the synthetic process.

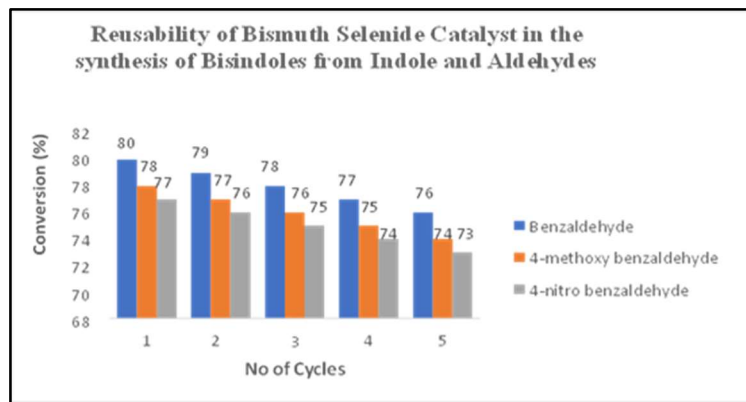


Fig.-1: Reusability of Catalyst

By using Scherrer's formula crystallite size was determined from the (015) peak:

$$D = 0.94\lambda / \beta \cos \theta$$

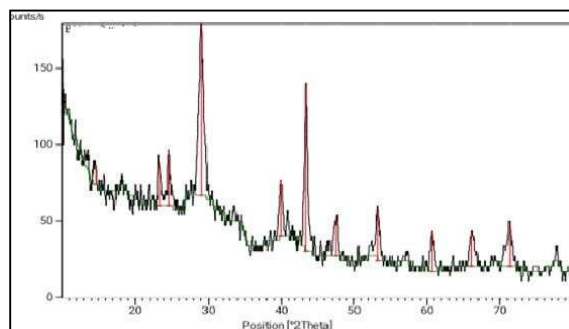


Fig.-2: XRD Spectra of Bi_2Se_3 Nano Catalyst

By using Scherrer's equation and XRD patterns the particle size (D) of the Bi_2Se_3 catalyst is determined and the average particle size was discovered to be 24.6 nm.

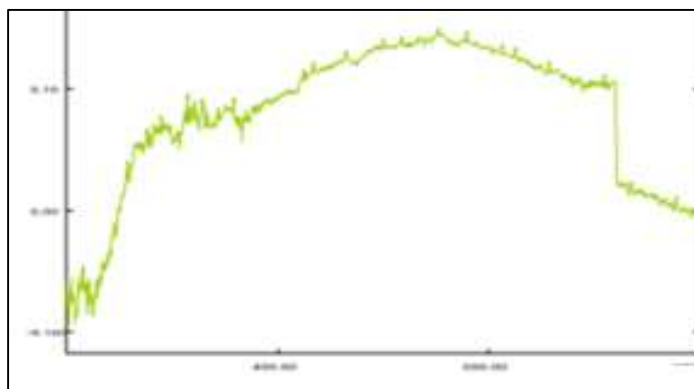


Fig.-3: U.V -DRS Spectrum of Bi_2Se_3 Nano Compound

UV- Spectroscopic Studies

The prepared compounds were recorded in the range of 200-800 nm in the UV-Vis spectrum. Figure-3 shows the UV-DRS spectrum of Bi_2Se_3 nanostructures synthesized in a KOH medium. No characteristic absorption peak is observed in the UV-Visible range due to the extremely narrow band gap in the case of nano- Bi_2Se_3 . The theoretical band gap energy for bulk Bi_2Se_3 is of 0.35 eV [optical] hence the absorption band does not fall in the range of 250-750 nm.

Morphology of the Catalyst

In order to understand the morphology of prepared Bismuth selenide samples, SEM, and TEM studies were taken up, which are shown in Fig.-4 and 5 respectively. The SEM images scanned under different magnifications, presented in given in Fig.-4 clearly indicate that crystallites were agglomerated and are embodied with micro to nano-sized entities in various shapes. However, the TEM images revealed rod-like nanostructures of Bi_2Se_3 , as shown in Fig.-5.

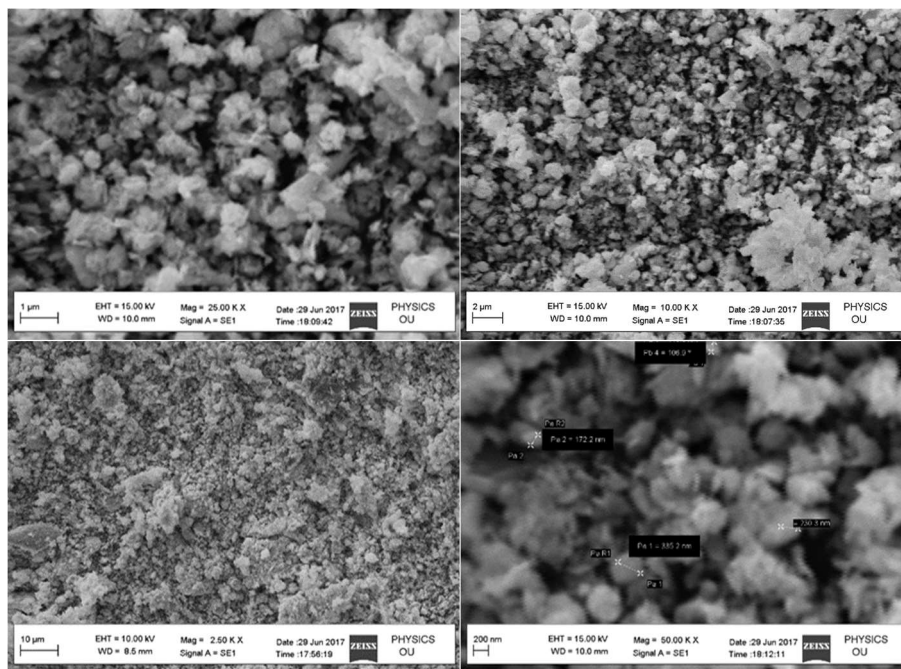


Fig.-4: SEM Images the As-Prepared Bismuth Selenide Under Different Magnifications

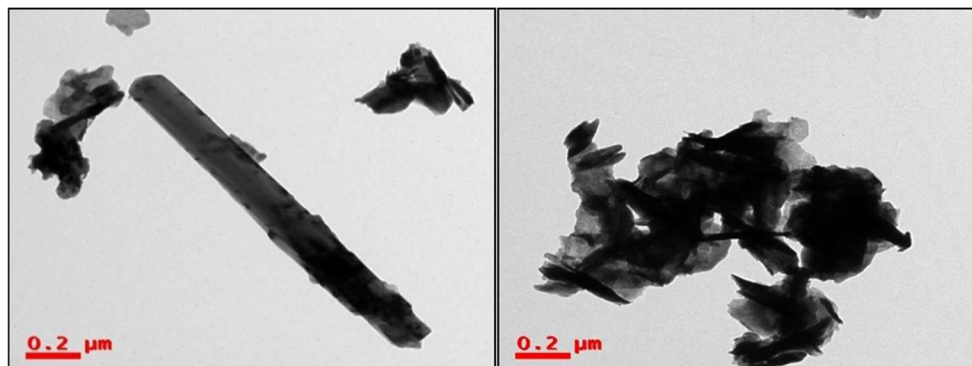


Fig.-5: Morphology From TEM- TEM Images of Nano Bi_2Se_3

X-ray Photoelectron Spectroscopy Analysis (XPS)

This spectroscopic technique is one of the most sensitive techniques that gives the exact elemental ratio present in the material or covering its surface, and also the bonding nature of the elements. Each element has its own fingerprint binding energy (B.E) value. The XPS spectrum depicts a plot of the number of electrons of an element versus the B.E (eV) and thus gives a specific set of peaks in the spectrum. By using the internal standard B.E values have been calibrated, and the C (1s) peak (284.6 eV). In Fig.-6. Se (3d) transition corresponds to the peak at 56 eV. Se (3d) spectrum is broad and highly asymmetric. For Bi (4f) core shows 2 peaks at 160 and 165 (eV). These values are in well agreement with those mentioned in the literature. Estimated from the peak area of Bi 4f and Se 3d the relative amounts were found to be stoichiometric.

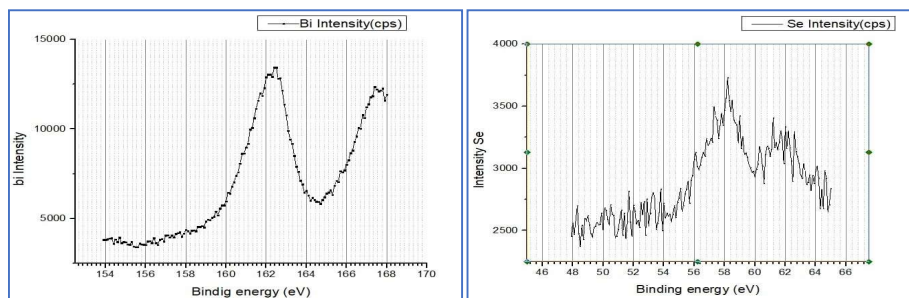


Fig.-6. XPS Spectra of Bi(4f) Bands of Bi₂Se₃ and XPS Spectra - Se (3d) Band

Table-2: Binding Energy (B.E) in XPS spectra of Nano Bi₂Se₃ particles:

Transitions	Binding energy(e.v)	
	Experimental	Reported
Bi 4f7/2	160	158.1
Bi 4f5/2	165	163.4
Se 3d	56	53.3

Thermal Analysis of Bi₂Se₃

Thermo gravimetric analysis (TGA) is used to evaluate the thermal stability of a material under study. It gives useful information about phase transitions, absorption, adsorption, desorption, and chemisorption also.¹⁴ The TGA spectrum of the prepared nano Bi₂Se₃ has been represented in Fig.-7 (Red line).

The curve shows that nano Bi₂Se₃ undergoes weight loss in three steps between 250 and 850°C, in addition to the thermaleffect at 100°C corresponding to the evaporation of surface moisture. The observed second and third peaks in Fig.-7 could be attributed to the weight losses arising from the thermaldecomposition of selenium yielding Bi₂Se_{3-x}.

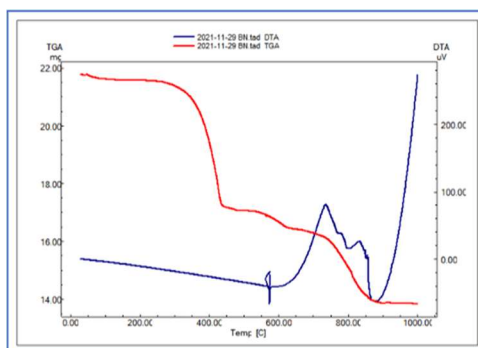


Fig.-7: Thermogravimetric Analysis of Bi₂Se₃

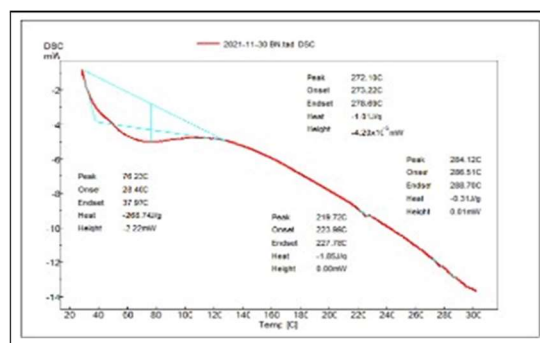


Fig.-8: Differential Scanning Calorimetric (DSC) image of Nano Bi₂Se₃

The blue line in Fig.-8 shows the DTA (Differential thermal analysis) spectrum of Bi₂Se₃. Two peaks are observed in this Figure at 780°C (exotherm peak) and 880°C (endotherm) respectively. The broad

endothermic peak at 880°C represents a dehydration reaction, while the exothermic peak indicates an oxidative reaction.

Differential Scanning Calorimetric (DSC) is one of the most efficient thermo analytical techniques used in the characterization of materials.¹⁵ This method measures the difference between the heat required to raise the temperature of the reference material and sample material as a function of temperature. In the present study, the DSC spectrum (Fig.-8) of the prepared nano bismuth selenide (Bi_2Se_3) depicts an endothermic peak at around 230°C.

Adsorption Studies and BET Analysis of the Catalyst

In order to have further insight into the as-prepared nano- Bi_2Se_3 catalyst, adsorption studies have been taken up. Observed results are presented in Fig.-9 and 10. Figure-9 reflects the adsorption isotherms of the catalyst suggesting that these isotherms reveal type-III multilayer adsorption, the contact between the adsorbent and adsorbate is smaller than that between the adsorbate. It is evident in this isotherm that the reactant species intake is slow until saturation. This enables the interaction of adsorbed reactive species and free reactive species by taking place on a given surface.^{16,17}

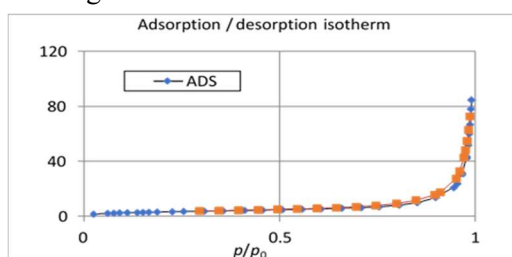


Fig.-9: Adsorption/Desorption Isotherms - Fresh and Reused Nano- Bi_2Se_3 Catalyst

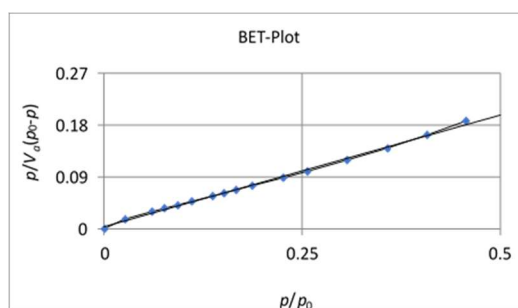


Fig.-10: BET Plots for Fresh and Reused Bi_2Se_3 nanocatalyst

Figure-10 Shows the BET plots of freshly prepared and reused catalysts after four cycles. These values cross each other, demonstrating that even after four cycles, the recovered catalyst maintains approximately the same efficiency. These additional findings showed that the pores of the catalyst lacked residential reactants or products, and they can be applied to the fifth cycle. In addition to the above observations, scanning electron microscopic (SEM) scans of recycled catalysts were also taken with a view to gain further insight into their catalytic activity. It is of interest to note that the morphology presented in the SEM images of the recycled catalyst under different magnifications (Fig.-11) is almost similar to the morphology of the freshly prepared catalyst.

RESULTS AND DISCUSSION

Synthetic Observations of Diindolylmethanes Under Solvothermal and Solvent-Free Conditions Using Nano-Bismuth Selenide Catalyst

The synthesis of bis(indolyl)methanes under a solvothermal process required 15-70 minutes depending on the nature of benzaldehyde and indole used. Data presented in Table-3 shows reaction times and quantitative product yields (%). But when the reactions are carried out in a solvent-free microwave environment, the reaction durations are drastically reduced, which could be explained by the in-situ creation of a higher percentage of activated molecules than in solvothermal processes. It is well known that during solvothermal reactions, a part of the molecules

formed in the reaction mixture by random collisions between reactant molecules disintegrate. According to Arrhenius, Eyring, and several other pioneers, the number of active molecules determines the reaction's pace.¹⁸

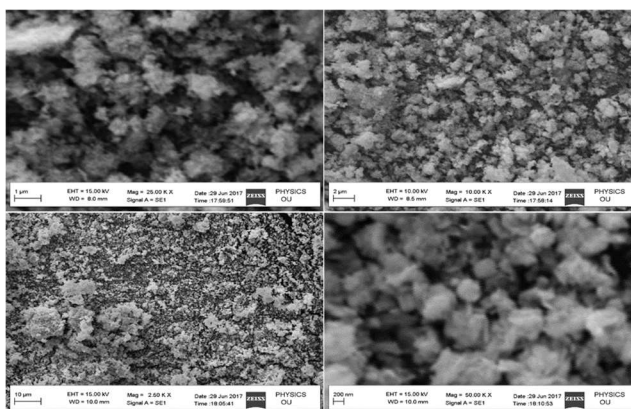
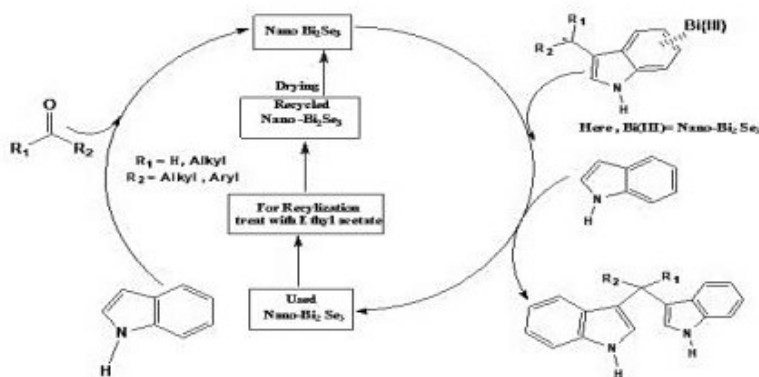


Fig.-11: SEM Images of the Recycled Bismuth Selenide

The propagating MW radiation can, however, heat the target compounds more easily in a microwave environment without heating the reaction vessel, producing a higher proportion of activated molecules than in a solvothermal environment. Rates accelerate as a result of time and energy savings.^{19,20} However, the reaction time significantly increased with the introduction of either electron donating or withdrawing group in the parent benzaldehyde irrespective of the indole used in the present studies. It is believed that the carbonium ion is generated when the C-3 position of indole attacks the carbonyl compound in the presence of a catalyst which in turn attacks the second indole molecule to afford bis(indolyl)methane as the end product (Scheme-2).



Scheme 2. Synthesis of Bis(indolyl) methanes and Recyclization of catalyst.

CONCLUSION

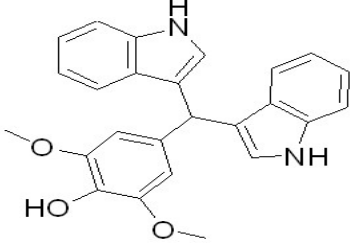
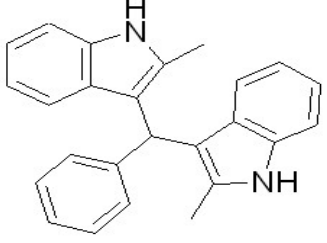
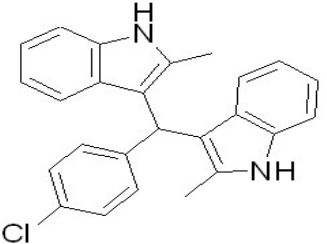
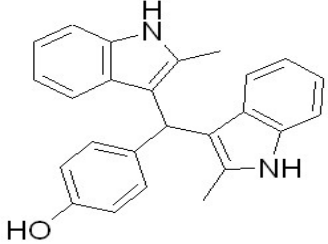
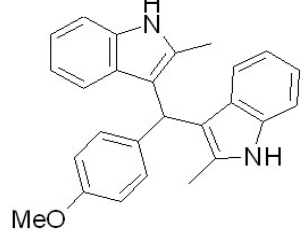
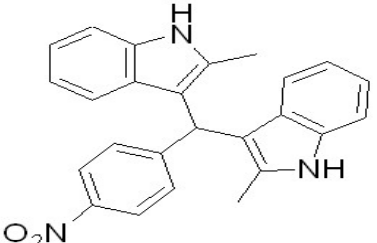
In conclusion, our current methodology does not require expensive chemicals. Excessive use of strong acids or salts can be reduced. Do not require excess solvents for the dissolution of reactants. This method makes use of a wide range of carbonyl compounds. On the whole, the yield of the products is high. Contrary to available methods, our method is considered to be a simple one and relatively yields are high.

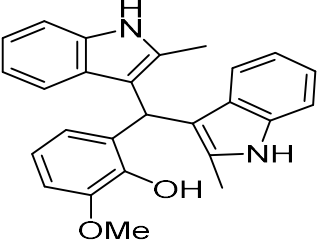
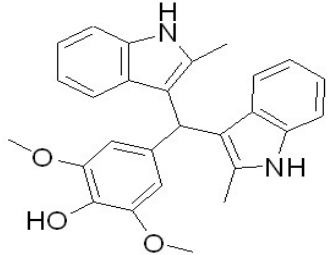
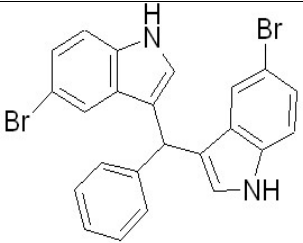
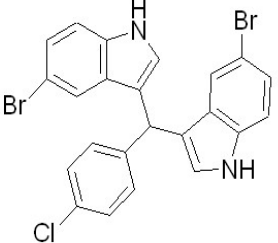
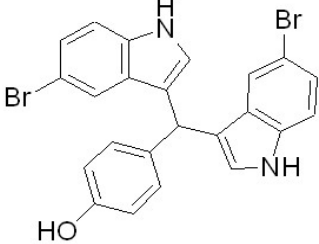
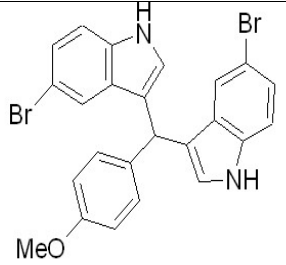
ACKNOWLEDGMENTS

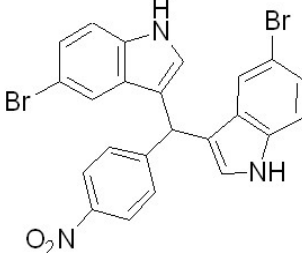
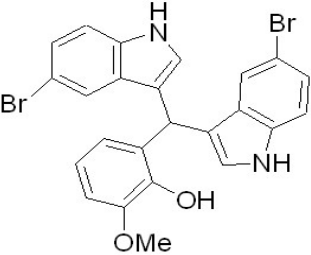
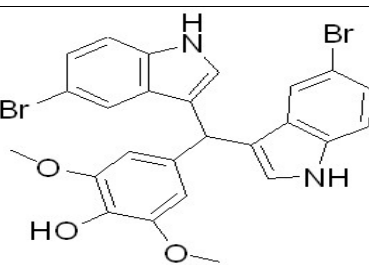
Authors gratefully acknowledge to Head, Department of Chemistry, Osmania University, and Hyderabad for facilities. Authors are highly indebted to Professor K. C. Rajanna(late) for his research contribution, Professor P. K. Sai Prakash (Former Dean, Faculty of Science, O.U), and Prof. T. Navaneeth Rao (Former Vice-chancellor, O.U), for constant encouragement. The authors are thankful to CSIR-IICT, Hyderabad, and CFRD (Central Facilities for Research and Development), O.U. for providing spectroscopic studies.

Table-3. One-pot synthesis of diindolylmethanes with Indole under solvothermal and microwave conditions (solvent-free) using Bismuth Selenide catalyst.

Indole	Aldehyde	Product	Solvothermal		M.W	
			R.T (min)	Yield (%)	R.T (min)	Yield (%)
Indole	Benzaldehyde		15	80	4	76
	4-Chloro Benzaldehyde		60	78	5	76
	4-hydroxy Benzaldehyde		50	76	2	72
	4-methoxy Benzaldehyde		90	78	7	75
	4-nitro Benzaldehyde		120	77	3.0	76
	3-methoxy,2-hydroxy benzaldehyde		30	78	4.0	75

	Syringaldehyde		30	76	2.0	74
2-methyl Indole	Benzaldehyde		15	80	5.0	78
	4-Chloro Benzaldehyde		60	76	4.0	72
	4-hydroxy Benzaldehyde		50	75	5.0	72
	4-methoxy Benzaldehyde		50	77	4.0	73
	4-nitro Benzaldehyde		40	76	2.0	74

	3-methoxy,2-hydroxy benzaldehyde		60	78	5.0	80
	Syringaldehyde		40	78	4.0	80
5-Bromo Indole	Benzaldehyde		20	85	5.0	82
	4-Chloro Benzaldehyde		60	75	40	78
	4-hydroxy Benzaldehyde		65	82	4.0	80
	4-methoxy Benzaldehyde		70	76	3.0	74

4-nitro Benzaldehyde		40	74	2.0	78
3-methoxy,2- hydroxy benzaldehyde		50	80	6.0	82
Syringaldehyde		50	82	4.0	80

CONFLICT OF INTERESTS

The authors declare that there is no conflict of interest.

AUTHOR CONTRIBUTIONS

All the authors contributed significantly to this manuscript, participated in reviewing/editing, and approved the final draft for publication. The research profile of the authors can be verified from their ORCID ids, given below:

M. Shanti  <http://orcid.org/0000-0001-9231-5744>

Vijayshekar Pulusu  <http://orcid.org/0000-0001-6832-3824>

S. Shylaja  <http://orcid.org/0000-0001-8715-6013>

G. Yaku  <http://orcid.org/0000-0001-7828-5649>

U. Umesh Kumar  <http://orcid.org/0000-0001-6677-6854>

Open Access: This article is distributed under the terms of the Creative Commons Attribution 4.0 International License (<http://creativecommons.org/licenses/by/4.0/>), which permits unrestricted use, distribution, and reproduction in any medium, provided you give appropriate credit to the original author(s) and the source, provide a link to the Creative Commons license, and indicate if changes were made.

REFERENCES

1. S. K. Mishra, S. Satpathy and O. Jepsen, *Journal of Physics: Condensed Matter*, **9(2)**, 461(1997)
2. Geoff Brumfiel, *Nature* **466(7304)**, 310(2010), <https://dx.doi.org/10.1038/466310a>
3. D. Hsieh, Y. Xia, D. Qian, L. Wray, J. H. Dil, F. Meier, J. Osterwalder, L. Patthey, J. G. Checkelsky, N. P. Ong, A. V. Fedorov, H. Lin, A. Bansil, D. Grauer, Y. S. Hor, R. J. Cava and M. Z. Hasan, *Nature*, **460**, 1101(2009), <https://doi.org/10.1038/nature08234>

4. Gehring, Pascal, Andrew Gaul, Alexander Hoyer, Kristina Vaklinova, Rutvik J. Mehta, Marko Burghard, Theodorian Borca-Tasciuc, David J. Singh, Klaus Kern, and Ganpati Ramanath, *Advanced Materials*, **28(30)**,6436(2016), <https://doi.org/10.1002/adma.201601256>
5. Ramin Ghorbani-Vaghei, Hojat Veisi, Hassan Keypour and Ahmad Ali Dehghani-Firouzabadi, *MolecularDiversity*,**14**,87(2010), <https://doi.org/10.1007/s11030-009-9150-z>
6. S. Min Nam, Y. Seul Jang, G. Eun Son, C. Ho Song, I. In, C. Pil Park, *Tetrahedron Letters*, **61**, 152(2020), <https://doi.org/10.1016/j.tetlet.2020.152178>
7. Laura Iglesias, Calista Aguilar, Debasish Bandyopadhyay and Bimal K. Banik, *SyntheticCommunications*, **40(24)**, 3678(2010),<https://doi.org/10.1080/00397910903531631>
8. S. Ramesh, D. Saravanan, *Organic Chemistry Current Research*, **9(1)**, 1(2020)
9. Leena Khanna, Mansi Shilpa Yadav, Neeti Misra, Pankaj Khanna, *Synthetic Communications Reviews*, **51(19)**, (2021)
10. H. Qin, J. Liu, W. Y. Fang, L. Ravindar, K. P. Rakesh, *European Journal of Medicinal Chemistry*, **194**, 112245(2020)
11. L. Khanna, S. Singhal, S. C. Jain, P. Khanna, *Chemistry Select*, **5**, 3420, <https://doi.org/10.1002/slct.201904783>
12. Ashish Bahuguna, Ashutosh Singh, Prateek Kumar, Divya Dhasmana, Venkata Krishnan, Neha Garg, *Computers in Biology and Medicine*,**116**, 103574(2020), <https://doi.org/10.1016/j.combiomed.2019.103574>
13. Arvind Singh, Kaur Gurpreet and Bubun Banerjee, *Current OrganicChemistry*, **24(6)**, 583(2020), <https://doi.org/10.2174/1385272824666200228092752>
14. A. W. Coats, J. P. Redfern, *Analyst* **88(1053)**, 906(1963), <https://doi.org/10.1039/AN9638800906>
15. B. Wunderlich, New York: Academic Press,137(1990)
16. J. M. Thomas, W.J. Thomas, Principles and Practice of Heterogeneous Catalysis (Second, revised ed.). Weinheim, Germany, (2014).
17. Schlögl, Robert, *Angewandte Chemie International*, **54(11)**, 3465(2015), <https://doi.org/10.1002/anie.201410738>
18. Connors, Kenneth Antonio, *Chemical Kinetics: The Study of Reaction Rates in Solution*, Wiley-VCH Verlag GmbH, (1990)
19. Moseley, D. Jonathan and C. Oliver Kappe, *Green Chemistry*, **13(4)**, 794,(2011), <https://doi.org/10.1039/C0GC00823K>
20. Lidström, Pelle, Jason Tierney, Bernard Watheyb, and Jacob Westmana, *Tetrahedron*, **57**, 9225(2001) [RJC-8247/2022]

SORPTION
AND ION EXCHANGE PROCESSES

Carbon Dioxide Adsorption Study on Rice Husk Activated Carbons by Artificial Neural Network (ANN)

Kishor Palle^{a,*}, Sambhani Naga Gayatri^a, Ramesh Kola^b,
Ch Sandhya Rani^c, P. Ramesh Babu^d, L. Vijayalakshmi^{e,**},
Seong Jin Kwon^e, and Md. Mustaq Ali^f

^a Chemistry Division, Department of H&S, CVR College of Engineering, Ibrahimpatnam,
Hyderabad, Telangana State, 501510 India

^b Department of Chemistry, Chaitanya Bharathi Institute of Technology (A), Gandipet, Hyderabad, Telangana, India

^c Department of Computer Science & Engineering, VNR Vignana Jyothi Institute of Engineering and Technology,
Hyderabad, Telangana, India

^d Department of Physics, Gokaraju Rangaraju Institute of Engineering & Technology, Hyderabad, Telangana, India

^e Department of Automotive Engineering, Yeungnam University, Gyeongsan-si, Republic of Korea

^f Department of Mathematics (H&S), Malla Reddy Engineering College (Autonomous), Main Campus,
Secunderabad, Telangana, India

*e-mail: drkishorepalle@gmail.com

**e-mail: lvl.phy@gmail.com

Received January 21, 2024; revised February 28, 2024; accepted February 28, 2024

Abstract—In this study, the effects of artificial neural networks on CO₂ adsorption on several types of rice husk activated carbon samples are investigated. Using conventional approach, the eight activated carbon samples are examined for carbon dioxide adsorption at 298 K and up to 1 bar pressure. The influence of altered training/validating ratios, various data initiation points, various training algorithms and number of neurons necessary for an artificial neural network model were investigated using ANN modelling. The work can give useful information on the effects of each of the investigated factors, which are crucial in ANN modelling and training techniques. The results may be used to create an optimum activated carbon, improved applications of gas and oil purification that plan to use artificial intelligence modelling in their evaluations.

Keywords: rice husk, activated carbons, CO₂ adsorption, artificial neural network

DOI: 10.1134/S1070427224020010

INTRODUCTION

A prominent source of biomass in South Asia, along with India and China, is rice husk. There is a high utilization value for rice husk as ash when compared to other farming bio-waste materials, mostly in the form of silica, and a low utilization value as husk. Organic matter from rice husks has been used for energy and has high value-added potential for other applications as well. A total of more than 650 million tons of rice are produced every year around the world, making it the third most significant cereal crop [1]. A major by-product of rice processing mills is rice husk, a protective

layer for rice grain [2, 3]. Rice husk contain, %: cellulose 32.24, hemicelluloses 21.34, lignin 21.44, water 8.11, extractives 1.82, and mineral ash 15.05, with a high percentage of 94.5–96.34% silica in its mineral ash [4, 5]. Figure 1 illustrates the components of rice husk.

Rice husks are notable for their low level of utilization when compared to scrap of wood and maize straw, but high level of utilization when compared to their ash [6, 7]. The silica in rice husk makes it an ideal silicon source. It is commonly used to synthesize cement, filter aids, silicides, and other materials [8, 9]. The silica in RHA is predominantly composed of amorphous cristobalite, which is predominant in the mineral [10].

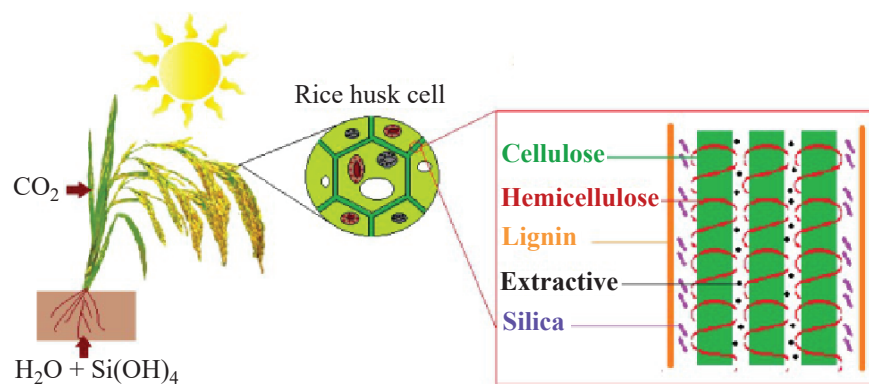


Fig. 1. Illustration of components of rice husk.

Reinforcement of cement can also be accomplished with rice husks [11]. In addition to serving as a catalyst carrier [12] and low-cost adsorbent [13], rice husk has a very good porous nature [14].

After petroleum and coal, natural gas is the world's third most used energy source. Presently, gases have a significant impact on the energy sector [15]. Gases are employed in a variety of applications, including industry and energy distribution. In terms of carbon emissions, however, gas pollution is half that of petroleum [16]. As a result, natural gas plays a significant role as a fuel that's environmentally friendly. Unconventional reservoirs are ultra-tight earth basements that can generate natural gas. Because CO_2 offers configurable features in terms of dissolving capacity and viscosity under varied working settings, it is considered one of the most often used approaches.

The ANN has been getting a lot of attention lately due to its precision in predicting intricate physical and chemical processes. The ANN model necessitates greater focus on testing, validation, and data points for training. Additionally, the number of neurons needed to train an ANN model cannot be computed quantitatively since mathematical computation is not available. Equally significant is the ANN algorithm in terms of model accuracy [17]. In light of the previous explanation regarding natural gases, this study investigated the adsorption of carbon dioxide on activated carbon samples. A study was conducted to demonstrate the use of neural network modeling and artificial intelligence for the adsorption capacity prediction of activated carbon samples. A study based on artificial intelligence may be useful for adsorption and production of CO_2 from unconventional gases and activated carbon preparations.

In order to comprehend the behaviour of activated carbons, sorption studies is often carried out at high pressure and temperature conditions in reservoir. Studying supercritical CO_2 sorption and simulating field operating circumstances are the objectives of high adsorption research [18]. In most practical research, equilibrium isotherm models are used to observe adsorption analysis; however, these models are not always the most precise. Most isotherm models have measurement issues with regard to porosity, pressure, and even temperature. Consequently, there is a clear need for more precise and comprehensive application modelling in order to better understand the relationship between sorption capacity and selectivity as well as the porous media under investigation, such as activated carbon.

The buoyancy effect commonly affects the analysis of CO_2 adsorption at working pressures of up to 200 bar, and this needs to be adjusted by the usage of equation for different states. Consequently, there is a notable increase in the uncertainty of the measurement [19]. Adjustments to the sample weight or isothermal pressure conditions are frequently used to determine adsorption capacity. These parameters and variables are associated to alter the circumstances that predominate. However, no study has combined field operational features in a thin porous medium with the distribution of pores for more creative applications and assessments of gas recovery.

Gopalan et al. investigated the studies of gas adsorption using AIML techniques by many researchers based on ML modelling of hydrogen adsorption in past research [20]. For this adsorption in nanoporous materials modeling based on Gaussian process regression (GPR) was applied. The number of hydrogen (n_1) was

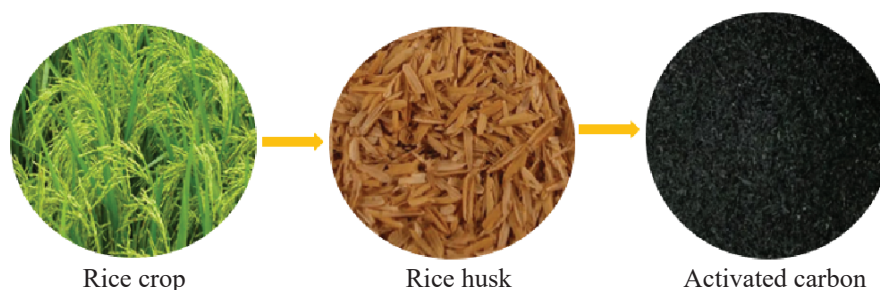


Fig. 2. Digital images of rice crop, rice husk and activated carbon.

calculated using GPR as a void fraction (ϕ), function of adsorption pressure and the greatest pit diameter. The accuracy of the generated machine learning model was comparable to that of Machine learning [21–24], large standard Monte–Carlo simulations [25] is employed in the adsorption studies isotherm modelling (S_{BET}) [26, 27] created an artificial neural network model to analyse the isotherms with surface area.

To predict adsorption created ANN model has been trained with the least amount of error and the highest level of accuracy. The constructed model was tested on 1000 data points gathered by a literature review and an experimental investigation, and it performed well. According to the findings, mesopores play an important role in limiting CO_2 absorption, whereas for gas adsorption micropores are required [28]. One more significant finding of the study was the effect of solid absorbents on gas desorption on textural parameters, as well as the sensitivity of specific parameters that may be evaluated. Wang et al. created a convolution neural networks model to predict carbon dioxide and nitrogen adsorption at 77k with varied porosity ranging from 3–7 nm of mesosphere to less than 2 nm of micropores to examine carbon dioxide and nitrogen adsorption by the influence of pore size distribution [29]. According to the established model, optimal adsorption exhibited by microporous surfaces [30–32].

MATERIALS AND METHODS

For this investigation, rice husk was collected from a rice mill near Telaprolu in Vijayawada, India. It was thoroughly cleansed with distilled water to remove any dirt or dust that had adhered, and it was then dried at 110°C overnight. For four hours, rice husks were calcined at various temperatures and in various atmospheres. The gas flow was kept at 40 mL per minute, and the temperature was set at 10°C per min [33]. At

different activation temperatures such as 400, 500, 600, and 700, four activated carbon samples from rice husk were prepared. An atmosphere of nitrogen-carbon dioxide was used for the process (18 dm^3/h nitrogen flow, 5 dm^3/h carbon dioxide flow). In all the experiments, time, $\text{N}_2\text{-CO}_2$ flow rate, and furnace heating rate remained the same. We treated the activated carbon with 1 M HCl solution for 20 h and left it behind. As a next step, deionized water was used to rinse the carbons until chloride ions were completely removed. In the following step, samples were dried for 16 h at 110°C . As a result, RHAC-400, RHAC-500, RHAC-600, and RHAC-700 were chosen for the activation process. RHAC stands for rice husk activated carbon. Digital images of rice crop, rice husk, and its activated carbon were shown in Fig. 2 [34].

BET method was used on a BELSORB II Instrument, Japan, to estimate the surface area of activated carbon samples. To remove the contaminants from samples, the adsorption measurements were preceded by heating at temperature of 250°C for 12 h with the heating rate of $1^\circ/\text{min}$ under the reduced pressure.

The porous structure parameters have been derived from the N_2 sorption isotherms.

Surface area (S_{BET}) estimated on the basis of the BET equation with the partial pressure in the range of $p/p_0 = 0.05\text{--}0.2$. This range was pointed independently for each material so that a linearity of function (1) were fulfilled:

$$f\left(\frac{p}{p_0}\right) = \frac{1}{W\left(\frac{p}{p_0} - 1\right)}, \quad (1)$$

where W is the mass of gas adsorbed at a relative pressure p/p_0 , p is the nitrogen pressure, p_0 is equal to 1.01 bar;



Fig. 3. Manual setup for CO₂ adsorption studies

Total pore volume (V_p , N₂) calculated from the maximum adsorption of nitrogen vapor for $p/p_0 = 0.99$;

Pores in a range of micropores (V_{micro} , N₂) and mesopores were evaluated using N₂ analysis at -196°C temperature by the density functional theory (DFT) method.

In this work, high purity CO₂ and He gases with a purity of 99.995% were used for adsorption and pre-measurement assortments. The gas was supplied by a local gas company Lakshmi agencies. The primary physicochemical parameters that could impact the adsorption process were investigated using sample characteristics. The CO₂ adsorption capacity of activated carbon samples was measured using thermal conducting detector-gas chromatography (TCD-GC) and a pneumatically controlled sample injector at 289 K and up to 1 bar [25]. Manual setup of CO₂ adsorption study represent in Fig. 3. A total of 20 evenly spaced segments were used to quantify adsorption and desorption at the same time. Training-to-validating ratios, initiation data points and alternating training algorithms were used in the ANN modelling [21].

Samples were crushed, screened, and homogenized in order to achieve particle sizes of 0.5–1 mm. In the present study, X-ray powder diffraction (XRD) patterns of the catalysts were recorded by a Rigaku Miniflex (Rigaku Corporation, Japan) X-ray diffractometer using Ni filtered Cu K_α radiation ($\lambda = 1.5418 \text{ \AA}$) with a scan speed of 2° min^{-1} and a scan range of $10\text{--}80^\circ$ at 30 kV and 15 mA. The BET surface area of the catalysts was measured at -196°C using a commercial multi-point QUADRASORB SI (Quantachrome Instruments, USA) by N₂ physisorption.

Artificial Neural Network Method

Based on research by North and colleagues, V_{micro} and V_{meso} levels had an impact on the amount of CO₂ that could be absorbed [35]. In accordance with additional study, porous carbons' large surface areas and small micropores promote more CO₂ adsorption. In order to better comprehend the functions of S_{BET} , V_{micro} , and V_{meso} , we selected input layer variables as neurons, which were subsequently sent to hidden layers and output layers. A typical neural network (NN) construction is shown in Fig. 4. When a neural network contains more than one hidden layer, it is referred to as a deep neural network (DNN). Weights are represented by lines connecting two nodes, which simulate input-output relationships [34].

RESULTS AND DISCUSSION

The textural properties of all the activated carbon samples were compiled in Table 1.

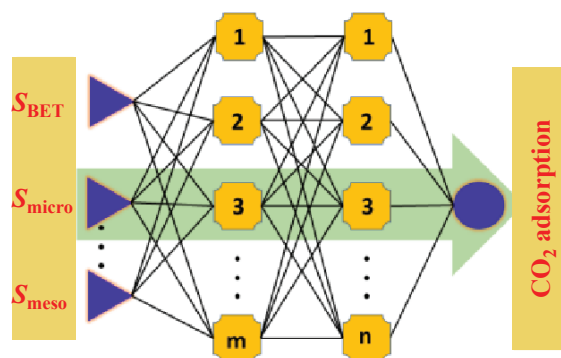


Fig. 4. Construction of ANN (artificial neural network)

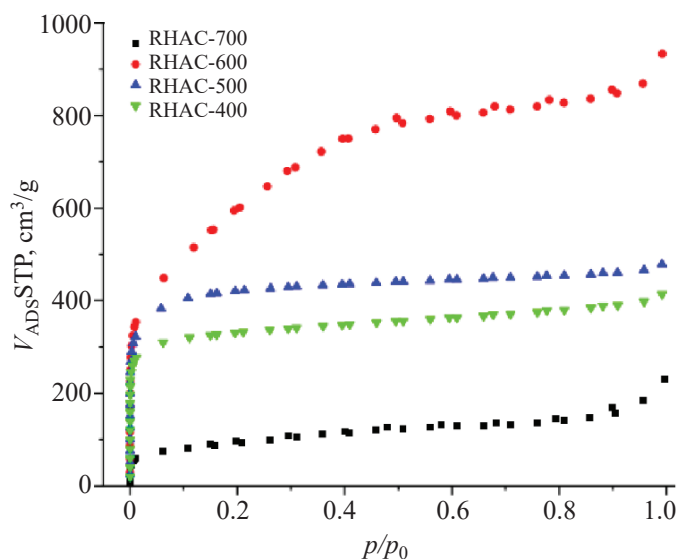
Table 1. Textural parameters for activated carbons, derived from N₂ adsorption isotherms at -196 °C

Sample	S_{BET} , m ² /g	V_p , N ₂ , cm ³ /g	V_{micro} , N ₂ , cm ³ /g
Zagazig	248	0.63	0.39
RHAC-500	576	0.72	0.52
RHAC-600	1074	1.42	0.45
RHAC-700	124	0.35	0.06

As a result of the isotherms, microporous samples exhibited high N₂ adsorption at low relative pressures. All carbon samples exhibited a notable increase in nitrogen adsorption at a temperature of -196°C as the activation temperature during thermal treatment increased. However, there was one exception to this trend. The carbon sample activated at the highest temperature (700°C) achieved the lowest nitrogen capacity.

The results of undermentioned adsorption-desorption isotherms of N₂ on the examined activated carbons are shown in Fig. 5.

Equation 2 is used to determine adsorption capacity of the activated carbon.

**Fig. 5.** The adsorption-desorption isotherms of N₂ for activated carbons.**Table 2.** Calculated mean squared error and R squared values for different neurons

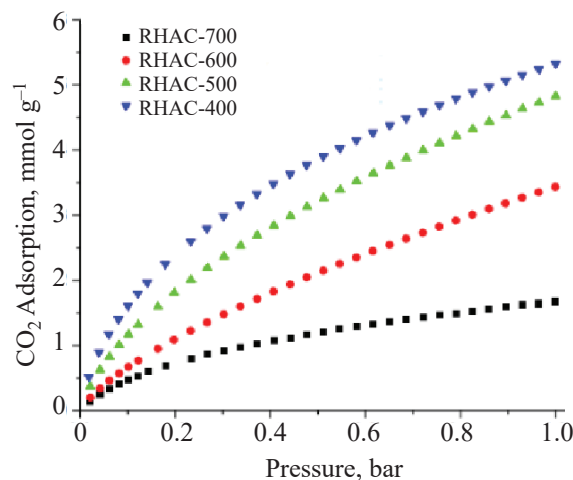
Hidden neurons	Mean squared error value (for test)	R squared value
4	0.0992	0.8971
5	0.0794	0.9064
6	0.1224	0.9895
7	0.0022	0.9875
8	0.0198	0.9658
9	0.1134	0.9121
10	0.2286	0.9062

$$q = \frac{m_i - m_f}{w} = \left(\frac{VM_w}{Rw} \right) \left(\frac{P_i}{Z_i T_i} - \frac{P_f}{Z_f T_f} \right), \quad (2)$$

$$Z = 1 + \frac{BP}{RT}. \quad (3)$$

An initial and final condition is indicated by the subscripts i and f. P , V , R , Z , and w stand for pressure, temperature, reactor volume, and universal gas constants for rice husk adsorption, respectively. Virial equation (Eq. 3) was used for the calculation of the compressibility factor [36]. An adsorption experiment was conducted at 0°C and 1 bar of pressure on activated carbon surfaces. The experimental CO₂ capacity at 0°C are given in Fig. 6.

The current investigation incorporated the input parameters of pressure and temperature. A process response or output variable was generated by

**Fig. 6.** CO₂ adsorption isotherms measured at 0°C.

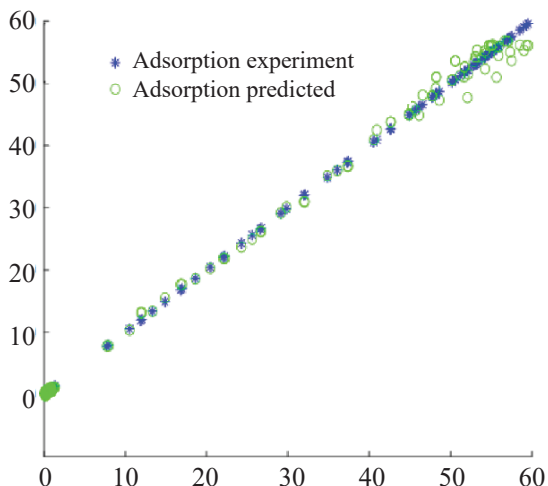


Fig. 7. Comparison of experimentally determined adsorption results and those predicted by the RNN LM algorithm.

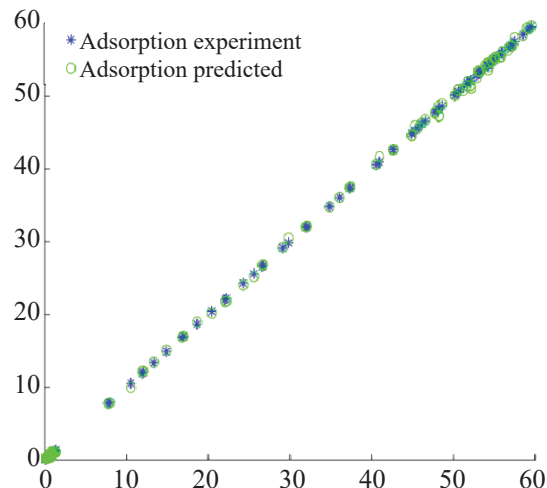


Fig. 8. Comparison of experimentally determined adsorption results and those predicted by the RNN BFGS algorithm.

adsorption on the CO_2 amount (AC) adsorption. By adjusting 4 to 10 number of neurons with a time step of 1, the adsorption model was created. ANN is trained utilizing the statistical parameter of mean square errors (MSE). The MSE and correlation coefficient (R^2) were calculated using Eqs. (4) and (5), respectively [37]. Table 2 represents calculated and recorded the mean squared error and R squared values.

$$\text{MSE} = \frac{1}{N} \sum_{i=1}^N (Y_{\text{predicted}} - Y_{\text{real}})^2, \quad (4)$$

$$R^2 = \frac{1}{N} \sum_{i=1}^N \frac{(Y_{\text{predicted}} - Y_{\text{real}})^2}{(Y_{\text{predicted}} - Y_{\text{mean}})^2}. \quad (5)$$

Best R squared value and lowest mean square error value 0.0022 given by adsorption models using seven

neurons. Therefore, the ANN model was generalized using this model. Figures 7 and 8 compare the adsorption results produced by the ANN model employing various algorithms using 7 neurons.

Data is normalised before being fed into a deep neural network in several research since the data came from a variety of sources. Non-normalized data points were used in this investigation because the dataset used from same experimental setup. The experiment in our lab yielded 117 CO_2 adsorption data, from this data randomly 80 were selected for neural network training using machine learning in MATLAB software. The deep learning model was tested using the remaining 27 data points.

Figure 9 shows that the predicted results are quite similar to experimental findings, with a MSE of

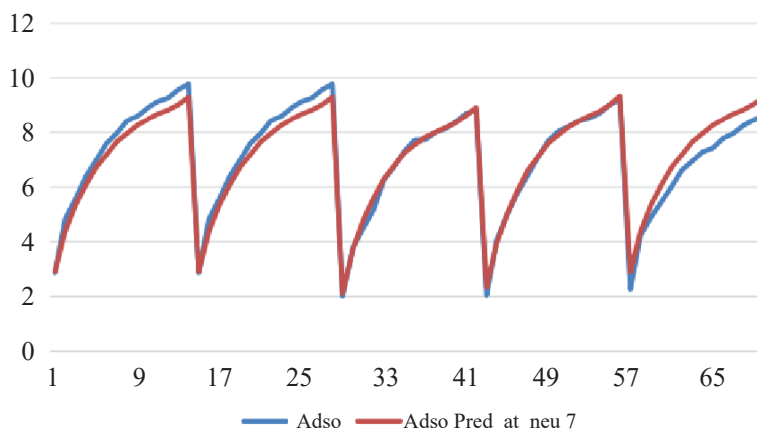


Fig. 9. Comparison of predicted and experimental results of adsorption using artificial neural network model.

just 2.315. In Fig. 9, the test data set is compared to experimental findings, and the results reveal that the trained model and experimental results are in excellent agreement.

The findings of this study can be used to evaluate the preliminary phases of measurements of carbon dioxide adsorption and predictions on restricted sources with great precision and accuracy utilizing various machine learning approaches based on source conditions and effects, and by the impact of processing conditions on carbon dioxide adsorption, carbon dioxide sequestration and improved recovery of oil and gas. Advanced and further research can be undertaken in order to examine the practicality of the suggested models to acquire real data from source and unconventional basins. This inquiry, on the other hand, is a first of its type and can serve as a useful benchmark for newly researched topics and expertise in crucial industries, particularly in the areas of viable productivity and energy sustainability.

CONCLUSIONS

We have generalized and optimized the mathematical model as for ANN algorithms, data initiation points and neurons. Adsorption predictions for lab experiments were accurate with this model and was used at greater pressures and temperatures to predict adsorption. Adsorption values and desorption processes can be optimized using ANN models in industry to compute adsorption values at very high temperatures and pressures.

FUNDING

This work was supported by ongoing institutional funding. No additional grants to carry out or direct this particular research were obtained.

CONFLICT OF INTEREST

The authors states that there is no conflict of interest.

REFERENCES

1. Song, X., Zhang, Y., Yan, C., Jiang, W., and Chang, C., *J. Colloid Interface Sci.*, 2013, 389, 213.
2. Nhapi, I., Banadda, N., Murenzi, R., Sekomo, C., and Wali, U., *Open Environmental Engineering Journal*, 2011, vol. 4, p. 170.

3. Zhang, J., Fu, H., Lv, X., Tang, J., and Xu, X., *Biomass and Bioenergy*, 2011, vol. 35, 464.
4. Masoud, M.S., El-Saraf, W.M., Abdel-Halim, A.M., Ali, A.E., Mohamed, E.A. and Hasan, H.M., *Arab. J. Chem.*, 2012, vol. 9, p. S1590.
5. Wan Ngah, W. and Hanafiah, M., *Bioresour. Technol.*, 2008, vol. 99, p. 3935.
6. Wang, W, Martin, J., Zhang, N., Ma, C., Han, A., and Sun, L., *J. Nanopart. Res.*, 2011, vol. 13, p. 6981.
7. Virtanen, T., Svedström, K., Andersson, S., Tervala, L., Torkkeli, M., Knaapila, M., Kotelnikova, N., Maunu, S.L., and Serimaa, R., *Cellulose*, 2012, vol. 19, p. 219.
8. Antiohos, S.K., Papadakis, V.G., and Tsimas, S., *Cem. Concr. Res.*, 2014, vol. 20, p. 61.
9. Adam, F. and Appaturi, J.N., and Iqbal, A., *Catal. Today*, 2012, vol. 190, p. 2.
10. Chandrasekhar, S., *J. Mater. Sci.*, 2003, vol. 38, p. 3159.
11. Jaturapitakkul, C. and Roongreung, B., *ASCE J. Mater. Civ. Eng.*, 2003, vol. 15, p. 470.
12. Shinde, A.B., Shrigadi, N.B., and Samant, S.D., *J. Chem. Technol. Biotechnol.*, 2003, vol. 78, p. 1234.
13. Srivastava, V.C., Mall, I.D., and Mishra, I.M., *Chem. Eng. J.*, 2008, vol. 140, p. 136.
14. Palle, K., Yadav, G.K., Kumar, P.S., et al., *High Energy Chem.*, 2023, vol. 57, p. 83.
15. Fakher, S. and Imqam, A., *SN Appl. Sci.*, 2020, vol. 2, p. 5.
16. Rani, S., Padmanabhan, E., and Prusty, B.K., *J. Pet. Sci. Eng.*, 2019, vol. 175, p. 634.
17. Palle, K., Vunguturi, S., Gayatri, S.N., et al., *MRS Commun.*, 2022, vol. 12, p. 434.
18. Abdulkareem, F.A. and Padmanabhan, E., *Can. Chem. Eng.*, 2020, ID 23838.
19. Singh, D.K., Krishna, K.S., Harish, S., Sampath, S., and Eswaramoorthy, M., *Angew. Chemie Int. Ed.* 2016, vol. 55, p. 2032.
20. Gopalan, A., Bucior, B.J., Bobbitt, N.S., and Snurr, R.Q., *Mol. Phys.*, 2019, vol. 117, p. 3683.
21. Pardakhti, M., Moharreri, E., Wanik, D., Suib, S.L., and Srivastava, R., *ACS Comb. Sci.*, 2017, vol. 19, p. 640.
22. Subraveti, S.G., Li, Z., Prasad, V., and Rajendran, A., *Ind. Eng. Chem. Res.*, 2019, vol. 58, ID 20412.
23. Meng, M., Qiu, Z., Zhong, R., Liu, Z., Liu, Y., and Chen, P., *Chem. Eng. J.*, 2019, vol. 368, p. 847.
24. Wang, L., Liu, M., Altazhanov, A., Syzdykov, B., Yan, J., Meng, X., and Jin, K., Abstracts of Papers, *Soc. Pet. Eng.-SPE Eur. Featur. 82nd EAGE Conf. Exhib. D*, 2020.
25. Daub, C.D., Patey, G.N., Jack, D.B., and Sallabi, A.K.,

- J. Chem. Phys.*, 2006, vol. 124, ID 114706.
26. Dureckova, H., Krykunov, M., Aghaji, M.Z., and Woo, T.K., *J. Phys. Chem. C*, 2019, vol. 123, p. 4133.
27. Zhang, Z., Schott, J.A., Liu, M., Chen, H., Lu, X., Sumpter, B.G., Fu, J., and Dai, S., *Angew. Chemie Int. Ed.*, 2019, vol. 58, p. 259.
28. Wang, S., Zhang, Z., Dai, S., and Jiang, D., *ACS Mater. Lett.*, 2019, vol. 1, p. 558.
<https://doi.org/10.1021/acsmaterialslett.9b00374>
29. Wang, S., Li, Y., Dai, S., and Jiang, D., *Angew. Chemie*, 2020, vol. 132, p. 19813.
<https://doi.org/10.1002/ange.202005931>
30. Fanourgakis, G.S., Gkagkas, K., Tylianakis, E., Klontzas, E., and Froudakis, G., 2019, *J. Phys. Chem. A*, vol. 123, p. 6080.
31. Jablonka, K.M., Ongari, D., Moosavi, S.M., and Smit, B., *Chem. Rev.*, 2020, vol. 120, p. 8066.
32. Erdem Günay, M. and Yıldırım, R., *Catal. Rev.-Sci. Eng.*, 2020, vol. 63, p. 120.
33. Palle, K., Vunguturi, S., Subba Rao, K., et al., *Chem. Pap.*, 2022, vol. 76, p. 7525.
34. Palle, K., Yadav, G.K.S., Gayatri, S.N., et al., *MRS Commun.*, 2022, vol. 12, p. 886.
35. Durá, G., Budarin, V.L., Castro-Osma, J.A., Shuttleworth, P.S., Quek, S.C.Z., Clark, J.H., and North, M., *Angew. Chem. Int. Ed.*, 2016, vol. 55, p. 9173.
<https://doi.org/10.1002/ange.201602226>
36. Ramezanipour Penchah, H., Ghaemi, A., and Godarziani, H., *Environ. Sci. Pollut. Res.*, 2021, vol. 28, p. 55754.
37. Hemmati, A., Ghaemi, A., and Asadollahzadeh, M., *Sep. Sci. Technol.*, 2021, vol. 56, p. 2734.

Publisher's Note. Pleiades Publishing remains neutral with regard to jurisdictional claims in published maps and institutional affiliations.
AI tools may have been used in the translation or editing of this article.



OPEN

An analytical characterization study on biofuel obtained from pyrolysis of *Madhuca longifolia* residues

S. Thiru¹, Ramesh Kola², Manish Kumar Thimmaraju³, C. Sowmya Dhanalakshmi⁴, Vipin Sharma⁵, P. Sakthi⁶, Lakshmana Phaneendra Maguluri⁷, L. Ranganathan⁸ & J. Isaac Joshua Ramesh Lalvani⁹✉

The current study focuses on examining the characteristics of biofuel obtained from the pyrolysis of *Madhuca longifolia* residues, since the selected forest residue was primarily motivated by its greater volatile matter content. The study used several analytical techniques to describe pyrolysis oil, char, and gas obtained from slow pyrolysis process conducted between 350 and 600 °C in a fixed-bed reactor. Initially, the effect of process temperature on product distribution was assessed to motivate maximum pyrolysis oil yield and found to be 44.2 wt% at pyrolysis temperature of 475 °C, while the yields of char and gas were 22.1 wt% and 33.7 wt%, respectively. In order to determine the suitability of the feedstock, the *Madhuca longifolia* residues were analyzed by TGA and FT-IR, which revealed that the feedstock could be a feasible option as an energy source. The characterization of pyrolysis oil, char, and gas has been done through various analytical methods like FT-IR, GC-MS, and gas chromatography. The physicochemical characteristics of the pyrolysis oil sample were examined, and the results showed that the oil is a viscous liquid with a lower heating value than conventional diesel. The FT-IR and GC-MS analysis of pyrolysis oil revealed the presence of increased levels of oxygenated chemicals, acids, and phenol derivatives. The findings of the FT-IR analysis of char indicated the existence of aromatic and aliphatic hydrocarbons. The increased carbon content in the char indicated the possibility of using solid fuel. Gas chromatography was used to examine the chemical structure of the pyrolysis gas, and the results showed the existence of combustible elements.

Keywords Forest residues, Pyrolysis, Fixed bed, FT-IR, GC-MS

The increased residents and transportation in the world is experiencing a need for huge amounts of energy and the repercussions of global warming. Meanwhile, the use of petroleum-based fuels is also increasing on a daily basis. Globally, energy output has significantly increased recently in order to equate the demand for conventional fuels¹. The carbon neutrality of biofuel possesses huge potential for reducing carbon emissions and existing fossil fuel dependence. Emissions of carbon can be effectively decreased by using alternative fuels. Burning fossil fuels is closely linked to a number of serious health issues. Burning fossil fuels for energy causes pollution in the air and water, which has an adverse effect on the surroundings. Sustainable energy is energy that can satisfy current energy demands without endangering future energy supplies and resources². Wind, solar, bioenergy, and hydroelectric are the four most important sustainable energy sources. Renewable organic material derived from

¹Department of Mechanical and Materials Engineering, University of Jeddah, 23218 Jeddah, Kingdom of Saudi Arabia. ²Department of Chemistry, Chaitanya Bharathi Institute of Technology (A), Gandipet, Hyderabad, Telangana 500075, India. ³Department of Pharmaceutical Analysis, Balaji Institute of Pharmaceutical Sciences, Narsampet, Warangal, Telangana 506331, India. ⁴Department of Mechanical Engineering, SNS College of Technology, Coimbatore, Tamil Nadu 641035, India. ⁵Department of Mechanical Engineering, Medi-Caps University, Indore, Madhya Pradesh 453331, India. ⁶Department of Electronics and Communication Engineering, M.Kumarasamy College of Engineering, Karur, Tamil Nadu 639113, India. ⁷Department of Computer Science and Engineering, Koneru Lakshmaiah Education Foundation, Vijayawada, Andhra Pradesh 522302, India. ⁸Department of Mechanical Engineering, Cambridge Institute of Technology, Tatisilwai, Ranchi, Jharkhand 835103, India. ⁹Faculty of Mechanical Engineering, Arba Minch Institute of Technology, Arba Minch University, PO Box 21, Arba Minch, Ethiopia. ✉email: isaac.jrl@amu.edu.et

plants and animals is called biomass. Biomass is an important fuel for cooking and heating. It can be burned directly to provide heat or converted to liquid and gaseous fuels via various bio- and thermochemical conversion processes³. Various low- and medium-cost agricultural and biological wastes can be transformed into biofuels. In comparison to biological techniques, thermochemical technologies offer much faster reaction times and greater feedstock flexibility. The three primary process techniques that can be employed to transform biomass into biofuel are physiochemical, thermochemical, and biochemical. Fermentation and anaerobic digestion are considered biochemical conversion processes. Pyrolysis, gasification, and combustion are considered thermochemical conversion processes. Compared to biochemical conversion processes, thermochemical conversion of biomass into biofuel is the most favorable method to provide energy for the future⁴. In biomass thermal conversion processes, biomass is broken down by applying heat, usually above 300 °C, in order to convert it into different types of energy, such as power, heat, or biofuels. The physical characteristics of the resulting biofuel depend on the presence of numerous components. A recent study represented that, out of the 181.5 billion tonnes of lignocellulosic wastes, only 4.5% is utilized each year⁵. Biofuel has primarily been produced using non-edible, oil-rich seeds and agro-forestry biomass wastes. However, any kind of biomass can be turned into biofuel through thermal cracking or pyrolysis.

In India, almost 22% of the land is covered with natural forest. *Madhuca longifolia*, a tree native to India, has remarkable potential. The tree is primarily cultivated on the Indo-Pakistan subcontinent. It belongs to the Sapotaceae family and is considered an Indian forest plant. The tree is abundant in Indian forests. Since ancient times, tribal peoples in India have cultivated this tree for various applications, including food, fuel, and fertilizer. The various parts and their numerous applications of the tree are also summarized in the literature⁶. Previously, many parts of the *Madhuca longifolia* tree have been utilized for producing biofuel. Mishra and Mohanty⁷ concentrated on the catalytic pyrolysis of seeds obtained from *Madhuca longifolia*. The authors conducted pyrolysis experiments with and without catalysts in a batch-type reactor and produced 51.2 wt% of pyrolysis oil. In this study, the utilization of catalysts reduced the yield of oil. Raj et al.⁸ used *Madhuca longifolia* wood and low-grade coal to produce producer gas using the co-gasification process and utilized it as a fuel for IC engines. The study found that the co-gasification system provides a viable solution for alternate power generation and may prove beneficial for small-scale enterprises. Shanmuga Priya and Rajalakshmi⁹ used pyrolysis and hydrothermal methods to produce functional carbon material from *Madhuca longifolia* leaves. In order to improve their internal properties, the produced carbon materials were further activated. Several analytical methods, including Fourier transform infrared spectroscopy (FT-IR) and scanning electron microscopy, were used to analyze the produced carbon materials and found that they can be used as environmentally friendly, low-cost electrode materials for supercapacitors.

Pyrolysis is a useful method for turning low-value biomass and biobased wastes into biofuel. It is a highly effective technique for turning biomass into a liquid intermediary that can be further processed into hydrocarbon biofuels. Pyrolysis is the key technology of biobased power generation in which solid biomass is converted into liquid, solid, and gaseous compounds. Pyrolysis oil is the combination of water and different organic molecules¹⁰. The pyrolyzed oils are used in multiple ways as low-grade fuels for furnaces and have a lot of possible ways to separate chemicals via cracking, hydrogenation and aqueous phase processing. It is also more important to select a proper biomass feedstock that will enable the requisite heat transfer rates to produce more pyrolysis oil yields. The selection of feedstock plays a significant role in achieving a better yield. Typically, land biomass wastes such as wood, wood bark, plant residue and shells are commonly used feedstocks. In some cases, microalgae also served as a beneficial feedstock. Other than the feedstocks characteristics, numerous factors, including reactor type, feedstock size and process time of the feedstock and volatile matters, also impact the yield of the biofuel¹¹. The most popular reactors for slow pyrolysis are drums, rotatory kilns and screw types. On the other side, fluidized beds, ablative reactor, vortex reactor and rotating disk reactors are suitable for fast pyrolysis. Biomass is a sustainable alternative source of renewable energy. Cellulose, hemicellulose and lignin are the basic natural polymeric materials present in biomass and extractives and minerals are the other two components present within the lignocellulosic material which distributes in different ratios¹². Previously, many authors have conducted pyrolysis reactions using different biomass residues in different reactors and their product yield under optimum conditions are displayed in Table 1.

The 3Rs—reduce, reuse, and recycle—contribute to long-term environmental development. Because forestry wastes are abundant in biomaterials, if employed, they might become the backbone of sustainable development, producing a variety of opportunities for future generations³⁰. Carrasco et al.³¹ carried out a pyrolysis test using Maine forest residues. The authors produced 61, 24 and 15 wt% of oil, char and gas. The total yield was predicted roughly up to 16% by mass and 40% by energy. Amutio et al.³² studied the feasibility of valorization of different forest residues, specifically bushes in a conical reactor. The reactor was set to 500 °C and the material utilized in this research yielded 80 wt% of oil with a maximum of 23 wt% char and 5 wt% gas fractions. The characterization study of the pyrolysis oil showed 35 wt% of water molecules in the oil, with a majority of phenols, ketones, acids, and furans. Several precise characterization approaches were used to find the information about biofuels. For characterization, the majority of previous pyrolysis studies dealt with FT-IR, Gas chromatography Mass Spectroscopy (GC-MS) or a combination of these. The spectroscopic techniques provide extremely significant details about its functional groups and can aid in the documentation of yields. Identifying the physiochemical nature of the pyrolysis biofuel is also important to understand the industrial applications of the products. Charon et al.³³ developed various analytical techniques to analyze six bio-oils obtained from hardwood, softwood and wheat grass. The result showed that the wood based pyrolysis oils were single-phase liquids, whereas the wheat grass pyrolysis oil was heterogeneous. The chromatography analysis of pyrolysis oil showed more than 100 elements. Schellekens et al.³⁴ utilized GC/MS to explore molecular characteristics of biofuels obtained from different agricultural residues. They discovered that, regardless of pyrolysis feedstocks, the process temperature

Biomass type	Reactor type	Temperature in °C	Particle size in mm	Heating rate in °C/min	Pyrolysis product yield in wt%			Reference
					Pyrolysis oil	Char	Gas	
Rice husk	Fixed bed	450	0.5–2.0	20	38.1	35.0	26.9	¹³
Wheat straw	Fixed bed	400	0.5–2.0	20	36.7	34.4	28.9	¹³
Cashew nut shell	Batch	400	0.25	22.5	40.0	30.0	30.0	¹⁴
<i>Xanthium strumarium</i>	Fixed bed	450	0.15–0.22	50	22.7	32.2	45.0	¹⁵
<i>Calophyllum inophyllum</i> shell	Fixed bed	425	425	40	41.0	#	#	¹⁶
<i>Eremurus spectabilis</i>	Fixed bed	500	0.22–0.85	50	34.6	#	#	¹⁷
Cotton stalk	Fixed bed	600	#	20	17.1	38.0	44.8	¹⁸
Napier grass stem	Fixed bed	500	0.2–2.0	30	32.2	#	#	¹⁹
<i>Anchusa azurea</i>	Fixed bed	450	0.6	100	31.3	37.6	31.2	²⁰
Eastern giant fennel stalks	Fixed bed	500	0.15–0.85	50	45.2	24.3	30.4	²¹
Rice straw	Fixed bed	500	#	10	43.3	28.0	–	²²
<i>Giant miscanthus</i>	Fixed bed	550	#	10	50.7	26.2	23.2	²³
Babool seeds	Fixed bed	450	0.4–1.0	25	38.3	#	#	²⁴
Switchgrass	Fixed bed	600	2.0	#	37.0	26.0	35.0	²⁵
Mustard de-oiled cake	Fixed bed	550	#	25	53.2	29.9	16.7	²⁶
Napier grass	Fixed bed	500	1.0–2.0	150	36.0	30.0	#	²⁷
Olive residue	Fixed bed	500	1.29	7	39.0	#	#	²⁸
Pine forest residues	Auger reactor	500	20.0	#	59.0	26.0	#	²⁹

Table 1. Pyrolysis of different biomass residues and product yields. #Not reported.

is an important factor that determines yield compositions. They also showed that the higher molecular weight products of all chemicals in char decreased as the reaction temperature increased.

The current study provides light on the characterization of the biofuels derived from *Madhuca longifolia* residues collected from mature trees. Pyrolysis of the collected residues was executed in a fixed bed reactor by changing the temperature from 350 to 600 °C, since this operating temperature yielded the maximum pyrolysis oil. The pyrolysis oil obtained under the maximum yield conditions was evaluated using various analytical methods and its physicochemical parameters were also assessed based on ASTM standards. Apart from pyrolysis oil, the char and pyrolysis gas were also examined to find their components. The key aim of the study was to define the subfractions acquired from the pyrolysis of *Madhuca longifolia* residues analytically and to determine their potential for commercial applications, since most of the previous studies concentrated on the utilization of wood, bark, seeds, seed cake, and leaves of *Madhuca longifolia*, no studies were identified on the utilization of residues for the production of biofuel via pyrolysis process. This study utilized various analytical techniques, including FT-IR, GC-MS, and gas chromatography, to characterize the produced biofuels. Furthermore, the pyrolysis oil was examined in its natural form to identify its basic components.

Materials and methods

Madhuca longifolia residues

Madhuca longifolia residues were collected from the west part of Tamil Nadu, India. The residues are a mixture of wood, wood bark, leaves and roots obtained from a single mature tree. The feedstocks were separated manually from other types of wood materials and washed with fresh water. Before starting the pyrolysis experiment, the moisture present in the samples was reduced by natural and vacuum drying. The collected residues were first ground in a ball mill (Laxmi Engineers, Rajasthan, India), and then sieved using a sieve shaker (Jayant Test Sieves, Sunshine Instruments, Coimbatore, India) to have an average diameter of less than 1.0 mm. The screened particles were dried naturally in an open sun for 2 weeks. Again, the naturally dried particles were kept in a furnace for 24 h, maintained at a temperature of 100 °C. For experimentation, the dried samples were stored in a tight container.

Pyrolysis reactor and procedure

The pyrolysis tests on *Madhuca longifolia* residues were conducted in a fixed-bed reactor. The reactor is made up of a cylindrical heater. It has 50 mm internal diameter and 100 mm height. For each experiment, 60 g of feedstock are kept inside the reactor. The reactor was heated by an external 2 kW cylindrical heater equipped with an ammeter and voltmeter setup. Pyrolysis experiments were conducted at temperatures ranging from 350 to 600 °C. For this, the heating rate was set to 20 °C/min. In order to measure the gas phase temperature of the reactor, two K-type thermocouples were provided inside the reactor at two different points. The desired

temperature was attained using a PID controller coupled to a furnace via an autotransformer. The setup had a top-opening system to release condensable volatiles. The volatile compounds released from the reactor are transferred into the volatile recovery unit, or condensing unit, where the condensable vapours are separated from the non-condensable gases. Volatile vapours are rapidly quenched inside the condenser, which prevents the subsequent reactions that turn condensable volatiles into permanent or non-condensable gases. In order to get maximum pyrolysis oil conversion, till the reactor reaches the atmospheric temperature, the condenser is supplied with an adequate quantity of ice water maintained at 5 °C. Inside the condenser, when the pyrolysis gas reaches 50 °C, the condensable pyrolysis oil and water usually begin to condense, whereas the phenolic compounds will begin to condense at 80 °C. It should be noted that the partial pressure of vapour compounds is also a function of composition, which is influenced by the type of feedstock and reactor operating conditions³⁵. The condensed liquid, called pyrolysis oil, can be collected in the jar kept at the bottom of the condenser. Figure 1 illustrates the reactor system. The current experimental setup that could have an impact on the pyrolysis yields is displayed in Table 2. In order to find the repeatability, each run was conducted three times, and the average was taken for the analysis.

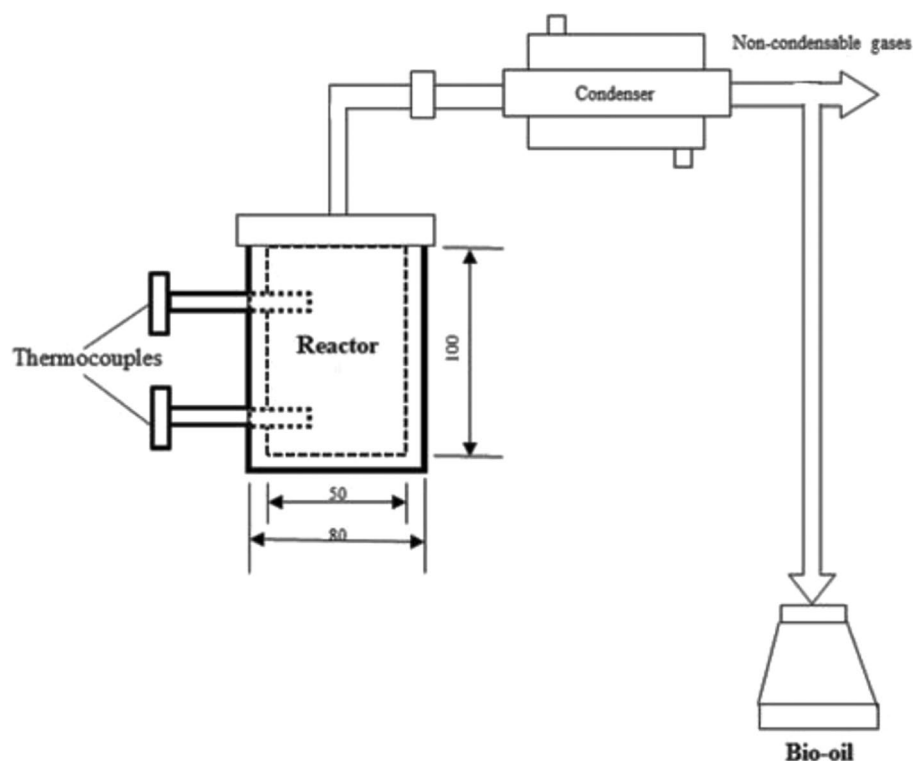


Figure 1. Experimental set up.

Case	Reactor temperature in °C	Particle size in mm	Feeding rate in grams
Run 1	350	1.0	60
Run 2	375	1.0	60
Run 3	400	1.0	60
Run 4	425	1.0	60
Run 5	450	1.0	60
Run 6	475	1.0	60
Run 7	500	1.0	60
Run 8	525	1.0	60
Run 9	550	1.0	60
Run 10	575	1.0	60
Run 11	600	1.0	60

Table 2. Experimental condition.

Characterization of feedstock and pyrolysis products

Proximate analysis

The proximate analysis of any biofuel or feedstock describes the volatile matter content (ASTM D3175), amount of moisture (ASTM D3173), ash (ASTM D3174) and fixed carbon. The analysis in this study on biomass samples was conducted in a muffle furnace according to the above mentioned ASTM standards with good temperature control and a good weight balancing machine (± 0.1 mg sensitivity). The formula used for the proximate analysis is given below.

$$\%M = \frac{\text{weight of sample before drying} - \text{weight of sample after drying}}{\text{weight of sample before drying}} \times 100 \quad (1)$$

$$\%VM = \frac{\text{oven - dried sample weight} - \text{weight of sample remaining after burning}}{\text{oven - dried sample weight}} \times 100 \quad (2)$$

$$\%A(\text{air - dried sample}) = \left(\frac{W_1}{W_2 \times \frac{T}{100}} \right) \times 100 \quad (3)$$

where W_1 = weight of ash, W_2 = initial weight of sample, T = percent of total solid.

$$\%FC = 100 - (\%M + \%VM + \%A) \quad (4)$$

Ultimate and lignocellulosic analysis

The ultimate analysis identifies the percent of carbon (C), hydrogen (H), nitrogen (N), sulfur (S), and oxygen (O) in the biomass sample and produces char according to the prescribed ASTM standards. This analysis yields the composition on ash-free basis. The analysis was carried out by using an elemental analyzer (EA 2400 Series II). The CHNS mode is based on the conventional PreglDumas technique, which involves burning samples in an atmosphere with just oxygen and collecting the combustion gases as a byproduct³⁶. For the analysis, a small amount of samples were fully burned and reduced to the constituent gases CO_2 , H_2O , N_2 , and SO_2 in the presence of oxygen and combustion reagents. The presence of carbon in the sample turns CO_2 , while H_2 to H_2O , N_2 to NO_x , and S to SO_2 . After being passed over a heated, high-purity copper surface, the gases exiting the combustion chamber lose all oxygen and turn any NO_x into N_2 . The identification of the production of CO_2 , H_2O , N_2 , and SO_2 gases yields the values of C, H, N, and S. The combusted gases are passed through a high-quality copper surface, which eliminates all oxygen and turns any NO_x into N_2 . The identification of the production of CO_2 , H_2O , N_2 , and SO_2 gases yields the values of C, H, N, and S.

The lignocellulosic content of the biomass samples is measured using the conventional wet chemistry method. This method is considered an effective one for the determination of the lignocellulosic content of any biomass material. The analysis was performed by consuming 0.5 g of biomass. The analysis was initiated by acid chlorination treatment using NaClO_2 and CH_3COOH combinations. The treatment was performed at a temperature of 75 °C. After that, more NaClO_2 and CH_3COOH are continuously added for successive cycles of chlorination. After filtration, the resulting solution is then cleaned with acetone and normal water. Cellulose and hemicellulose were found at the end of the filtration process, and the amount of lignin in the sample was determined by a two-step sulfuric acid hydrolysis process.

Thermogravimetric analysis

Thermogravimetric analysis (TGA) and derivative thermogravimetry (DTG) has been extensively utilized to explore thermal processes and kinetics of any organic material. It measures the mass loss of the material regarding temperature and time. Analysis of TGA helps in the preparation, design, and process of the industrial pyrolysis system³⁷. The TGA study provides extensive experimental data regarding the pyrolysis performance of biomass. The analysis was carried out using a TGA analyzer (TGA701) by heating the sample to 600 °C at a heating rate of 20 °C/min.

FT-IR analysis

FT-IR quantification techniques for volatile compounds relevant to pyrolysis have been established by many literature in recent years. FT-IR spectroscopy was used to analyze the microstructures of feedstock, pyrolysis oil and char products. For the analysis, the potassium bromide (KBr) disk approach was used to prepare the samples. The compressed alkali metal halide pellet method, also known as the KBr pellet or disk method, is a widely used technique for handling solid samples³⁸. The KBr disk approach is a valuable method in IR spectrometry. In this method, the samples are converted into powdered form and combined with an IR transparent salt, like KBr, to lower the sample's concentration and improve the spectrum. To eliminate water molecules from the KBr, it is pulverized into 200 mesh sizes and dried at 110 °C. For the preparation of the pellet, 200 mg of powdered KBr is blended with a 1% sample, and the combined sample is then pressed into the disk. The spectra were acquired using a Bruker Tensor 27 spectrometer (Bruker, Germany) with 4 cm^{-1} resolution between 4000 and 400 cm^{-1} .

GC-MS analysis

Thermo GC—trace ultra-version: 5.0, Thermo MS DSQ II supplied by Thermo Scientific Corporation was used to conduct GC-MS analysis of the oil. Quartz wool was placed at one end of a pre-weighed quartz tube, which had a

25 mm length and 0.5 mm ID and samples weighing 0.5 mg were placed for the analysis. The split injector of the GC inlet port was set to 280 °C and a split ratio of 20:1 was selected for analysis. A DB 35-MS capillary standard non-polar column of length 30 m, diameter 0.25 mm and 0.25 µm film thickness was used for the separation of pyrolysis yields. The temperature program was set to 40 °C, held for 2 min and then ramped to 280 °C at a rate of 6 °C/min. The interface temperature was set to 280 °C and the mass spectrometer's ion source to 230 °C, and the scanning was performed in the range of 50–550 *m/z*.

Physical characterization of pyrolysis oil

The various physical characteristics of the pyrolysis oil were found by following different ASTM protocols. To find viscosity, a Redwood viscometer (Model: SICBRV-01, Shambhavi Imp., Mumbai) was used. The density was found by weighing known volume. The Sciencetech supplied Cleave Land Flash Point Kit (Model SE-224) was utilized to measure the flash point.

Determination of heating value

The higher heating value of the pyrolysis products was measured on a Parr-6772 (Parr Instrument Company, Illinois, USA) apparatus according to ASTM D240 protocol. The values displayed are calculated with 0.6% accuracy and are based on the average of several experiments.

Gas chromatography

With the use of a Shimadzu gas analyzer (Model: GC-2014, Shimadzu Corporation), the produced gas obtained at 475 °C was examined to find its gas sub-fractions. The analysis was done using a splitless injection unit armed with a micropack with a carbon column of 1 mm diameter. The accuracy of the chromatogram was ± 1% (0.01 °C) the range of the thermal conductivity detector was 400 °C and the linear heating range was set to 20 °C/min up to 250 °C.

Ethics statement

All experimental and laboratory tests were performed in accordance with the relevant guidelines and regulations.

Permission to collect biomass residue

The residues used for this study were collected from plants on private lands and we obtained permission from the landowner to access the areas and collect the residues.

Results and discussion

Characterization of feedstock

Proximate and ultimate analysis

The elemental analysis of the feedstock is found as follows: C = 47.2%, H = 5.9%, N = 3.6%, S = 1.2% and O = 42.1%. C and O are available more than H and N. When biomass is pyrolyzed, the higher concentration of O content results in oxygenated products. Lower levels of S and N suggest that during pyrolysis, it releases fewer SO_x and NO_x. The empirical formula derived from elemental analysis is CH_{1.489}N_{0.065}O_{0.669}. It is well known that a material having lower H/C and O/C ratio have higher energy content³⁹. The proximate analysis shows lower ash and moisture levels. Initially, the moisture level was more, but it was reduced by the continuous drying process. For pyrolysis, the biomass must have a moisture content of less than 10%⁴⁰. The selection of appropriate biomass material for pyrolysis is the key process. The physicochemical analysis of the present biomass reported in Table 3 shows its suitability. The selected residue has a volatile matter content of 71.26%. Typically, biomass with a higher volatile matter content yields large amounts of biogas and oil⁴¹. The yield of pyrolysis products increases directly proportional to the amount of volatile materials extracted. Almost 90% of the volatile content in the feedstock is lost during pyrolysis to produce biofuels. Biomass with a high level of volatile content is generally chosen for pyrolysis since it is more reactive and readily devolatilized. For the pyrolysis process, the amount of ash in biomass should be minimal⁴². The ash content of the residue is 4.50%, which is lower than coal, switchgrass, barley straw and wheat straw mentioned in the literature³⁹. The yield of the pyrolysis products and process efficiency are directly impacted by the ash present in the feedstock. So the ash content in the feedstock is an important parameter for the pyrolysis process. Yildiz et al.⁴³ reported that adding ash to the pyrolysis process resulted in higher amounts of non-condensable gases and water while decreasing the yields of pyrolysis oil. The cellulose, hemicellulose and lignin contents are 18.04, 45.18 and 32.78% respectively. From proximate and ultimate analysis, it can be understood that the selected feedstock is suitable for the production of biofuel. Table 3 indicates the result of proximate, ultimate analysis of *Madhuca longifolia* residues.

TGA and DTG analysis

For the pyrolysis process, finding thermal behavior of the feedstock is important before conducting the experimental process. The TGA and DTG analysis of the *Madhuca longifolia* residues are revealed in Fig. 2. The figure indicates the results of the DTG curves at a 20 °C/min heating rate. The decomposition of the sample may be affected by differences in heat transfer and kinetic rates. It can be found that heating rates primarily influence the stages of pyrolysis. Increasing heating rates alter the maximum weight loss point at different temperature ranges⁴⁴. The peaks observed in DTG represent the point or temperature at which the rate of weight loss reaches its maximum. In an inert atmosphere, the solid heats up in three different regimes. In the first regime, only heating takes place, followed by pyrolysis in the second regime, and further heating in the third regime if there is char remaining. The heat applied to the biomass breaks down its constituents. It is the process

Parameter	Value in wt%
Proximate analysis	
Moisture	5.98
Ash	4.50
Volatile matter	71.26
Fixed carbon ^a	18.24
Ultimate analysis (dry ash basis)	
C	47.2
H	5.9
N	3.6
S	1.2
O ^a	42.1
H/C molar ratio	1.489
O/C molar ratio	0.669
Empirical formula	CH _{1.489} N _{0.065} O _{0.669}
HHV (MJ/kg)	17.54
Component analysis	
α-Cellulose	18.04
Hemicellulose	45.18
Lignin	32.78

Table 3. Proximate and ultimate analysis of *Madhuca longifolia* residues. ^aBy difference.

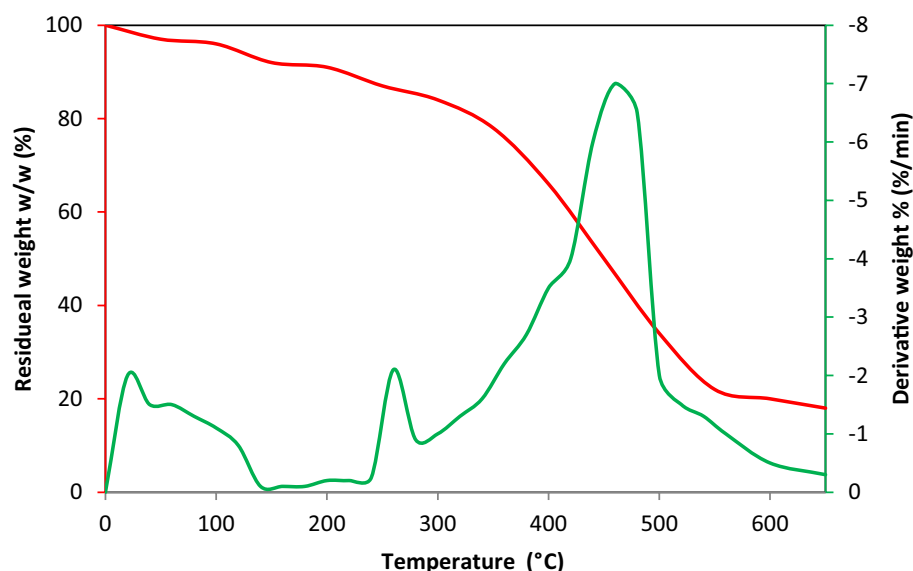


Figure 2. TGA and DTG analysis of *Madhuca longifolia* residue.

of decomposing a chemical compound into smaller components through various chemical reactions. Here, the mass loss function of residues is detected in three phases. The first phase represents the evaporation of moisture, in which ~ 12% of mass loss occurs due to the removal of moisture at < 140 °C. Furthermore, two exothermic peaks can be seen in the analysis at 245 °C and 457 °C. Between 345 °C and 520 °C a maximum mass loss of ~ 75% was observed. Additionally, the DTG curve for this stage reveals a peak at 457 °C with a maximum mass loss rate of 1.22 mg/min. Mass loss during this stage are linked to the disintegration of hemicellulose, which represents active pyrolysis, and the disintegration of cellulose and lignin, which represents active and passive pyrolysis⁴⁵. Notably, the sample displayed its largest weight loss at its peak temperature, indicating a high degree of thermal degradation reactivity. The results of this study are in line with those of Dwivedi et al.⁴⁴. Around 450 °C, all parts of the biomass material break down extremely and lose their maximum weight. The weight loss differential decreases after 460 °C and reaches zero after 600 °C. For last stage above 600 °C, the degradation of biomass decreases and almost same after that. The residues that remained at the end of the TGA analysis represent the presence of ash. The percentage of ash, which may be computed at around 5% by weight, is the quantity of material that remains after reaching 600 °C.

FT-IR analysis

The peaks, which are also called absorbance bands, match with the various vibrations of the sample's atoms when it is contacted in the infrared region of the electromagnetic spectrum. The x-axis in the spectra denotes the infrared spectrum, and the y-axis denotes the quantity of infrared light transmitted or absorbed by the sample. In the spectra, the peaks are attributable to the specific functional group. A greater concentration of the appropriate functional group or bond is indicated by a stronger absorption peak. Figure 3 illustrates FT-IR analysis of *Madhuca longifolia* residue. The figure shows plots between wavenumber and transmittance spectra. The existence of water, phenolic compounds, aromatic and other impurities in the feedstock was confirmed by the peak at 3605.5 cm^{-1} which was linked to the O–H group⁴⁶. The possible existence of alkanes was suggested by the adsorption bond 2865.6 cm^{-1} , which was linked to the C–H stretching vibration⁴⁷. A C≡C deformation-attributed adsorption bond at 1402.9 cm^{-1} revealed the existence of alkynes⁴⁸, whereas an adsorption bond at 1610.3 cm^{-1} associated with C=O stretching vibration indicated the existence of aldehyde, ketones, or carboxylic acids⁷. Alkanes were identified by the peak 1368.1 cm^{-1} ascribed to C–H bending and the existence of ethers, alcohols, and carboxylic acid was indicated by the adsorption band 1217.9 cm^{-1} attributable to C–O bending. The identification of O–H bending stretching is responsible for the existence of mono- and polycyclic aromatic compounds between 931.4 cm^{-1} .

Pyrolysis product yields

The impact of reactor temperature on pyrolysis yield distributions is displayed in Fig. 4. The temperature was changed in increasing pattern from 350 to 600 °C to assess the product yield at the interval of 25 °C. All the experiments were conducted by keeping particle size < 1.0 mm. According to the results, the yield of pyrolysis oil enhanced from 33.1 wt% to 41.7 wt% at 350 to 500 °C and then decreases to 37.5 wt% at 600 °C. This typical nature of the product is depends on several reactions, both primary and secondary, occur during pyrolysis, producing condensable and non-condensable gaseous products. The condensable gases were further condensed to produce pyrolysis oil. Through the production of non-condensable fragments, secondary processes aid in increasing the gas yield⁴⁹. Inside the reactor, the primary reaction occurs more frequently at lower temperatures and as the reaction temperature increases, more vapour is formed which improves the formation of more condensable volatiles (oil yield). The production of pyrolysis oil, however, decreased after a particular temperature when secondary reactions became more prevalent at a higher temperature⁵⁰. As the reaction temperature rises, more volatiles are formed, which decreases the yield of char. The development of char decreases steadily at elevated temperatures because of the considerable loss of volatiles or secondary breakdown of char. According to Chutia et al.⁵¹, the secondary breakdown of the primary volatiles also produces certain non-condensable vapours, which further increase the yield of gas. It was also confirmed by the results that when the changed from 350 to 600 °C, the char yield decreased from 41.6 wt% to 10.2 wt% and the gas yield increases from 25.3 wt% to 52.3 wt%. Table 4 shows the tests results of *Madhuca longifolia* pyrolysis in wt% and Table 5 shows mass balance of the yield.

Characteristics of pyrolysis oil

It is important to pay attention to the quality of the pyrolysis oil produced by the pyrolysis process, which is considerably influenced by the pyrolysis temperature. The pyrolysis oil produced at a lower pyrolysis temperature (< 300 °C) generally has higher moisture content and a lower viscosity. In contrast, pyrolysis oil produced at a higher pyrolysis temperature (> 600 °C) has a higher viscosity and lower moisture content⁵². Furthermore, the temperature during pyrolysis can have an impact on the chemical composition of the oil. Pyrolysis oils typically

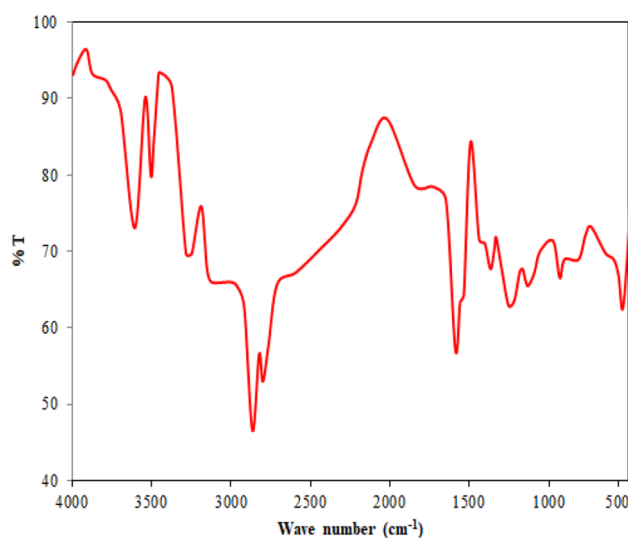


Figure 3. FT-IR analysis of *Madhuca longifolia* residue.

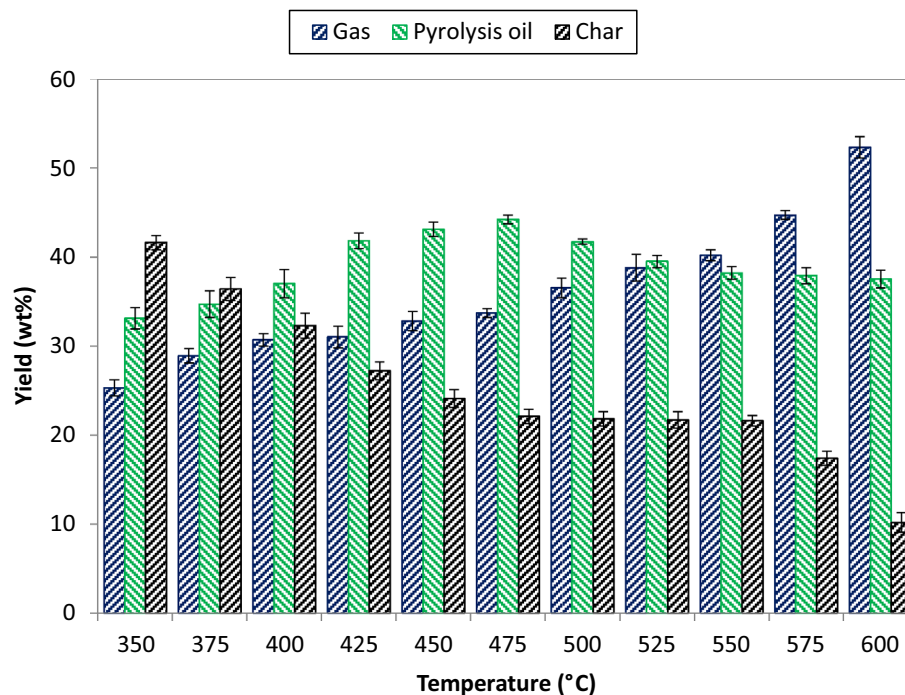


Figure 4. Pyrolysis product distributions.

Case	Temperature in °C	Test 1			Test 2			Test 3		
		Gas	Pyrolysis oil	Char	Gas	Pyrolysis oil	Char	Gas	Pyrolysis oil	Char
Run 1	350	25.0	33.0	42.0	25.7	33.3	41.5	25.3	33.1	41.4
Run 2	375	28.5	34.4	36.2	28.9	34.8	36.5	29.2	34.7	36.5
Run 3	400	30.6	37.0	32.0	30.9	37.4	32.6	30.4	36.8	32.4
Run 4	425	31.2	41.5	27.6	31.0	42.1	27.0	30.8	41.7	27.1
Run 5	450	32.8	43.4	24.0	32.6	43.2	24.1	33.0	42.8	24.2
Run 6	475	33.9	44.2	22.5	34.0	44.2	21.6	33.3	44.1	22.2
Run 7	500	36.6	41.6	21.5	36.6	41.7	22.2	36.4	41.8	21.8
Run 8	525	38.6	39.1	21.4	39.1	39.7	22.1	38.7	39.7	21.7
Run 9	550	40.0	38.0	21.3	40.4	38.4	22.0	40.2	38.2	21.6
Run 10	575	44.3	37.6	17.0	44.9	38.0	18.0	44.9	38.0	17.3
Run 11	600	51.8	37.4	9.6	52.5	37.9	10.4	52.6	37.3	10.5

Table 4. Tests results of *Madhuca longifolia* pyrolysis in wt%

		Unit	Run 1	Run 2	Run 3	Run 4	Run 5	Run 6	Run 7	Run 8	Run 9	Run 10	Run 11
Input	Biomass	Gram	60.00	60.00	60.00	60.00	60.00	60.00	60.00	60.00	60.00	60.00	60.00
Output ^a	gas ^b	Gram	15.18	17.34	18.42	18.60	19.68	20.22	21.90	23.28	24.12	26.82	31.38
	Pyrolysis oil	Gram	19.86	20.82	22.20	25.08	25.86	26.52	25.02	23.70	22.92	22.74	22.50
	Char	Gram	24.96	21.84	19.38	16.32	14.46	13.26	13.08	13.02	12.96	10.44	06.12
Mass in/mass out		–	1.00	1.00	1.00	1.00	1.00	1.00	1.00	1.00	1.00	1.00	1.00

Table 5. Mass balance. ^aAverage from test 1, test 2 and test 3 in Table 4. ^bComputed by material balance.

contain higher concentrations of aldehydes and fatty acids at lower temperatures. On the other hand, aromatic substances like catechol and phenol are likely to increase at higher temperatures. In this study, the pyrolysis oil obtained at maximum oil yield conditions (475 °C) was taken for the physical and chemical characterization study.

Physical analysis

It was of interest to examine the physical properties of pyrolysis oil since it is very important to describe the application of the produced oil. Table 6 demonstrates the physical characteristics of the produced pyrolysis oil and other pyrolysis oils derived from various feedstocks. The table also compared the physical nature of conventional diesel. The pyrolysis oil fraction had a distinct appearance compared to conventional diesel fuel. The pyrolysis oil was dark brown and more viscous than diesel. In general, the typical pyrolysis oil has water components of about 25 wt% or more. In contrast, the water content of the derived *Madhuca longifolia* oil was less than 20 wt%. Viscosity is a crucial characteristic of pyrolysis oil, which represents the flow ability of any liquid. The higher viscosity of the fuel disturbs the pumping and atomization during burning. Pyrolysis oil is derived from a variety of biomasses under varying operating conditions and has a different range of viscosities. The viscosity of pyrolysis oil derived from *Madhuca longifolia* residues shows 4.0 cSt, which is higher than the value obtained from *Mimusops elengi*, sugarcane leaves, and napier grass. Despite being produced under the same operating conditions, the bio-oil derived from two different feedstocks has different viscosities. For instance, at 50 °C, the viscosity of the pyrolysis oil made from wheat straw, pine, and ensyn was shown to be 11 cSt, 46 cSt, and 50 cSt, respectively⁵³. The variation in viscosity is determined by the structure and composition of the parent feedstocks. The density of the pyrolysis oil is found to be another important physical characteristic. The density of the typical pyrolysis oil is found in the range of 1000–1250 kg/m³. This variation is primarily caused by the type of biomass used for the pyrolysis process. The density of the *Madhuca longifolia* pyrolysis oil is found to be 995 kg/m³ which is less than all pyrolysis oils produced from the various feedstocks listed in Table 6. The water content in the pyrolysis oil has some adverse effects while burning. The presence of water molecules reduces the calorific value of the oil and is also responsible for corrosiveness and instability. The pyrolysis oil produced in this study has a pH value of 4.7, which is consistent with other studies. The lower pH value indicated the existence of acidic chemicals. The higher flash point of the pyrolysis oil (130 °C) indicates that it can be stored safely at room temperature.

Chemical analysis

Figure 5 displays the transmission mode FT-IR spectra for pyrolysis oil between 4000 and 400 cm⁻¹. The higher amount of alcohols and phenols is shown by the O–H stretch at 3268.5 cm⁻¹. The existence of phenolic or O–H groups holds major percentage in pyrolysis oil⁵⁷. The appearance of alkanes is shown by the C–H stretch at 2835.5 cm⁻¹ and 2649.6 cm⁻¹. The appearance of alkenes is exposed by the C=C stretch at 1574.7 cm⁻¹. The existence of alcohol is shown by the C–O stretch at 942.1 cm⁻¹ and the appearance of aromatic compounds is indicated by the C–H bend at 857.8 cm⁻¹. The bio-oil revealed an abundance of aliphatic compounds and

Property	<i>Madhuca longifolia</i> [This study]	<i>Albizia amara</i> ¹¹	<i>Mimusops elengi</i> oil ⁵²	Sugarcane leaves ⁵⁴	Napier grass ⁵⁵	Waste paper ⁵⁶	Diesel	Unit
Appearance	Dark brown	#	Dark brown	Dark brown	Dark brown	#	Yellowish	–
Density	995	1050	1130	1089	1274	1205	855	kg/m ³
Viscosity	4.0	4.2	1.42	0.69	2.32	20	2.3	cSt
Flash point	130	160	#	#	#	200	57	°C
Odour	Smoky	#	Smoky	#	#	#	Aromatic	–
pH value	4.7	3.6	4.22	2.12	2.3	1.5	–	–
Calorific value	22.27	18.63	18.14	27.39	19.79	13.10	43.6	MJ/kg
Water content	19	#	#	8.26	48.15	#	–	wt%

Table 6. Physical characteristics of *Madhuca longifolia* and other pyrolysis oils. #Not reported.

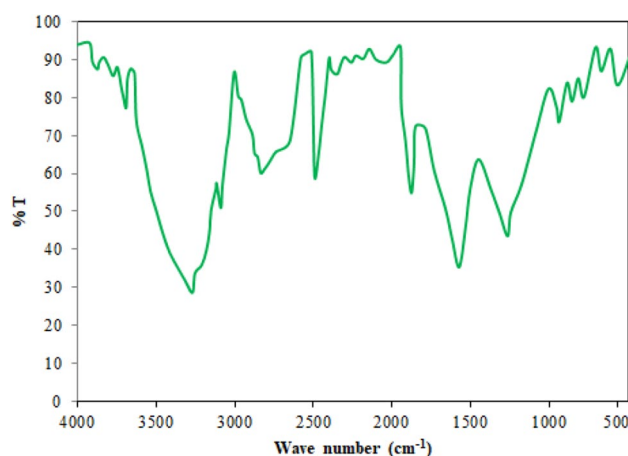


Figure 5. FT-IR analysis of pyrolysis oil.

alcohols. The functional groups of oxygenated C–O and O–H indicate that the pyrolysis oil was significantly hydro-oxygenated, making it naturally acidic. The heating value of pyrolysis oil is reduced when oxygenated functional groups are present. The existence of acids, phenols, alcohols, and aliphatic was also present in different types of pyrolysis oil reported earlier^{58,59}. GC–MS analysis can also be used to justify the aforementioned functional groups in pyrolysis oil⁵⁷.

In GC–MS, the volatile matter present in the oil sample is separated and identified using the NIST library. For the analysis, the liquid sample is converted into a vapour which can be carried by a carrier gas (He). The sample is then transported by the gas over a long, thin glass column coated with a chemical. As the vaporized compounds are strapped into the column, they slow down when they interact with the stationary phase. Depending on their individual chemical characteristics, different compounds will take different amounts of time to reach the end of the column. After the separation process, the compounds are moved to the mass spectrometer (MS). The MS acts as a sensor that recognizes the vaporized compounds and mass information. The structural and chemical characteristics of molecules can be identified, measured, and ascertained using mass information. Generally, pyrolysis oil has over 300 different components due to their complexity⁶⁰. This analysis found more than 60 chemicals in the oil, but the peak areas of more than 0.1% are presented in Table 7. The substance found in pyrolysis oil was formed by the cracking lignocellulosic content of the feedstock. Among several chemical groups found in mahua pyrolysis oil, phenolic elements, saturated fatty acids, alkanes, alkenes and branched hydrocarbons were found to be the majority in the oil. The most important substances in the oil are phenols and their derivatives. At the retention times of 11.52 and 30.58 min, phenol and 3,4-dimethylphenol were identified

RT/min	Name of the compounds	Chemical formula	Area %
6.25	2,5-Dimethyl-phenol	C ₈ H ₁₀ O	7.21
6.94	o-Cresol	C ₇ H ₈ O	2.20
8.05	2-Methyl-benzo-furane	C ₉ H ₈ O	1.25
8.33	Octanoic acid	C ₈ H ₁₆ O ₂	2.01
10.08	2-Methoxy-4-methyl-phenol	C ₈ H ₉ O ₂	2.68
11.52	Phenol	C ₆ H ₆ O	4.94
13.50	Hexadecane	C ₁₆ H ₃₄	0.97
14.81	4-Ethyl-2-methoxy-phenol	C ₉ H ₁₂ O ₂	3.10
16.07	Propanone	C ₃ H ₆ O	2.88
17.00	Butanoic acid	C ₄ H ₈ O ₂	3.14
17.97	n-Octadecanoic acid	C ₁₈ H ₃₆ O ₂	0.87
19.75	1,103,10 -Terphenyl, 50-phenyl-	C ₂₄ H ₁₈	3.01
21.22	1,2-Benzenediol	C ₆ H ₆ O ₂	3.55
21.58	Guaiacol	C ₇ H ₈ O ₂	4.58
23.41	2,2'-dioxospirilloxanthin	C ₄₂ H ₅₆ O ₄	0.74
26.29	Hydroquinone	C ₆ H ₆ O ₂	1.99
27.77	3-Methoxy-phenol	C ₇ H ₈ O ₂	2.24
28.60	γ-Sitosterol	C ₂₉ H ₅₀ O	0.55
29.45	Syringol	C ₈ H ₁₀ O ₃	1.58
29.90	9-Tetradecenoic acid	C ₁₄ H ₂₆ O ₂	2.88
30.11	1,3,5 Trimethoxybenzene	C ₉ H ₁₂ O ₃	2.97
30.58	Phenol, 3,4-dimethyl-	C ₈ H ₁₀ O	12.25
30.60	Chlorodecaborane	C ₁ H ₁₃ B ₁₀	1.18
31.01	Tocopheryl methyl ether	C ₂₉ H ₅₀ O ₂	1.22
31.36	l-Limonene	C ₈ H ₁₂ O	2.66
31.92	2-Propanol, 1-(hexadecyloxy)	C ₁₉ H ₄₀ O ₂	1.27
32.28	1,3-Dimethyl-4-azaphenanthrene	C ₁₅ H ₁₃ N	2.55
32.76	Farnesol	C ₁₅ H ₂₆ O	1.81
33.37	Campesterol	C ₂₈ H ₄₈ O	4.50
33.99	3-Hydroxy-2-methylpyridine	C ₆ H ₇ NO	1.28
34.28	Undecane	C ₁₁ H ₂₄	2.10
34.50	Octadecanenitrile	C ₁₈ H ₃₅ N	1.08
35.14	Dodecylcyclohexanol	C ₁₈ H ₃₆ O	0.27
35.77	Piperidine-2,5-dione	C ₅ H ₇ NO ₂	1.29
36.04	2,5-Piperazinedione, 3-benzyl-6-isopropyl-	C ₁₄ H ₁₈ N ₂ O ₂	0.63
36.70	2-hexadecyloxy ethanol	C ₁₈ H ₃₈ O ₂	4.61
38.03	2-(2-Isopropenyl-5-methyl-cyclopentyl)-acetamide	C ₁₁ H ₁₉ NO	0.94

Table 7. GC–MS analysis of the pyrolysis oil.

up to an area percentage of 4.94 and 12.25 respectively. Guaiacol occupies the area of 4.58% and Campesterol occupies the area of 3.50%. Guaiacol is a potential component or precursor to green fuels⁶¹. It is believed that guaiacol provides 85% of the world's vanillin supply. Whereas, campesterol can be used as a precursor for a variety of steroid hormones. 2-hexadecyloxyethanol occupies an area of 4.61% at a retention time of 36.70 min. It is used for various applications, including medicine⁶². Farnesol appears in the pyrolysis oil at a retention time of 32.76 min. Due to its antibacterial properties, farnesol has been used as an organic mite insecticide and as an antiperspirant in cosmetic items. The GC-MS results indicate that derived pyrolysis oil has many fuel-like components, which is suitable replacement for conventional fuel. Apart from that, the compounds identified in the analysis can be separated to be used as feed material for chemical industries.

During the thermal pyrolysis process, the components of biomass decompose at different rates and with different reaction processes since the reaction is complex and partially dependent on reactor designs and thermal processing parameters. Many studies have previously verified the interactions between the lignocellulosic content of the woody biomass⁶³. Hemicellulose and lignin react with each other during pyrolysis to increase the formation of phenolic compounds produced from lignin and inhibit the production of hydrocarbons. Lignin has a major impact on cellulose during pyrolysis since it prevents levoglucosan polymerization, which lowers the formation of char. On the other hand, the reaction between cellulose and hemicellulose has less of an impact on the production and dispersion of pyrolysis products. The primary phase of cellulose pyrolysis is a series of disintegration and polymerization processes that take place at temperatures below 300 °C and form lower molecular components such as furan, hydroxyl acetaldehyde, glycoaldehyde, and formic acid. The main component of pyrolysis vapor is often anhydrosugars, primarily levoglucosan, which are produced by the breaking of glycosidic linkages and dehydrating processes⁶⁴. Above 300 °C, levoglucosan endures relocation and hydration, which produces levoglucosenone. Further cyclization reactions resulted in the formation of stable oxygenated chemicals. The furanic compounds present in the pyrolysis oil are obtained from hemicellulose-based pyrolysis. These compounds were produced due to the dehydration of reducing sugars. The mannose and galactose present in the hemicellulose endure a dehydration reaction to form the hydroxymethyl group⁶⁵. The production of phenol, cresol, guaiacol, and syringol are the primary results of lignin pyrolysis. Guaiacol has two distinct types of carbon-oxygen linkages, which are present in most of the lignin-derived compounds.

Characteristics of char

FT-IR analysis

FT-IR spectral characteristics of char are displayed in Fig. 6. The spectra were captured between 4000 and 400 cm^{-1} . There could be an acidic or alcoholic composition causing the strong O-H bond stretching vibration at 3404.7 cm^{-1} . The vibration at 1605.2 cm^{-1} is indicative of the carboxylic acid in the char⁶⁶. There are alkynes, aliphatic, ketonic, esters and aromatic compounds within the char, which were recognized by the peaks appearing at 1977.6, 1359.4 and 1075.4 cm^{-1} respectively. According to Brodowski et al.⁶⁷, the reactive functional groups present in char, likely O-containing carboxylic, are associated with the broad sensitive zones that engage with polar organic elements and mineral phases. As a result, porous char has oxygen groups that may be good for soil in order to enhance its physical characteristics.

Chemical composition

Table 8 displays the approximate composition present in char. Raw feedstock was converted into char, which led to decreased volatile and moisture contents with increased fixed carbon and ash fractions. It has been suggested that the fixed carbon in char is naturally resilient to biological degradation. Generally, pyrolysis char has higher fixed carbon and lower volatile matters. The ash present in the char is cautiously attractive if it is used in soil for agronomy and carbon sequestration. The pyrolysis char has fixed carbon content of 52.7% and volatile matter and ash of 28.85% and 16.14%, respectively. Elemental analysis demonstrates that the pyrolysis of biomass increased carbon content while decreasing hydrogen, oxygen and sulfur in char compared to feedstock material

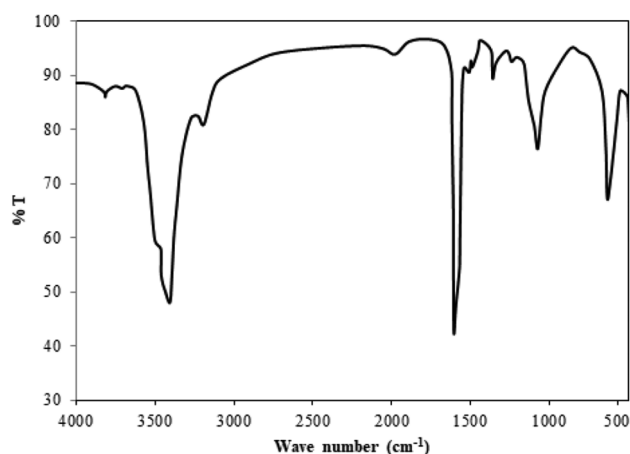


Figure 6. FT-IR spectra of char.

Component	Moisture	Ash	Volatile matter	Fixed carbon ^a
Value in %	2.31	16.14	28.85	52.7

Table 8. Proximate analysis of char. ^aBy difference.

(Table 9). Pyrolysis of *Madhuca longifolia* residues modified the constituent carbon molecules to produce char with higher aromatic carbon and less hydrogen and oxygen⁶⁸. The decrease in oxygen-containing species in char may be due to dehydration and the decarboxylation process. Sulfur content in char may have decreased as a result of organic sulfur decomposition at elevated temperatures. The H/C and O/C molar ratios were identified as 0.623 and 0.373. It helps to determine the durability of the char against degradation. For char, a half-life of over a 1000 years is anticipated when the O/C ratio is less than 0.2⁶⁹. The volatile matter in char is made up of molecules with greater H/C ratios, while the fixed carbon has a lower hydrogen concentration. The HHV of the char components was identified as 21.2 MJ/kg.

Characteristics of gas

Table 10 shows the elements of the non-condensable gas fractions. The finding shows a variety of combustible hydrocarbons. The components were identified as CH₄, CO₂, CO, O₂ and H₂ in different ratios. An average concentration of 33.1% of CO₂ was found in the gas, along with 6.8% of CO. Increased CO₂ production is primarily caused by the water–gas shifting process of CO and breakdown of C–O and –COOH groups⁶⁹. According to Sowmya Dhanalakshmi and Madhu⁷⁰, the reverse Boudouard process amongst char and produced CO₂ might be the cause of the increased CO level. According to Tinwala et al.⁷¹, the identification of CO and CH₄ in pyrolysis gas is the outcome of the secondary cracking of produced volatiles and the production of higher CO₂ is also caused by the deprivation of cellulosic content. This increased CO₂ percentage suggests that the *Madhuca longifolia* residues contain oxygenated elements and it is noteworthy that the concentration of CO in the pyrolysis gas rose at higher temperatures due to secondary cracking process. The observations revealed that the pyrolysis gas contains 17.3% flammable methane. Methane is formed at medium and elevated pyrolysis temperatures due to deterioration of benzyl and methoxyl groups. On the other side, the formation of hydrogen is due to the hydrolysis of aromatic components.

Applications of pyrolysis product yields

Biomass can be a valuable resource for the pyrolysis process, providing a variety possibilities to increase its added value and produce bioproducts that are in high demand. Pyrolysis oil, or bio-oil, char, and gas are the three main products derived from the pyrolysis process. Nowadays, the usefulness of pyrolysis oils as a renewable fuel is gaining more interest. The raw pyrolysis oil can be used as a low-grade fuel for furnaces and boilers. The pyrolysis oils are generally more difficult to combine with synthetic fuels derived from petroleum. However, the substances derived from pyrolysis oils have a wide range of applications in the medical, cosmetic, and pharmaceutical industries. The oil contains phenols and their derivatives, which are frequently utilized in food preparation, transport, and colorants⁷². The fatty acid composition present in the oil can potentially be utilized for producing natural pesticides. Anyhow, the pyrolysis oil made from *Madhuca longifolia* residues eventually replaces fossil asphalt because of its considerable heating value. The calorific value of the oil indicates that it is almost 40% more than that of diesel fuel, making it suitable for forestry residues. So the produced pyrolysis oil can be used as a low-grade fuel for furnaces and boilers. The char produced in this study can be used as a substitute for traditional solid fuels. Further study is needed to convert the produced char into activated carbon. However, it can be compressed into charcoal briquettes or used to make gunpowder. The utilization of char is largely contingent upon the composition of the material to be pyrolyzed. Due to the higher surface area and porosity of the char, it is most frequently used as an adsorbent material. The pyrolysis gas can also be used as a source for producing heat for various heating processes. The produced pyrolysis gas is a mixture of intriguing molecules that includes considerable amounts of H₂, CH₄, and higher hydrocarbons. Moreover, post-treatment might increase the amount of these molecules, making them a valuable source of biomolecules.

Component	C	H	N	S	O ^a	H/C	O/C	HHV
Value in %	60.4	3.3	0.9	1.3	34.1	0.623	0.373	21.2

Table 9. Elements of char. ^aBy difference.

Component	H ₂	O ₂	CO	CH ₄	CO ₂	N ₂
Value in %	2.6	10.9	6.8	17.3	33.1	25.5

Table 10. Averaged gas composition of pyrolysis gas.

Challenges and opportunities

The pyrolysis oil comprises hydrocarbons, oxygenated compounds, and nitrogenated compounds, as indicated in Table 3. Compounds containing oxygen have the potential to lower its calorific value, stability, and flow ability. The existence of nitrogenated compounds can lead to NO_x emissions during combustion. So it is very essential to improve the hydrocarbon ratios in pyrolysis oil. The extraction of oxygenated compounds from pyrolysis can be done by various pyrolysis steps, including dehydration, decarbonylation, decarboxylation, and hydrodeoxygenation; however, studies on the extraction of nitrogenated compounds from pyrolysis oil are rare. According to Li et al.⁷³, selective adsorption or hydrodenitrogenation can be used to remove nitrogenated compounds. These methods can also ensure the pyrolysis oil has a better calorific value, higher hydrocarbon content, higher stability, and a lower viscosity. Before solving the pyrolysis task, researchers need to think about the examination of pyrolysis mechanisms. To enhance current global kinetic systems, new experimental methods with molecular-level understanding are required. During pyrolysis, the feedstock is heated, and the produced volatiles are collected and quantified. But the characterization of liquid- and solid-phase intermediates was generally omitted as a result of their shorter lifespans and complexity. Therefore, the absence of experimental data related to condensed-phase intermediates may simplify the development of liquid- and solid-phase reaction mechanisms. It is also obvious that the prediction of heat profiles of feedstock inside the reactor is difficult due to the lack of experimental data. So, further study is needed to analyze the heat transfer phenomena of the lignocellulosic particle. In order to increase the production of pyrolysis oil from *Madhuca longifolia* residues, catalytic pyrolysis have been suggested on commercial and laboratory scales. Instead of a fixed-bed reactor, the residues can be pyrolyzed in other types of reactors, such as fluidized-bed reactors, microwave-assisted reactors, ablative reactors, etc., to improve the selective product output. Based on the research, an optimization study is also recommended.

Conclusion

Pyrolysis is a potential choice to produce alternative fuel by utilizing forestry residues. *Madhuca longifolia* residues contain a higher percentage of volatile matters (71.26%), lower moisture (5.98%), ash (4.50%), and sulfur (1.20%) were pyrolyzed in a batch-type fixed-bed reactor at temperatures between 350 and 600 °C. The products produced from the pyrolysis were analyzed using several analytical characterization techniques. The variations in product yields have been noted between different operating temperatures, and the maximum pyrolysis oil yield of 44.2 wt% was found at a temperature of 475 °C. The gaseous yield continuously developed, whereas the char yield reduced as the temperature exceeded 475 °C. The FT-IR analysis of the pyrolysis oil showed the presence of different functional groups such as O–H, C=O, C–H and C=C. The GC–MS analysis of the pyrolysis oil showed the existence of different major chemicals such as 3,4-dimethylphenol, 2,5-dimethylphenol, phenol, guaiacol, 2-hexadecyloxy ethanol, campesterol and butanoic acid. The physicochemical characteristics of the pyrolysis oil show that the presence of water-based molecules and its higher viscosity restrict its direct usage in furnaces and engines; however, it can be used as a low-grade fuel and can be upgraded for further usage. The potential applications of pyrolysis char as an adsorbent and biofertilizer were revealed by the qualitative examination. Gas chromatography results of the pyrolysis gas demonstrated its use as gaseous fuel by confirming the presence of combustible components.

Data availability

The data generated or analyzed during this study are available within the article.

Received: 27 December 2023; Accepted: 19 June 2024

Published online: 26 June 2024

References

- Mohan, I., Panda, A. K., Volli, V. & Kumar, S. An insight on upgrading of biomass pyrolysis products and utilization: Current status and future prospect of biomass in India. *Biomass Convers. Biorefin.* **14**(5), 6185–6203. <https://doi.org/10.1007/s13399-022-02833-2> (2024).
- Rahman, M. M., Aravindakshan, S. & Matin, M. A. Design and performance evaluation of an inclined nozzle and combustor of a downdraft moving bed gasifier for tar reduction. *Renew. Energy* **172**, 239–250. <https://doi.org/10.1016/j.renene.2021.02.156> (2021).
- Kumar, G. et al. A comprehensive review on thermochemical, biological, biochemical and hybrid conversion methods of bio-derived lignocellulosic molecules into renewable fuels. *Fuel* **251**, 352–367. <https://doi.org/10.1016/j.fuel.2019.04.049> (2019).
- Rahman, M. M., Henriksen, U. B., Ahrenfeldt, J. & Arnavat, M. P. Design, construction and operation of a low-tar biomass (LTB) gasifier for power applications. *Energy* **204**, 117944. <https://doi.org/10.1016/j.energy.2020.117944> (2020).
- Seah, C. C. et al. Co-pyrolysis of biomass and plastic: Circularity of wastes and comprehensive review of synergistic mechanism. *Results Eng.* <https://doi.org/10.1016/j.rineng.2023.100989> (2023).
- Gupta, A., Chaudhary, R. & Sharma, S. Potential applications of mahua (*Madhuca indica*) biomass. *Waste Biomass Valoriz.* **3**, 175–189. <https://doi.org/10.1007/s12649-012-9107-9> (2012).
- Mishra, R. K. & Mohanty, K. Pyrolysis characteristics, fuel properties, and compositional study of *Madhuca longifolia* seeds over metal oxide catalysts. *Biomass Convers. Biorefin.* **10**, 621–637. <https://doi.org/10.1007/s13399-019-00469-3> (2020).
- Raj, R., Singh, D. K. & Tirkey, J. V. Co-gasification of Low-grade coal with *Madhuca longifolia* (Mahua) biomass and dual-fuelled mode engine performance: Effect of biomass blend and engine operating condition. *Energy Convers. Manag.* **269**, 116150. <https://doi.org/10.1016/j.enconman.2022.116150> (2022).
- Shanmuga Priya, M. & Rajalakshmi, R. Comparison of porous carbon electrodes derived from *Madhuca longifolia* leaves by hydrothermal technique and direct pyrolysis techniques. *Asian J. Chem.* **35**(4), 1037–1043 (2023).
- Madhu, P. et al. Co-Pyrolysis of hardwood combined with industrial pressed oil cake and agricultural residues for enhanced bio-oil production. *J. Chem.* <https://doi.org/10.1155/2022/9884766> (2022).
- Rahman, M. M., Henriksen, U. B. & Ciolkosz, D. Startup process, safety and risk assessment of biomass gasification for off-grid rural electrification. *Sci. Rep.* **13**(1), 21395. <https://doi.org/10.1038/s41598-023-46801-w> (2023).
- Anandaram, H. et al. Co-pyrolysis characteristics and synergistic interaction of waste polyethylene terephthalate and woody biomass towards bio-oil production. *J. Chem.* <https://doi.org/10.1155/2022/3699076> (2012).

13. Biswas, B. *et al.* Pyrolysis of agricultural biomass residues: Comparative study of corn cob, wheat straw, rice straw and rice husk. *Bioresour. Technol.* **237**, 57–63. <https://doi.org/10.1016/j.biortech.2017.02.046> (2017).
14. Moreira, R. & dos Reis Orsini, R., Vaz, J. M., Penteadó, J. C. & Spinacé, E. V., Production of biochar, bio-oil and synthesis gas from cashew nut shell by slow pyrolysis. *Waste Biomass Valoriz.* **8**, 217–224. <https://doi.org/10.1007/s12649-016-9569-2> (2017).
15. Durak, H. Pyrolysis of *Xanthium strumarium* in a fixed bed reactor: Effects of boron catalysts and pyrolysis parameters on product yields and character. *Energy Sources Part A.* **38**(10), 1400–1409. <https://doi.org/10.1080/15567036.2014.947446> (2016).
16. Alagu, R. M., Sundaram, E. G. & Natarajan, E. Thermal and catalytic slow pyrolysis of *Calophyllum inophyllum* fruit shell. *Bioresour. Technol.* **193**, 463–468. <https://doi.org/10.1016/j.biortech.2015.06.132> (2015).
17. Aysu, T. Catalytic pyrolysis of *Eremurus spectabilis* for bio-oil production in a fixed-bed reactor: Effects of pyrolysis parameters on product yields and character. *Fuel Process. Technol.* **129**, 24–38. <https://doi.org/10.1016/j.fuproc.2014.08.014> (2015).
18. Chouhan, A. P. S. A slow pyrolysis of cotton stalk (*Gossypium arboreum*) waste for bio-oil production. *J. Pharm. Chem. Biol. Sci.* **3**(2), 143–149 (2015).
19. Mohammad, I. *et al.* Pyrolysis of Napier grass in a fixed bed reactor: Effect of operating conditions on product yields and characteristics. *BioResources* **10**(4), 6457–6478. <https://doi.org/10.15376/biores.10.4.6457-6478> (2015).
20. Aysu, T., Durak, H., Güner, S., Bengü, A. Ş & Esim, N. Bio-oil production via catalytic pyrolysis of *Anchusa azurea*: Effects of operating conditions on product yields and chromatographic characterization. *Bioresour. Technol.* **205**, 7–14. <https://doi.org/10.1016/j.biortech.2016.01.015> (2016).
21. Aysu, T. & Küçük, M. M. Biomass pyrolysis in a fixed-bed reactor: Effects of pyrolysis parameters on product yields and characterization of products. *Energy* **64**, 1002–1025. <https://doi.org/10.1016/j.energy.2013.11.053> (2014).
22. Park, J., Lee, Y., Ryu, C. & Park, Y. K. Slow pyrolysis of rice straw: Analysis of products properties, carbon and energy yields. *Bioresour. Technol.* **155**, 63–70. <https://doi.org/10.1016/j.biortech.2013.12.084> (2014).
23. Lee, Y., Ryu, C., Park, Y. K., Jung, J. H. & Hyun, S. Characteristics of biochar produced from slow pyrolysis of Geodae-Uksae 1. *Bioresour. Technol.* **130**, 345–350. <https://doi.org/10.1016/j.biortech.2012.12.012> (2013).
24. Garg, R., Anand, N. & Kumar, D. Pyrolysis of babool seeds (*Acacia nilotica*) in a fixed bed reactor and bio-oil characterization. *Renew. Energy* **96**, 167–171. <https://doi.org/10.1016/j.renene.2016.04.059> (2016).
25. Imam, T. & Capareda, S. Characterization of bio-oil, syn-gas and bio-char from switchgrass pyrolysis at various temperatures. *J. Anal. Appl. Pyrolysis* **93**, 170–177. <https://doi.org/10.1016/j.jaap.2011.11.010> (2012).
26. Vulli, V. & Singh, R. K. Production of bio-oil from de-oiled cakes by thermal pyrolysis. *Fuel* **96**, 579–585. <https://doi.org/10.1016/j.fuel.2012.01.016> (2012).
27. Lee, M. K., Tsai, W. T., Tsai, Y. L. & Lin, S. H. Pyrolysis of napier grass in an induction-heating reactor. *J. Anal. Appl. Pyrolysis* **88**(2), 110–116. <https://doi.org/10.1016/j.jaap.2010.03.003> (2010).
28. Pütün, A. E., Uzun, B. B., Apaydin, E. & Pütün, E. Bio-oil from olive oil industry wastes: Pyrolysis of olive residue under different conditions. *Fuel Process. Technol.* **87**(1), 25–32. <https://doi.org/10.1016/j.fuproc.2005.04.003> (2005).
29. Puy, N. *et al.* Valorisation of forestry waste by pyrolysis in an auger reactor. *Waste Manag.* **31**(6), 1339–1349. <https://doi.org/10.1016/j.wasman.2011.01.020> (2011).
30. Shikha, F. S., Rahman, M. M., Sultana, N., Mottalib, M. A. & Yasmin, M. Effects of biochar and biofertilizer on groundnut production: A perspective for environmental sustainability in Bangladesh. *Carbon Res.* **2**(1), 10. <https://doi.org/10.1007/s44246-023-00043-7> (2023).
31. Carrasco, J. L. *et al.* Pyrolysis of forest residues: An approach to techno-economics for bio-fuel production. *Fuel* **193**, 477–484. <https://doi.org/10.1016/j.fuel.2016.12.063> (2017).
32. Amutio, M. *et al.* Flash pyrolysis of forestry residues from the Portuguese Central Inland Region within the framework of the BioREFINA-Ter project. *Bioresour. Technol.* **129**, 512–518. <https://doi.org/10.1016/j.biortech.2012.11.114> (2013).
33. Charon, N. *et al.* Multi-technique characterization of fast pyrolysis oils. *J. Anal. Appl. Pyrolysis* **116**, 18–26. <https://doi.org/10.1016/j.jaap.2015.10.012> (2015).
34. Schellekens, J. *et al.* Molecular characterization of biochar from five Brazilian agricultural residues obtained at different charring temperatures. *J. Anal. Appl. Pyrolysis* **130**, 106–117. <https://doi.org/10.1016/j.jaap.2018.01.020> (2018).
35. Papari, S. & Hawboldt, K. A review on condensing system for biomass pyrolysis process. *Fuel Process. Technol.* **180**, 1–13. <https://doi.org/10.1016/j.fuproc.2018.08.001> (2018).
36. Hu, Y., Stevens, D. M., Man, S., Crist, R. M. & Clogston, J. D. Total drug quantification in prodrugs using an automated elemental analyzer. *Drug Deliv. Transl. Res.* **9**, 1057–1066. <https://doi.org/10.1007/s13346-019-00649-8> (2019).
37. Oyedun, A. O., Tee, C. Z., Hanson, S. & Hui, C. W. Thermogravimetric analysis of the pyrolysis characteristics and kinetics of plastics and biomass blends. *Fuel Process. Technol.* **128**, 471–481. <https://doi.org/10.1016/j.fuproc.2014.08.010> (2014).
38. Coates, J. Interpretation of infrared spectra, a practical approach. *Encycl. Anal. Chem.* **12**, 10815–10837 (2000).
39. McKendry, P. Energy production from biomass (part 1): Overview of biomass. *Bioresour. Technol.* **83**(1), 37–46. [https://doi.org/10.1016/S0960-8524\(01\)00118-3](https://doi.org/10.1016/S0960-8524(01)00118-3) (2022).
40. Sowmya Dhanalakshmi, C. *et al.* Flash pyrolysis experiment on albizia odoratissima biomass under different operating conditions: A comparative study on bio-oil, biochar, and noncondensable gas products. *J. Chem.* <https://doi.org/10.1155/2022/9084029> (2022).
41. Rahman, M. M. Test and performance optimization of nozzle inclination angle and swirl combustor in a low-tar biomass gasifier: A biomass power generation system perspective. *Carbon Resour. Convers.* **5**(2), 139–149. <https://doi.org/10.1016/j.crccon.2022.01.002> (2022).
42. Gray, M. R., Corcoran, W. H. & Gavalas, G. R. Pyrolysis of a wood-derived material. Effects of moisture and ash content. *Ind. Eng. Chem. Process Des. Dev.* **24**(3), 646–651. <https://doi.org/10.1021/i200030a020> (1985).
43. Yildiz, G. *et al.* Effect of biomass ash in catalytic fast pyrolysis of pine wood. *Appl. Catal. B.* **168**, 203–211. <https://doi.org/10.1016/j.apcatb.2014.12.044> (2015).
44. Dwivedi, K. K., Karmakar, M. K. & Chatterjee, P. K. Thermal degradation, characterization and kinetic modeling of different particle size coal through TGA. *Therm. Sci. Eng. Prog.* **18**(100523), 2020. <https://doi.org/10.1016/j.tsep.2020.100523> (2020).
45. Leng, E. *et al.* A comprehensive review on lignin pyrolysis: Mechanism, modeling and the effects of inherent metals in biomass. *Fuel* **309**, 122102. <https://doi.org/10.1016/j.fuel.2021.122102> (2022).
46. Liew, R. K. *et al.* Oil palm waste: An abundant and promising feedstock for microwave pyrolysis conversion into good quality biochar with potential multi-applications. *Process. Saf. Environ. Prot.* **115**, 57–69. <https://doi.org/10.1016/j.psep.2017.10.005> (2018).
47. Mishra, R. K. & Mohanty, K. Pyrolysis kinetics and thermal behavior of waste sawdust biomass using thermogravimetric analysis. *Bioresour. Technol.* **251**, 63–74. <https://doi.org/10.1016/j.biortech.2017.12.029> (2018).
48. Chintala, V., Kumar, S., Pandey, J. K., Sharma, A. K. & Kumar, S. Solar thermal pyrolysis of non-edible seeds to biofuels and their feasibility assessment. *Energy Convers. Manag.* **153**, 482–492. <https://doi.org/10.1016/j.enconman.2017.10.029> (2017).
49. Kaushik, V. S., Dhanalakshmi, C. S., Madhu, P. & Tamilselvam, P. Co-pyrolysis of neem wood bark and low-density polyethylene: Influence of plastic on pyrolysis product distribution and bio-oil characterization. *Environ. Sci. Pollut. Res.* **29**(58), 88213–88223. <https://doi.org/10.1007/s11356-022-21746-1> (2022).
50. Horne, P. A. & Williams, P. T. Influence of temperature on the products from the flash pyrolysis of biomass. *Fuel* **75**(9), 1051–1059. [https://doi.org/10.1016/0016-2361\(96\)00081-6](https://doi.org/10.1016/0016-2361(96)00081-6) (1996).
51. Chutia, R. S., Kataki, R. & Bhaskar, T. Characterization of liquid and solid product from pyrolysis of *Pongamia glabra* deoiled cake. *Bioresour. Technol.* **165**, 336–342. <https://doi.org/10.1016/j.biortech.2014.03.118> (2014).

52. Maulinda, L. *et al.* The influence of pyrolysis time and temperature on the composition and properties of bio-oil prepared from tanjong leaves (*Mimusops elengi*). *Sustainability* **15**(18), 13851. <https://doi.org/10.3390/su151813851> (2023).
53. Sipilä, K., Kuoppala, E., Fagernäs, L. & Oasmaa, A. Characterization of biomass-based flash pyrolysis oils. *Biomass Bioenergy* **14**(2), 103–113. [https://doi.org/10.1016/S0961-9534\(97\)10024-1](https://doi.org/10.1016/S0961-9534(97)10024-1) (1998).
54. Kumar, M., Upadhyay, S. N. & Mishra, P. K. Pyrolysis of sugarcane (*Saccharum officinarum* L.) leaves and characterization of products. *ACS Omega* **7**(32), 28052–28064. <https://doi.org/10.1021/acsomega.2c02076> (2022).
55. Suintivarakorn, R., Treedet, W., Singbua, P. & Teeramaetawat, N. Fast pyrolysis from Napier grass for pyrolysis oil production by using circulating Fluidized Bed Reactor: Improvement of pyrolysis system and production cost. *Energy Rep.* **4**, 565–575. <https://doi.org/10.1016/j.egy.2018.08.004> (2018).
56. Islam, M. N., Beg, M. R. A. & Islam, M. R. Pyrolytic oil from fixed bed pyrolysis of municipal solid waste and its characterization. *Renew. Energy* **30**(3), 413–420. <https://doi.org/10.1016/j.renene.2004.05.002> (2005).
57. Bhattacharjee, N. & Biswas, A. B. Pyrolysis of orange bagasse: Comparative study and parametric influence on the product yield and their characterization. *J. Environ. Chem. Eng.* **7**(1), 102903. <https://doi.org/10.1016/j.jece.2019.102903> (2019).
58. Biradar, C. H., Subramanian, K. A. & Dastidar, M. G. Production and fuel quality upgradation of pyrolytic bio-oil from *Jatropha Curcas* de-oiled seed cake. *Fuel* **119**, 81–89. <https://doi.org/10.1016/j.fuel.2013.11.035> (2014).
59. Mulimani, H. V. & Navindgi, M. C. Production and characterization of bio-oil by pyrolysis of Mahua de-oiled seed cake. *Chem. Sel.* **3**(4), 1102–1107. <https://doi.org/10.1002/slct.201702198> (2018).
60. Lu, Q., Li, W. Z. & Zhu, X. F. Overview of fuel properties of biomass fast pyrolysis oils. *Energy Convers. Manag.* **50**(5), 1376–1383. <https://doi.org/10.1016/j.enconman.2009.01.001> (2009).
61. Saidi, M. *et al.* Upgrading of lignin-derived bio-oils by catalytic hydrodeoxygenation. *Energy Environ. Sci.* **7**(1), 103–129. <https://doi.org/10.1039/C3EE43081B> (2014).
62. Wu, W. *et al.* Chemical characterization of rice straw-derived biochar for soil amendment. *Biomass Bioenergy* **47**, 268–276. <https://doi.org/10.1016/j.biombioe.2012.09.034> (2012).
63. Kan, T., Strezov, V. & Evans, T. J. Lignocellulosic biomass pyrolysis: A review of product properties and effects of pyrolysis parameters. *Renew. Sustain. Energy Rev.* **57**, 1126–1140. <https://doi.org/10.1016/j.rser.2015.12.185> (2016).
64. Stefanidis, S. D. *et al.* A study of lignocellulosic biomass pyrolysis via the pyrolysis of cellulose, hemicellulose and lignin. *J. Anal. Appl. Pyrolysis* **105**, 143–150. <https://doi.org/10.1016/j.jaap.2013.10.013> (2014).
65. Yang, H. *et al.* Hemicellulose pyrolysis mechanism based on functional group evolutions by two-dimensional perturbation correlation infrared spectroscopy. *Fuel* **267**, 117302. <https://doi.org/10.1016/j.fuel.2020.117302> (2020).
66. Yao, Y. *et al.* Biochar derived from anaerobically digested sugar beet tailings: Characterization and phosphate removal potential. *Bioresour. Technol.* **102**(10), 6273–6278. <https://doi.org/10.1016/j.biortech.2011.03.006> (2011).
67. Brodowski, S., Amelung, W., Haumaier, L., Abetz, C. & Zech, W. Morphological and chemical properties of black carbon in physical soil fractions as revealed by scanning electron microscopy and energy-dispersive X-ray spectroscopy. *Geoderma* **128**(1–2), 116–129. <https://doi.org/10.1016/j.geoderma.2004.12.019> (2005).
68. Bian, R. *et al.* Pyrolysis of crop residues in a mobile bench-scale pyrolyser: product characterization and environmental performance. *J. Anal. Appl. Pyrolysis* **119**, 52–59. <https://doi.org/10.1016/j.jaap.2016.03.018> (2016).
69. Quan, C., Xu, S., An, Y. & Liu, X. Co-pyrolysis of biomass and coal blend by TG and in a free fall reactor. *J. Therm. Anal. Calorim.* **117**, 817–823. <https://doi.org/10.1007/s10973-014-3774-7> (2014).
70. Sowmya Dhanalakshmi, C. & Madhu, P. Biofuel production of neem wood bark (*Azadirachta indica*) through flash pyrolysis in a fluidized bed reactor and its chromatographic characterization. *Energy Sources Part A.* **43**(4), 428–443. <https://doi.org/10.1080/15567036.2019.1624893> (2021).
71. Tinwala, F., Mohanty, P., Parmar, S., Patel, A. & Pant, K. K. Intermediate pyrolysis of agro-industrial biomasses in bench-scale pyrolyser: Product yields and its characterization. *Bioresour. Technol.* **188**, 258–264. <https://doi.org/10.1016/j.biortech.2015.02.006> (2015).
72. Negahdar, L. *et al.* Characterization and comparison of fast pyrolysis bio-oils from pinewood, rapeseed cake, and wheat straw using ¹³C NMR and comprehensive GC×GC. *ACS Sustain. Chem. Eng.* **4**(9), 4974–4985. <https://doi.org/10.1021/acssuschemeng.6b01329> (2016).
73. Li, F., Srivatsa, S. C. & Bhattacharya, S. A review on catalytic pyrolysis of microalgae to high-quality bio-oil with low oxygenous and nitrogenous compounds. *Renew. Sustain. Energy Rev.* **108**, 481–497. <https://doi.org/10.1016/j.rser.2019.03.026> (2019).

Author contributions

S.T., C.S.D. and J.I.J.R.L. designed the project. R.K. and V.S. supervised. M.K.T. and P.S. conceptualized the study, L.P.M. and L.R. prepared the draft.

Competing interests

The authors declare no competing interests.

Additional information

Correspondence and requests for materials should be addressed to J.I.J.L.

Reprints and permissions information is available at www.nature.com/reprints.

Publisher's note Springer Nature remains neutral with regard to jurisdictional claims in published maps and institutional affiliations.



Open Access This article is licensed under a Creative Commons Attribution 4.0 International License, which permits use, sharing, adaptation, distribution and reproduction in any medium or format, as long as you give appropriate credit to the original author(s) and the source, provide a link to the Creative Commons licence, and indicate if changes were made. The images or other third party material in this article are included in the article's Creative Commons licence, unless indicated otherwise in a credit line to the material. If material is not included in the article's Creative Commons licence and your intended use is not permitted by statutory regulation or exceeds the permitted use, you will need to obtain permission directly from the copyright holder. To view a copy of this licence, visit <http://creativecommons.org/licenses/by/4.0/>.

© The Author(s) 2024



1 of 1

[Download](#) [Print](#) [Save to PDF](#) [Save to list](#) [Create bibliography](#)*Journal of the Balkan Tribological Association* • Volume 30, Issue 2, Pages 192 - 207 • 2024**Document type**

Article

Source type

Journal

ISSN

13104772

[View more](#)

LINEAR REGRESSION AND ARTIFICIAL NEURAL NETWORK-BASED WEAR PERFORMANCE PREDICTION OF AL 7050 ALLOY REINFORCED BY NANOPARTICLES OF WOLFRAM CARBIDE

[Kumar Sahu S.^a](#) ; [Priyadharshini V.J.^b](#); [Kola R.^c](#); [Tukaram Tale V.^d](#); [Prabakaran S.^e](#); [Rajendiran M.^f](#)
 [Save all to author list](#)^a Department of Mechanical Engineering, Veer Surendra Sai University of Technology, Odisha, Burla, India^b Department of Physics, Mailam Engineering College, Villupuram, Tamil Nadu, Tindivanam, India^c Department of Chemistry, Chaitanya Bharathi Institute of Technology (A), Gandipet, Telangana, Hyderabad, India^d Department of Mechanical Engineering, JSPMS Rajarshi Shahu College of Engineering, Maharashtra, Pune, India[View additional affiliations](#) [Full text options](#) [Export](#) **Abstract**

Author keywords

Sustainable Development Goals

SciVal Topics

Metrics

Abstract

This study investigates into the wear performance of the Al 7050 alloy, which can be enhanced by adding WC nanoparticles as reinforcement. Friction force and wear resistance are important parameters in materials science and engineering, which need to be considered. Through an analysis of the effects of nanoparticle reinforcement, this study aims to address these significant issues. Wear tests were used to assess how the material behaved under different circumstances, and the Al 7050 alloy's wear resistance was significantly increased, when WC nanoparticles were added. This reinforcement not only extends the lifetime of mechanical components but it also helps to achieve the broader goal of creating sustainable engineering solutions. Optimization, which was guided by the Taguchi-based design of experiments and had the dual goals of reducing frictional force (Fr) and specific wear rate (Swr), was

Cited by 0 documents

Inform me when this document is cited in Scopus:

[Set citation alert >](#)**Related documents**

Recognition and Optimization of Wear Behaviour of Al 6081 with Polymeric Nanocomposites Using Machine Learning

Kumar, J. , Pawar, S.R. , Ashish (2023) *Proceedings of the 4th International Conference on Smart Electronics and Communication, ICOSEC 2023*Wear Behavior of Glass Fiber Reinforced Composite with Nanoparticles of Al₂O₃ through Artificial Neural NetworkKhan, M.A.A. , Anitha, D. , Balguri, P.K. (2024) *AIP Conference Proceedings*

An Advanced Machine Learning Based Wear Optimization of Nano Particles Reinforced with High Strength Metal Matrix Composite

Chinthamu, N. , Coumaressin, T. , Lal, B. (2023) *Proceedings of the 4th International Conference on Smart Electronics and Communication, ICOSEC 2023*[View all related documents based on references](#)

Find more related documents in Scopus based on:

[Authors >](#) [Keywords >](#)

a significant part of the study. It was demonstrated by the very encouraging results, that an appropriate set of optimal parameters can significantly reduce wear and friction, which can improve engineering applications. Additionally, machine learning techniques—more specifically, ANNs and linear regression—were applied to forecast Swr and Fr. These models provided a data-driven approach to material reaction prediction without a great deal of testing. The artificial neural network (ANN) model exhibited remarkable overall accuracy of 85.81%, indicating its capacity to offer accurate and efficient techniques for the estimation of wear and friction properties. Altogether, this work validates the potential of Al 7050/WC composites to increase wear resistance and to reduce friction, and it marks a major advancement in materials science and engineering technology. The optimization of input parameters and the use of machine learning models can be very beneficial for researchers and engineers. These techniques provide more reliable, efficient, and sustainable engineering solutions for a range of industries. © 2024, Scibulcom Ltd.. All rights reserved.

Author keywords

Artificial Neural Network; linear regression; optimization; weanalysis; wear prediction

Sustainable Development Goals  

SciVal Topics  

Metrics 

References (12)

[View in search results format >](#)

All

[BibTeX export](#)   [Print](#)  [E-mail](#)  [Save to PDF](#)

[Create bibliography](#)

- 1 Shanmugapriya, Sivamaran, V., Padma Rao, A., Senthil Kumar, P., Selvamani, S.T., Mandal, T.K.

Sol-gel derived Al₂O₃/Gr/HAP nanocomposite coatings on Ti-6Al-4V alloy for enhancing tribo-mech properties and antibacterial activity for bone implants

(2022) *Applied Physics A: Materials Science and Processing*, 128 (8), art. no. 635. Cited 13 times.

<http://www.springer.com/materials/journal/339>

doi: 10.1007/s00339-022-05784-7

[View at Publisher](#)

-
- 2 López-Ojeda, L., Vargas-Gutiérrez, G.

High wear resistance and better pitting corrosion resistance of AISI 316L stainless steel by a self-protective oxy-nitrocarburizing paste ([Open Access](#))

(2022) *Journal of Materials Research and Technology*, 16, pp. 1803-1813. Cited 5 times.

<http://www.elsevier.com/journals/journal-of-materials-research-and-technology/2238-7854>

doi: 10.1016/j.jmrt.2021.12.118

[View at Publisher](#)

- 3 Sardar, S., Karmakar, S.K., Das, D.
High stress abrasive wear characteristics of Al 7075 alloy and 7075/Al₂O₃ composite
(2018) *Measurement: Journal of the International Measurement Confederation*, 127, pp. 42-62. Cited 64 times.
doi: 10.1016/j.measurement.2018.05.090
View at Publisher
-
- 4 Naik, P., Acharya, S.K., Sahoo, P., Pradhan, S.
Abrasive wear behaviour of orange peel (biowaste) particulate reinforced polymer composites
(2021) *Proceedings of the Institution of Mechanical Engineers, Part J: Journal of Engineering Tribology*, 235 (10), pp. 2099-2109. Cited 21 times.
<http://pij.sagepub.com/content/by/year>
doi: 10.1177/1350650121991412
View at Publisher
-
- 5 Ikubanni, P.P., Oki, M., Adeleke, A.A., Agboola, O.O.
Optimization of the tribological properties of hybrid reinforced aluminium matrix composites using Taguchi and Grey's relational analysis
(2021) *Scientific African*, 12, art. no. e00839. Cited 34 times.
<https://www.journals.elsevier.com/scientific-african>
doi: 10.1016/j.sciaf.2021.e00839
View at Publisher
-
- 6 ZHANG, X.-M., CHEN, Z.-Y., LUO, H.-F., ZHOU, T., ZHAO, Y.-L., LING, Z.-C.
Corrosion resistances of metallic materials in environments containing chloride ions: A review
(2022) *Transactions of Nonferrous Metals Society of China (English Edition)*, 32 (2), pp. 377-410. Cited 80 times.
<https://www.journals.elsevier.com/transactions-of-nonferrous-metals-society-of-china>
doi: 10.1016/S1003-6326(22)65802-3
View at Publisher
-
- 7 Hanish Anand, S., Venkateshwaran, N., Sai Prasanna Kumar, J.V., Kumar, D., Ramesh Kumar, C., Maridurai, T.
Optimization of Aging, Coating Temperature and Reinforcement Ratio on Biosilica Toughened in-situ Al-TiB₂ Metal Matrix Composite: a Taguchi Grey Relational Approach (Open Access)
(2022) *Silicon*, 14 (8), pp. 4337-4347. Cited 18 times.
http://www.springer.com/chemistry/inorganic/journal/12633?cm_mmc=AD-_-Journal-_-PSE10941_V1-_-12633
doi: 10.1007/s12633-021-01232-y
View at Publisher

- 8 Banerjee, T., Dey, S., Sekhar, A.P., Datta, S., Das, D.
Design of Alumina Reinforced Aluminium Alloy Composites with Improved Tribo-Mechanical Properties: A Machine Learning Approach

(2020) *Transactions of the Indian Institute of Metals*, 73 (12), pp. 3059-3069. Cited 31 times.
<http://www.springerlink.com/content/121470/>
doi: 10.1007/s12666-020-02108-2

View at Publisher
-
- 9 Panneerselvam, T., Kandavel, T.K., Kishore, P.
Experimental Investigation on Cutting Tool Performance of Newly Synthesized P/M Alloy Steel Under Turning Operation

(2019) *Arabian Journal for Science and Engineering*, 44 (6), pp. 5801-5809. Cited 28 times.
<https://link.springer.com/journal/13369>
doi: 10.1007/s13369-019-03763-4

View at Publisher
-
- 10 Kishore, P., Kumar, P.M., Dinesh, D.
Wear analysis of Al 5052 alloy with varying percentage of tungsten carbide

(2019) *AIP Conference Proceedings*, 2128, art. no. 040003. Cited 73 times.
<http://scitation.aip.org/content/aip/proceeding/aipcp>
ISBN: 978-073541870-7
doi: 10.1063/1.5117965

View at Publisher
-
- 11 Canakci, A., Ozsahin, S., Varol, T.
Prediction of Effect of Reinforcement Size and Volume Fraction on the Abrasive Wear Behavior of AA2014/B₄C_p MMC_s Using Artificial Neural Network

(2014) *Arabian Journal for Science and Engineering*, 39 (8), pp. 6351-6361. Cited 67 times.
<https://link.springer.com/journal/13369>
doi: 10.1007/s13369-014-1157-9

View at Publisher
-
- 12 Pramod, R., Veeresh Kumar, G.B., Gouda, P.S.S., Mathew, A.T.
A Study on the Al₂O₃ reinforced Al7075 Metal Matrix Composites Wear behavior using Artificial Neural Networks (Open Access)

(2018) *Materials Today: Proceedings*, Part 2 5 (5), pp. 11376-11385. Cited 51 times.
<https://www.sciencedirect.com/journal/materials-today-proceedings>
doi: 10.1016/j.matpr.2018.02.105

View at Publisher

About Scopus

[What is Scopus](#)

[Content coverage](#)

[Scopus blog](#)

[Scopus API](#)

[Privacy matters](#)

Language

[日本語版を表示する](#)

[查看简体中文版本](#)

[查看繁體中文版本](#)

[Просмотр версии на русском языке](#)

Customer Service

[Help](#)

[Tutorials](#)

[Contact us](#)

ELSEVIER

[Terms and conditions](#) ↗ [Privacy policy](#) ↗ [Cookies settings](#)

All content on this site: Copyright © 2025 Elsevier B.V. ↗, its licensors, and contributors. All rights are reserved, including those for text and data mining, AI training, and similar technologies. For all open access content, the relevant licensing terms apply.

We use cookies to help provide and enhance our service and tailor content. By continuing, you agree to the use of cookies ↗.



Influence of Nb⁵⁺ and La³⁺ ions on physical properties of the quaternary TeO₂-ZnO-Nb₂O₅-La₂O₃ glass system

V. Kamalaker^a, N. Chanakya^b, J. Hema Madhuri^b, N. Jahangeer^c, M. Maheshwar Reddy^c, Ch. Ramesh^d, P. Muralikrishna^e, G. Upender^b  

[Show more](#) 

 Share  Cite

<https://doi.org/10.1016/j.ceramint.2024.07.463> 

[Get rights and content](#) 

Abstract

Quaternary based tellurite glasses in the composition 75TeO₂-10ZnO-(15-x)Nb₂O₅-xLa₂O₃ (0 ≤ x ≤ 9 mol%) were synthesized through the melt-quenching method. X-ray diffraction (XRD), Energy dispersive X-ray (EDX) alongside color mapping images, X-ray photoelectron spectroscopy (XPS), Fourier transform infrared (FTIR), Raman, Differential scanning calorimetry (DSC), UV-Vis absorption and DC conductivity studies were carried out to comprehend the influence of both Nb⁵⁺ and La³⁺ ions on the structural dependent properties of the glasses. Both XRD and DSC patterns have affirmed the amorphous nature of all the glasses. XPS studies asserted the stable oxidation states of all the constituent elements of the glasses. The Raman and FTIR analyses emphasized that the TZNL glasses are comprised of TeO₃, TeO₃₊₁, TeO₄ and NbO₆ units. The DSC analysis disclosed that the inclusion of La₂O₃ content in the place of Nb₂O₅ has improved the thermal stability (ΔT) of the glasses and also prevented the crystallization. DSC studies affirmed that these glasses have exhibited higher thermal stability, suggesting that these glasses might be useful for optoelectronic devices and optical fiber drawing applications. The optical band gap (E_{opt}) and Urbach energy (ΔE) of these glasses were observed to be non-linearly varied with the addition of La₂O₃ content. DC conductivity (σ) was observed to be decreased and the activation energy (E_{act}) was found to be increased with increasing La₂O₃ content.

Introduction

In the modern world of science and technology, the tellurite (TeO₂) glasses have drawn the wide attention due to their high refractive indexes ($n > 2.0$), high infrared transmittance including in the near IR region of the spectrum (0.35–6 μm) [1,2], low phonon energy and high chemical durability [3], the possibility of varying the compositions of the glass within wide limits, and higher solubility of the cations of rare-earth elements in comparison to B₂O₃, P₂O₅ and SiO₂ glasses. These characteristics of TeO₂ based glasses have rendered them promising candidates for optical fiber, lasers and optical amplifier devices [4]. The main drawback of TeO₂ glasses is the low glass transition temperature (T_g) of 290 °C which prevents its usage in suitable applications. This can be partially eliminated by adding the high-melting oxides, like ZnO, Nb₂O₅ and WO₃ etc. to TeO₂ [5,6]. Hence, several attempts were made to improve T_g of TeO₂ based glasses. Importantly, TeO₂-ZnO glasses have been extensively investigated for their technological importance by reducing the optical band gap, and raising the refractive index [7]. Also, it was found that the inclusion of Nb₂O₅ to TeO₂ based glasses makes the glass to improve the vitrification and to increase the refractive index [8]. In the literature, the numerous spectroscopic investigations have been reported on TeO₂-Bi₂O₃-ZnO, TeO₂-Nb₂O₅-Bi₂O₃, and TeO₂-TiO₂-Nb₂O₅ glasses [[9], [10], [11]].

Importantly, La₂O₃ containing glasses have drawn the attention of researchers because of their significant usage as electrical, luminescent and laser materials. As compared with Li⁺, Na⁺, K⁺ and Mg²⁺, Ca²⁺, Sr²⁺, Ba²⁺ ions etc., rare-earth (RE) ions with higher cationic field strengths [12] can effectively suppress the devitrification of the glass and also increase the glass transition temperature (T_g) as well as the chemical stability [13]. Therefore, the RE ions are widely introduced to improve the properties of the glass, among which La₂O₃ is the most common RE oxide. The incorporation of La³⁺ ions into TeO₂ based glass network

increased the optical band gap (E_{opt}) and reduced the refractive index (n) [14]. On contrary, for ZnO-B₂O₃ [15] and B₂O₃-CoO [16] glasses, it was found that the addition of La₂O₃ reduced the ' E_{opt} ' and increased the ' n '.

In view of the above, we made an investigation in the present glass system TeO₂-ZnO-Nb₂O₅-La₂O₃ to increase T_g and to modify the optical properties like optical band gap (E_{opt}) and refractive index (n) by varying heavy metal oxide La₂O₃ in the place of Nb₂O₅. The inclusion of these oxides to TeO₂-ZnO composition might provide a new glass system that might exhibit high thermal stability and chemical resistance as compared with other well-known TeO₂ glasses. Furthermore, the incorporation of heavy metal oxides like Nb₂O₅ and La₂O₃ could suppress the tendency of the glass towards the crystallization thereby enhances the thermal stability of these glasses.

Hitherto there is no particular investigations were carried out on TeO₂-ZnO-Nb₂O₅-La₂O₃ glass system and also the correlation between the physical and spectroscopic properties of these glasses. For this reason, we found it is interesting to carry out the influence of La₂O₃ on the structural, thermal, optical and electrical properties of niobium zinc tellurite glasses.

Section snippets

Experimental methods

The glasses with composition 75TeO₂-10ZnO-(15-x)Nb₂O₅-xLa₂O₃ (x=0, 3, 5, 7 and 9mol%) were prepared by the melt quenching.

The detailed compositions of the prepared samples together with their codes are given below. TZNL1:

75TeO₂-10ZnO-15Nb₂O₅ TZNL2: 75TeO₂-10ZnO-12Nb₂O₅-3La₂O₃ TZNL3: 75TeO₂-10ZnO-10Nb₂O₅-5La₂O₃ TZNL4:

75TeO₂-10ZnO-8Nb₂O₅-7La₂O₃ TZNL5: 75TeO₂-10ZnO-6Nb₂O₅-9La₂O₃

All the chemicals purchased from Sigma-Aldrich with 99.9% purity were used for the sample preparation. The details of ...

X-ray diffraction

Fig. 1 clearly demonstrates the crystal free XRD patterns of TZNL1, TZNL3 and TZNL5 glasses since these exhibited a characteristic broad hump in between 20 and 30° for 2θ, arguably indicating the vitreous nature of the understudied glasses. The observed patterns were found to be consistent with the previous literature [17,18]. ...

Energy dispersive X-ray spectra (EDX)

Recording EDX spectra is of essence to verify the purity of the chemical composition of the prepared glasses and it is illustrated in Fig. 2a-c for a typical TZNL1, TZNL3 ...

Conclusions

New and transparent tellurite glasses with composition 75TeO₂-10ZnO-(15-x)Nb₂O₅-xLa₂O₃ (x=0, 3, 5, 7 and 9mol%) were prepared by the melt quenching. The measured BEs verified that TZNL glasses explicitly contain Te, Zn, Nb, La, and O elements along with their most stable oxidization states. FTIR and Raman analysis clearly suggests the progressive formation of TeO₃₊₁/TeO₃ units at the expense of TeO₄ units with increasing La₂O₃ content. The structural alterations resulting from the formation ...

CRedit authorship contribution statement

V. Kamalaker: Writing – original draft, Methodology, Conceptualization. **N. Chanakya:** Writing – original draft, Software, Formal analysis, Data curation. **J. Hema Madhuri:** Validation, Project administration, Investigation, Formal analysis. **N. Jahangeer:** Resources, Data curation. **M. Maheshwar Reddy:** Resources, Validation. **Ch. Ramesh:** Formal analysis, Data curation. **P. Muralikrishna:** Resources, Data curation. **G. Upender:** Writing – review & editing, Supervision. ...

Declaration of competing interest

All the authors are hereby declare that there are no conflicts of interest to declare and all the authors are hereby consented to publish this data in your esteemed journal because of its renowned reputation in the field of spectroscopic properties of amorphous materials. ...

References (49)

J. Hrabovsky *et al.*

[Optical, magneto-optical properties and fiber-drawing ability of tellurite glasses in the TeO₂-ZnO-BaO ternary system](#)

J. Non-Cryst. Solids (2024)

Melek Fidan *et al.*

[Optical, structural, physical, and nuclear shielding properties, and albedo parameters of TeO₂-BaO-B₂O₃-PbO-V₂O₅ glasses](#)

J. Phys. Chem. Solid. (2022)

Navaneetha Pujari *et al.*

[Effect of Li₂O content on structural and optical properties of Li₂O-TeO₂-As₂O₃-B₂O₃ glasses](#)

J. Phys. Chem. Solid. (2021)

N. Elkhoshkhany *et al.*

[Influence of Sm₂O₃ addition on Judd-Ofelt parameters, thermal and optical properties of the TeO₂-Li₂O-ZnO-Nb₂O₅ glass system](#)

Mater. Char. (2018)

H. Chen *et al.*

[Spectroscopic properties of Er³⁺ doped TeO₂-BaO \(Li₂O, Na₂O\)-La₂O₃ glasses for 1.5-μm optical amplifiers](#)

J. Non-Cryst. Solids (2005)

TieFeng Xu *et al.*

[Spectral properties and thermal stability of Er³⁺/Yb³⁺ codoped tungsten-tellurite glasses](#)

Opt. Mater. (2006)

N. Elkhoshkhany *et al.*

[Shimaa Shahin, Synthesis and optical properties of new fluoro-tellurite glass within \(TeO₂-ZnO-LiF-Nb₂O₅-NaF\) system](#)

J. Non-Cryst. Solids (2017)

N. Elkhoshkhany *et al.*

[Optical Properties of quaternary TeO₂-ZnO-Nb₂O₅-Gd₂O₃ glasses](#)

Ceram. Int. (2014)

E. Yousef *et al.*

[Effect of ZnO and Bi₂O₃ addition on linear and non-linear optical properties of tellurite glasses](#)

J. Non-Cryst. Solids (2007)

Yanling Wang *et al.*

[Physical properties and optical band gap of new tellurite glasses within the TeO₂-Nb₂O₅-Bi₂O₃ system](#)

Mater. Chem. Phys. (2009)



View more references

Cited by (1)

[Enhancement of topological network and yellow emission in Dy³⁺-doped tellurite glasses via Nb₂O₅ modification](#)

2025, Journal of Alloys and Compounds

[Show abstract](#) 

[View full text](#)

© 2024 Elsevier Ltd and Techna Group S.r.l. All rights are reserved, including those for text and data mining, AI training, and similar technologies.



All content on this site: Copyright © 2025 Elsevier B.V., its licensors, and contributors. All rights are reserved, including those for text and data mining, AI training, and similar technologies. For all open access content, the Creative Commons licensing terms apply.



Restoration of Magnetic Order in Heavy Metal Doped Spin Glass

S. Shanmukharao Samatham¹, Akhilesh Kumar Patel², Parul Khandelwal³, S. Shravan Kumar Reddy¹,
Gowrinaraidu Babbadi⁴, M. Chandra Sekhar¹, Muralikrishna Patwari⁵, and K. G. Suresh³

¹Department of Physics, Chaitanya Bharathi Institute of Technology, Gandipet, Hyderabad 500 075, India

²Research Centre for Magnetic and Spintronic Materials, National Institute for Materials Science, Tsukuba, Ibaraki 305 0047, Japan

³Magnetic Materials Laboratory, Department of Physics, Indian Institute of Technology Bombay, Powai, Mumbai 400 076, India

⁴Department of Physics, Government College (Autonomous), Rajahmundry 533 105, Andhra Pradesh, India

⁵Department of Chemistry, Chaitanya Bharathi Institute of Technology, Gandipet, Hyderabad 500 075, India

A systematic evolution of 4d-element triggered restoration of long-range magnetic order in a spin glass compound $\text{Mn}_{0.7}\text{Fe}_{0.3}\text{NiGe}$, $\text{Mn}_{0.7}\text{Fe}_{0.3-x}\text{Rh}_x\text{NiGe}$, will be reported in detail with the help of x-ray diffraction, bulk magnetization and ac-susceptibility measurements. The variation of lattice parameters, Mn-Mn bond lengths in the *ab*-plane and along *c*-direction with *x* will be determined by analysing the room temperature x-ray diffraction patterns, complying with Ni_2In -type hexagonal structure. In order to uncover the type of spin-glass behaviour, the frequency-dependent ac-susceptibility cusp and relative shift in the freezing temperature will be analysed. Sherrington-Kirkpatrick criterion will be employed to understand the magnetic correlations with increasing Rh concentration. Origin of ferromagnetism in $x = 0.3$, possible exhibition of exchange bias (field cooled or zero-field cooled) in spin glass compounds of the series will be examined. Additionally, the effect of hydrostatic pressure on the spin-glass compounds will be investigated with an intent to restore the ferromagnetism by affecting the Mn-Mn distance.

Index Terms—Magnetism, Heusler alloys, spin-glass, exchange bias, hydrostatic pressure

I. INTRODUCTION

RESTORATION OF hidden/masked/clustered long-range magnetic order, using non-thermal external perturbations is always a thought-provoking subject in condensed matter physics. Loss of magnetism in an alloy with constituent magnetic elements can be routed from the screening of spins by the conduction electrons, formation of clusters, deficit of exchange interaction strength, disordered spins due to thermal fluctuations, prevention of magnetic order due to large frustration parameter, correlated phase transition at the quantum critical point, etc. Such hidden, otherwise masked, magnetism may be restored with the help of external non-thermal perturbations such as magnetic field H , pressure p and substitution x . The tuning of atomic/magnetic interactions through chemical pressure (i.e., replacement of constituent element with a different magnetic/non-magnetic element), limited to the solvability level though, is a commonly practiced means.

Heusler alloys have continued to be on the frontline research for their multi-functional properties such as shape memory effect, large magnetocaloric effect, exchange bias, negative thermal expansion, spintronics, spin-filters etc. Some of these are reported to show complex magnetic behavior with various magnetic ground states such as ferromagnetic, antiferromagnetic, ferrimagnetic, coexistence of two magnetic phases, short-range order such as spinglass, magnetic glass and re-entrant spin glass. Though, many potential compounds have resulted from the interchanging of 3d-transition metals, recently heavy metal (Rh and Pt) based Heusler compounds have been reported to be a good fertile for the technological applications by showing large spontaneous exchange bias [1] and skyrmion characteristics [2].

Our present study aims to outline the evolution of struc-

tural transformation and long-range magnetic order with increase of Rh concentration for Fe in a spin glass compound $\text{Mn}_{0.7}\text{Fe}_{0.3}\text{NiGe}$ and manifestation of short-range magnetic correlations. Complete replacement of Fe by Rh resulted in a long-range ferromagnetism with a saturation magnetic moment of about $2.18 \mu_B/\text{f.u.}$

II. EXPERIMENTAL METHODS

Polycrystalline $\text{Mn}_{0.7}\text{Fe}_{0.3-x}\text{Rh}_x\text{NiGe}$ with nominal compositions of x ranging from 0 to 0.3 are prepared by arc melting the constituent elements (of at least 4N purity) in Argon gas flow-environment. Room temperature x-ray diffraction patterns are recorded on powder specimens using $\text{Cu-K}\alpha$ radiation. Magnetization as a function of temperature and magnetic field is measured using 70 kOe-SQUID-Vibrating Sample Magnetometer down to 2 K and in fields up to 70 kOe. The measurements were taken both in zero-field-cooled warming (ZFC) and field-cooled-warming (FCW) methods where ZFC and FCW carry their usual meaning.

III. RESULTS AND DISCUSSION

MnNiGe exhibits a martensitic transition from Ni_2In -hexagonal ($P6_3/mmc$) to TiNiSi -type orthorhombic ($Pnma$) structure below 470 K [3]. In addition, paramagnetic to antiferromagnetic (canted-spin structure) transition at 346 K (T_N^M) and to a ferromagnetic austenite transition (T_C^A) at 205 K are reported [4]. A large difference of about 140 K between T_N^M and T_C^A creates a room to tune the magnetic and structural properties of MnNiGe . Recent report by Liu *et al.* [5] reveals that the gradual replacement of Mn by Fe i.e., $\text{Mn}_{1-x}\text{Fe}_x\text{NiGe}$ helps to establish Ni_2In -type hexagonal structure down to 2 K and enhances the ferromagnetic interactions.

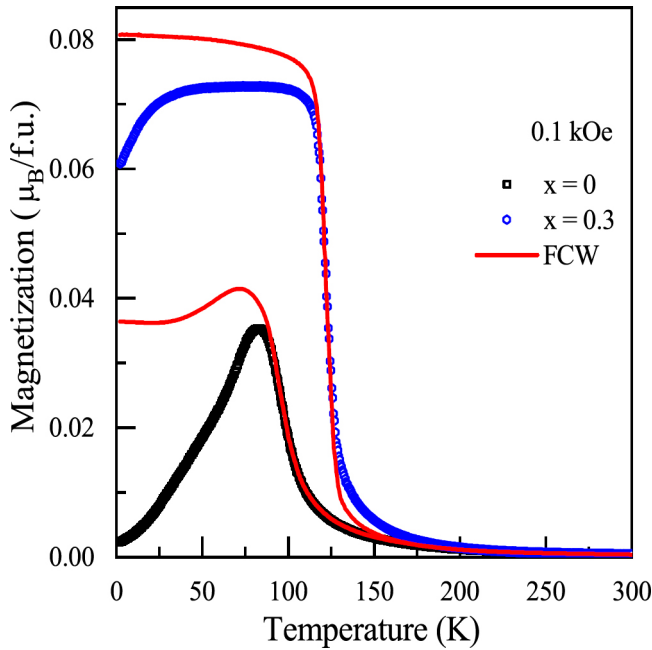


Fig. 1. ZFC (partly filled squares and circles) and FCW (continuous red line) $M-T$ of $\text{Mn}_{0.7}\text{Fe}_{0.3}\text{NiGe}$ ($x = 0$) and $\text{Mn}_{0.7}\text{Rh}_{0.3}\text{NiGe}$ ($x = 0.3$). $x = 0$: $M-T$ exhibits a peak around $T = 82.8$ K before falling sharply to an almost zero magnetization value, resembling a spin-glass-like behaviour. $x = 0.3$: $M-T$ shows a sharp rise below 120 K before reaching an almost temperature independent behavior, depicting a typical ferromagnetic behaviour.

Nevertheless, the competing magnetic interactions resulted in a spin-glass like state for the compositions above $x \sim 0.26$. Though earlier study reports ferromagnetism in $x = 0.3$ [6], a systematic evolution of magnetic interactions with increasing Rh concentration is unaccounted for in the literature.

Fig. 1 shows the temperature dependent ZFC and FCW magnetization curves of two end compositions of the series $\text{Mn}_{0.7}\text{Fe}_{0.3-x}\text{Rh}_x\text{NiGe}$ i.e., $x = 0$ and 0.3. $x = 0$ exhibits a peak at about 80 K and a down-turn of magnetization to an almost zero magnetic moment value along with a large bifurcation between ZFC and FCW. This behaviour resembles the spin-glass like nature. On the other hand, $x = 0.3$ exhibits a sharp rise below 120 K and saturation at low temperatures, indicating ferromagnetic behaviour. Fig. 2 shows the magnetization isotherms from 0 to 70 kOe measured at 2 K. $M-H$ shows non-saturating behavior for $x = 0$ as expected for spin-glass compounds while $x = 0.3$ exhibits saturation above 13 kOe, inferring to soft-ferromagnetic behaviour.

IV. SUMMARY

In the full paper, we discuss the systematic effect of heavy 4d-metal Rh substitution on the spin glass behavior of $\text{Mn}_{0.7}\text{Fe}_{0.3}\text{NiGe}$ using the combined results of x-ray diffraction, dc-magnetization and ac-susceptibility measurements. At room temperature, all the compounds are found to crystallize in Ni_2In -type hexagonal austenite structure. The austenite high-temperature paramagnetic to low-temperature spin-glass-like transition is observed for $x = 0, 0.1$ and 0.2. A long range ferromagnetic ordering is achieved upon complete replacement

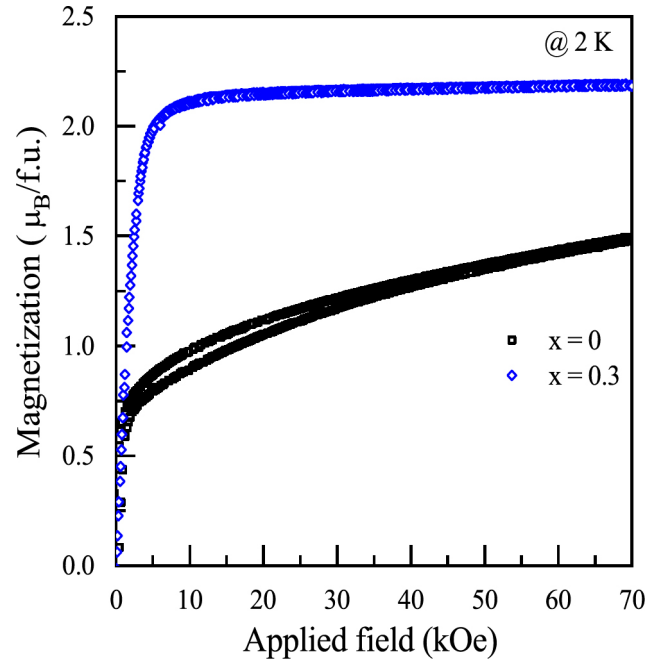


Fig. 2. $M-H$ isotherms at 2 K. $x = 0$: $M-H$ exhibits neither linear nor saturating nature even in an applied field of 70 kOe. Non-saturation along with hysteretic behaviour indicates spin-glass-like nature. $x = 0.3$: $M-H$ increases sharply and linearly up to a technical saturation magnetic field of about 13 kOe and attains magnetic saturation in higher fields.

of Fe by Rh. Importantly, the spin-glass compounds are expected to show spontaneous exchange bias i.e., in zero-field cooled mode, because of inherent competing interactions.

ACKNOWLEDGEMENT

SSS and MCS acknowledge the financial support from UGC-DAE CSR through a Collaborative Research Scheme (CRS) project number CRS/2022-23/01/712. AKP, PK and KGS acknowledge IRCC and Department of Physics for providing the magnetization (SVSM) facility.

REFERENCES

- [1] A. K. Nayak, M. Nicklas, S. C. adn Panchanana Khuntia, C. Shekhar, A. Kalache, M. Baenitz, Y. Skourski, V. K. Guduru, A. Puri, U. Zeitler, J. M. D. Coey, and C. Felser, "Design of compensated ferrimagnetic heusler alloys for giant tunable exchange bias." *Nature Mater*, vol. 4, p. 679684, 2015.
- [2] A. K. Nayak, V. Kumar, T. Ma, P. Werner, E. Pippel, R. Sahoo, F. Damay, U. K. Rossler, C. Felser, and S. S. P. Parkin, "Magnetic antiskyrmions above room temperature in tetragonal heusler materials." *Nature*, vol. 548, pp. 561–566, 2017.
- [3] H. Fjellvg and A. Andresen, "On the crystal structure and magnetic properties of mnnige," *Journal of Magnetism and Magnetic Materials*, vol. 50, no. 3, pp. 291–297, 1985.
- [4] W. Bazela, A. Szytua, J. Todorovi, Z. Tomkowicz, and A. Ziba, "Crystal and magnetic structure of nimnge," *physica status solidi (a)*, vol. 38, no. 2, pp. 721–729, 1976.
- [5] E. Liu, W. Wang, L. Feng, W. Zhu, G. Li, J. Chen, H. Zhang, G. Wu, C. Jiang, H. Xu, and F. de Boer, "Stable magnetostructural coupling with tunable magnetoresponsive effects in hexagonal ferromagnets." *Nat Commun*, vol. 3, p. 873, 2012.
- [6] S. S. Samatham, A. K. Patel, A. V. Lukoyanov, E. D. Baglasov, and K. G. Suresh, "Magnetism of 3d and 4d doped $\text{mn}_{0.7}\text{t}_{0.3}\text{ni}_{1-x}\text{ge}_x$ ($t = \text{fe, co, ru}$ and rh): bulk magnetization and ab initio calculations," *J. Phys.: Condens. Matter*, vol. 31, p. 495804, 2019.



Investigations on MWO_4 ($M = Cu, Zn, Cd$ and Sn) nanostructures for detecting toluene gas at room temperature

E. Praveen Kumar^a, N. Chanakya^a, Ayesha Siddiqua^a, Kurugundla Gopi Krishna^b,
B. Vijaya Kumar^c, P. Muralikrishna^d, G. Upender^{a,*}

^a Department of Physics, Osmania University, Hyderabad 500 001, Telangana State, India

^b Department of Physics, CMR Technical Campus, Medchal, Hyderabad 501 401, Telangana State, India

^c Department of Chemistry, Osmania University, Hyderabad 500 001, Telangana State, India

^d Department of Chemistry, Chaitanya Bharathi Institute of Technology, Hyderabad 500 075, India

ARTICLE INFO

Keywords:

Gas sensors
Semiconductors
Metal tungstates
SnWO₄
Toluene and chemoresistance

ABSTRACT

Constructing the room temperature (RT) based semiconductor gas sensors is pivotal for its commercialization. In this investigation, four well-known tungstate based CuWO₄, ZnWO₄, CdWO₄ and SnWO₄ nanomaterials were prepared by the hydrothermal method. These materials were characterized by XRD, FESEM, TEM, EDX, DFT, BET surface area, XPS, FTIR and UV-Vis DRS. The selectivity alongside the response of these compounds were tested by sensing gases like 1-butanol (C₄H₁₀O), acetone (C₃H₆O), ethanol (C₂H₆O), benzene (C₆H₆), toluene (C₆H₅CH₃) and xylene (C₈H₁₀). The gas sensing studies performed on these compounds conclusively disclose that these sensors have adequate sensitivity and response to detect the tested gases at RT. Among these compounds, owing to unique crystal structure α -SnWO₄ sensor exhibits an enormous selectivity with a response of 12.32 towards the detection of toluene and the detection limit is 5 ppm. Compared to the other compounds, SnWO₄ offers the shortest conducting pathways viz. O-Sn-O-Sn/O-W-O-W-O which facilitated the effective charge transport for sensing toluene gas at RT.

1. Introduction

An upsurge in the economic growth resulted from the rapid rate of industrialization have led to the extensive emission of toxic, flammable and volatile organic compounds (VOCs) like toluene, xylene, benzene, 1-butanol, ethanol and methanol etc. [1,2]. As a consequence, an imbalance occurs in the climate which is extremely harmful to the health of living beings. The VOCs are found to be used excessively in wood furniture, paints, varnishes, adhesives and cosmetics etc. [3]. Nevertheless, the prolonged exposure to the above-mentioned gases even at very low concentrations (ppm) may affect the vital internal organs and eventually causes various cancers [4,5]. Among VOCs, the toluene (up to 200 ppm) inhalation may cause skin irritation, lacrimation, irregular heartbeat, dementia, ataxia, insomnia and various neurologic deficits [6]. A short time exposure to the toluene above 200 ppm may cause drowsiness, headache, nausea, visual impairment and many more to quote and even a continuous exposure with a high ppm level may lead to death also [7]. Therefore, it is the most pressing requirement of the present time to detect this gas and warn the living beings in the

industries surroundings in order to reduce the threat from this gas. To detect these gases, the various techniques like gas chromatography, laser absorption spectroscopy and gas sensors were developed [8,9]. Nonetheless, the gas sensors based devices have been considered as promising to detect these gases because of its flexibility, inexpensive, light-weight, portable and less power consumption [10]. At present, the gas sensors based on semiconductor metal oxides (SMO) have been drawing the wide attention of researchers.

Tungstate based SMO's have potential applications in photoluminescence, optical fibres, scintillators, photocatalysts, lithium-ion batteries, solar cells, gas sensors and supercapacitors etc. [11] because of their significant physical, chemical, electrical and optical properties. Among tungstate groups, CuWO₄ (indirect band gap, 2.2 eV), ZnWO₄ (direct band gap, 3.91 eV), CdWO₄ (indirect band gap, 3.27 eV) and SnWO₄ (indirect band gap, 2.1 eV) have been well studied for several applications because of their functional properties [12–15]. Importantly, these are cost-effective, high chemical stability and non-toxic. It should be noted that all of these compounds are n-type semiconductors (SC). CuWO₄, ZnWO₄ and CdWO₄ have common wolframite structure

* Corresponding author.

E-mail address: upenderg@osmania.ac.in (G. Upender).

<https://doi.org/10.1016/j.sna.2024.115094>

Received 7 November 2023; Received in revised form 19 January 2024; Accepted 30 January 2024

Available online 2 February 2024

0924-4247/© 2024 Elsevier B.V. All rights reserved.

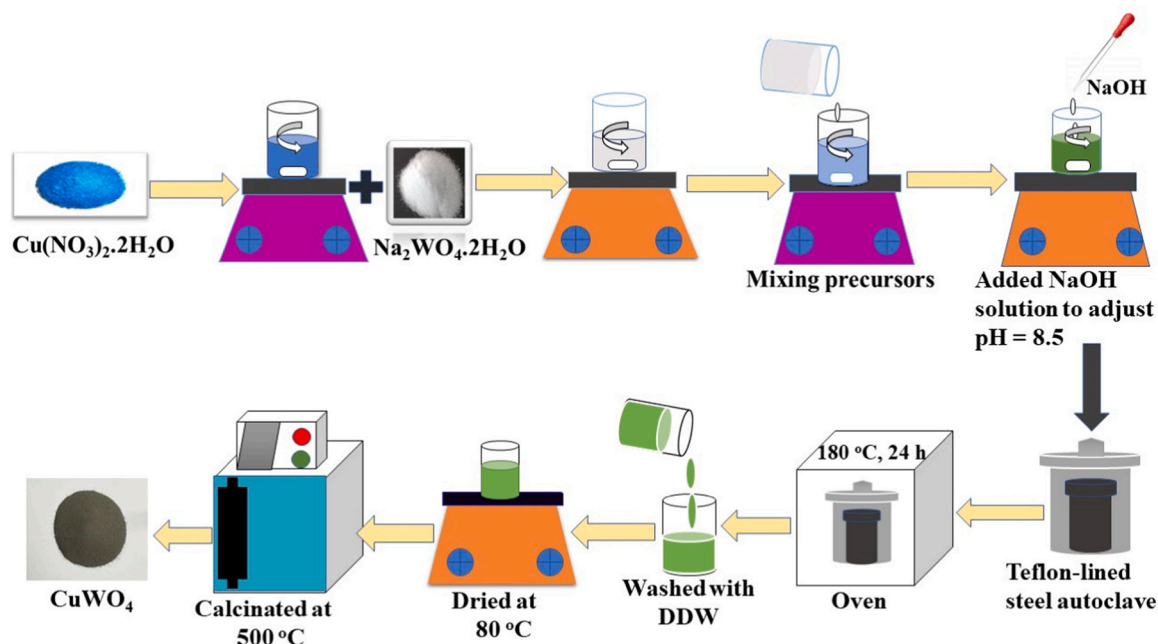


Fig. 1. Schematic of the synthesis of CuWO_4 .

and thus preferred in this study. These compounds are capable of converting O_2 to O_2^- at RT which is crucial for detecting the gases at RT. Especially much attention has been devoted to SnWO_4 (stannous tungstate) compound because of its structural versatility viz., $\alpha\text{-SnWO}_4$ and $\beta\text{-SnWO}_4$ [16]. But the former is more stable at temperature $< 670^\circ\text{C}$ and the latter is highly stable at temperature $> 670^\circ\text{C}$ so the phase transition occurs at 670°C [16]. Keeping in view the potential applications of $\alpha\text{-SnWO}_4$ than that of $\beta\text{-SnWO}_4$, the former compound is preferred in this study.

The literature survey has clearly shown that limited reports are available on the gas-sensing properties of individual CuWO_4 , ZnWO_4 , CdWO_4 and SnWO_4 compounds and essentially no proper study was available towards the gas sensing applications using these semiconducting compounds. The gas sensing response measured through chemoresistance of any compound semiconductor is also a function of the conducting pathway and electron density of these compounds. It is noteworthy that even though all the compounds have the same compositional formula i.e. MWO_4 ($M = \text{divalent metal cation}$) but their functional properties are significantly different owing to their unique crystal structure along with their cation/anion orientations. Particularly SnWO_4 has unique crystal structure among these four compounds. Therefore, a detailed study on these compounds is essentially required to further examine the gas sensing performance of these compounds. Apart from this, hitherto no report is available in the literature on the toluene gas sensing at RT by these compounds. Based on the aforesaid considerations, we have undertaken the present study to thoroughly investigate the gas sensing properties of these compounds at RT as an operating temperature and also to study the influence of various parameters on their gas sensing behavior. Their properties were studied by XRD, FE-SEM, TEM, BET, XPS, FTIR, DFT and UV-Vis DRS and the proper gas sensing mechanism is also discussed in detail.

2. Experimental section

The following chemicals used in the present study are analytical grade and utilized without any further purification and purchased from S.D. Fine-Chem. Ltd. Copper (II) nitrate trihydrate ($\text{Cu}(\text{NO}_3)_2 \cdot 3\text{H}_2\text{O}$), Zinc (II) chloride dihydrate ($\text{ZnCl}_2 \cdot 2\text{H}_2\text{O}$), Cadmium chloride monohydrate ($\text{CdCl}_2 \cdot \text{H}_2\text{O}$), Tin (II) chloride dihydrate ($\text{SnCl}_2 \cdot 2\text{H}_2\text{O}$) and

Sodium tungstate dihydrate ($\text{Na}_2\text{WO}_4 \cdot 2\text{H}_2\text{O}$).

2.1. Synthesis of MWO_4 ($M = \text{Cu, Zn, Cd and Sn}$)

The hydrothermal method was employed in the synthesis of MWO_4 ($M = \text{Cu, Zn, Cd and Sn}$) compounds. As shown in Fig. 1, at the beginning the stoichiometric amounts of $\text{Cu}(\text{NO}_3)_2 \cdot 3\text{H}_2\text{O}$ and $\text{Na}_2\text{WO}_4 \cdot 2\text{H}_2\text{O}$ were dissolved separately in double distilled (DD) water under constant stirring on magnetic stirrer. Then $\text{Na}_2\text{WO}_4 \cdot 2\text{H}_2\text{O}$ solution was slowly mixed drop after drop with $\text{Cu}(\text{NO}_3)_2 \cdot 3\text{H}_2\text{O}$ solution under constant stirring. At this time the pH of this resultant solution was adjusted to 8.5 by adding NaOH solution and stirred continuously for 1 h. Thereafter, the obtained solution was shifted into Teflon-lined steel autoclave (100 ml) and heated at 180°C for 24 h. Now, this mixture was brought down slowly to RT and this final precipitate was shifted to a beaker, washed with DD water, and ethanol for several times. Later, this was dried at 80°C for overnight and then ground it into a fine powder. Likewise, the above procedure was adopted to synthesize ZnWO_4 and CdWO_4 compounds except the pH 7 was maintained. However, CuWO_4 powder was calcinated at 500°C for 3 h to get the final phase of this compound.

2.1.1. Synthesis of SnWO_4

In order to synthesize SnWO_4 , firstly the calculated individual amounts of $\text{SnCl}_2 \cdot 2\text{H}_2\text{O}$ and $\text{Na}_2\text{WO}_4 \cdot 2\text{H}_2\text{O}$ were dissolved in HCl and DD water, respectively under constant stirring. Secondly, $\text{Na}_2\text{WO}_4 \cdot 2\text{H}_2\text{O}$ solution was added drop by drop to $\text{SnCl}_2 \cdot 2\text{H}_2\text{O}$ solution under continuous stirring for 30 min, thereafter ethylene glycol was slowly added to this mixture whose pH was adjusted to 7 by adding NaOH solution. Thirdly, this solution was poured into Teflon-lined steel autoclave (100 ml) and kept in an oven at 180°C for 24 h, subsequently the resultant mixture was naturally cooled down to RT. Then the precipitate was washed with DD water as well as ethanol for several times and dried at 80°C . Lastly, it was ground into fine powder then calcinated at 300°C for 3 h. Hereafter, CuWO_4 , ZnWO_4 , CdWO_4 and SnWO_4 are referred to as CuW, ZnW, CdW and SnW, respectively.

2.2. Characterization techniques

The powder X-ray diffraction (XRD) patterns of these compounds

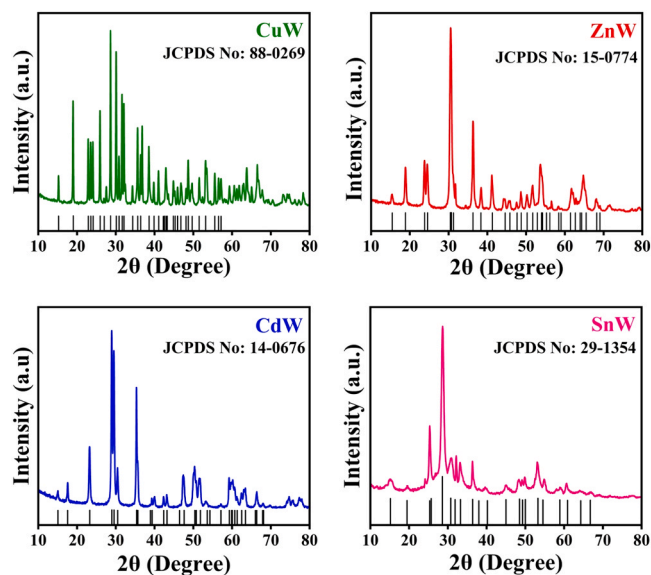


Fig. 2. XRD patterns of CuW, ZnW, CdW and SnW compounds.

were recorded in the scan range 10 to 80° (2 θ) on Rigaku MiniFlex 600 X-ray diffractometer with a Cu K α radiation source ($\lambda = 1.5406 \text{ \AA}$). Fourier Transform Infrared (FTIR) spectra were recorded in between 500–1200 cm^{-1} by IR prestige (Shimadzu, Japan) using KBr pellet method. UV-Vis diffuse reflectance spectra (DRS) of the compounds were recorded in the range 200–800 nm at RT using a JASCO V650 UV-VIS spectrophotometer in absorption and reflection mode wherein BaSO $_4$ was used as reference. The morphology and elemental compositions of the compounds were investigated with field emission scanning electron microscope (FESEM, Carl Zeiss Evo 18). High resolution transmission electron microscopy (HRTEM) images were recorded using JEM – 2100 Plus Electron Microscope. The X-ray photoelectron spectra (XPS) were carried out on Thermo Scientific K-ALPHA spectrometer

using Al K α radiation (1486.6 eV). The surface area of these compounds was recorded using the BELSORB II instrument from the N $_2$ adsorption-desorption at liquid nitrogen temperature and the surface areas were measured using Brunauer-Emmett-Teller (BET) technique. The details of “density functional theory (DFT)” calculations are presented in Electronic Supplementary Information (ESI).

2.3. Gas sensor preparation

Firstly, a square glass substrate of 2.5 cm was ultrasonicated in DD water then in acetone for 30 min each, subsequently dried in the air. Secondly, the required amount of the gas sensing compound was added with few drops of ethylene glycol and ground for an hour to make fine paste. Thirdly, this paste was uniformly coated on the glass substrate and dried at 80 °C. Finally, silver paste was applied on both edges of glass substrate to form electrodes and heated at 200 °C for 3 h. The gas sensing activity of the understudied sensors was evaluated on the basis of “the chemoresistance phenomenon” with the help of Keithley 6517B electrometer. The gas sensing kit is shown in ESI (Fig. S1). Using a digital humidity controller (Humitherm, India), the relative humidity in the sensor chamber was measured (60%) and then respective gas was purged into the gas chamber. Consequently, the chemoresistance of the respective sensor was recorded.

3. Results and discussion

3.1. XRD

The RT powder XRD of hydrothermally derived CuW, ZnW, CdW and SnW compounds were recorded to study with regard to their phase purity and crystallinity. The recorded XRD data of each compound is depicted in Fig. 2. The CuW exhibited its typical peaks at $2\theta = 15.3^\circ, 19.1^\circ, 28.7^\circ, 30.1^\circ, 31.6^\circ, 32.1^\circ$ and 55.6° which are matched with their corresponding Bragg’s crystal planes (010), (100), (1–1-1), (111), (020), (-111) and (1–11) respectively [17]. The CuW consists of triclinic (anorthic) unit cell whose space group is P1 (JCPDS card No 88–0269) [17]. The lattice parameters of CuW are $a = 4.7044 \text{ \AA}$, b

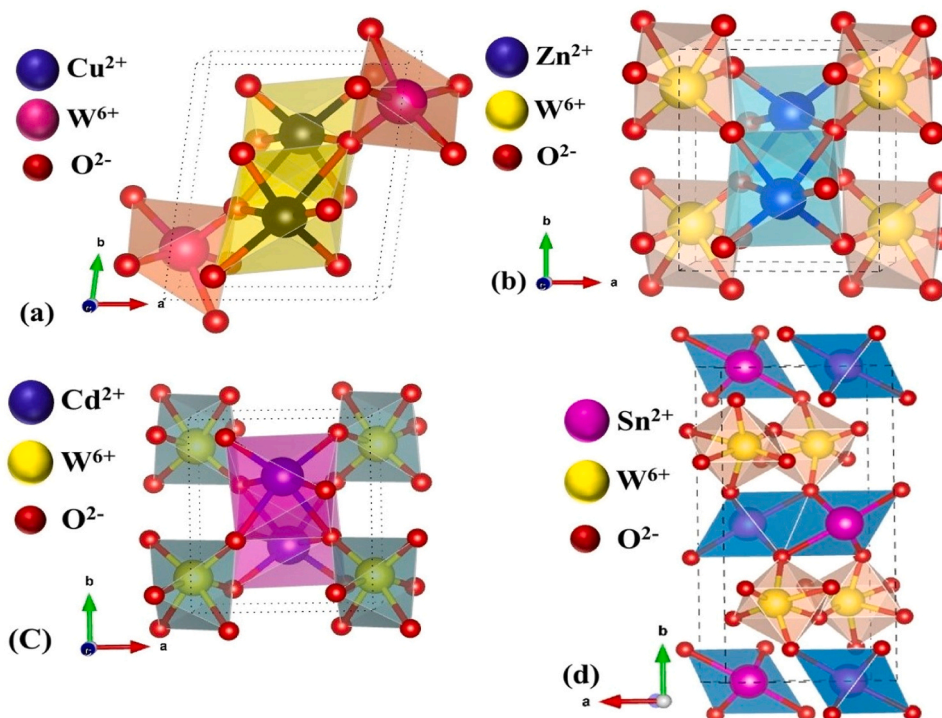


Fig. 3. Unit cells (VESTA view) of (a) CuW, (b) ZnW, (c) CdW and (d) SnW compounds.

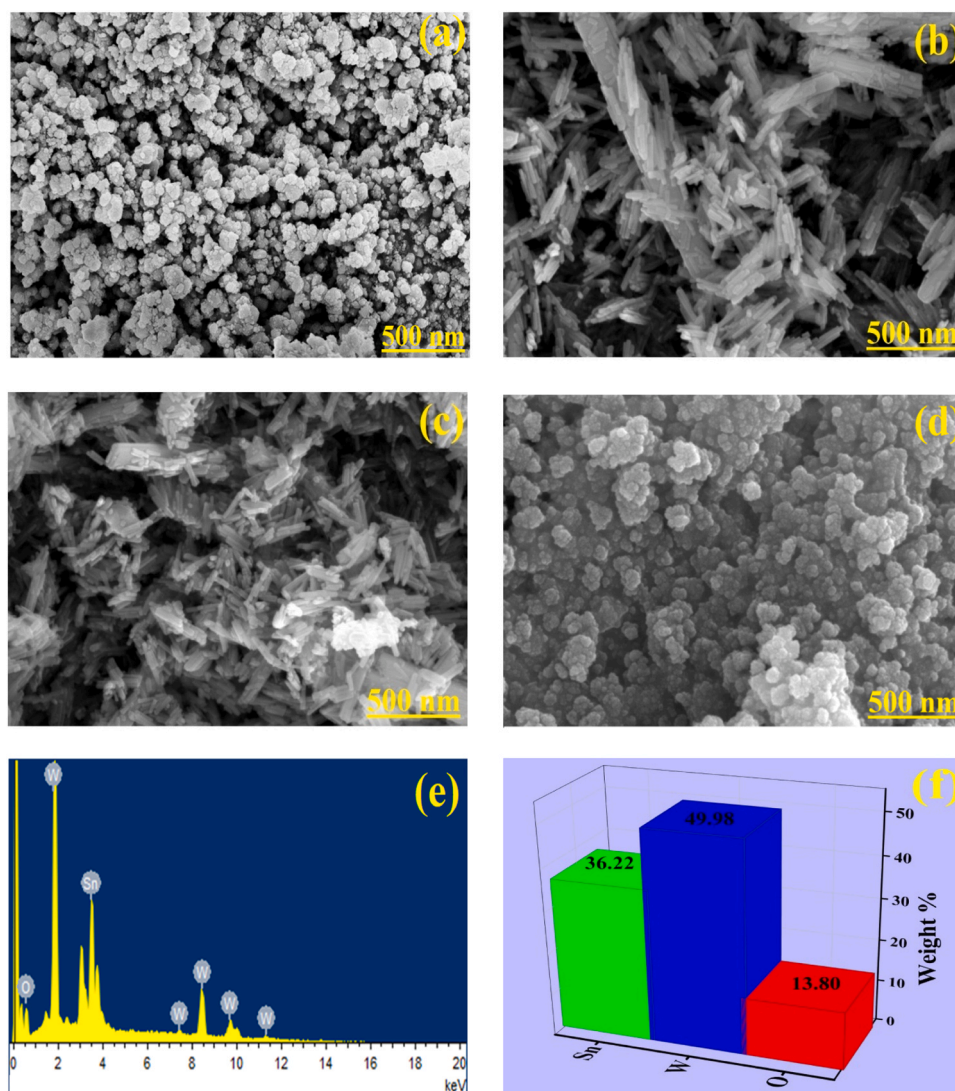


Fig. 4. FESEM images of (a) CuW (b) ZnW (c) CdW (d) SnW (e) EDX spectra of SnW and (f) wt% of Sn, W and O.

$= 4.8756 \text{ \AA}$, $c = 5.8362 \text{ \AA}$ and it has 2 formula units [18]. The Bragg peaks of ZnW positioned at 19.0° , 23.8° , 24.5° , 30.6° , 36.3° , 41.2° , 48.6° , 51.8° , 64.5° and 71.4° which are correlated to (100), (011), (110), (111), (002), (121), (220), (-202) , (-311) and (041) respectively. The obtained diffraction patterns of ZnW were observed to be in accordance with the monoclinic phase of ZnW (JCPDS card No. 15-0774) together with space group P2/c and it has 2 formula units [19]. The lattice parameters of ZnW are $a = 4.702 \text{ \AA}$, $b = 5.718 \text{ \AA}$, $c = 4.93 \text{ \AA}$ [20]. The CdW displayed XRD peaks at 15.26° , 17.76° , 23.46° , 29.13° , 29.72° , 30.64° , 35.51° , 47.57° , 50.28° , 51.67° which are clearly correlated with their corresponding Bragg planes of (010), (100), (110), (-111) , (111), (020), (002), (022), (-202) and (221) respectively. The observed XRD patterns indicate that CdW is crystallized in monoclinic lattice with wolframite structure with space group P2/c (JCPDS card No. 14-0676) [21]. The lattice parameters of CdW are $a = 5.0595 \text{ \AA}$, $b = 5.8668 \text{ \AA}$, $c = 5.0762 \text{ \AA}$ and it has 2 formula units [22]. The characteristic peaks of SnW positioned at $2\theta = 15.2^\circ$, 25.0° , 28.3° , 30.6° , 32.7° , 35.9° , 53.1° and 60.0° are indexed to crystal planes (020), (111), (121), (040), (210), (002), (161) and (123). The appeared peaks confirm that the prepared SnW has grown in the orthorhombic crystal structure together with ' α ' phase whose space group is Pnna (JCPDS card No. 29-1354) and it has 4 formula units [23]. The lattice parameters are $a = 5.627 \text{ \AA}$, $b = 11.649 \text{ \AA}$, $c = 4.997 \text{ \AA}$ [24]. It is well-established fact in the literature that α -SnW (α -SnWO₄) phase is thermodynamically more

stable at lower temperature than β -SnWO₄. The cell volumes of CuW, ZnW, CdW and SnW are 132.86, 132.54, 150.68 and 327.54 \AA^3 , respectively. The diffraction patterns observed for CuW, ZnW, CdW and SnW are found to be well correlated with the literature. The intense diffraction peaks seen in Fig. 2 clearly indicate the high crystallinity of these compounds. Moreover, the absence of the additional peaks asserted that all the compounds have grown in the single phase only. Especially, α -SnW is free from quite dominant phases of SnO, SnO₂ and WO₃. The average crystallite size of all the compounds were computed by considering the full width at half maximum (FWHM) of the highest intense Bragg peak using the below Debye-Scherrer's formula.

$$D = \frac{0.9\lambda}{\beta \cos\theta} \quad (1)$$

where D is an average crystallite size, λ is X-rays wavelength, β is FWHM, θ is diffraction angle of the crystal plane in radians [25]. The average crystallite size of CuW, ZnW, CdW and SnW were estimated to be 39, 14, 25 and 12 nm, respectively. The unit cells, drawn by VESTA, of CuW, ZnW, CdW and SnW are presented in Fig. 3.

3.2. FESEM, TEM and surface area analysis

Since the surface morphology have critical impact on electrical,

Table 1
EDX elemental analysis of CuW, ZnW, CdW and SnW.

Element	CuW		ZnW		CdW		SnW	
	wt%	Atom%	wt%	Atom%	wt%	Atom%	wt%	Atom%
W	53.13	12.99	43.60	8.60	50.38	14.78	49.98	18.88
O	25.62	71.98	35.20	79.60	21.25	71.62	13.80	59.92
Cu	21.25	15.03	-	-	-	-	-	-
Zn	-	-	21.20	11.80	-	-	-	-
Cd	-	-	-	-	28.37	13.61	-	-
Sn	-	-	-	-	-	-	36.22	21.19

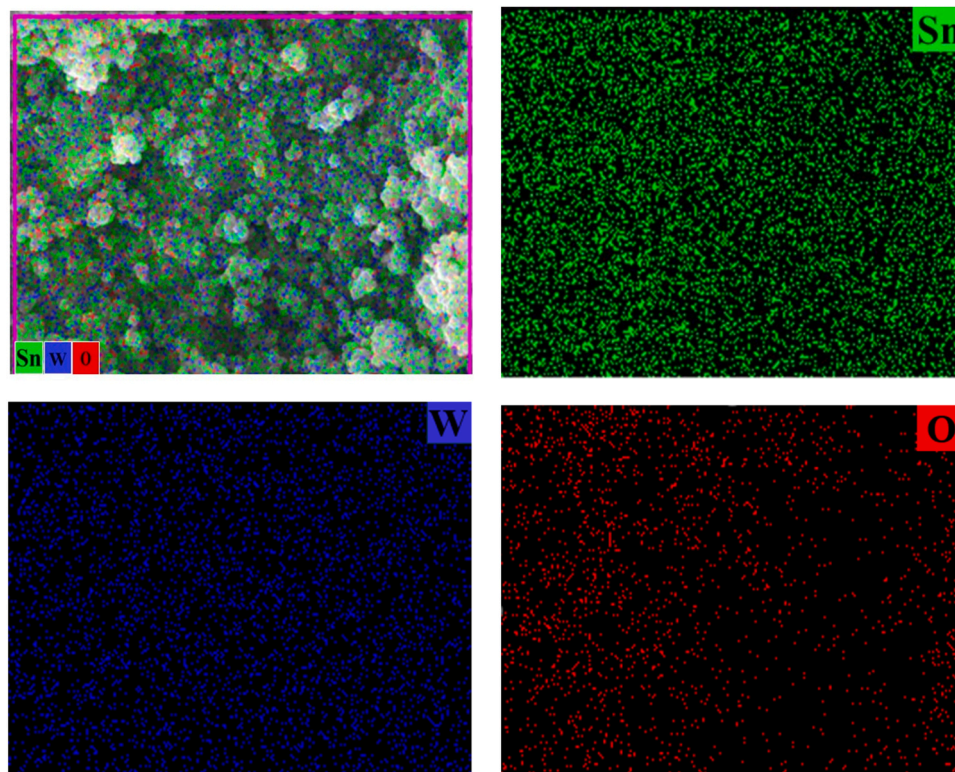


Fig. 5. Elemental colour mapping images of SnW.

optical, and gas-sensing behaviour, thus, morphology of the compounds are included here and were examined with FESEM. Fig. 4(a-d) shows the surface morphology of CuW, ZnW, CdW and SnW. It can be seen that both CuW and SnW compounds are composed with nanospheres of varied sizes whereas both ZnW and CdW compounds are made of nanorods of varied sizes. As shown in Fig. 4(a-d), CuW has more agglomerated nanospheres grown like cauliflower as compared to SnW, on the other hand, ZnW and CdW have exhibited a compact arrangement of nanorods. The elemental analysis, EDX spectra, recorded on typical SnW is illustrated in Fig. 4(e) which explicitly demonstrates the existence of Sn, W and O elements only whose respective wt% is displayed in Fig. 4(f). No impurities were noticed during the EDX scan, asserts that SnW has formed in its pure form. This is also true for CuW, CdW and ZnW. In addition, the wt% and atomic% of Cu, Zn, Cd and Sn, W and O are presented in Table 1. The color mapping images of a typical SnW (Fig. 5) were also recorded not only to check Sn, W and O distribution but also to examine the presence of impurities. The green (Sn), blue (W) and red (O) color spots noticed in all the images clearly signifies that these elements exist homogeneously, uniformly and equally distributed throughout SnW compound and is necessary for obtaining reliable and repeatable gas sensing activity.

TEM images and its selective area electron diffraction (SAED) patterns together with lattice spacing of CdW and SnW compounds were

recorded and depicted in Fig. 6(a-d). The CdW consist of nanorods with an average diameter 25–40 nm. Similarly, the SnW contains nanoparticles with an average diameter 12–15 nm. Fig. 6(c,d) display the SAED patterns of CdW and SnW corresponding to (100), (−111), (002), (022), (221) and (111), (040), (051), (331) crystal planes, respectively. In addition, Fig. 6(e-f) depicts HRTEM image wherein the lattice fringes of (100), (−111), (022) crystal planes of CdW and (111), (040), (051) crystal plane of SnW were observed and their respective lattice spacing's are estimated to be 0.51, 0.32, 0.19 nm and 0.36, 0.28, 0.21 nm. In addition, the high resolution FESEM images of CuW and ZnW are also incorporated in ESI (Fig. S2).

Fig. 7 presents the BET adsorption-desorption isotherms of CuW, ZnW, CdW and SnW compounds and BET surface area of these compounds are respectively measured to be 20.4, 19.6, 17.8 and 24.2 m²/g, suggesting that SnW has slightly high surface area than the remaining compounds. The more surface area of SnW is ascribed to the less agglomeration of nanospheres than that of CuW. Also, this observation is consistent with FESEM image analysis.

3.3. X-ray photoelectron spectroscopy (XPS)

The binding energy (BE) of the elements presented in all the compounds were evaluated with reference to BE of C 1s (284.68 eV) [26].

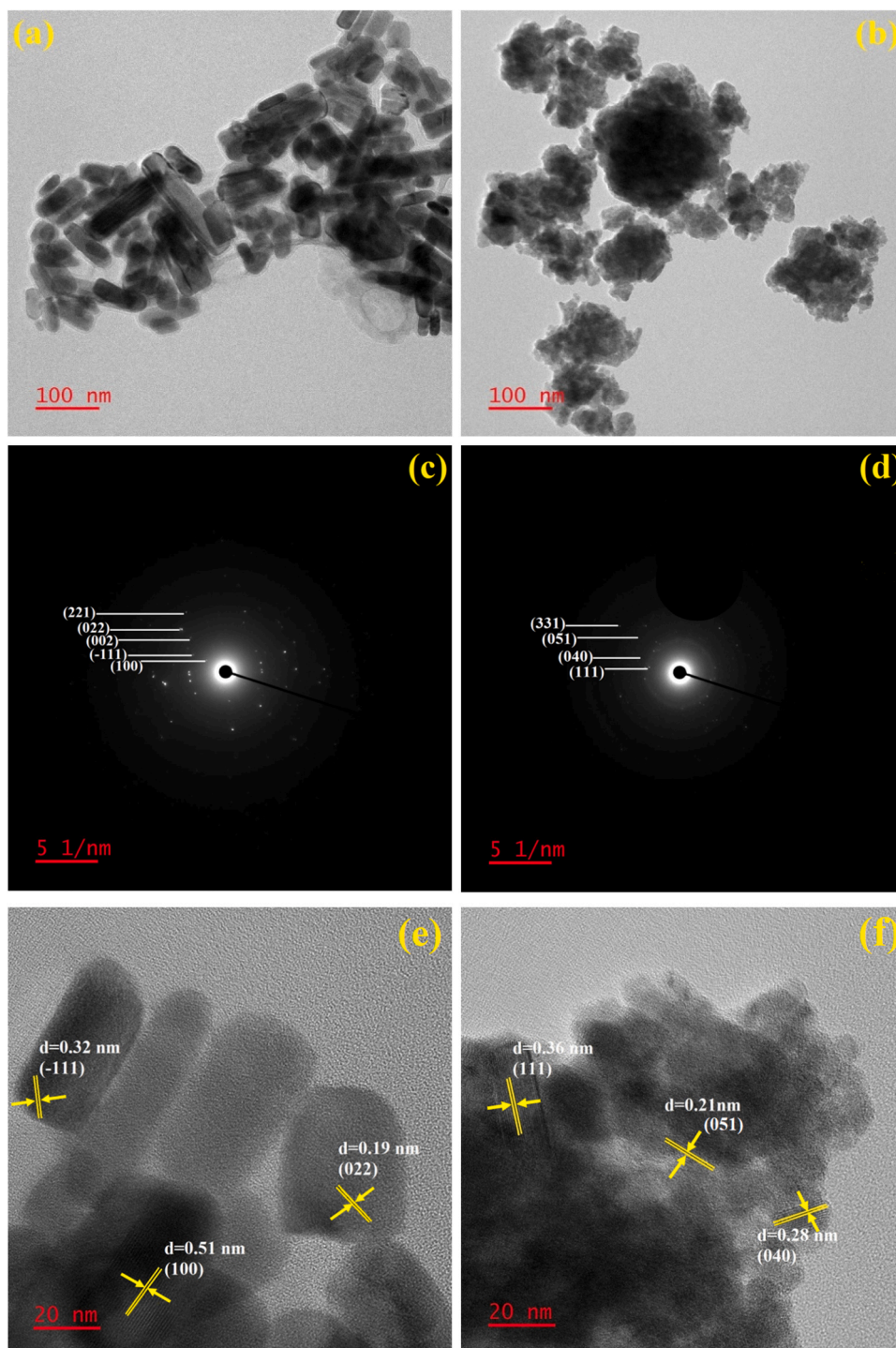


Fig. 6. TEM images and SAED patterns of CdW (a,c) and SnW (b,d) and HRTEM images of CdW (e) and SnW (f).

Fig. 8(a-d) illustrates the survey spectra of CuW, ZnW, CdW and SnW, respectively. The respective BE positions with regard to the elements of CuW, ZnW, CdW and SnW compounds are manifestly suggests that no impurity elements are present except the chemical elements belonging to these compounds. Thus, XPS analysis has testified the purity of all the compounds. Fig. 9(a) is the high resolution (HR) XPS of Cu 2p wherein BE peaks occurred at 935.5 and 955.1 eV because of Cu 2p_{3/2} and Cu 2p_{1/2} respectively, suggesting Cu (+2) chemical state. Besides, the appearance of satellite peaks at 943.1, 949.1 and 962.7 eV also clearly substantiate the +2 chemical states of Cu ions [27,28]. Fig. 9(b) presents HR XPS of Zn 2p in which the two intense peaks positioned at 1021.6

and 1044.8 eV are attributed to Zn 2p_{3/2} and Zn 2p_{1/2} respectively, asserting +2 chemical state of Zn [29]. The HR XPS of Cd 3d is depicted in Fig. 9(c), the appearance of 404.9 and 411.7 eV, respectively originated from Cd 3d_{5/2} and Cd 3d_{3/2}, confirming Cd (+2) chemical state [30]. Fig. 9(d) illustrates HR XPS of Sn 3d, it has two BE peaks situated at 490.5 and 498.9 eV, respectively linked to Sn 3d_{5/2} and Sn 3d_{3/2}, clearly avowed the Sn (+2) chemical state [23]. The HR XPS of both W 4f and O 1s were recorded for SnW compound and are shown in Fig. 9(e) and Fig. 9(f), respectively. Fig. 9(e) contains two BE peaks observed at 39.1 and 41.1 eV respectively ascribed to W 4f_{7/2} and W 4f_{5/2}, obviously indicates W (+6) chemical state [31]. Fig. 9(f) exhibits BE peaks at 532.8

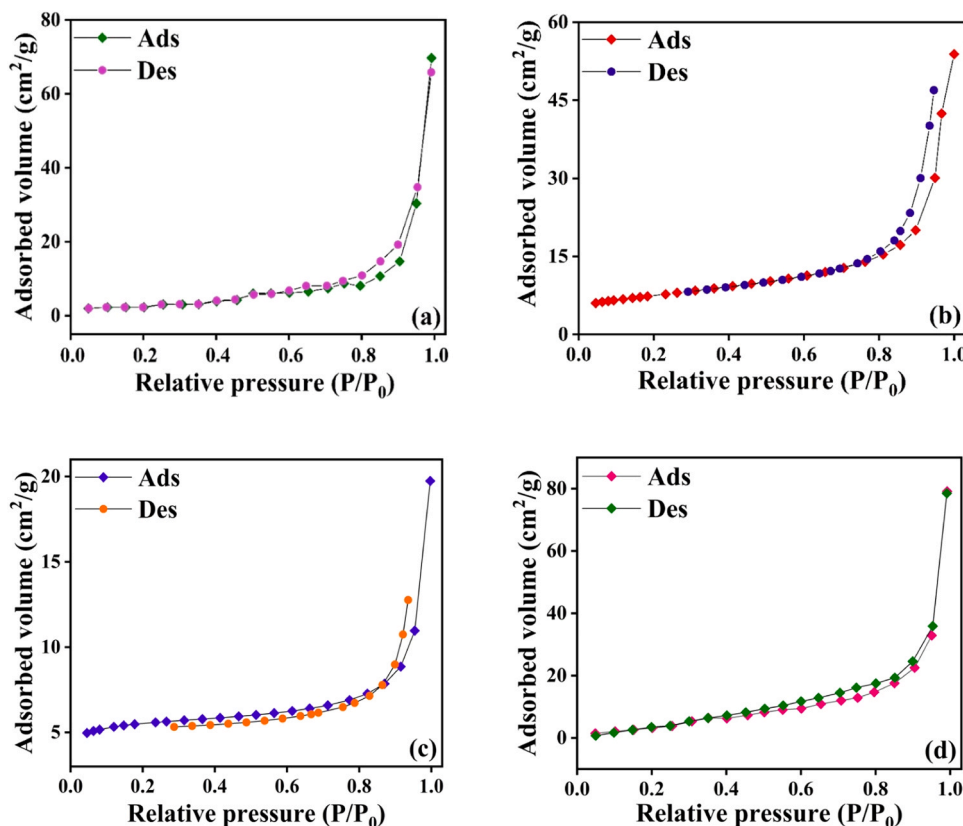


Fig. 7. Nitrogen adsorption–desorption isotherms curve of (a) CuW, (b) ZnW, (c) CdW and (d) SnW.

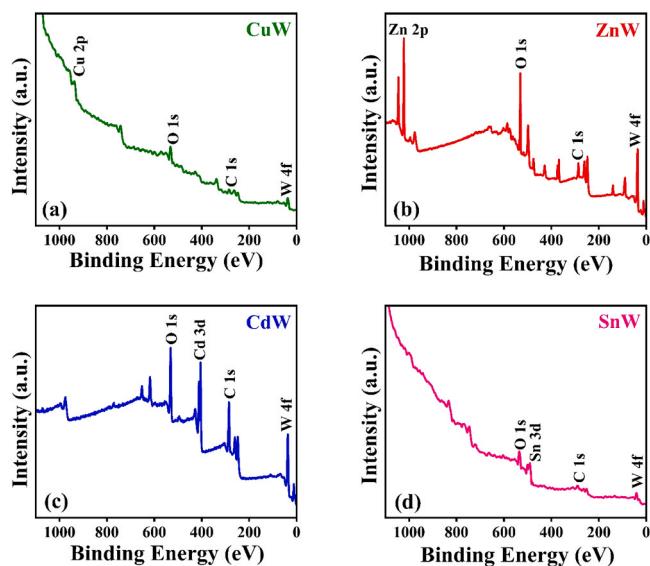


Fig. 8. XPS survey spectra of (a) CuW, (b) ZnW, (c) CdW and (d) SnW.

and 534.9 eV are respectively associated with lattice oxygens of Sn-O/W-O and chemisorbed oxygens of OH⁻/O₂ [32]. The BE's of W 4f of CuW, ZnW and CdW and O 1s of CuW, ZnW and CdW are also included in ESI (Fig. S3). BE's of all the respective constituent elements of CuW, ZnW, CdW and SnW compounds are given in Table 2.

3.4. FTIR spectra

FTIR spectra of CuW, ZnW, CdW and SnW compounds (Fig. 10) were

recorded to determine various metal oxygen vibrations together with type of bonding that are present in these samples. The IR spectrum of CuW has predominant IR bands which are observed at 467, 538, 588, 713, 808 and 908 cm⁻¹. The peaks situated at 808 and 908 cm⁻¹ could be assigned to stretching vibration of W-O of WO₆ octahedra or O-W-O vibrations. The band at 467 cm⁻¹ could be due to Cu-O-W vibrations, 538 and 713 cm⁻¹ are attributed to Cu-O stretching vibrations [28,33,34]. The band at 588 cm⁻¹ is owing to W-O-W linkages. The ZnW shows IR bands at 468, 532, 663, 837 and 878 cm⁻¹. The IR bands located at 468 and 532 cm⁻¹ are assigned to in-plane deformation of longer W-O bonds in WO₄²⁻ groups [35,36]. The band 663 cm⁻¹ is assigned to Zn-O-W stretching vibrations [37]. The bands at 837 and 878 cm⁻¹ are originated either from W-O symmetric stretching vibrations or from symmetric stretching of O-W-O in WO₆ octahedron [38]. All the characteristic absorption peaks of CdW are found to exist in its IR spectrum (Fig. 10). The peaks positioned at 410 and 460 cm⁻¹ are connected to the in-plane deformation of the WO₄²⁻ group, the peaks noticed at 521 and 585 cm⁻¹ are believed to be originated from Cd-O stretching vibrations of CdO₆. The peak situated at 717 cm⁻¹ is associated with W-O stretching vibrations, the intense peak 835 cm⁻¹ is owing to Cd-O-W stretching vibrations. The strong peak at 889 cm⁻¹ is linked to the symmetric stretching of O-W-O in WO₆ [21]. FTIR spectra of SnW show the vibrational bands at 451, 543, 715, 895 and 956 cm⁻¹. The 451 cm⁻¹ is attributed to the presence of Sn-O-W linkages. IR band located around 543 cm⁻¹ is assigned to Sn-O stretching vibrations and the strong IR band about 715 cm⁻¹ is originated from W-O stretching vibrations of (WO₆)²⁻ octahedron. The 895 and 956 cm⁻¹ are linked to symmetric stretching of W-O-W or O-W-O in WO₆ groups [24,39].

3.5. UV-Vis diffuse reflectance spectra

To determine the optical properties of CuW, ZnW, CdW and SnW compounds, UV-Vis DRS measurements were performed as depicted in

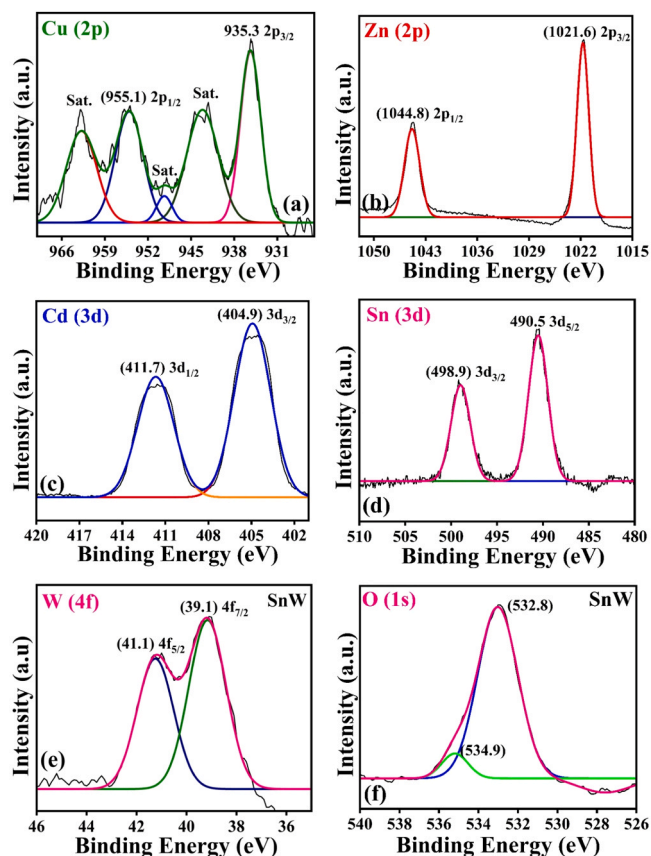


Fig. 9. High resolution XPS spectra of (a) Cu, (b) Zn, (c) Cd, (d) Sn (e) W and (f) O.

Fig. 11 (a-d) and their respective inset images. As illustrated in Fig. 11(a) (inset), CuW absorption bands lies between 300–530 nm with the center peak situated at 315 and other bands located at 590 and 785 nm [31]. The main transitions involved are named as the ligand to metal charge transfer which are hereafter called as LMCT and also due to metal-to-metal charge transfer which are termed as MMCT [40]. The valance band (VB) of CuW is mainly resulted from Cu 3d and O 2p orbitals while its conduction band (CB) is majorly dominated by W 5d than the other orbitals such as O 2p, Cu 3d [41,42]. From the earlier reports, it is understood that Cu 3d orbitals have more energy than O 2p, hence, Cu 3d orbital appears to be dominant on the top of VB than O 2p [41]. The absorption seen at 315 nm arises from the electronic transitions from O 2p (VB) to W 5d orbitals (CB) in WO₆ octahedron. Besides, the absorption bands at 590 and 785 nm are ascribed to the electronic transitions from O 2p (VB) to Cu 3d (CB) within CuO₆ octahedron and intra-band d-d transitions of Cu²⁺ ions, respectively. As depicted in Fig. 11 (b) (inset), ZnW exhibited the prominent bands centered at 291 and 381 nm which show an intense absorption capability over the entire spectrum [43]. The VB of ZnWO₄ is constituted with the hybridization of Zn 4s, W 5d and O 2p orbitals while the CB is composed mainly with the hybridization of W 5d and O 2p [44]. The absorption bands noticed at 291 and 381 nm are originated the electron transfer from O 2p to W 5d and charge transfer might occur from oxygen defects to W 5d,

Table 2
Binding energies (eV) of CuW, ZnW, CdW and SnW compounds.

Compound	O 1s	W 5/2	W 7/2	Cu 1/2	Cu 3/2	Zn 1/2	Zn 3/2	Cd 3/2	Cd 5/2	Sn 3/2	Sn 5/2
CuW	530.8	37.6	35.5	955.1	935.5	-	-	-	-	-	-
ZnW	530.3	37.5	35.4	-	-	1044.8	1021.6	-	-	-	-
CdW	531.3	36.7	34.7	-	-	-	-	411.7	404.9	-	-
SnW	532.8	41.1	39.1	-	-	-	-	-	-	498.9	490.5

respectively.

As displayed in Fig. 11 (c) (inset), the CdW has absorption bands at 288 and 320 nm [21]. The VB of CdW is mainly composed of O 2p and W 5d with a lighter contribution from Cd 5s and Cd 4d and its CB is made of O 2p and W 5d wherein W 5d contributes to top of CB [45,46]. The band 288 nm caused by LMCT which is assigned to the electron transition from O 2p (VB) to W 5d (CB). Besides, CdW has oxygen defects which create energy levels in between VB and CB. These are accountable for the absorption band 320 nm. As presented in Fig. 11 (d) (inset), the SnW exhibited the absorption bands at 291, 442 and 562 nm [47]. The DFT calculations presented in Fig. 12 (i-ii) illustrates the band structure and density of states of SnW which discerns that Sn 5s together with O 2p orbitals contributes to VB while W 5d orbitals are majorly contributing

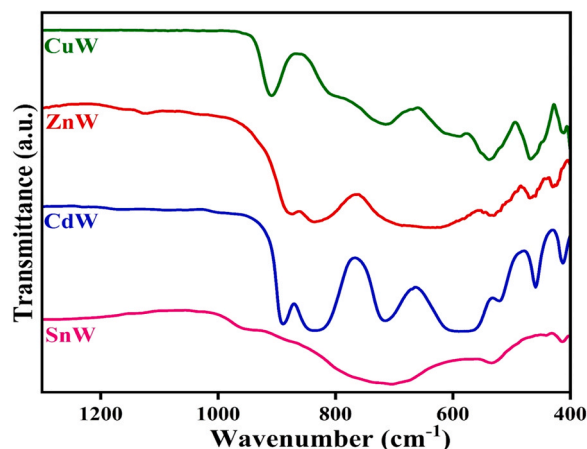


Fig. 10. FTIR spectra of CuW, ZnW, CdW and SnW compounds.

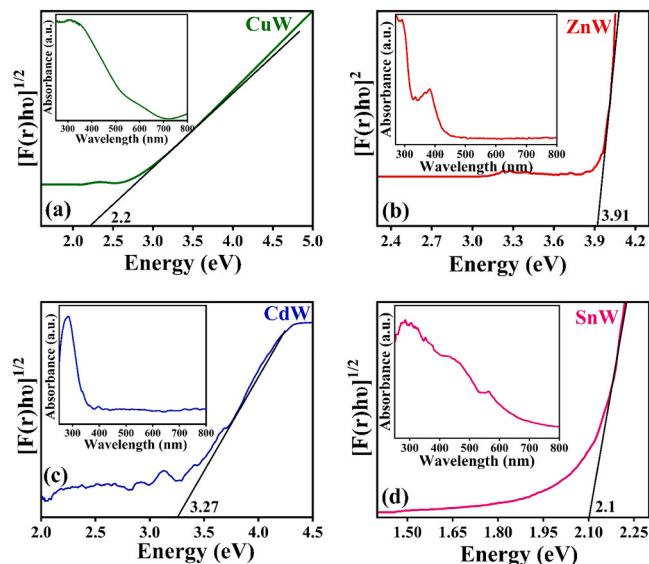


Fig. 11. Kubelka-Munk plots of (a) CuW, (b) ZnW, (c) CdW and (d) SnW compounds. (Insets of each figure show their respective UV-Vis DRS spectra).

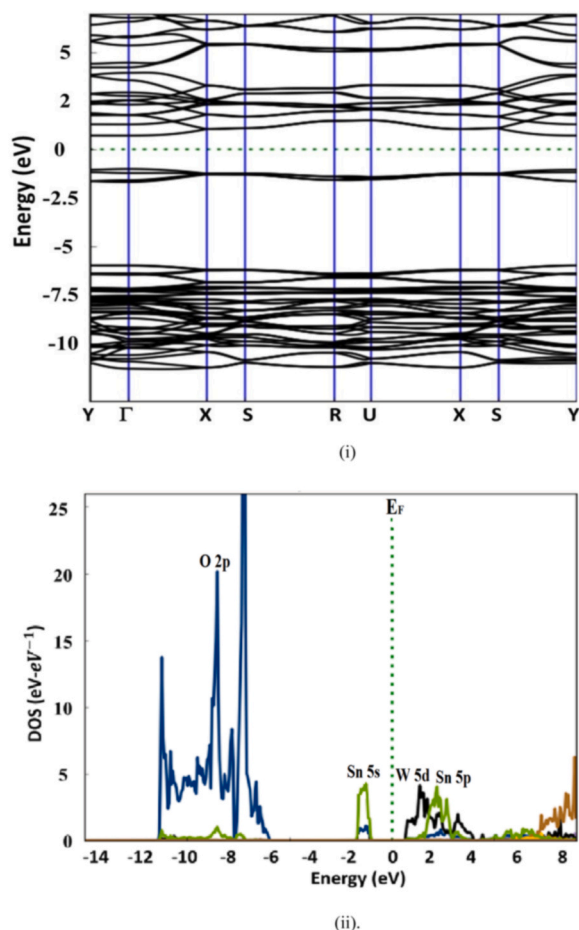


Fig. 12. The electronic band structure (i) and the density of states of SnW (ii).

to bottom of CB with minor contributions from O 2p and Sn 5s. The strong absorption band 291 nm is attributed to the electron transitions from the deeply located O 2p \rightarrow W 5d [48]. The other broad and intense absorption band 442 nm is mainly ascribed to the electron transition from the combined hybridized orbital O 2p + Sn 5s \rightarrow W 5d or Sn 5s \rightarrow O 2p whereas the weak absorption band 562 nm is assigned to an electron transition from Sn 5s to W 5d state, but this transition may occur with less probabilities since it is s \rightarrow d transitions [48]. The optical band gap (E_g) values of CuW, ZnW, CdW and SnW were computed using the Kubelka-Munk function, shown in Fig. 11(a-d), in accordance with the compounds direct/indirect band gap transitions. The obtained E_g values of CuW, ZnW, CdW and SnW, respectively are 2.2, 3.91, 3.27 and 2.1 eV, denoting that SnW has the lowest band gap than the rest of the compounds.

3.6. Gas sensing properties

The gas sensing properties of CuW, ZnW, CdW and SnW compounds were investigated at RT as an operating temperature. Preparing RT gas sensors is crucial since it plays an essential role in its wide commercial usage, thus, these compounds were tested at RT. Initially, the selectivity of CuW, ZnW, CdW and SnW compounds was tested for sensing of an individual volatile organic compound (VOC) gases like 1-Butanol ($C_4H_{10}O$), Acetone (C_3H_6O), Ethanol (C_2H_6O), Benzene (C_6H_6), Toluene ($C_6H_5CH_3$), Xylene (C_8H_{10}) (a total of 6 gases). This was done by recording the resistance change of these gas sensing compounds in the presence of air and gas as a function of time and this phenomenon is termed as chemoresistance. As per the literature, a typical 100 ppm of each gas concentration was chosen to examine the efficacy of these

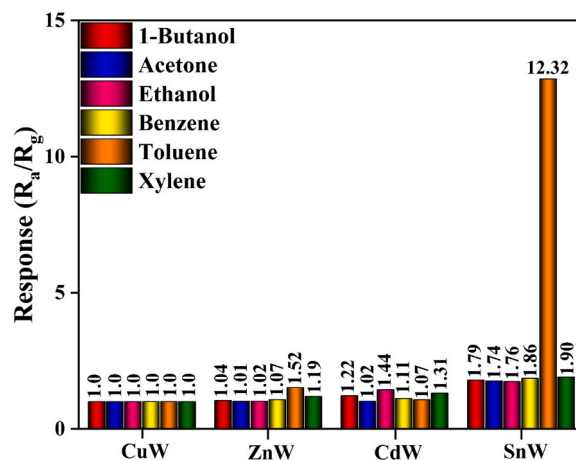


Fig. 13. Selectivity of CuW, ZnW, CdW and SnW sensors at RT of various gases (100 ppm).

sensing compounds. Initially, the sensor was placed in the chamber and measured its resistance as a function of time using 6517 B Keithley (R_a) and then each gas of 100 ppm was purged into this chamber and measured the resistance change of the sensor (R_g). The response (S) of all the sensors is computed by $S = R_a/R_g$ (since $R_a > R_g$ for n-type) [49]. All the obtained results were illustrated in Fig. 13. These results demonstrated that all the sensors showed the response for all the tested gases, however, SnW sensor displayed the highest selectivity with the highest response (12.32) for $C_6H_5CH_3$ gas. The 'S' of SnW is observed to be in the order of $C_6H_5CH_3 > C_8H_{10} > C_6H_6 > C_4H_{10}O > C_2H_6O > C_3H_6O$. In general, the response time (t_{res}) is equal to the time taken by the sensor to detect 90% of the total resistance change in the presence of air (base resistance) and after injecting the gas. Similarly, the recovery time (t_{rec}) is the time taken by the sensor to reach 90% of the base resistance (in air) after withdrawal of the tested gas. As displayed in Fig. 14, the t_{res}/t_{rec} of CuW, ZnW, CdW and SnW towards $C_6H_5CH_3$ were measured to be 161/44, 143/56, 68/34 and 105/90 s. The resistance graphs of CuW, ZnW, CdW and SnW sensors for the remaining gases are depicted in ESI (Fig. S4(i-v)). These results establish the fact that SnW sensor improved the $C_6H_5CH_3$ sensing drastically at RT than the existing literature (Table 3). The dynamic response is essential in order to check the efficacy of the sensors. For this purpose, the response of SnW sensor at different ppm level of the analyte gas i.e., 5, 10, 25, 50, 75 and 100 were recorded. Thus, Fig. 15 depicts the dynamic response-recovery behaviour of SnW sensors towards $C_6H_5CH_3$. The repeatability for any gas sensor is considered as key factor, hence, the same was conducted in five cycles and presented in Fig. 16. In this study, every time 50 ppm of $C_6H_5CH_3$ gas purged into the gas chamber and recorded the response of SnW sensor. The obtained results ensured that the sensor has nearly the same response and also substantiate that these sensors have a prominent repeatability towards $C_6H_5CH_3$. Since the stability of any gas sensor play pivotal role for its practical use, thus, the stability measurements were also highlighted in the present study. Fig. 17 reflects the response values of these sensors recorded for every 10 days. After 30 days, the response values has slightly changed by few degrees, conclusively demonstrating that this SnW sensor is more reliable candidate to detect $C_6H_5CH_3$ even after 4 cycles at RT. Moreover, the efficiency of this sensor for $C_6H_5CH_3$ gas detection is also compared with the earlier reports in the literature and a detailed comparison is presented in Table 3. It is clearly demonstrated that among all the mentioned sensors, SnW sensor has manifested the detection of the lowest ppm up to 5 ppm, hence, it exhibits superior sensing ability for toluene gas at RT.

3.6.1. Gas sensing mechanism

When SnW sensor is placed in the gas sensing chamber, the oxygen

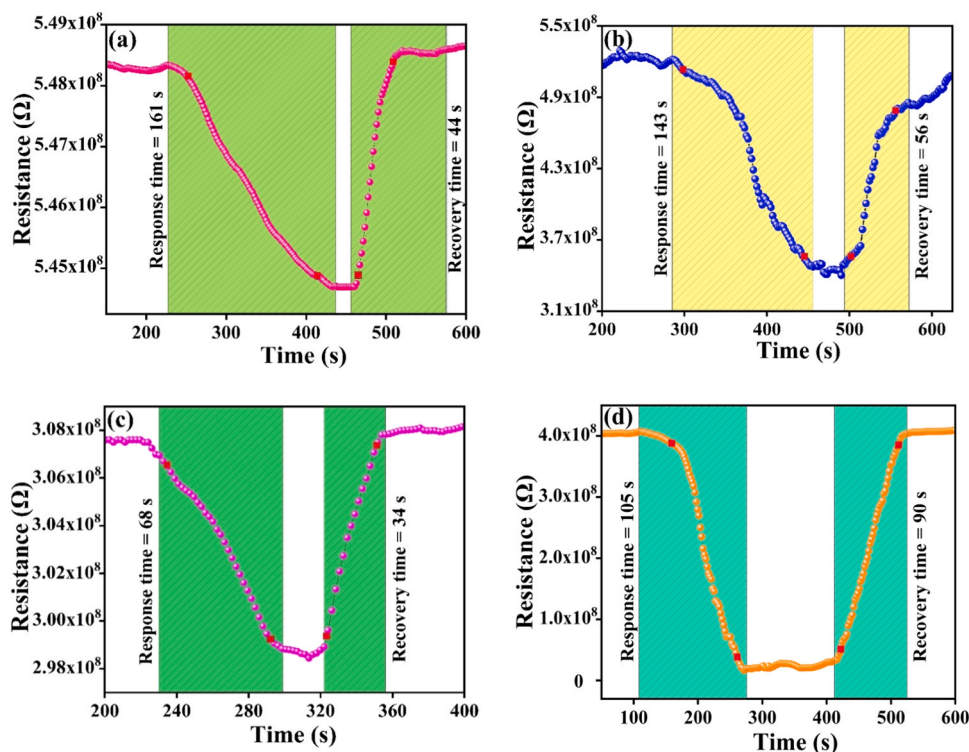


Fig. 14. Response and recovery of (a) CuW (b) ZnW (c) CdW and (d) SnW at RT.

Table 3

Comparison of toluene gas response with other compounds in the literature.

Sensor	Toluene Concentration (ppm)	Operating Temperature ($^{\circ}$ C)	Response (R_a/R_g)	Ref.
Au/ZnO nanoparticles	100	377	1	[50]
NiO/Fe ₂ O ₃	8000	RT	33	[51]
ZnO hexagonal nanotubes	700	RT	5.11	[52]
3D-TiO ₂ /graphene-CNT	500	RT	42.9	[53]
ZnFe ₂ O ₄	100	300	10	[54]
NiO/SnO ₂	50	330	11	[55]
Pd-ZnO	100	240	11	[56]
Pt-WO ₃	100	220	8	[57]
In ₂ O ₃ nanotubes	100	340	10.9	[58]
Co ₃ O ₄	100	150	6.08	[59]
SnWO ₄	100	RT	12.32	Present work

molecules presented in the air are chemisorbed, hereafter it is referred to as O₂ (ads), on the surface of SnW layer (Eq. 2). As a consequence, these O₂ (ads) molecules oxidize the conduction band (CB) of SnW sensor thereby the former becomes negatively charged as O₂⁻ (ads) (Eq. 3) oxygen anions (Fig. 18(i)-a,c) as a consequence electron depletion layer (EDL) forms around SnW particles in which the electrons might overcome the surface barrier potential. Basically, the adsorbed oxygen molecules grab the electrons mainly from W 5d orbitals in CB of SnW wherein these electrons are transferred from O 2p + Sn 5s (VB) due to the lower band gap of SnW (2.1 eV). In addition, oxygen vacancies of SnW also reduce the adsorbed oxygens as SnW is endowed with adequate oxygen vacancies essentially acts as electron donors. When SnW sensor is exposed to toluene gas, the O₂ (ads) molecules on the sensor surface strongly interacts with these gas molecules thereby releases plentiful electrons back into CB of SnW (Eq. 4). Thus, the width of the EDL decreases (Fig. 18(i)-b,d) as a result the resistance of SnW sensor

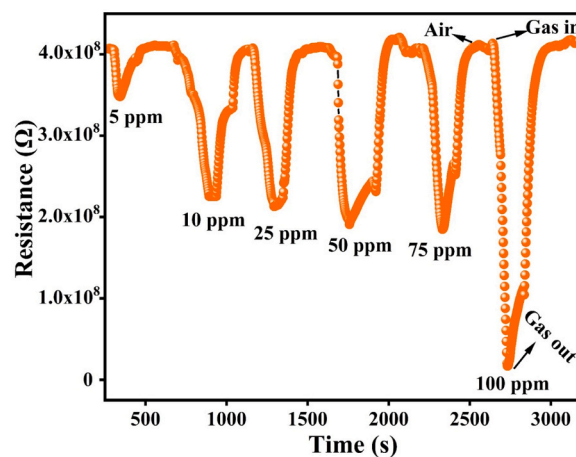


Fig. 15. Dynamic response-recovery of SnW sensor at RT.

decreased. Furthermore, SnW sensor has more surface area than the other compounds which might facilitate more active sites for adsorption of more oxygen molecules. The barrier potential (work function) of SnW (4.4 eV) is moderately lower than that of other compounds CuW (5.65 eV), ZnW (5.02 eV) and CdWO₄ (4.5 eV) as a result the electrons are easily migrated onto the surface to interact the adsorbed oxygens [22,60,61]. The SnW sensor offers multiple conducting path channels for the electrons to flow in between anode and cathode electrodes than CuW, ZnW and CdW since it has distinctive structure than the rest of the compounds. SnW is made of regular repeated Sn-O and W-O layers whereas CuW, ZnW and CdW have no such pattern. In SnW, the atoms that exist in 'bc' plane than that of 'ab' and 'ac' might contribute more to the conducting path channels. These are termed as the shortest bond distances on crystal plane 'bc' than that of the remaining crystal planes. From Fig. 3(d), it is viewed that the 'bc' plane has O-Sn-O-Sn and O-W-O-W-O and O-Sn-O-W-O/O-W-O-Sn-O conducting path channels.

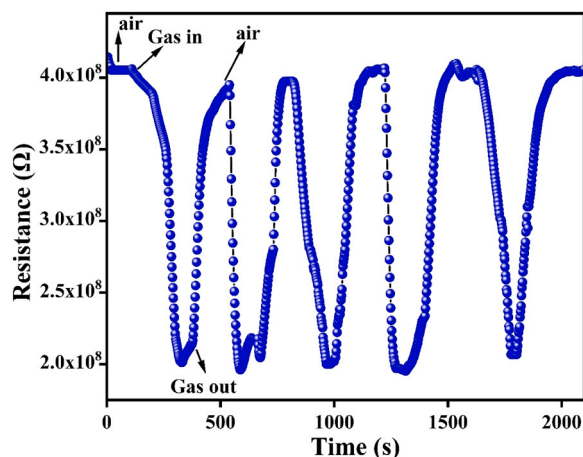


Fig. 16. Repeatability of SnW sensor towards 50 ppm.

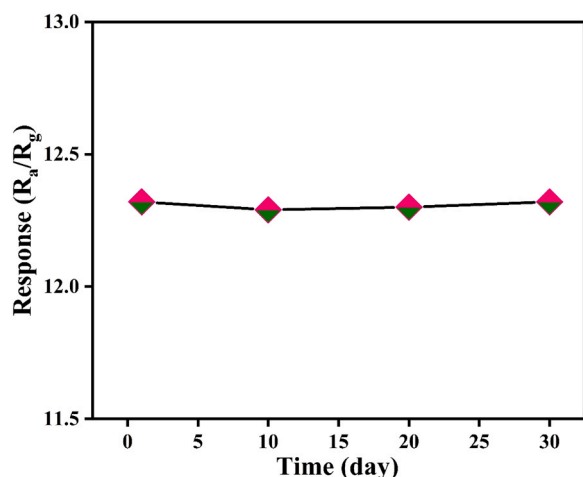


Fig. 17. Stability of SnW sensor for 30 days at RT.

However, O-Sn-O-Sn/O-W-O-W-O has the shortest route against O-Sn-O-W-O/O-W-O-Sn-O, clearly suggesting that the charge transport takes place effectively via the former route than that of the latter (Fig. 18 (ii)). On the other hand, CuW, ZnW and CdW have O-W-O-Cu-O-W-O, O-W-O-Zn-O-W-O and O-W-O-Cd-O-W-O conducting paths, respectively. These long path ways might provide higher resistance than O-Sn-O-W-O/O-W-O-Sn-O to the charge carriers as a result SnW sensors offers higher response as compared to CuW, ZnW and CdW sensors. The SnW sensor has the other following advantages over CuW, ZnW and CdW. The SnW has more formula units ($Z = 4$) than CuW ($Z = 2$), ZnW ($Z = 2$) and CdW ($Z = 2$) as a result SnW has more electron density than CuW, ZnW and CdW, therefore, the higher is the electron density higher is the response. Importantly, Sn 5s (lone pair electrons) contributes to both VB and CB which leads to effective hybridization among Sn 5s, O 2p and W 5d orbitals in SnW whereas this kind of hybridization lacks in the other sensing CuW, ZnW and CdW compounds. The SnW is endowed with the lowest E_g in comparison to CuW, ZnW and CdW and is also accountable for SnW to exhibit the significant response at RT. When SnW sensor exposed to $C_6H_5CH_3$ gas which releases more electrons by reacting with $O_{2(ads)}^-$ than the rest of the gases (except C_8H_{10}) (Eqs. (4) - (9)), thereby it increases the electron density in the CB of SnW, reducing the potential barrier and diminishes the resistance of this sensor and improves the response. Furthermore, $C_6H_5CH_3$ gas has relatively low activation energy in comparison to C_8H_{10} at RT. Therefore, SnW has exhibited more response to $C_6H_5CH_3$ than that of other tested gases. [62–65].

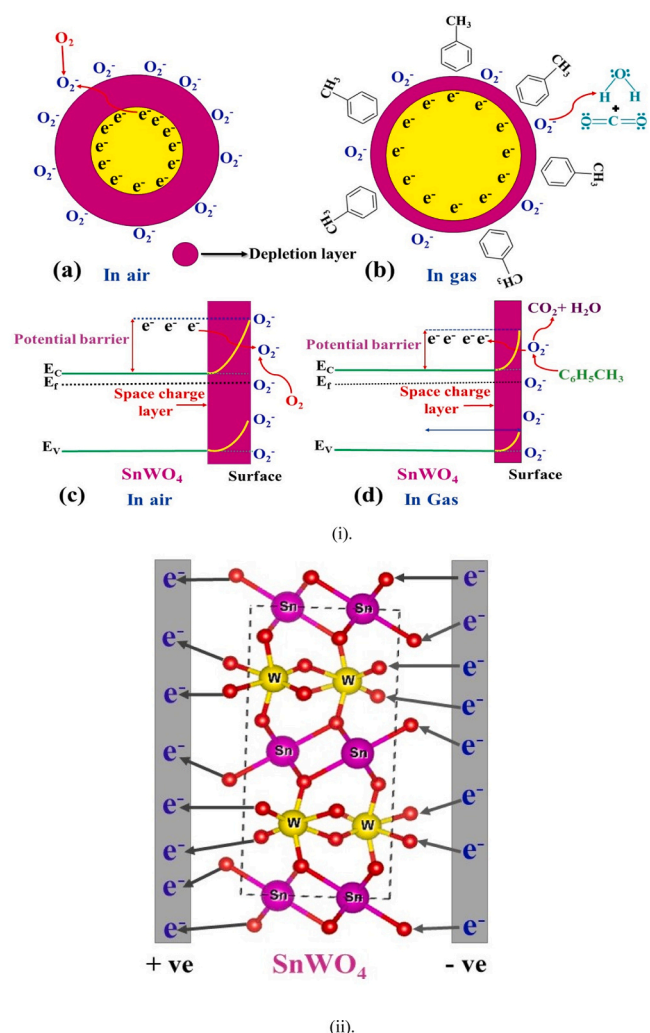
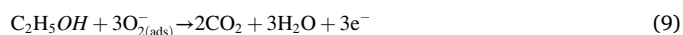
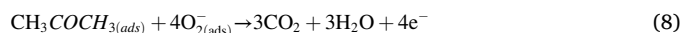
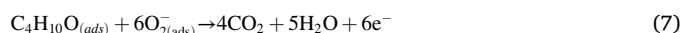
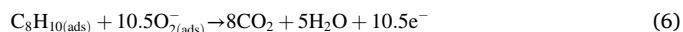
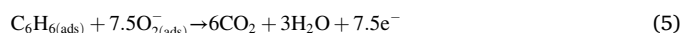
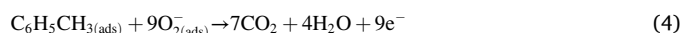


Fig. 18. A schematic illustration of the plausible mechanism of toluene gas sensing (i), the electron conducting pathways in SnW (ii).



4. Conclusions

In summary, XRD analysis vividly demonstrated that hydrothermal derived $CuWO_4$, $ZnWO_4$, $CdWO_4$ and $SnWO_4$ nanomaterials were grown in triclinic, monoclinic, monoclinic and orthorhombic crystal structures respectively. FESEM images indicated the rod like morphology for ZnW and CdW whereas spherical like structures for CuW and SnW compounds. The DFT and UV-Vis DRS analysis of SnW are well correlated.

BET surface analysis of CuW, ZnW, CdW and SnW compounds were respectively measured to be 20.4, 19.6, 17.8 and 24.2 m²/g, suggests that SnW has more surface area against other compounds. The higher response with the lowest detection limit of 5 ppm for toluene gas sensing at RT by SnW is ascribed to its shortest transport route of O-Sn-O-Sn and O-W-O-W-O. In comparison to the other compounds, SnW has a unique crystal structure wherein Sn-O layers alternatively stacked with W-O layers as a result it exhibited improved gas sensing at RT. The highest sensitivity and stability of SnW for toluene gas sensing at RT as compared to the other compounds is resulted from the interplay between the crystal structure and hybridization of Sn 5s, O 2p with W 5d. The lower work function of SnW (4.4 eV) than CuW (5.65 eV), ZnW (5.02 eV) and CdWO₄ (4.5 eV) is also another significant parameter for the highest gas sensing.

Author statement

E. Praveen Kumar: Conceptualization, Characterization analysis, Writing-Original draft. **N. Chanakya:** Methodology, Resources. **Ayesha Siddiqua:** Formal analysis, Validation. **Kurugundla Gopi Krishna:** Resources, Validation. **B. Vijaya Kumar:** Resources, Visualization. **P. Muralikrishna:** Resources, Validation. **G. Upender:** Supervision, Writing-Review and Editing.

Declaration of Competing Interest

The authors declare that they have no known competing financial interests or personal relationships that could have appeared to influence the work reported in this paper.

Data availability

No data was used for the research described in the article.

Acknowledgements

The one of the authors (Dr. G. Upender) profoundly thank Science and Engineering Research Board (SERB, under DST, Government of India) for providing the financial support under SURE scheme (File No. SUR/2022/003708).

Appendix A. Supporting information

Supplementary data associated with this article can be found in the online version at [doi:10.1016/j.sna.2024.115094](https://doi.org/10.1016/j.sna.2024.115094).

References

- Mohammad Raza Miah, Minghui Yang, Shahjalal Khandaker, M.Mahbubul Bashar, Abdulmohsen Khalaf Dhahif Alsukaibi, Hassan M.A. Hassan, Hussein Znad, Md. Rabiul Awual, Polypyrrole-based sensors for volatile organic compounds (VOCs) sensing and capturing: a comprehensive review, *Sens. Actuator A Phys.* 347 (2022) 113933.
- S.P. Subin David, S. Veeralakshmi, J. Sandhya, S. Nehru, S. Kalaiselvam, Room temperature operable high sensitive toluene gas sensor using chemiresistive Ag/Bi₂O₃ nanocomposite, *Sens. Actuators B Chem.* 320 (2020) 128410.
- K. Dutta, P.P. Chattopadhyay, Chia-Wei Lu, Mon-Shu Ho, P. Bhattacharyya, A highly sensitive BTX sensor based on electrochemically derived wall connected TiO₂ nanotubes, *Appl. Surf. Sci.* 354 (2015) 353–361.
- K. Dutta, B. Bhowmik, A. Hazra, P.P. Chattopadhyay, P. Bhattacharyya, An efficient BTX sensor based on p-type nanoporous titania thin films, *Micro Reliab.* 55 (2015) 558–564.
- Jingyu Shi, Jiawei Xiong, Liang Qiao, Chunbao Liu, Yi Zeng, Facile MOF-on-MOF isomeric strategy for ZnO@Co₃O₄ single-shelled hollow cubes with high toluene detection capability, *Appl. Surf. Sci.* 609 (2023) 155271.
- Christopher M. Filley, Cerebral white matter disorders, *Encycl. Hum. Brain* (2002) 715–731.
- C.M. Filley, W. Halliday, B.K. Kleinschmidt-Demasters, The effects of toluene on the central nervous system, *J. Neuroopathol. Exp. Neurol.* 63 (2004) 1–12.
- Sheng Zhou, Linguang Xu, Kui Chen, Lei Zhang, Benli Yu, Tongtong Jiang, Jingsong Li, Absorption spectroscopy gas sensor using a low-cost quartz crystal tuning fork with an ultrathin iron doped cobaltous oxide coating, *Sens. Actuators B Chem.* 326 (2021) 128951.
- Qingting Li, Wen Zeng, Yanqiong Li, Metal oxide gas sensors for detecting NO₂ in industrial exhaust gas: recent developments, *Sens. Actuators B Chem.* 359 (2022) 131579.
- Xinwei Chen, Tao Wang, Yutong Han, Wen Lv, Bolong Li, Chen Su, Min Zeng, Jianhua Yang, Nantao Hu, Yanjie Su, Zhi Yang, Wearable NO₂ sensing and wireless application based on ZnS nanoparticles/nitrogen-doped reduced graphene oxide, *Sens. Actuators B Chem.* 345 (2021) 130423.
- R. Dhilip Kumar, S. Karuppachamy, Microwave-assisted synthesis of copper tungstate nanopowder for supercapacitor applications, *Ceram. Int.* 40 (2014) 12397–12402.
- Yu Liu, Xinghua Li, Xiaowei Li, Changlu Shao, Chaohan Han, Jiayu Xin, Dongxiao Lu, Luyao Niu, Yujing Tang, Yichun Liu, Highly permeable WO₃/CuWO₄ heterostructure with 3D hierarchical porous structure for high-sensitive room-temperature visible-light driven gas sensor, *Sens. Actuators B Chem.* 365 (2022) 131926.
- Praveen Kumar, Shilpi Verma, Nataša. Čelan Korošič, Boštjan Žener, Urška Lavrenčič. Stangar, Increasing the photocatalytic efficiency of ZnWO₄ by synthesizing a Bi₂WO₆/ZnWO₄ composite photocatalyst, *Catal. Today* 397–399 (2022) 278–285.
- Weina Xu, Chunhua Zheng, Hao Hua, Qi Yang, Lin Chen, Yi Xi, Chenguo Hu, Synthesis and photoelectrochemical properties of CdWO₄ and CdS/CdWO₄ nanostructures, *Appl. Surf. Sci.* 327 (2015) 140–148.
- Kayla J. Pyper, Taylor C. Evans, Bart M. Bartlett, Synthesis of α-SnWO₄ thin-film electrodes by hydrothermal conversion from crystalline WO₃, *Chin. Chem. Lett.* 26 (2015) 474–478.
- Shiyue Yao, Min Zhang, Junwei Di, Zuoshan Wang, Yumei Long, Weifeng Li, Preparation of α-SnWO₄/SnO₂ heterostructure with enhanced visible-light-driven photocatalytic activity, *Appl. Surf. Sci.* 357 (2015) 1528–1535.
- Neha Jatav, Jyoti Kuntail, Danish Khan, Arup Kumar De, Indrajit Sinha, AgI/CuWO₄ Z-scheme photocatalyst for the degradation of organic pollutants: experimental and molecular dynamics studies, *J. Colloid Interface Sci.* 599 (2021) 717–729.
- V. Gajraj, C.R. Mariappan, CuWO₄: a promising multifunctional electrode material for energy storage as in redox active solid-state asymmetric supercapacitor and an electrocatalyst for energy conversion in methanol electro-oxidation, *J. Electroanal. Chem.* 895 (2021) 115–504.
- Mohammad Taghi Turchi Moghadam, Majid Seifi, Fatemeh Jamali, Sadegh Azizi, Mohammad Bagher Askari, ZnWO₄-CNT as a superior electrode material for ultra-high capacitance supercapacitor, *Surf. Interfaces* 32 (2022) 102134.
- S. Vinayaraj, K. Brijesh, P.C. Dhanush, H.S. Nagaraj, ZnWO₄/SnO₂ composite for supercapacitor applications, *Phys. B Condens. Matter* 596 (2020) 412369.
- S.P. Sai Sushma, G. Swarupa, T. Nagesh, P. Someshwar Pola, B.V. Rajitha, B. Vijaya Kumar, G. Upender, Enhanced photocatalytic activity of CdWO₄/BaTiO₃ heterostructure for dye degradation, *N. J. Chem.* 45 (2021) 1972–19732.
- A.Mano Priya, R.Kalai Selvan, B. Senthilkumar, M.K. Satheshkumar, C. Sanjeeviraja, Synthesis and characterization of CdWO₄ nanocrystals, *Ceram. Int.* 37 (2011) 2485–2488.
- Renkun Huang, Hao Ge, Xiujuan Lin, Yonglang Guo, Rusheng Yuan, Xianzhi Fu, Zhaohui Li, Facile one-pot preparation of α-SnWO₄/reduced graphene oxide (RGO) nanocomposite with improved visible light photocatalytic activity and anode performance for Li-ion batteries, *RSC Adv.* 3 (2013) 1235–1242.
- Fahad A. Alharthi, M. Shashank, J. Shashikanth, R. Viswantha, Abdulaziz Ali Alghamdi, Jaris. Algethami, Mabkhoot A. Alsaiani, Mohammed S. Jalalah, Nagaraju Ganganagappa, Hydrothermal synthesis of α-SnWO₄: application to lithium-ion battery and photocatalytic activity, *Ceram. Int.* 47 (2021) 10242–10249.
- Khamael Ibrahim Abdul Wahid, Chiheb Chaker, Hanen Chaker, Ni-doped SnO₂ thin films for NO₂ gas sensing application, *Sens. Actuator A Phys.* 360 (2023) 114498.
- Akshai Shyam, S. Aryalakshmi, Sudip K. Batabyal, Ramasubramanian Swaminathan, Exploration of the broadband photodetection feasibility of BiCuOS based heterostructure, *Sens. Actuator A Phys.* 360 (2023) 114559.
- Xi-Tao Yin, Davoud Dastan, Farzan Gity, Jing Li, Zhicheng Shi, Najlaa D. Alharbi, Ying Liu, Xiao-Ming Tan, Xiao-Chun Gao, Xiao-Guang Ma, Lida Ansari, Gas sensing selectivity of SnO₂-xNiO sensors for homogeneous gases and its selectivity mechanism: experimental and theoretical studies, *Sens. Actuator A Phys.* 354 (2023) 114273.
- T.V.M. Sreekanth, K. Prasad, Jihyung Yoo, Jonghoon Kim, Kisoo Yoo, CuWO₄ as a cost-effective electrocatalyst for urea oxidation reaction, *Inorg. Chem. Commun.* 154 (2023) 110933.
- Maurice I. Osotsi, Daniel K. Macharia, Bo Zhu, Zhaojie Wang, Xiaofeng Shen, Zixiao Liu, Lisha Zhang, Zhigang Chen, Synthesis of ZnWO_{4-x} nanorods with oxygen vacancy for efficient photocatalytic degradation of tetracycline, *Prog. Nat. Sci.: Mater. Int.* 28 (2018) 408–415.
- Feng Rong, Qifang Lu, Haixin Mai, Dehong Chen, Rachel A. Caruso, hierarchically porous WO₃/CdWO₄ fiber-in-tube nanostructures featuring readily accessible active sites and enhanced photocatalytic effectiveness for antibiotic degradation in water, *ACS Appl. Mater. Interfaces* 13 (2021) 21138–21148.
- V. Vinesh, M. Preeyanahaa, T.R. Naveen Kumar, Muthupandian Ashokkumar, C. L. Bianchi, B. Neppolian, Revealing the stability of CuWO₄/g-C₃N₄ nanocomposite for photocatalytic tetracycline degradation from the aqueous environment and DFT analysis, *Environ. Res.* 207 (2022) 112112.

- [32] N.F. Andrade Neto, Y.G. Oliveira, J.H.O. Nascimento, M.R.D. Bomio, F.V. Motta, Influence of pH variation on CuWO₄, CuWO₄/WO₃ and CuWO₄/CuO structures stabilization: study of the photocatalytic properties under sunlight, *J. Mater. Sci. Mater. Electron.* 31 (2020) 18221–18233.
- [33] M. Thirupathi, J. Vinoth Kumar, M. Vahini, C. Ramalingam, E.R. Nagarajan, A study on divergent functional properties of sphere like CuWO₄ anchored on 2D graphene oxide sheets towards the photocatalysis of ciprofloxacin and electrocatalysis of methanol, *J. Mater. Sci. Mater. Electron.* 30 (2019) 10172–10182.
- [34] Seied Mahdi Pourmortazavi, Mehdi Rahimi-Nasrabadi, Morteza Khalilian-Shalamzari, Hamid Reza Ghaeni, Seiedeh Somayyeh Hajmirsadeghi, Facile chemical synthesis and characterization of copper tungstate nanoparticles, *J. Inorg. Organomet. Polym.* 24 (2014) 333–339.
- [35] Parada Siri Wong, Titipun Thongtem, Anukorn Phuruangrat, Somchai Thongtem, Hydrothermal synthesis, characterization, and optical properties of wolframite ZnWO₄ nanorods, *CrystEngComm* 13 (2011) 1564–1569.
- [36] Y. Keereta, T. Thongtem, S. Thongtem, Fabrication of ZnWO₄ nanofibers by a high direct voltage electrospinning process, *J. Alloy. Compd.* 509 (2011) 6689–6695.
- [37] N.S. Pavithra, G. Nagaraju, S.B. Patil, Ionic liquid assisted hydrothermal synthesis of ZnWO₄ nanoparticles used for photocatalytic applications, *Ionics* 27 (2021) 3533–3541.
- [38] Changlin Yu, Jimmy C. Yu, Sonochemical fabrication, characterization and photocatalytic properties of Ag/ZnWO₄ nanorod catalyst, *Mater. Sci. Eng. B* 164 (2009) 16–22.
- [39] Rao Ede Sivasankara, Subrata Kundu, Microwave synthesis of SnWO₄ nanoassemblies on DNA scaffold: a novel material for high performance supercapacitor and as catalyst for butanol oxidation, *ACS Sustain. Chem. Eng.* 3 (2015) 2321–2336.
- [40] Swagata Dey, Rebecca A. Ricciardo, Heather L. Cuthbert, Patrick M. Woodward, Metal-to-metal charge transfer in AWO₄ (A = Mg, Mn, Co, Ni, Cu, Or Zn) compounds with the wolframite structure, *Inorg. Chem.* 53 (2014) 4394–4399.
- [41] Charles R. Lhermitte, Bart M. Bartlett, Advancing the chemistry of CuWO₄ for photoelectrochemical water oxidation, *Acc. Chem. Res.* 49 (2016) 1121–1129.
- [42] Pankaj Raizada, Sonali Sharma, Abhinandan Kumar, Pardeep Singh, Aftab Aslam Parwaz Khan, Abdullah M. Asiri, Performance improvement strategies of CuWO₄ photocatalyst for hydrogen generation and pollutant degradation, *J. Environ. Chem. Eng.* 8 (2020) 104230.
- [43] Zhongyi Sheng, Dingren Ma, Qing He, Kai Wu, Liu Yang, Mechanism of photocatalytic toluene oxidation with ZnWO₄: a combined experimental and theoretical investigation, *Catal. Sci. Technol.* 9 (2019) 5692–5697.
- [44] Parada Siri Wong, Titipun Thongtem, Anukorn Phuruangrat, Somchai Thongtem, Hydrothermal synthesis, characterization, and optical properties of wolframite ZnWO₄ nanorods, *CrystEngComm* 13 (2011) 1564–1569.
- [45] Tingjiang Yan, Liping Li, Wenming Tong, Jing Zheng, Yunjian Wang, Guangshe Li, CdWO₄ polymorphs: selective preparation, electronic structures, and photocatalytic activities, *J. Solid State Chem.* 184 (2011) 357–364.
- [46] M.G. Brik, V. Nagirnyi, M. Kirm, Ab-initio studies of the electronic and optical properties of ZnWO₄ and CdWO₄ single crystals, *Mater. Chem. Phys.* 134 (2012) 1113–1120.
- [47] M.M.P. Barros, K.C. Almeida, S.A. Silva, G. Botelho, Synthesis and characterization of α -SnWO₄ powders obtained by microwave-assisted hydrothermal method, *Ceramica* 68 (2022) 236–241.
- [48] Zhehao Zhu, Pranab Sarker, Chenqi Zhao, Lite Zhou, Ronald L. Grimm, Muhammad N. Huda, Pratap M. Rao, Photoelectrochemical properties and behavior of α -SnWO₄ photoanodes synthesized by hydrothermal conversion of WO₃ films, *ACS Appl. Mater. Interfaces* 9 (2017) 1459–1470.
- [49] Mohd Yaseen Lone, Avshish Kumar, Nagma Ansari, Samina Husain, Mohammad Zulfeqar, Ravi Chand Singh, Mushahid Husain, Enhancement of sensor response of as fabricated SWCNT sensor with gold decorated nanoparticles, *Sens. Actuator A Phys.* 274 (2018) 85–93.
- [50] K. Suematsu, K. Watanabe, A. Tou, Y. Sun, K. Shimano, Ultraselective, toluene-gas sensor: nanosized gold loaded on zinc oxide nanoparticles, *Anal. Chem.* 90 (2018) 1959–1966.
- [51] K. Arshak, I. Gaidan, NiO/Fe₂O₃ polymer thick films as room temperature gas sensors, *Thin Solid Films* 495 (2006) 286–291.
- [52] D. Acharyya, P. Bhattacharyya, Alcohol sensing performance of ZnO hexagonal nanotubes at low temperatures: a qualitative understanding, *Sens. Actuators B Chem.* 228 (2016) 373–386.
- [53] Y. Seekaew, A. Wisitsoraat, D. Phokharatkul, C. Wongchoosuk, Room temperature toluene gas sensor based on TiO₂ nanoparticles decorated 3D graphene-carbon nanotube nanostructures, *Sens. Actuators B Chem.* 279 (2019) 69–78.
- [54] C. Dong, X. Liu, X. Xiao, S. Du, Y. Wang, Monodisperse ZnFe₂O₄ nanospheres synthesized by a nonaqueous route for a highly selective low-ppm-level toluene gas sensor, *Sens. Actuators B Chem.* 239 (2017) 1231–1236.
- [55] L. Liu, Y. Zhang, G. Wang, S. Li, L. Wang, Y. Han, High toluene sensing properties of NiO-SnO₂ composite nanofiber sensors operating at 330 °C, *Sens. Actuators B Chem.* 160 (2011) 448–454.
- [56] Z. Lou, J. Deng, L. Wang, L. Wang, T. Fei, T. Zhang, Toluene and ethanol sensing performances of pristine and PdO-decorated flower-like ZnO structures, *Sens. Actuators B Chem.* 176 (2013) 323–329.
- [57] S. Vallejos, I. Gràcia, E. Figueras, C. Cané, Nanoscale heterostructures based on Fe₂O₃@WO_{3-x} nanoneedles and their direct integration into flexible transducing platforms for toluene sensing, *ACS Appl. Mater. Interfaces* 7 (2015) 18638–18649.
- [58] C. Xiao, L. Changbai, Z. Jinbao, L. Li, L. Haiying, H. Yue, Toluene-sensing properties of In₂O₃ nanotubes synthesized by electrospinning, *J. Semicond.* 35 (2014) 064005.
- [59] C. Zhao, B. Huang, J. Zhou, E. Xie, Synthesis of porous Co₃O₄ nanonetworks to detect toluene at low concentration, *Phys. Chem. Chem. Phys.* 16 (2014) 19327–19332.
- [60] Songcan Wang, Lianzhou Wang, Recent progress of tungsten and molybdenum based semiconductor materials for solar hydrogen production, *Tungsten* 1 (2019) 19–45.
- [61] Pan Li, Xian Zhao, Chun-jiang Jia, Honggang Sun, Liming Sun, Xiufeng Cheng, Li Liu, Weiliu Fan, ZnWO₄/BiOI heterostructures with highly efficient visible light photocatalytic activity: the case of interface lattice and energy level match, *J. Mater. Chem. A* 1 (2013) 3421–3429.
- [62] Yotsarayuth Seekaew, Anurat Wisitsoraat, Ditsayut Phokharatkul, Chatchawal Wongchoosuk, Room temperature toluene gas sensor based on TiO₂ nanoparticles decorated 3D graphene-carbon nanotube nanostructures, *Sens. Actuators B Chem.* 279 (2019) 69–78.
- [63] Dongzhi Zhang, Junfeng Wu, Peng Li, Yuhua Cao, Zhimin Yang, Hierarchical nanoheterostructure of tungsten disulfide nanoflowers doped with zinc oxide hollow spheres: benzene gas sensing properties and first-principles study, *ACS Appl. Mater. Interfaces* 11 (2019) 31245–31256.
- [64] Liupeng Zhao, Chaoge Zhou, Yun Zhou, Tianshuang Wang, Fangmeng Liu, Xu Yan, Geyu Lu, Peng Sun, Simple preparation of yolk-shell ZnCr₂O₄ microspheres and their application to xylene gas sensor, *Sens. Actuators B Chem.* 390 (2023) 133929.
- [65] Lili Sun, Yun Guo, Yao Hu, Shengsen Pan, Zheng Jiao, Conductometric n-butanol gas sensor based on Tourmaline@ZnO hierarchical micro-nanostructures, *Sens. Actuators B Chem.* 337 (2021) 129793.

E. Praveen Kumar received his master's degree in physics from Department of Physics, Osmania University, Hyderabad, India (2022). His research areas of interest are gas sensing, supercapacitors and photocatalysis of various metal oxide based semiconductors.

N. Chanakya received his master's degree in physics from Nizam College, Osmania University, Hyderabad, India (2018). His current research areas of interest are glasses, gas sensing, gas hydrates and photocatalysis.

Ayesha Siddiqua completed her master's degree in physics from Department of Physics, Osmania University, Hyderabad, India (2022). Currently, she is pursuing Ph.D (Osmania University) in the field of gas sensing and supercapacitors.

Kurugundla Gopi Krishna received his master's degree from Department of Physics, Sri Venkateswara University, Tirupati and he is currently pursuing Ph.D in Physics from NIT, Goa, India. He is also working as an Assistant Professor of Physics at CMR Technical Campus, Hyderabad. His research area of interest is gas sensing of various metal oxide based semiconductors.

B. Vijaya Kumar received his Doctorate degree in Chemistry from Osmania University, Hyderabad, India (2011). Presently, he is working as an Assistant Professor of Chemistry at Osmania University. His research areas of interest are photocatalysis and gas sensing of various metal oxide based semiconductors.









P. Muralikrishna received his Doctorate degree in Chemistry from Kakatiya University, Hanamkonda, India (2009). Presently, he is working as an Assistant Professor of Chemistry at CBIT, Hyderabad. His research areas of interest are photocatalysis and gas sensing of various metal oxide based semiconductors.

G. Upender received his Doctorate degree in Physics from Osmania University, Hyderabad, India (2010). He was recipient of Dr. D.S. Kothari PDF from UGC, New Delhi and carried out the work at School of Physics, University of Hyderabad, Hyderabad (2012). Presently, he is working as an Associate Professor of Physics at Osmania University. His research areas of interest are glasses, photocatalysis, supercapacitors, solid oxide fuel cells and gas sensing.

RESEARCH ARTICLE | FEBRUARY 07 2024

Magnetic field-induced narrow first-order and metamagnetic phase transitions of Nd_5Ge_3

Special Collection: [68th Annual Conference on Magnetism and Magnetic Materials](#)

S. Shanmukharao Samatham  ; Venkateswara Yenugonda ; Gowrinaidu Babbadi ;
Muralikrishna Patwari ; Arjun K. Pathak ; P. Manuel; D. Khalyavin; Stephen Cottrell; A. D. Hillier ;
K. G. Suresh 



AIP Advances 14, 025216 (2024)

<https://doi.org/10.1063/9.0000636>

Articles You May Be Interested In

Magnetic and magnetocaloric properties of ball milled Nd_5Ge_3

J. Appl. Phys. (April 2012)

Competing magnetic interactions in the intermetallic compounds Pr_5Ge_3 and Nd_5Ge_3

J. Appl. Phys. (March 2011)

Giant spontaneous magnetization jumps in $\text{LaFe}_{12}\text{B}_6$

Appl. Phys. Lett. (March 2016)







Special Topics Open for Submissions

[Learn More](#)

Magnetic field-induced narrow first-order and metamagnetic phase transitions of Nd_5Ge_3

Cite as: AIP Advances 14, 025216 (2024); doi: 10.1063/9.0000636
Submitted: 22 September 2023 • Accepted: 23 December 2023 •
Published Online: 7 February 2024



S. Shanmukharao Samatham,^{1,2,a)}  Venkateswara Yenugonda,^{2,3}  Gowrinaridu Babbadi,⁴ 
Muralikrishna Patwari,⁵  Arjun K. Pathak,^{3,b)}  P. Manuel,⁶ D. Khalyavin,⁶ Stephen Cottrell,⁶
A. D. Hillier,⁶  and K. G. Suresh² 

AFFILIATIONS

¹ Department of Physics, Chaitanya Bharathi Institute of Technology, Gandipet, Hyderabad 500 075, India

² Magnetic Materials Laboratory, Department of Physics, Indian Institute of Technology Bombay, Mumbai 400 076, India

³ Department of Physics, SUNY Buffalo State University, Buffalo, New York 14222, USA

⁴ Department of Physics, Government College (Autonomous), Rajahmundry 533 105, Andhra Pradesh, India

⁵ Department of Chemistry, Chaitanya Bharathi Institute of Technology, Gandipet, Hyderabad 500 075, India

⁶ ISIS Neutron and Muon Source, Rutherford Appleton Laboratory, Science and Technology Facilities Council, Didcot OX11 0QX, United Kingdom

Note: This paper was presented at the 68th Annual Conference on Magnetism and Magnetic Materials.

^{a)} **Author to whom correspondence should be addressed:** shanmukharao_physics@cbit.ac.in

^{b)} **Also at:** GE Research, Niskayuna, New York 12309, USA.

ABSTRACT

We report on the magnetic behaviour of Nd_5Ge_3 by investigating through magnetization, neutron diffraction and muon spin relaxation measurements. Temperature dependent-magnetization, muon depolarization rate (λ), initial asymmetry (A_0) and the stretched exponent (β) show a clear anomaly at the Néel temperature $T_N \sim 54$ K. However, the short-range correlated ferromagnetic interactions below T_N are inferred from the diffuse scattering mechanism as revealed by zero-field neutron diffraction data. Narrow first order phase transition is due to the competing interaction of a high temperature weak-antiferromagnetic and low temperature glassy states. Magnetic field-induced reentrant spin glass state from a magnetic glass state is observed, before it transforms to a ferromagnetic state.

© 2024 Author(s). All article content, except where otherwise noted, is licensed under a Creative Commons Attribution (CC BY) license (<http://creativecommons.org/licenses/by/4.0/>). <https://doi.org/10.1063/9.0000636>

I. INTRODUCTION

Nd_5Ge_3 is reported to exhibit dual magnetic transitions; AFM order ($T_N \sim 50$ K) and a second AFM order ($T_1 \sim 30$ K).¹⁻³ The second AFM transition is determined on the basis of the disappearance of a critical field (H_{cr}), remanent magnetization and a cusp in $\chi(T)$ at 26 K.² The observation of an easy destruction of zero field cooled (ZFC)- T_1 transition in field-cooled (FC) mode (in an applied field of 100 Oe) and absence of a specific heat anomaly at T_1 (both under ZFC and FC) lead us to believe a spin-glass like structure coexisting with long-range AFM order. In Nd_5Ge_3 , antiferromagnetic order is reported to occur at a temperature (52 ± 2) K.¹ The strongly coupled degrees of freedom in Nd_5Ge_3 are inferred from

the field-induced sudden jumps in isothermal magnetization, specific heat versus magnetic field and field-dependent resistivity below T_1 by Maji *et al.*³

Maji *et al.*,⁴ point out that the glassy state formation below T_1 is due to geometric frustration originating from the triangular arrangement of Nd atoms in the 6g position, using χ_{ac} , magnetic relaxation and thermoremanent magnetization measurements. At $T < 10$ K, magnetic structure of Nd_5Ge_3 is of the spin wave type.⁵ In the present work, we have reported/confirmed temperature driven first order phase transition and cluster-glass behaviour below 30 K and a weak antiferromagnetic state at 50 K. Neutron diffraction measurements suggest short-range magnetic correlations while Nd_5Ge_3 undergoes a field-induced ferromagnetic state eventually.

II. EXPERIMENTAL METHODS

Nd_5Ge_3 was prepared by arc-melting method as discussed in Ref. 4. X-ray diffraction (Cu- K_α radiation) pattern was collected at room temperature. The magnetization was measured using 7 T/2 K SQUID-VSM (Quantum Design, USA), in ZFC, field-cooled cooling (FCC) and field-cooled warming (FCW) modes. Powder neutron diffraction (ND) time of flight and muon spin relaxation (μSR) measurements were performed on WISH diffractometer and EMU instrument at ISIS, Rutherford Appleton Laboratory, United Kingdom respectively. μSR measurements were performed down to 2 K in zero field (ZF) and longitudinal field (LF) configurations. Muon relaxation function is given by $P_z(t) = [N_F(t) - \alpha N_B(t)]/[N_F(t) + \alpha N_B(t)]$, in which α is the calibration constant.

III. RESULTS AND DISCUSSION

A. Magnetization and neutron diffraction

Nd_5Ge_3 crystallizes in Mn_5Si_3 -type hexagonal structure ($P6_3/mcm$) as evident from the Rietveld refined⁶ x-ray diffraction pattern shown in Fig. 1(a). The lattice parameters $a = b = 8.7512(3)$ Å and $c = 6.6341(2)$ Å are in agreement with those reported in Refs. 2, 4, and 7. Figure 1(b) depicts the magnetization as a function of temperature $M(T)$. In 200 Oe, ZFC curve shows two peaks around 46.5 and 32.8 K which are in agreement with the literature.³ However, FCC magnetization does not exhibit a peak at T_i ,

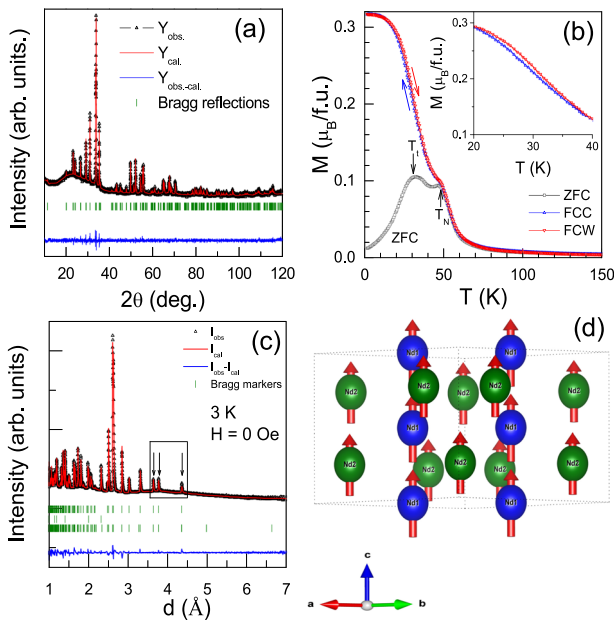


FIG. 1. (a) Rietveld refined x-ray diffraction of Nd_5Ge_3 at $T = 300$ K, crystallizing in the hexagonal structure. (b) $M(T)$ measured in a ZFC, FCC and FCW protocols. Inset: An enlarged view of FCC and FCW magnetization curves, showing a narrow thermal hysteresis. (c) Refined neutron diffraction pattern at 3 K, after H is made zero from 60 kOe. The magnetic peaks are indicated by arrows enclosed in a box. (d) Magnetic structure. $4d$ (Nd_1) and $6g$ (Nd_2), depicted in blue and green, order ferromagnetically along c -direction with unequal moments $1.81(4) \mu_B$ and $1.66(3) \mu_B$, respectively.

indicating that the low- T phase is more susceptible to the magnetic field due to prevailing FM interactions in the paramagnetic state (note that $T_i \approx \theta_W$, Weiss temperature). T_N is the AFM transition while T_f (T_f hereafter) is ascribed to spin-glass freezing temperature.^{3,4}

Figure 1(c) shows refined ND pattern at 3 K on d -spacing scale, measured after reducing the field to zero from 60 kOe. The magnetic peaks are indicated by arrows in the box. As evident from the magnetic structure of Nd_5Ge_3 shown in Fig. 1(d), Nd_1 at $4d$ -position possesses $1.81(3) \mu_B$ while Nd_2 at $6g$ -position has $1.66(3) \mu_B$. This infers to the field-induced ferromagnetic state. The magnetic moment $1.72 \mu_B/\text{Nd}$, at 3 K in the irreversible state, obtained from the refinement agrees well with that of from the magnetization data. However, magnetic fields of the order of 500 kOe are required to reach the magnetization saturation ($M_s = 3.5 \mu_B$ of Nd^{+3}) in the c -direction.² At $H = 0$ kOe, after applying 60 kOe, the nearest neighbour Nd_1 - Nd_1 ($4d$ - $4d$) inter-atomic distance and Nd_1 - Nd_2 ($4d$ - $6g$) inter-layer distance are found to be $3.3150(1)$ and $3.7581(2)$ Å respectively. These values are slightly less compared to zero-field values. Under 60 kOe, the inter-layer distance is observed to reduce from $3.7866(2)$ to $3.7553(1)$ Å. The decrease in the inter-layer distance can cause an enhancement of ferromagnetic interactions between the $4d$ and $6g$ positions.

B. Muon spin relaxation

Shown in Figs. 2(a) and 2(b) are the zero-field (ZF) asymmetry $A(t)$ plots for the temperatures below and above T_N , respectively. $A(t)$ curves are fit using a stretched exponential form of the muon decay function; $A(t) = A_0 \exp[-(\lambda t)^\beta] + \text{BG}^{8-10}$ where A_0 is an initial asymmetry, λ is the muon decay rate and β is the stretched exponent. A non-decaying function is used as the background (BG) function as the muon stops in the silver sample holder, fixed at $\text{BG} = 0.013746$ for the present case. Figure 2(c) shows the temperature variation of initial asymmetry $A_0(T)$. It is nearly independent of temperature down to 60 K below which it abruptly increases. Nevertheless, A_0 decreases rapidly between 0.2 (at 50 K) to 0.06 (at 30 K). At low temperatures, A_0 varies very weakly with temperature. The rapid decrease of initial asymmetry below 60 K is suggestive of antiferromagnetic order while A_0 is constant in the paramagnetic state. Further, a diverging relaxation rate $\lambda(T)$ from $T = 92$ K is shown in the Fig. 2(d) λ is $0.11 \mu\text{s}^{-1}$ at 92 K and reaches to a value of about $1 \mu\text{s}^{-1}$ while approaching T_N . λ in the paramagnetic state fits well to the critical scaling law $\lambda(T) = \lambda(0)[(T/T_N) - 1]^{-\beta_{\mu\text{SR}}}$ ^{11,12} where T_N is the antiferromagnetic ordering temperature and $\beta_{\mu\text{SR}}$ (not to be confused with the stretched exponential β) is the critical exponent; T_N and $\beta_{\mu\text{SR}}$ being equal to 54 K and 0.43, respectively. While the obtained T_N from the fit is in close agreement with the magnetization measurements, the critical exponent is indicative of three-dimensional Heisenberg model ($\beta_{\text{critical}} = 0.367$).¹³ Further reducing the temperature below 30 K, λ exhibits a plateau down to 9 K with a value of $\sim 0.2 \mu\text{s}^{-1}$. Thereafter, λ drops to $0.04 \mu\text{s}^{-1}$ at 2 K. This transition, also reflected in $A_0(T)$ and $\beta(T)$, is in good agreement with the freezing temperature observed in ZFC magnetization. Figure 2(e) shows the temperature variation of the stretched exponent β . ($\beta = 1$ at $T > 100$ K) decreases with decreasing temperature, exhibits a minimum of less than ~ 0.2 around the Néel

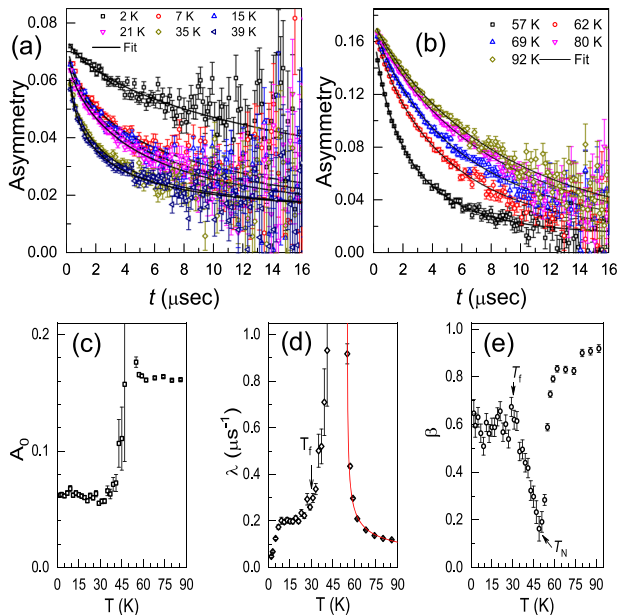


FIG. 2. ZF-time dependence of asymmetry for temperatures (a) below and (b) above T_N . The data is fit using stretched exponential function. (c) The temperature variation of the initial asymmetry, $A_0(T)$. Loss of A_0 is evident below T_N . (d) $\lambda(T)$, showing an abrupt increase of λ at the magnetic transition temperature while recovering below T_N . Again λ exhibits a slope change near T_f . Critical scaling fit to $\lambda(T)$ in the paramagnetic region gives $T_N \sim 54$ K. (e) The temperature dependence of the stretched exponent β . It exhibits a minimum at T_N and becomes temperature independent ($\beta_{\text{avg}} \sim 0.6$) below $T_f \sim 30$ K.

temperature, but then recovers, reaching a value of ~ 0.6 at approximately T_f . Below T_f , β exhibits a plateau, with an average value of ~ 0.6 . Though, the reduced β indicates the spin-glass behaviour, it is twice that of reported for a concentrated spin glass ($\beta \sim 1/3$ below T_g).^{8,11,12,14,15} In this case, $\beta(T)$ should be somewhat less than 1 and should be independent of temperature.⁸ However, in Nd_5Ge_3 , the low-temperature glassy state is a result of competing ferro and antiferro-magnetic interactions. $\beta_{\text{avg}} \sim 0.6$ below the freezing temperature for Nd_5Ge_3 may be the result of the same local cluster-moment environment for the muon relaxation below T_f with a unique single relaxation time and competing ferromagnetic and antiferromagnetic interactions.^{16,17}

C. Glassy behaviour

In re-entrant spin glass (RSG) systems; (i) a second order phase transition (SOPT) occurs from high- T long-range order to low- T glassy state with overlapping FCC and FCW curves (no thermal hysteresis),^{18,19} (ii) large thermomagnetic irreversibility (TMI)²⁰ in low fields due to ZFC and FCC separation starts to decrease with increasing H and becomes zero when the high- T long-range order phase is established below T_f , (iii) ZFC-magnetization relaxes with time while that of FCC does not relax and (iv) the sign reversal of CHUF (cooling and heating in unequal fields) protocol²¹ does not seem to affect the RSG transition except that the absolute TMI

changes monotonically with sign. On the other hand, in MG systems; (i) a marked thermal hysteresis between FCC and FCW arises due to arrested kinetics of first order magnetic phase transition, (ii) TMI is observed to increase with H , (iii) FCC magnetization relaxes with time while ZFC does not relax, (iv) low- T magnetic behavior is affected by the sign inequality of the CHUF protocol (discussed later) and (v) $M(H)$ virgin curve ($H: 0 \rightarrow H_{\text{max}} \rightarrow 0 \rightarrow -H_{\text{max}} \rightarrow 0 \rightarrow H_{\text{max}}$).^{22–24}

Figures 3(a)–3(f) show $M(T)$ measured in ZFC, FCC and FCW processes. ZFC- $M(T)$ in 200 Oe shows two peaks around 46.5 and 32.8 K respectively, denoted as T_N (Néel temperature) and T_f , which are in agreement with the literature.³ As the field strength is increased, $M(T_f)$ increases significantly and the peak becomes more pronounced and sharper while the peak at T_N smears out. However, FCC- $M(T)$ does not show a peak at T_f in 200 Oe indicating that the low- T phase is more susceptible to magnetic field. This also

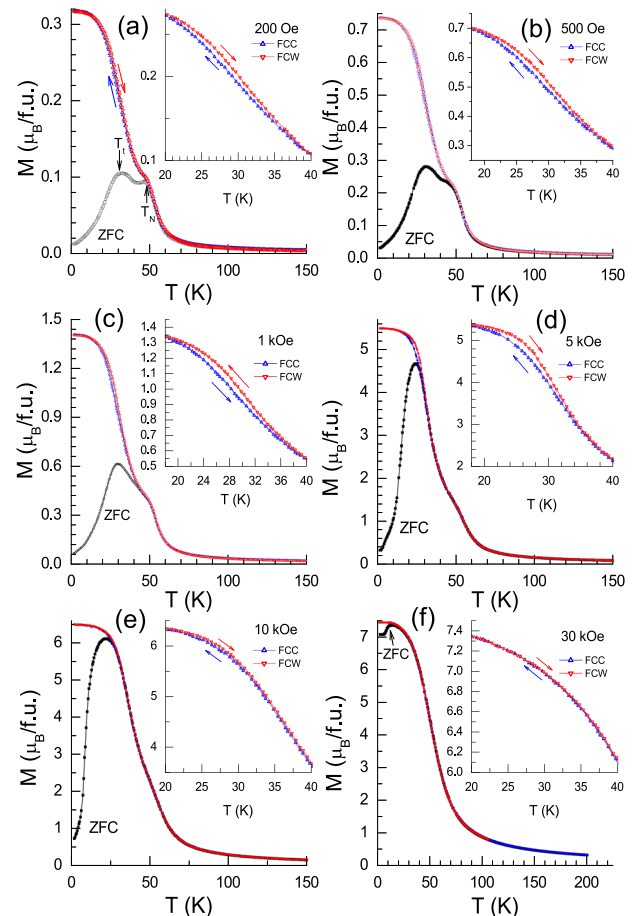


FIG. 3. (a)–(f) ZFC, FCC and FCW $M(T)$ in a few representative fields. T_N gets smeared out while ZFC- $M(T_f)$ is enhanced as H is increased. FCC and FCW curves saturate below 15 K. Insets: Enlarged view of FCC and FCW. Above 15 K and below 40 K, a narrow but distinct thermal hysteresis of FCC and FCW is noticed up to about 10 kOe, above which it vanishes.

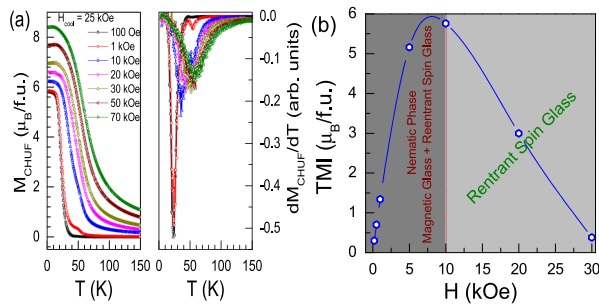


FIG. 4. (a) Left-panel: $M_{\text{CHUF}}(T)$ in different labeled measuring fields (H_{meas}) after cooling the system in 25 kOe (H_{cool}). For negative CHUF sign, two transitions while one transition for positive sign are noticed in terms of peaks represented by dM_{CHUF}/dT in the right panel. (b) TMI- H phase diagram. TMI increases up to H_{cr} and decreases thereafter (see text for explanation).

points out that the ZFC state is not an equilibrium state of the system. Eventually in higher fields, T_N is suppressed and ferromagnetic state emerges. The enlarged view of FCC and FCW from 20–40 K is shown in the insets of Figs. 3(a)–3(f). It is observed that the FCC and FCW curves exhibit a narrow thermal hysteresis in the temperature range $T \in [15, 40 \text{ K}]$. The measurements were repeated to confirm the narrow thermal hysteresis between FCC and FCW curves. Eventually, the thermal hysteresis ceases out in high magnetic fields.

Figure 4(a) shows magnetization, measured using CHUF protocol. Every time, the sample is cooled in the presence of 25 kOe ($H_{\text{cool}} > H_{\text{cr}}$) from 300 to 2 K and $M_{\text{CHUF}}(T)$ is measured in different magnetic fields as shown in the left panel of Fig. 4(a). Field-induced irreversible behaviour of FM state is evident from $M_{\text{CHUF}} > M_{\text{ZFC}}$ in fields of $H < H_{\text{cr}}$ while the magnetization values are comparable when $H > H_{\text{cr}}$. $M_{\text{CHUF}}(T)$ exhibits two recognizable transitions [i.e., two peaks in dM_{CHUF}/dT respectively at 26 and 52 K shown in Fig. 4(a)-right panel] for negative CHUF ($H_{\text{meas}} < H_{\text{cool}}$) while one transition (i.e., one peak in dM_{CHUF}/dT) for positive sign ($H_{\text{meas}} > H_{\text{cool}}$). This behaviour is in resemblance of MG state in $H < H_{\text{cr}}$ while RSG state in $H > H_{\text{cr}}$.

An investigation of magnetic relaxation and dynamic behavior of ac-susceptibility by Maji *et al.*^{4,25} suggests RSG state. Nonetheless, the thermal hysteresis between FCC and FCW, initial increase of TMI with H up to a certain field [Fig. 4(b)] and non-overlapping of ZFC and FCC curves hint the presence of MG with ZFC state being the non-equilibrium state. Furthermore, the virgin curve is observed to lie partly outside the envelope at 2.2 K.³ However, the separation between virgin curve and envelope is small compared to some of the typical phase coexistence compounds; doped-CeFe₂.^{26,27}

IV. SUMMARY

Summarizing, the magnetic properties of Nd₅Ge₃ have been studied using magnetization, neutron diffraction and muon spin relaxation (μSR) measurements. Nd₅Ge₃ undergoes an antiferromagnetic transition at $T_N \sim 54 \text{ K}$, followed by a low temperature glassy state. Zero-field neutron diffraction studies reveal short-range ferromagnetic correlations. Besides, a field-induced reentrant spin

glass state from a magnetic glass state is reported before the system transforms to a ferromagnetic state.

ACKNOWLEDGMENTS

S.S.S., Y.V. and K.G.S. acknowledge STFC for the Newton-Bhabha Fund to carry out neutron diffraction (ND) experiments (RB1610200) and JNCASR-Bangalore and DST-India for the financial support to perform muon spin relaxation measurements through Indian Access (RB1768039). S.S.S. thanks Akhilesh Kr. Patel for the help in ND experiments and Science and Engineering Research Board, India for Core Research Grant (CRG/2022/007993). This work was supported by the NSF, Launching Early-Career Academic Pathways in the Mathematical and Physical Sciences (LEAPS-MPS) program under Award No. DMR-2213412.

AUTHOR DECLARATIONS

Conflict of Interest

The authors have no conflicts to disclose.

Author Contributions

S. Shanmukharao Samatham: Conceptualization (lead); Data curation (equal); Formal analysis (equal); Funding acquisition (lead); Investigation (lead); Methodology (equal); Writing – original draft (lead); Writing – review & editing (equal). **Venkateswara Yenu-gonda:** Data curation (equal); Formal analysis (equal). **Gowrinaridu Babbadi:** Data curation (supporting); Investigation (supporting). **Muralikrishna Patwari:** Writing – original draft (supporting). **Arjun K. Pathak:** Funding acquisition (lead); Writing – review & editing (supporting). **P. Manuel:** Data curation (equal); Formal analysis (equal); Writing – review & editing (supporting). **D. Khalyavin:** Data curation (equal); Formal analysis (equal); Writing – review & editing (supporting). **Stephen Cottrell:** Data curation (equal); Formal analysis (equal); Writing – review & editing (supporting). **A. D. Hillier:** Data curation (equal); Writing – review & editing (supporting). **K. G. Suresh:** Conceptualization (equal); Supervision (equal); Writing – review & editing (equal).

DATA AVAILABILITY

The data that support the findings of this study are available from the corresponding author upon reasonable request.

REFERENCES



- P. Schobinger-Papamontellos and K. Buschow, *Journal of Magnetism and Magnetic Materials* **49**, 349–356 (1985).
- T. Tsutaoka, A. Tanaka, Y. Narumi, M. Iwaki, and K. Kindo, *Physica B: Condensed Matter* **405**, 180–185 (2010).
- B. Maji, K. G. Suresh, and A. K. Nigam, *EPL (Europhysics Letters)* **91**, 37007 (2010).
- B. Maji, K. G. Suresh, and A. K. Nigam, *J. Phys.: Condens. Matter* **23**, 506002 (2011).
- A. P. Vokhmyanin, B. Medzhi, A. N. Pirogov, and A. E. Teplykh, *Physics of the Solid State* **56**, 34 (2014).
- J. Rodriguez-Carvajal, *Physica B: Condensed Matter* **192**, 55–69 (1993).

- ⁷K. H. J. Buschow and J. F. Fast, *Physica Status Solidi (b)* **21**, 593–600 (1967).
- ⁸I. A. Campbell, A. Amato, F. N. Gygax, D. Herlach, A. Schenck, R. Cywinski, and S. H. Kilcoyne, *Phys. Rev. Lett.* **72**, 1291 (1994).
- ⁹R. M. Pickup, R. Cywinski, and C. Pappas, *Physica B: Condensed Matter* **397**, 99 (2007).
- ¹⁰M. T. F. Telling, J. Dann, R. Cywinski, J. Bogner, M. Reissner, and W. Steiner, *Physica B: Condensed Matter* **289–290**, 213 (2000).
- ¹¹R. Cywinski, S. H. Kilcoyne, and C. A. Scott, *J. Phys.: Condens. Matter* **3**, 6473 (1991).
- ¹²M. T. F. Telling, K. S. Knight, F. L. Pratt, A. J. Church, P. P. Deen, K. J. Ellis, I. Watanabe, and R. Cywinski, *Phys. Rev. B* **85**, 184416 (2012).
- ¹³S. N. Kaul, *J. Magn. Mater.* **53**, 5 (1985).
- ¹⁴A. Keren, P. Mendels, I. A. Campbell, and J. Lord, *Phys. Rev. Lett.* **77**, 1386 (1996).
- ¹⁵R. Renzi and S. Fanesi, *Physica B: Condensed Matter* **289–290**, 209 (2000).
- ¹⁶C. Shrivani, “Microscopic coexistence of antiferromagnetic and spin glass states in disordered perovskites,” Ph.D. thesis, ETH-Zürich, 2015.
- ¹⁷H. Klauss, M. Hillberg, W. W. M. A. C. de Melo, F. Litterst, M. Fricke, J. Hesse, and E. Schreier, *Phys. Rev. Lett.* **47**, 201–204 (1981).
- ¹⁸M. Gabay and G. Toulouse, *Phys. Rev. Lett.* **47**, 201–204 (1981).
- ¹⁹S. Niidera and F. Matsubara, *Phys. Rev. B* **75**, 144413 (2007).
- ²⁰K. Binder and A. P. Young, *Rev. Mod. Phys.* **58**, 801–976 (1986).
- ²¹A. Banerjee, A. K. Pramanik, K. Kumar, and P. Chaddah, *J. Phys.: Condens. Matter* **18**, L605 (2006).
- ²²M. K. Chattopadhyay, S. B. Roy, and P. Chaddah, *Phys. Rev. B* **72**, 180401 (2005).
- ²³S. B. Roy, M. K. Chattopadhyay, P. Chaddah, J. D. Moore, G. K. Perkins, L. F. Cohen, K. A. Gschneidner, and V. K. Pecharsky, *Phys. Rev. B* **74**, 012403 (2006).
- ²⁴V. K. Sharma, M. K. Chattopadhyay, and S. B. Roy, *Phys. Rev. B* **76**, 140401 (2007).
- ²⁵B. Maji and K. Suresh, *Journal of Alloys and Compounds* **605**, 29–33 (2014).
- ²⁶S. Roy, P. Chaddah, V. Pecharsky, and K. Gschneidner, *Acta Materialia* **56**, 5895–5906 (2008).
- ²⁷A. Haldar, K. G. Suresh, and A. K. Nigam, *Phys. Rev. B* **78**, 144429 (2008).

Room temperature sensing of ammonia and formaldehyde gases through novel anisotype heterojunction of p-Co₃O₄/n-Gd_{0.1}Ce_{0.9}O_{2-δ} as highly responsive and stable sensors

D. Satya Vardhan^a, Ch Sameera Devi^b, P. Nagaraju^c, P. Muralikrishna^d, B. Vijaya Kumar^e, G. Upender^a  

Show more 

 Share  Cite

<https://doi.org/10.1016/j.matchemphys.2023.128694> 

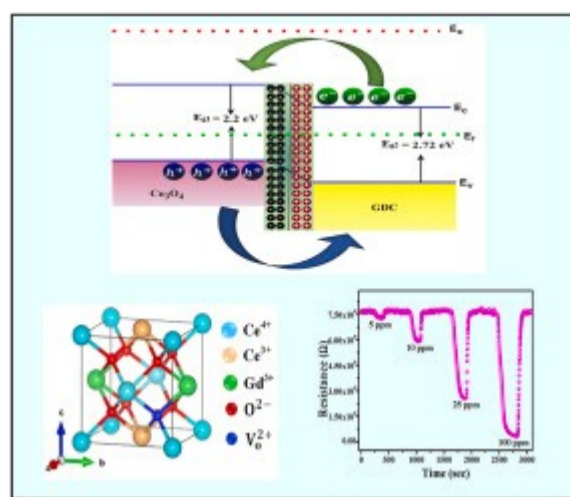
[Get rights and content](#) 

Highlights

- NH₃, CH₂O gases of each 5 ppm were predominantly detected by these sensors at RT.
- 2:1 Co₃O₄/GDC and 1:2 Co₃O₄/GDC exhibited rapid response than parent compounds.
- A_{1g} mode from Raman analysis revealed the formation of defects in heterostructures.
- O₂⁻ species played crucial role than O²⁻ and O⁻ at RT in chemisorption and in gas sensing.
- Heterostructures exhibited the high repeatability, stability, sensed multiple gases.

Abstract

The development of the room temperature (RT) gas sensors is absolute need. Hydrothermally and sol-gel derived Co₃O₄ and Gd_{0.1}Ce_{0.9}O_{2-δ} (GDC) were used to fabricate the novel heterostructures in the ratio of 1:1 Co₃O₄/GDC, 2:1 Co₃O₄/GDC and 1:2 Co₃O₄/GDC. These samples were scientifically analysed through X-ray diffraction (XRD), Field emission scanning electron microscope (FESEM), Energy dispersive X-ray (EDX) spectra, X-ray photoelectron spectroscopy (XPS), Fourier transform infrared spectroscopy (FTIR), Raman, UV-Vis-Diffuse reflectance spectra (DRS) and photoluminescence (PL). XRD, XPS together with FTIR and Raman spectra are the testimonial of the formation of Co₃O₄, GDC and their heterostructures. Interestingly, the performed gas sensing studies conclusively disclose that these sensors have adequate sensitivity to detect the tested gases at RT. Furthermore, O₂⁻ species played crucial role than O²⁻ and O⁻ in chemisorption and gas sensing mechanism. Additionally, 2:1 Co₃O₄/GDC and 1:2 Co₃O₄/GDC exhibited an enormous selectivity and highly responsive towards the detection of formaldehyde (CH₂O) and ammonia (NH₃), respectively. 2:1 Co₃O₄/GDC/1:2 Co₃O₄/GDC offered the high response (S) of 106.59/83.52 for CH₂O/NH₃ gas. In fact, the formation of anisotype p-n/n-p rather than isotype p-p/n-n junctions in 2:1 Co₃O₄/GDC and 1:2 Co₃O₄/GDC endowed these two heterostructures to exhibit quick response even at low ppm of selected gases. The outcome of this work might provide strategy for the design of novel sensing materials to detect multiple gases.



[Download: Download high-res image \(319KB\)](#)

[Download: Download full-size image](#)

Introduction

The ever-lasting progress in the science and technology has been considered as a two-edged sword since on one hand it comforts human beings on the other hand it imbalances the ecology. Various industries have been releasing volatile organic gases (VOCs) into the atmosphere resulting severe environmental pollution. Among various air pollutants, ammonia (NH_3) was recognised as combustible and equally hazardous. A few ppm level of NH_3 might severely impact the internal and external organs thereby making human beings highly susceptible to epidemics. Adding to this, prolonged exposure to NH_3 might result in blindness as well as enema of the lungs, eventually leads to death. In this regard, Occupational Safety and Health Administration (OSHA) declared that the permissible NH_3 subjection limit at working places is about 10min towards 35ppm [[1], [2], [3], [4]]. This is the reason why NH_3 gas sensors are essentially in demand for air quality monitoring. Besides, formaldehyde (CH_2O) is also creating serious threat to living beings by damaging eyes, nose and respiratory tract at low ppm concentrations [5]. Therefore, NH_3 and CH_2O sensors with high response, more selectivity, long-term stability and preferably low detection limit are highly in demand. Nonetheless, most of the developed sensors operate at high working temperatures ($>100^\circ\text{C}$). Hence, it is still a challenge to develop a new type of gas sensors with a high response to detect low ppm level of these gases at room temperature as an operating temperature. On the contrary, the gas leakage in industries has become most common issue. In order to prevent such tragedies in the industries an early detection of such gases is necessary.

In the recent past, metal oxide semiconductors (MOS) have extensively investigated in sensing such gases at ppm or ppb levels. In the last decade, to further improve the response sensitivity, enhance the response time (t_{res}) with high durability and reduce the operating temperature of semiconductor (SC) gas sensors and its composites based on transition metal oxides (TMO) were explored extensively. Semiconductor materials such as SnO_2 [6], In_2O_3 [7], WO_3 [8], ZnO [9] have proven to be excellent gas sensors. However, p- Co_3O_4 has gained widespread attention of the scientists due to its multiple oxidation states which is prone to adsorb more oxygen in the atmosphere resulting high sensing ability towards many VOCs [10]. Equally, in the recent past n- CeO_2 has emerged as the novel compound for the gas sensors applications [11] and also explored on a large scale for several applications including catalysis and the opto-electronic devices, owing to its multi valence including 4f shell electron [12]. Indeed, several attempts were made, especially rare-earths doping, to tailor the properties of CeO_2 to optimize its gas sensing performance. At large, Gd^{3+} added to CeO_2 has proven to amplify its catalytic and transport properties and also yielded the better gas sensing [[13], [14], [15], [16]]. Adding to this, recently, our group reported that Gd^{3+} doped CeO_2 (GDC), prepared by pulsed laser deposition, is highly effective gas sensor towards the detection of acetone gas [17]. Some of the recently developed NH_3 , CH_2O and the other gas sensors have highlighted the importance of the gas sensing by the various materials [[18], [19], [20], [21], [22], [23], [24], [25]]. Our extensive scientific search disclosed that no detailed investigation was reported so far on p- Co_3O_4 coupled with n-GDC.

In view of the above, the present investigation was aimed to deal with gas sensing properties of p- Co_3O_4 integrated with n-Gd doped CeO_2 (GDC) by forming p-n junctions. The different ratios were designed, using p- Co_3O_4 with n-GDC, vis-a-vis 1:1 Co_3O_4 /GDC, 2:1 Co_3O_4 /GDC, 1:2 Co_3O_4 /GDC with a view to fabricate for the detection of multiple gases with low ppm at RT as an operating temperature. The reason behind making compounds by these ratios is to incorporate varied p-n/p-p/n-n junctions in the respective heterostructures. By viewing the compounds, it is apparent that unequal proportions of p-n junctions might form in both 2:1 Co_3O_4 /GDC, 1:2 Co_3O_4 /GDC than that of 1:1 Co_3O_4 /GDC which certainly causes these heterostructures to exhibit more response to detect the gases at low detection limit.

Section snippets

Starting materials

The chemicals such as $\text{Co}(\text{NO}_3)_2 \cdot 6\text{H}_2\text{O}$ (S.D. Fine Chem. 98.5%), $\text{CO}(\text{NH}_2)_2$ (S.D. Fine Chem. 98.5%), $(\text{NH}_4)_2[\text{Ce}(\text{NO}_3)_6]$ (S.D. Fine Chem. 95%), $\text{Gd}(\text{NO}_3)_3 \cdot 6\text{H}_2\text{O}$ (Sigma-Aldrich Chem. 99.9%), HNO_3 (S.D. Fine Chem. 99.5%), $(\text{CH}_2\text{OH})_2$ (S.D. Fine Chem. 97%), $\text{C}_6\text{H}_8\text{O}_7$ (S.D. Fine Chem.), $\text{C}_2\text{H}_5\text{OH}$ (S.D. Fine Chem.), $\text{C}_3\text{H}_6\text{O}$ (S.D. Fine Chem.), NH_4OH (S.D. Fine Chem. AR 25%) were used as received in the synthesis of the compounds. ...

Co_3O_4 nanoparticles

Co_3O_4 nanoparticles were prepared through well-known one-pot hydrothermal method. The ...

X-ray diffraction

The crystal phases were identified with XRD technique and the investigated XRD traces of all the compounds are presented in Fig. 2(i) wherein Co_3O_4 exhibited peaks at $2\theta = 19^\circ, 31.3^\circ, 36.8^\circ, 38.5^\circ, 44.8^\circ, 55.7^\circ, 59.3^\circ$ and 65.2° which are indexed to crystal planes (111), (220), (311), (222), (400), (422), (511) and (440), respectively [26,27]. The Co_3O_4 has cubic-spinel crystal geometry with Fd-3m space group (JCPDS card No.43-1003) along with a lattice constant 8.0837 \AA with formula units ...

Gas sensing properties

In order to determine the sensors efficacy, in fact it is essential to measure the sensor's selectivity. To establish this fact, 100ppm of few volatile organic reducing gases like Acetone ($\text{C}_3\text{H}_6\text{O}$), Ammonia (NH_3), Methanol (CH_3OH), Ethanol ($\text{C}_2\text{H}_6\text{O}$), Benzene (C_6H_6), Formaldehyde (CH_2O) and the operating temperature as RT were selected to investigate the response of Co_3O_4 , GDC, 1:1 $\text{Co}_3\text{O}_4/\text{GDC}$, 2:1 $\text{Co}_3\text{O}_4/\text{GDC}$ and 1:2 $\text{Co}_3\text{O}_4/\text{GDC}$ sensors and the obtained results were illustrated in Fig. 12. Among the ...

Gas sensing mechanism

In p- Co_3O_4 , the Fermi level (E_f) lies close to VB while in n-GDC the Fermi level inclined towards CB. As reported, the work functions (ϕ) of p- Co_3O_4 (GDC) are 6.1 eV (4.6 eV) [63,64]. When p- Co_3O_4 is combined with n-GDC in accordance with 2:1/1:2 ratios, since ' ϕ ' of p- Co_3O_4 is larger than GDC, at the intimated interface the electrons from CB (Ce 4f+O 2p) of n-GDC migrates to VB (Co 3d+O 2p) of p- Co_3O_4 wherein the diffused electrons, especially Ce^{3+} 4f electrons combine with holes along ...

Conclusions

In a nutshell, RT based gas sensors using Co_3O_4 and GDC were successfully synthesized. All the employed experimental investigations notably advocated the formation of Co_3O_4 and GDC along with their heterostructures. Using these compounds, three tuneable ratios viz., 1:1, 2:1 and 1:2 were designed to improve the gas sensing performance. The research findings discerned that O_2^- species were instrumental in $\text{NH}_3/\text{CH}_2\text{O}$ detection mechanism. Amongst all the compounds, 2:1 $\text{Co}_3\text{O}_4/\text{GDC}$ and 1:2 $\text{Co}_3\text{O}_4/\text{GDC}$...

CRedit authorship contribution statement

D. Satya Vardhan: Conceptualization, Characterization analysis, Writing – original draft. **Ch Sameera Devi:** Methodology, Resources. **P. Nagaraju:** Resources, Validation. **P. Muralikrishna:** Funding acquisition, Formal analysis. **B. Vijaya Kumar:** Investigation, Visualization. **G. Upender:** Supervision, Writing – review & editing. ...

Declaration of competing interest

The authors declare that they have no known competing financial interests or personal relationships that could have appeared to influence the work reported in this paper. ...

Acknowledgements

The one of the authors (Dr. G. Upender) profoundly thank Science and Engineering Research Board (SERB, under DST, Government of India) for providing the financial support under SURE scheme (File No. SUR/2022/003708). ...

References (78)

Leila Vatandoust *et al.*

[Fabrication of ZnO-MWCNT nanocomposite sensor and investigation of its ammonia gas sensing properties at room temperature](#)

Synth. Met. (2021)

Madhukar Poloju *et al.*

[Improved gas sensing performance of Al doped ZnO/CuO nanocomposite based ammonia gas sensor](#)

Mater. Sci. Eng. B (2018)

Jebran Ahmad *et al.*

[Designing copper–nickel hybrid nanoparticles based resistive sensor for ammonia gas sensing](#)

Mater. Chem. Phys. (2023)

I-Ping Liu *et al.*

[Ammonia sensing performance of a platinum nanoparticle-decorated tungsten trioxide gas sensor](#)

Sensor. Actuator. B Chem. (2019)

Yan Chen *et al.*

[Design and evaluation of Cu- modified ZnO microspheres as a high performance formaldehyde sensor based on density functional theory](#)

Appl. Sur. Sci. (2020)

Caihong Fang *et al.*

[Coralloid SnO₂ with hierarchical structure and their application as recoverable gas sensors for the detection of benzaldehyde/acetone](#)

Mater. Chem. Phys. (2010)

Aijun Yang *et al.*

[Single ultrathin WO₃ nanowire as a superior gas sensor for SO₂ and H₂S: selective adsorption and distinct I-V response](#)

Mater. Chem. Phys. (2020)

Mingli Yin *et al.*

[One-pot synthesis of Co-doped ZnO hierarchical aggregate and its high gas sensor performance](#)

Mater. Chem. Phys. (2015)

D.N. Oosthuizen *et al.*

[Gas sensors based on CeO₂ nanoparticles prepared by chemical precipitation method and their temperature-dependent selectivity towards H₂S and NO₂ gases](#)

Appl. Surf. Sci. (2020)

Noriya Izu *et al.*

[Resistive oxygen gas sensors based on CeO₂ fine powder prepared using mist pyrolysis](#)

Sensor. Actuator. B Chem. (2002)



[View more references](#)

Cited by (5)

[Nanostructured hexagonal S-doped CeO₂ for effective Rh-B and MB dye degradation](#)

2025, Journal of Molecular Structure

Citation Excerpt :

...Specifically, the Ce possesses 6 s, 5d, and 4f states while the O ions have 2p states. The VB in pure CeO₂ (CS-0) resulted from a combination of Ce 5d and O 2p states [49], whereas VB in S-doped CeO₂ might have a significant contribution from S 3p orbitals apart from the above-mentioned states. On the other hand, the CB is predominantly composed of Ce 4f, Ce 5d, O 2p and S 3p orbitals....

[Show abstract](#) 

[Hydrothermal synthesis and gas sensing properties of lamellar Nickel Titanate](#)

2025, Journal of Alloys and Compounds

[Show abstract](#) 

[Selective trimethylamine sensors based on Co³⁺O⁴ modified WO³ spheres](#)

2024, Journal of Alloys and Compounds

Citation Excerpt :

...Compared with n-type materials, some p-type metal oxides have abundant oxygen adsorption, good redox behavior, and high catalytic efficiency, so they have obvious advantages of low operating temperature and high selectivity, especially for the selective oxidation of volatile organic compounds (VOCs) [22–26]. In p-type MOS materials, Co₃O₄ is considered an excellent material for dye degradation, energy storage, and gas detection due to its significant catalytic and oxygen adsorption properties [27–29]. In this paper, MOF derived Co₃O₄ nanoparticles were grown on WO₃ spheres by a simple solution treatment....

[Show abstract](#) 

[Novel p-Co³⁺O⁴/n-SnWO⁴ Heterostructure: Room Temperature Ethanol Gas Sensor](#)

↗

2024, Journal of Inorganic and Organometallic Polymers and Materials

[High Sensitivity Bi₂O₃/Ti₃C₂T_x Ammonia Sensor Based on Improved Synthetic MXene Method at Room Temperature](#) ↗

2024, Sensors

[View full text](#)

© 2023 Elsevier B.V. All rights reserved.





All content on this site: Copyright © 2025 Elsevier B.V., its licensors, and contributors. All rights are reserved, including those for text and data mining, AI training, and similar technologies. For all open access content, the Creative Commons licensing terms apply.



Full Length Article

Natural background outdoor gamma radiation levels and mapping of associated risk in Siddipet district of Telanagana State, India

K. Vinay Kumar Reddy ^a, G. Srinivas Reddy ^b, P. Muralikrishna ^c, S. Shravan Kumar Reddy ^a, B. Sreenivasa Reddy ^a  [Show more](#)  Share  Cite<https://doi.org/10.1016/j.nuclphysbps.2023.08.006> [Get rights and content](#) 

Abstract

Studies on natural background outdoor environmental radioactivity levels were conducted in Siddipet district of Telangana state, India. The investigation was carried out in the major villages/mandal head quarters of the district using scintillation detector (NaI(Tl)) based μ R- survey meter. The exposure rates measured on ground level and at 1 m height from ground (in μ R.h⁻¹) were converted into absorbed dose rates (in nGy.h⁻¹) and annual effect doses (mSv) using appropriate conversion factors. The natural background radiation levels at 1 m height were found to vary from 139 nGy h⁻¹ to 435 nGy h⁻¹ with an average of 235±47 nGy h⁻¹. The background radiation levels were observed to follow the normal distribution with a little deviation at the outliers. The excess lifetime cancer risk (ELCR) was also estimated.

Introduction

The natural background radiation is categorized into external and internal. The external radiation is incident directly on the body while in case of internal it enters into the body by ingestion/inhalation and damages the tissues within the human body. Natural background gamma radiation is of terrestrial origin. It comes under external radiation. Internal radiation is due to radon/thoron and their progeny as well as the radiological dosage derived from primary radionuclides through food, drink, and other environmental exposures [1]. Natural background gamma radiation is of significant role in total dose due to natural sources [12]. The source of radiation exposure is the presence of primordial radionuclides existing at trace elements in soils and materials used for construction. The variability of the radiation levels is dependent of geochemical composition of rocks which cause the formation of soils. With certain exceptions, such as shale, high radiation levels are connected with volcanic rocks like granite and low radiation levels are with sedimentary rocks [2]. The existence of trace amounts of the naturally occurring radioactive elements, uranium, thorium, and potassium in soil and rocks is the main cause of external exposure in the outdoors. The presence of radionuclides in the building materials as well as the surrounding geology can be the main causes of the indoor exposures [13].

In the model villages of Erravalli and Narasannapet in the Siddipet district of Telangana state, India, studies were held to estimate the radiation levels in indoor environs under the double bed room housing project [14]. The levels of natural background gamma radiation in the indoor environs of the model villages were identified to have a few abnormalities. Further, the study revealed that indoor radiation levels in these villages were elevated and comparable to the values obtained across the nation, but comparable to the natural background gamma radiation levels observed elsewhere in the state (Hyderabad and other places) [15], [5], [3]. Keeping in view of the above, it was planned to extend the study to the entire district of Siddipet. The present paper deals with the natural background gamma radiation levels in different villages / mandals (administrative head quarters for a group of few villages) of Siddipet district of Telangana state in indoors and outdoors. This study will be useful in supplementing the available nationwide data and to assess the radiation burden receiving by the population of this area in finding the safe human habitat.

Section snippets

Experimental

The study area of district has a total area of 3,842.33 square kilometers with the latitude and longitude of 18.10° N and 78.85° E respectively. The location is under the vicinity of Karimnagar granulitic terrain (KGT). Geological properties of the study area also include the presence of granitic rocks from the Peninsular Gneissic Complex. The special significance of the present work lies in observing the influence of constructions of major irrigation projects on natural background gamma ...

Results and discussion

The levels of natural background gamma radiation across the Siddipet district of Telangana state, India involve the implementation of μ R-survey meter. Table 1 presents the average of natural background radiation levels at different mandals in outdoors of the study area. The estimated natural background gamma radiation levels on ground were identified to vary between 148 nGy h⁻¹ and 487 nGy h⁻¹ with an average of 243±54 nGy h⁻¹. The same measured at 1 m height was observed to vary from 139 nGy h ...

Conclusions

The outdoor natural background radiation levels were estimated in Siddipet district of Telangana state, India. The levels, doses and excess lifetime cancer risk were observed to be higher in the study area. The elevated levels can be attributed to the local geological formations. The granitic rocks, good host for radioactive elements, present in the region result in the higher activity concentration. ...

Declaration of Competing Interest

The authors declare that they have no known competing financial interests or personal relationships that could have appeared to influence the work reported in this paper. ...

Acknowledgement

Authors thank Prof. K. Rama Reddy, Prof. P. Yadagiri Reddy and Prof. Ch. Gopal Reddy for their constant help and encouragement in the present study. Authors thank the Principal & Management of Chaitanya Bharathi Institute of Technology; and the Principal & Management of Mahatma Gandhi Institute of Technology for their support at various stages of the project.

Funding: The authors disclosed receipt of the following financial support for the research, authorship, and/or publication of this ...

[Special issue articles](#) [Recommended articles](#)

References (19)

M. Rafique *et al.*

[Evaluation of excess life time cancer risk from gamma dose rates in Jhelum valley](#)

J. Radiat. Res. Appl. Sci. (2014)

H. Taskin *et al.*

[Radionuclide concentrations in soil and lifetime cancer risk due to gamma radioactivity in Kirklareli](#)

Turkey J. Environ. Radioact. (2009)

K. Vinay Kumar Reddy *et al.*

[Baseline studies of radon/thoron concentration levels in and around the Lambapur and Peddagattu areas in Nalgonda district, Andhra Pradesh, India](#)

Radiat. Meas. (2003)

UNSCEAR

[Sources and Effects of Ionizing Radiation](#)

(2000)

J. Sanjurjo-Sánchez *et al.*

Geologic materials and gamma radiation in the built environment

Environ. Chem. Lett. (2017)

B. Sreenivasa Reddy *et al.*

Natural back ground radiation levels in the environment: urban khammam environs-A case study

Environ. Geochem. (2002)

M. Sreenath Reddy *et al.*

Study of natural background gamma radiation levels in Hyderabad and its surroundings, Andhra Pradesh, India

Indian J. Pure Appl. Phys. (2010)

K. Vinay Kumar Reddy *et al.*

Environmental radioactivity studies in the proposed Lambapur and Peddagattu uranium mining areas of Andhra Pradesh, Andhra Pradesh, India

Radiat. Prot. Dosim. (2012)

B. Sreenivasa Reddy *et al.*

Estimation of natural background gamma radiation levels in dwellings of Khammam district, Andhra Pradesh, India

Radiat. Prot. Environ. (2005)

There are more references available in the full text version of this article.

Cited by (1)

[Quantifying the Natural Radioactivity and Assessing the Radiation Risks in Different Rock Types at Wadi Nassib Area](#)



2024, Journal of Physics: Conference Series

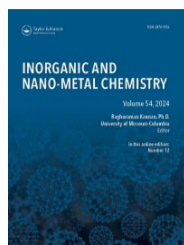
[View full text](#)

© 2023 Elsevier B.V. All rights reserved.



All content on this site: Copyright © 2025 Elsevier B.V., its licensors, and contributors. All rights are reserved, including those for text and data mining, AI training, and similar technologies. For all open access content, the Creative Commons licensing terms apply.





67

Views

0

CrossRef
citations to date

0

Altmetric

Research Article

Platycladus Orientalis mediated green synthesis of crystalline palladium nanoparticles as a potential and promising nano catalyst in the degradation of dyes for mitigation of environmental pollution

Aruna Kumari K, Bhagavanth Reddy G, Ramadevi V & Vasantha Mittepalli 

Received 09 Dec 2022, Accepted 27 Jan 2024, Published online: 08 Feb 2024

 Cite this article

<https://doi.org/10.1080/24701556.2024.2313225>

 Full Article

 Figures & data

 References

 Citations

 Metrics

 Read this article

 Reprints & Permissions

 Share

Related Research

People
also
read

Recommended
articles

Cited
by

The effects of biosynthesized silver nanoparticle on oxidative stress parameters in model organism *Artemia salina* (Linnaeus, 1758) >

İlkay Ünal et al.
Inorganic and Nano-Metal Chemistry
Published online: 23 Feb 2024

Controlled synthesis and tuned fluorescence properties of NaGdF₄:Yb, Er up-conversion nanocrystals through one-step hydrothermal approach >

Yu Wang et al.
Inorganic and Nano-Metal Chemistry
Published online: 20 Feb 2024

Opto-structural, morphological analysis of green synthesized AgNiCuO nanocomposites and their photocatalytic activity >

Abstract

In the current study, PdNPs were synthesized in a greener way using *Platycladus orientalis* leaves extract (PO) as a reducing agent with stabilizing ability. UV-Vis Spectroscopy (UV-Vis), Fourier Transform Infrared Spectroscopy (FTIR), X-Ray Diffraction (XRD), Transmission Electronic Microscopy (TEM) and Dynamic Light Scattering (DLS) were implicated in the characterization of nanoparticles. The structural and the morphological studies were determined using TEM and XRD analysis while UV-Vis and FTIR studies further confirmed the presence of optical, physical and chemical properties. The images of TEM manifested spherical NPs with an average size of 8 ± 3 nm. Phytochemicals present in the leaf extract enabled the reduction of Pd⁺² to Pd⁰ and also acted as a stabilizing agent. Later, the catalytic property of PdNPs, reduction of dyes like Rhodamine B (RhB), Methyl Orange (MO) and Crystal Violet (CV) was investigated. This green preparation method of making small spherical shaped PdNPs were successfully applied for the reduction of organic dyes.

Q Keywords: Palladium nanoparticles *Platycladus orientalis* methyl orange

Acknowledgments

All the authors are thankful to the Head, Department of Chemistry, Osmania University, Palamuru University for providing laboratory facilities. Authors also express their gratitude to Matrusri Engineering College, Hyderabad. We thank Central facilities and Research development (CFRD) of Osmania University, and SAIF, IIT Madras analytical team for providing spectral analytical facilities.

Disclosure statement

No potential conflict of interest was reported by the author(s).

[◀ Previous article](#)

[View latest articles](#)

[Next article ▶](#)

Log in via your institution

▶ [Access through your institution](#)

Log in to Taylor & Francis Online

▶ [Log in](#)

Restore content access

▶ [Restore content access for purchases made as guest](#)

Purchase options *

[Save for later](#)

PDF download + Online access

- 48 hours access to article PDF & online version
- Article PDF can be downloaded
- Article PDF can be printed

USD 64.00 [🛒 Add to cart](#)

Issue Purchase

- 30 days online access to complete issue
- Article PDFs can be downloaded
- Article PDFs can be printed

USD 836.00 [🛒 Add to cart](#)

* Local tax will be added as applicable

Information for

[Authors](#)
[R&D professionals](#)
[Editors](#)
[Librarians](#)
[Societies](#)

Open access

[Overview](#)
[Open journals](#)
[Open Select](#)
[Dove Medical Press](#)
[F1000Research](#)

Opportunities

[Reprints and e-prints](#)
[Advertising solutions](#)
[Accelerated publication](#)
[Corporate access solutions](#)

Help and information

[Help and contact](#)
[Newsroom](#)
[All journals](#)
[Books](#)

Keep up to date

Register to receive personalised research and resources by email

 [Sign me up](#)





  



Copyright © 2025 **Informa UK Limited** [Privacy policy](#) [Cookies](#) [Terms & conditions](#) [Accessibility](#)

Registered in England & Wales No. 01072954
5 Howick Place | London | SW1P 1WG

Harnessing durable antimicrobial cellulose cotton fabric coated with silver nanoparticles via a green approach for photocatalytic applications

Chandra Sekhar Espenti ^a, T.V. Surendra ^b, K.S.V. Krishna Rao ^c, Mushtaq Ahmad Ansari ^d, Kummara Madhusudana Rao ^e  ,
Sung Soo Han ^e  

[Show more](#) 

 Share  Cite

<https://doi.org/10.1016/j.molliq.2024.126483> 

[Get rights and content](#) 

Highlights

- Silver nanoparticles (AgNPs) were synthesized in an eco-friendly manner using leaf extract from *Bryophyllum pinnatum*.
- The synthesized nanoparticles were characterized using FTIR, XRD, UV-Visible spectroscopy, and EDX analysis.
- The antibacterial activity of the CCF-BP-AgNPs was tested against harmful bacteria, including *Escherichia coli*, *Bacillus subtilis*, and *Staphylococcus aureus*.
- The nanoparticles were produced from natural, environmentally friendly, and easily accessible raw materials.
- The photocatalytic activity of the coated cloth was assessed by observing the degradation of the organic dye Congo Red (CR) under simulated sunlight.

Abstract

Growing concern regarding microbial infections has prompted significant research into antimicrobial textiles. This study presents a green, eco-friendly approach to imparting antimicrobial properties to cellulose cotton fabric (CCF) by depositing silver nanoparticles (AgNPs) synthesized using *Bryophyllum pinnatum* (BP) leaf extract as a natural reducing agent. To improve the durability of AgNPs on CCF, an environmentally friendly method was used to synthesize AgNPs, which were subsequently applied to biocompatible CCF using BP leaf extract as a natural reducing agent. Owing to the presence of phytochemicals, the AgNPs were rapidly produced with a uniform size and shape under ambient conditions. The synthesized nanoparticles were characterized using techniques such as ultraviolet–visible spectroscopy, Fourier-transform infrared spectroscopy (FTIR), scanning electron microscopy (SEM) coupled with energy dispersive X-ray (EDX) spectrophotometry, and X-ray diffraction (XRD) analysis to confirm their size (average size 60.4 ± 8.5 nm), morphology, and crystalline structure. Subsequently, the CCF was coated with these AgNPs using an eco-friendly deposition method. The mechanical properties of the treated fabric were assessed to ensure that the coating process did not compromise the fabric's integrity or safety for human use. The results indicated that the CCF–BP–AgNPs retained

its mechanical strength and exhibited no cytotoxic effects, regarding it suitable for various applications in healthcare, apparel, and household textiles. The antibacterial activity of the CCF–BP–AgNPs was evaluated by measuring zone inhibition against *Escherichia coli*, *Bacillus subtilis*, and *Staphylococcus aureus*. The photocatalytic activity of the coated cloth was assessed by observing the breakdown of organic dye Congo Red (CR) in simulated sunlight. Interestingly, the CCF–BP–AgNPs demonstrated effective photocatalytic degradation of CR, revealing its potential for wastewater treatment and environmental remediation applications. The fabric's antimicrobial properties remained intact throughout the photocatalytic process, enabling disinfection and pollutant breakdown to occur simultaneously.

Graphical abstract

Schematic representation of the formation of silver nanoparticles on CCF.



[Download: Download high-res image \(109KB\)](#)

[Download: Download full-size image](#)

Introduction

Nanotechnology alters and enhances numerous advancements and initiatives: data innovation and prescription, transportation, energy, nutrition security, and several ecological applications. The subsequent section provides an overview of the rapidly developing advantages and uses of nanotechnology. The use of metal nanomaterials and nanocomposites in biological, biomedical, pharmaceutical, and textile applications in our daily lives is an emerging field of nanotechnology. Researchers have recently concentrated on formulating “smart fabrics” incorporating flexible nanoscale sensors and electronics for health monitoring and solar energy storage devices. Additionally, they are merging various metal nanomaterials and nanoparticles into assorted household and personal care materials to enhance their functionality, such as the incorporation of antibacterial silver nanoparticles (AgNPs) in soap [1], [2]. The addition of AgNPs to cellulose cotton fabric (CCF) is of great importance in a wide range of multifunctional applications, including sportswear, clothing, fashion, undergarments, medicine, and textiles [3], [4], [5], [6], [7]. Several researchers have explored means of adding AgNPs to CCF by chemically reducing Ag ions with NaBH₄, glucose, citrate, ascorbates, and hydrazine and subsequently using a coating method [8], [9], [10]. In the past decade, there has been a significant focus on employing green techniques to synthesize AgNPs from environmentally sustainable materials, aiming to address the previously mentioned issues. Furthermore, the use of these materials not only reduces silver ions to AgNPs, but also generates AgNP stability. In addition, coating with AgNPs provides strong binding ability and uniform distribution on CCF, thereby improving their long-term antibacterial properties, which can keep us healthy [11], [12].

Green chemistry's holistic approach towards sustainability and safety renders it important. We can improve the environment, economy, and health by incorporating green chemistry into scientific research, industry, and education [13], [14], [15], [16], [17], [18]. Over the last few decades, most research groups have concentrated on the fabrication of AgNPs because of their versatile and unique physicochemical properties, variety, and broad range of applications in diverse fields. Among the few nanometal particles (NMPs) used in biomedical applications, AgNPs stand out as one of the most fundamental and interesting NPs. Researchers have proven the potential anti-bacterial, anti-fungal, anti-cancer, and mechanical properties of AgNPs. Researchers are currently using the bio-reduction method to obtain NMPs from multiple plant parts, such as the leaves, flowers, pods, fruits, stems, strips, and root extracts [19], [20], [21], [22], [23], [24], [25], [26], [27], [28]. During production, phytochemicals and polyphenols in different plant parts aid NMPs bio-reduction and stabilization. These chemicals also exhibit antibacterial and medical uses. Chandra et al. [21] used biosynthesized *Terminalia chebula* (TC) leaf extract for biomedical applications yielded superior results revealing that the bio-synthesized TC–SNPs were effective at killing bacteria and especially effective against human pathogens like *Bacillus subtilis* (ATCC 6633) and *Escherichia coli* (ATCC 25922). Espenti et al. developed a strategy to bio-reduce the amount of silver in nanoparticles by extracting the bark of the *Syzygium cumini* (SC) plant. AgNPs were rapidly synthesized using the eco-friendly aqueous extracts of SC

stem bark. In addition to reducing Ag ions, the SC extract controlled the size of the AgNPs it produced, resulting in an average size of approximately 14nm. Evidence of AgNPs production was provided by investigations using TEM, UV–visible spectroscopy, FTIR, and DLS. The produced nanoparticles exhibited improved antibacterial activity against *Bacillus subtilis* and *Escherichia coli* [29]. Espenti et al. reported the bio-reductive production of nanosized AgNPs utilizing *L. acidissima* aqueous leaf and bark extracts. The investigation yielded nanoparticles with average diameters of 25 ± 26 and 12 ± 14 nm for the leaf and bark extracts, respectively. Synthesized AgNPs proved more efficient against *E. coli* and *B. subtilis*. In addition, UV–vis spectrometric analysis derived the rate constant (k_{obs}) [30].

Tropical and subtropical countries are home to *Bryophyllum pinnatum* (BP), also known as the alive plant, wonder leaf, or cathedral chimes. It shares a certain characteristic with a few other members of its genus: copious smaller-than-expected plantlets on the borders of its phylloclade's [31]. BP leaves exhibit various biological activities, such as anthelmintic, immunosuppressive, hepatoprotective, anti-diabetic, anti-nociceptive, anti-ulcer, anti-inflammatory, antioxidant, nephroprotective, anticonvulsant, analgesic, neuropharmacological, antihypertensive, and antipyretic properties [32], [33], [34]. Moreover, they are abundant in alkaloids, flavonoids, terpenoids, saponins, tannins, phenols, and glycosides [35]. The multifunctional phytochemicals found in BP leaf extract inspired our synthesis of AgNPs, which we subsequently applied to CCF. Finally, we examined the performance of CCF–BP–AgNPs as antibacterial agents and Congo Red (CR) removal from industrial textiles to determine their prospective use in industrial textiles.

The increasing prevalence of microbial infections necessitates innovative solutions in antimicrobial textiles. Traditional chemical methods of synthesizing AgNPs pose environmental and health risks, underscoring the requirement for green alternatives. This study introduces a novel, eco-friendly means of synthesizing AgNPs using BP leaf extract, which is rich in bioactive phytochemicals. The BP-synthesized AgNPs were incorporated into CCF, resulting in a durable, biocompatible antimicrobial textile. The significance of this approach lies in its adherence to green chemistry principles, ensuring safety and sustainability while providing effective antibacterial and photocatalytic properties. This dual functionality positions the CCF–BP–AgNPs as a promising solution to healthcare and environmental applications.

Section snippets

Materials

Sigma-Aldrich provides silver nitrate (AgNO_3), which was acquired at an impurity level of $\geq 99.5\%$. BP leaves that had just been harvested were collected from areas surrounding Tamil Nadu. Aldrich Chemical Ltd. in Mumbai, India, and the local textile market supplied nutrient agar (AR) and CR dye respectively. Double-distilled water (DDW) was utilized for all experiments. ...

Fabrication of CCF–BP–Ag nanocomposite

In the present study, a CCF–BP–AgNPs nanocomposite was developed using a “green approach” method. First, we produced AgNPs from aqueous Ag ions using an aqueous BP leaf extract, which contains numerous phenols, tannins, glucosides, terpenoids, and flavonoids that potentially aid in the reduction process. During reduction, the color of the solution turns brown, clearly indicating the formation of AgNPs using BP as a reducing agent (graphical abstract). Thereafter, we analyzed the synthesized ...

Conclusion

The current work describes a simple means of producing AgNPs utilizing aqueous BP leaf extract. The proposed approach is compatible with green chemistry principles, as the plant extract is a two-in-one molecule that potentially reduces the number of AgNPs produced while also keeping them stable. BP extract enables the simple manufacture of BP–Ag–NPs. According to green chemistry principles, the synthesis approach is effective since the plant extract possesses two qualities. For example, ...

CRedit authorship contribution statement

Chandra Sekhar Espenti: Investigation, Formal analysis, Data curation, Conceptualization. **T.V. Surendra:** . **K.S.V. Krishna Rao:** . **Mushtaq Ahmad Ansari:** . **Kummara Madhusudana Rao:** . **Sung Soo Han:**

Declaration of competing interest

The authors declare that they have no known competing financial interests or personal relationships that could have appeared to

influence the work reported in this paper. ...

Acknowledgements and Funding sources

K.M. Rao would like to acknowledge the National Research Foundation (NRF) of South Korea, funded by the Ministry of Education, Science, and Technology, (grant number: NRF-2 2019R1I1A3A01063627) and the authors acknowledge and extend their appreciation to the Researchers Supporting Project Number (RSPD2024R996), King Saud University, Riyadh, Saudi Arabia for supporting this study. ...

[Recommended articles](#)

References (56)

A.U. Toro *et al.*

[Functional finishing of textile materials using silver-based functionalized nanoparticles: health perspectives](#)

J. Barman *et al.*

[The role of nanotechnology based wearable electronic textiles in biomedical and healthcare applications](#)

Mater. Today Commun. (2022)

P. Velusamy *et al.*

[Recent advances in the development of antimicrobial nanotextiles for prevention of infectious diseases transmission in healthcare workers](#)

Green Chem. Sustainable Textiles (2021)

P. Behera *et al.*

[Supramolecular complex catalyzed green synthesis of 9-\(2-Ethylhexyl\) carbazole: Structural, optical and DFT investigations](#)

J. Mol. Struct. (2024)

R.K. Shekunti *et al.*

[Efficient green synthesis of a potential novel nosylation reagent and its DFT study](#)

Phosphorus, Sulfur, Silicon Related Elements (2023)

B. Sharma *et al.*

[Nano-biofertilizers as bio-emerging strategies for sustainable agriculture development: Potentiality and their limitations](#)

Sci. Total Environ. (2023)

C.S. Espenti *et al.*

[Bio-synthesis and characterization of silver nanoparticles using Terminalia chebula leaf extract and evaluation of its antimicrobial potential](#)

Mater. Lett. (2016)

R.B. Pandhare *et al.*

[Anti-urolithiatic activity of Bryophyllum pinnatum Lam. hydroalcoholic extract in sodium oxalate-induced urolithiasis in rats](#)

J. Tradit. Complement. Med. (2021)

J. Devillers *et al.*

[The usefulness of the agar-well diffusion method for assessing chemical toxicity to bacteria and fungi](#)

Chemosphere (1989)

K.C. Lee *et al.*

[Size effect of Ag nanoparticles on surface plasmon resonance](#)

Surf. Coat. Technol. (2008)



[View more references](#)

Cited by (0)

[View full text](#)

© 2024 Elsevier B.V. All rights are reserved, including those for text and data mining, AI training, and similar technologies.



All content on this site: Copyright © 2025 Elsevier B.V., its licensors, and contributors. All rights are reserved, including those for text and data mining, AI training, and similar technologies. For all open access content, the Creative Commons licensing terms apply.





Synergistic effects of graphene oxide and limestone calcined clay cement on mechanical properties and durability of concrete

Chava Venkatesh¹ · V. Mallikarjuna² · G. Mallikarjuna Rao³ · Santosh Kalyanrao Patil⁴ · B. Naga kiran⁵ · M. K. Yashwanth⁶ · C. Venkata Siva Rama Prasad⁷ · G. Sree Lakshmi Devi⁸

Received: 20 April 2024 / Revised: 18 June 2024 / Accepted: 28 June 2024 / Published online: 3 July 2024
© The Author(s), under exclusive licence to Springer Nature Switzerland AG 2024

Abstract

This study investigates the synergistic effects of graphene oxide (GO) and limestone calcined clay cement (LC3) on the mechanical properties and durability of concrete. Various concrete mixes were prepared, including a reference mix, conventional concrete with 0.04% GO, and LC3 mixes with different clinker to calcined clay ratios (50:30, 45:35, and 40:40), both with and without GO. The mechanical properties were evaluated through compressive strength and split tensile strength tests, while durability was assessed using rapid chloride permeability, rapid chloride migration, water absorption, and corrosion rate measurements. The results revealed that the incorporation of GO in conventional concrete significantly improved both mechanical and durability properties. Among the LC3 mixes, the 45:35 clinker to calcined clay ratio exhibited the best performance. The combination of GO and LC3 resulted in remarkable enhancements, with the LC3 mix containing 0.04% GO and a 45:35 clinker to calcined clay ratio demonstrating the highest strength and durability performance. A strong positive correlation between compressive strength and split tensile strength was observed, and a power function equation was derived to predict split tensile strength based on compressive strength. The findings highlight the potential of combining GO and optimized LC3 for the development of sustainable and high-performance concrete with enhanced mechanical properties and durability.

Keywords Graphene oxide · Limestone calcined clay cement · Mechanical properties · Durability · Synergistic effects · Sustainable concrete

1 Introduction

Concrete, the world's most extensively utilized construction material, is projected to see a surge in production, reaching an astounding 18 billion tonnes annually by the middle of the 21st century [1, 2]. However, the manufacturing

of ordinary Portland cement (OPC), the essential binding agent in concrete, poses a significant environmental challenge, contributing to nearly 8% of the world's total CO₂ emissions [3]. In an effort to curb the ecological footprint of cement production and foster sustainable building practices, there is an increasing focus on developing innovative

✉ Chava Venkatesh
chvenky288@gmail.com

¹ Department of Civil Engineering, CVR College of Engineering, Vastunagar, Mangalpalli, Ibrahimpatnam, Telangana 501510, India

² Department of Civil Engineering, V. R. Siddhartha Engineering College, Vijayawada, India

³ Department of Civil Engineering, Chaitanya Bharathi Institute of Technology, Gandipet, Telangana, India

⁴ Department of Civil Engineering, K J College of Engineering and Management Research, Pune, Maharashtra 411048, India

⁵ Department of Civil Engineering, Rajeev Gandhi Memorial College of engineering and technology, Nandyal District, Andhra Pradesh, India

⁶ Department of Civil Engineering, Maharaja Institute of Technology Mysore, Mandya, Karnataka 571477, India

⁷ Department of Civil Engineering, Malla Reddy Engineering College, Secunderabad, Telangana 500100, India

⁸ Department of Civil Engineering, Nalla Malla Reddy Engineering College, Medchal District, Hyderabad, Telangana 500088, India

Advancements in predicting scour depth induced by turbulent wall jets: A comparative analysis of mathematical formulations and machine learning models

Cite as: AIP Advances 14, 055008 (2024); doi: 10.1063/5.0203444

Submitted: 13 February 2024 • Accepted: 11 April 2024 •

Published Online: 3 May 2024



View Online



Export Citation



CrossMark

Kamalini Devi,^{1,a)}  Jnana Ranjan Khuntia,^{1,b)}  Mohd Aamir Mumtaz,^{2,c)}  Mohamed H. Elgamal,^{2,d)} 
and Bhabani Shankar Das^{3,e)} 

AFFILIATIONS

¹Civil Engineering Department, Chaitanya Bharathi Institute of Technology (A), Hyderabad 500075, India

²Civil Engineering Department, College of Engineering, Imam Mohammad Ibn Saud Islamic University (IMSIU), Riyadh 11432, Saudi Arabia

³Civil Engineering Department, National Institute of Technology, Patna 800005, India

^{a)}Email: kamalinidevi1@gmail.com

^{b)}Email: jnanaranjan444@gmail.com

^{c)}Author to whom correspondence should be addressed: mmaamir@imamu.edu.sa

^{d)}Email: mhelgamal@imamu.edu.sa

^{e)}Email: bsd.nitrkl@gmail.com

ABSTRACT

This study examines the scour depth induced by turbulent wall jets and proposes novel mathematical formulations to predict the depth of scouring. Through a comprehensive gamma test, key parameters influencing the scour depth are identified, including the apron length, densimetric Froude number, median sediment size, tailwater level, Reynolds number, and Froude number of the jet. Regression analysis is subsequently conducted to establish relationships between the dependent parameter and the aforementioned independent variables. A comparative analysis is then undertaken between the measured scour depths and those predicted by existing equations from previous studies. Furthermore, predictive models leveraging the support vector machine, artificial neural network with particle swarm optimization, M5 tree algorithm, gene expression programming, and adaptive neuro-fuzzy inference system (ANFIS) are developed using the collected data. Statistical metrics are employed to evaluate the performance of each model and the regression equation. The effectiveness of each model in predicting scour depth is demonstrated. Notably, ANFIS yields a coefficient of determination of 0.809 and a root mean square error (RMSE) of 1.585. Multi-nonlinear regression analysis exhibits a coefficient of determination of 0.752 and an RMSE of 0.421, while the M5 tree achieves a coefficient of determination of 0.739 and an RMSE of 1.874, demonstrating superior performance compared to other machine learning techniques and regression equations employed in this study.

© 2024 Author(s). All article content, except where otherwise noted, is licensed under a Creative Commons Attribution (CC BY) license (<https://creativecommons.org/licenses/by/4.0/>). <https://doi.org/10.1063/5.0203444>

I. INTRODUCTION

Scouring refers to the erosion or removal of sediments from the bed of a water body, such as a river or channel, due to the kinetic energy of flowing water. Among varieties of scouring mechanisms, a scour hole due to turbulent wall jets is one that occurs when a

high-velocity fluid jet impinges on a boundary wall or a submerged structure, causing turbulence and changes in the flow characteristics. The maximum scour depth caused by turbulent wall jets depends on various factors, including the velocity and discharge of the jet, sediment properties, bed material composition, and the geometry of the channel or water body. Additionally, scour depth is influenced by

A comparative assessment of biomethane potential of fresh fecal matter and fecal sludge and its correlation with malodor

Short Research and Discussion Article Published: 16 April 2024


Volume 31, pages 31619–31631, (2024) [Cite this article](#)



Environmental Science and Pollution Research

[Aims and scope](#)

[Submit manuscript](#)

[Atun Roy Choudhury](#), [Neha Singh](#), [Jitesh Lalwani](#), [Mallikarjuna Goriparthi Rao](#), [Bhanu Prakash Konyala](#), [Chiradeep Nadella](#), [Abhishek Nayakwadi](#) & [Sankar Ganesh Palani](#) 

 215 Accesses [Explore all metrics](#) →

Abstract

Comprehensive and proper management of fecal sludge (FS) is an ongoing concern in many nations. Decentralized fecal sludge treatment plants (FSTPs) are effective in this regard; however, many have experienced strong public opposition based partly on suspicion of malodor. Fecal sludge and freshly generated fecal matter (FM) samples from various FSTPs were collected, characterized, and investigated for biomethane potential. The homogenized

**Department of Civil Engineering, Chaitanya Bharathi Institute of Technology, Gandipet,
500075, Hyderabad, India**

Mallikarjuna Goriparthi Rao

Contributions

All authors contributed to the study's conception and design. Material preparation, data collection, and analysis were performed by Atun Roy Choudhury, Konyala Bhanu Prakash, Nadella Chiradeep, and Nayakwadi Abhishek. The first draft of the manuscript was written by Atun Roy Choudhury, Neha Singh, Sankar Ganesh Palani, Jitesh Lalwani, and Goriparthi Mallikarjuna Rao, and all authors commented on previous versions of the manuscript. All authors read and approved the final manuscript.

Corresponding author

Correspondence to [Sankar Ganesh Palani](#).

Ethics declarations

Ethics approval

Not applicable.

Consent for publication

Not applicable.

Competing interests

The authors declare no competing interests.

Additional information

Responsible Editor: Ta Yeong Wu

Publisher's Note

Experimental Study on Hardened State Properties of Self-Curing Concrete

K. Vishnu¹, K. Jagannatha Rao², V. Bhikshma³

¹Research scholar, Department of Civil Engineering, University College of Engineering, Osmania University, Hyderabad, India.

²Professor & Head of Civil Engineering Department, Chaitanya Bharathi Institute of Technology, Hyderabad, India.

³Professor, Department of Civil Engineering, University College of Engineering, Osmania University, Hyderabad, India.

Abstract

Concrete is the mostly used construction material in the modern world. However, with the rise of urbanization, heavy use of concrete has started to threaten the humankind due to its disastrous effect on environment. Steel and concrete industries are one of the major CO₂ producing industries. Statistics show that an average person uses 1 m³ of concrete in a year making it the most used material and the cement production on global scale may reach 4800 Million Metric tons by 2030 and India being the second largest producer in 2018 with 290 million metric tons. To control this a new environment-friendly structural materials should be utilized instead of ordinary concrete to cope with environmental problems. This has led to the search for alternate sustainable materials to replace Cement.

With good success, mineral admixtures have been used to partially replace cement. The technical advantage of using these mineral admixtures is the improvement of many properties in the fresh and hardened phases, including enhanced durability in acidic environments and higher ultimate strength of Concrete. GGBS (Ground granulated blast furnace slag) reaction is both hydraulic and pozzolanic because of the particle shape and increased hydration, GGBS concrete has greater particle packing.

Curing of concrete place a major role on strength development and durability of concrete. Improper curing can affect the concrete performance and durability easily. In conventional curing this is achieved by external curing applied after mixing, placing and finishing. Water is maximum utilized commodity and because of this the day- by-day level of the water table is going down. If water has to be purchased for construction works, the cost of construction rises much higher. Also, in case of concreting works done at heights, vertical members, sloped roofs and pavements, continuous curing is very difficult.

The performance of self-curing concrete using PEG as self-curing agent with different molecular weights concluded that addition of hydrophilic chemicals in water which is mixed in concrete reduces the evaporation of water.

The research identifies Durability properties of the concrete higher for mix C20G1.5P at 7, 14, and 28 days for M20 and M40 grades, However, for the M60 grade, the mix ratio C10G1P demonstrates the highest strength, suggesting the influence of concrete grade in combination with Ground Granulated Blast Furnace Slag (GGBS) and Polyethylene Glycol (PEG 400). Increasing the supplementary cementitious material and self-curing agent strength and durability of concrete increases and up to certain point and then decreases. In addition, the micro structural analyses have been carried out for



Investigation on Mechanical properties of self-curing concrete containing GGBS

Kampilla.Vishnu¹, K.Jagannatha Rao², V.Bhikshma³

¹Research scholar, Department of Civil Engineering, University College of Engineering, Osmania University, Hyderabad, India.

²Professor & Head of Civil Engineering Department, Chaitanya Bharathi Institute of Technology, Hyderabad, India.

³Senior Professor, Department of Civil Engineering, University College of Engineering, Osmania University, Hyderabad, India.

Abstract

Curing of concrete nothing but maintaining adequate moisture levels in the preliminary stages of concrete to development its respective properties. However, practical limitations are making difficult to curing. Consequently, researchers have explored the self-curing agents as a solution. These agents aim to decrease water evaporation from the concrete and enhance its water retention ability compared to conventional concrete.

The present investigation involves the use of self-curing agent viz., polyethylene glycol (PEG) of molecular weight 400 (PEG 400) for dosages of range from 0% to 2% by weight of cement added and Ground granulated blast furnace slag (GGBS) added 0% to 40% by replacing cement. Self-curing concrete containing GGBS was developed for M20, M40 and M60 grades of concrete. Compressive strength, split tensile strength and flexural strength properties of self-curing concrete containing GGBS and conventional concrete are evaluated. There is an increase about 10% - 15% in mechanical properties of self-curing concrete containing GGBS mixes observed when compared to conventional concrete.

Keywords: Self-curing concrete; Conventional concrete; Polyethylene glycol (PEG-400); Compressive strength; Flexural strength; Split tensile strength.

Prediction of Strength and Fresh Properties of Steel Fiber Reinforced Self Compacting Concrete Using Artificial Intelligence Approach

Dr. G. Mallikarjuna Rao¹, Mandha Sandhya², B. Raja Rajeshwari², Manikanta Vangari² and E.R. Aruna³

¹Department of Civil Engineering, Chaitanya Bharathi Institute of Technology, Hyderabad, Telangana, India

²Department of Civil Engineering, Vardhaman College of Engineering, Shamshabad, Hyderabad, Telangana, India

³Department of Information Technology, Vardhaman College of Engineering, Shamshabad, Hyderabad, Telangana, India

*Correspondence to:

Dr. G. Mallikarjuna Rao
Department of Civil Engineering,
Chaitanya Bharathi Institute of Technology,
Hyderabad, Telangana, India
E-mail: mallikarjunaraog_civil@cbit.ac.in

Received: September 19, 2023

Accepted: December 01, 2023

Published: December 06, 2023

Citation: Rao GM, Sandhya M, Raja Rajeshwari B, Vangari M, Aruna ER. 2023. Prediction of Strength and Fresh Properties of Steel Fiber Reinforced Self Compacting Concrete Using Artificial Intelligence Approach. *NanoWorld J* 9(S4): S470-S476.

Copyright: © 2023 Rao et al. This is an Open Access article distributed under the terms of the Creative Commons Attribution 4.0 International License (CCBY) (<http://creativecommons.org/licenses/by/4.0/>) which permits commercial use, including reproduction, adaptation, and distribution of the article provided the original author and source are credited.

Published by United Scientific Group

Abstract

Concrete utilization is increased with the rapidly growing construction industry, compaction is the main exertion that arisen in the concrete. Self-compacting concrete (SCC) is a flowable concrete that can flow under its own weight in the congested reinforcements without any need for external vibration. As the lesser usage of aggregates leads to the decrease in stiffness of SCC which may cause the earlier formation of cracks, adding fibers increase the stiffness of SCC, and also it has a lot of consequences for finding out fresh and mechanical properties. This study mainly focuses on the application of Artificial Neural Networks (ANN) to predict the fresh and mechanical properties of steel fiber reinforced SCC. In the proposed model nine input parameters and seven output parameters are considered for modeling. For training and testing of the data along with regression analysis was performed using MATLAB using the ANN tool. It is used for the complete modeling and one hidden layer and ten neurons and 1000 epochs. The model performance was evaluated based on three metrics sets which includes correlation coefficient (R^2), root mean square error (RMSE) and mean absolute percentage error (MAPE). The obtained correlation coefficient value will be between 0.9 and 1, which implies good accuracy of prediction.

Keywords

Artificial neural network, Self-compacting concrete, Steel fibers, Regression analysis, Nanotechnology

Introduction

Concrete is a key building material that has historically proved useful all over the world. Around the world, especially in the industrial regions, there has been a significant increase in the usage of concrete. For the incorporation of nanoparticles in nanofibers, three main techniques were identified. The most commonly mentioned one is direct blending electrospinning, where the nanoparticles are encapsulated and/or entrapped in the nanofibers [1, 2]. Now, in present days there is an alternative for the usage of conventional concrete in regard to it saves time as well as better quality in both fresh and hardened states. The alternative and new construction material is SCC. SCC is one of the novel concrete varieties that has recently seen widespread use. The development of SCC, among other trends and advancements in the construction sector, offers a standard potential and attractive interest to use secondary raw materials and byproducts as mineral additives (fly ash, GGBS, metakaolin, etc.) [3-5]. SCC is also acknowledged as self-consolidated concrete which eliminates the compaction of concrete without vibration and not affecting its engineering properties. SCC was developed to reduce the cost of skilled labor, manpower and eliminates the compaction problems. SCC avoids noise pollution due to vibration by compacting itself. In addi-

[< Back](#)

ARTICLE

Experimental and analytical investigation of a model towards predicting the compressive stress–strain behavior of Graded Glass Fiber Reinforced Concrete (GGFRC) using fiber reinforcing index

Hanuma Kasagani , S. R. R. Teja Prathipati , Srikanth Koniki , C. B. K. Rao 

First published: 18 January 2024

<https://doi.org/10.1002/suco.202300055>

Citations: 1

Abstract

The stress–strain behavior of graded glass fiber reinforced concrete (GGFRC) is a crucial factor in its performance and appropriateness for diverse applications. In the present study, experimental and analytical methods were used to develop a model for the stress–strain behavior of GGFRC under uniaxial loading. The experimental program is designed to investigate the impact of mono glass fibers (3, 6, 12, and 20 mm) with varying volume fractions (0.1%–0.5%) and graded glass fibers (combinations of 3 + 6 + 12 + 20 mm) on the behavior of concrete of M50 grade. By grading glass fiber lengths in the concrete, GGFRC's pre-peak strength and post-peak deformation have increased, allowing the composite to control the various scales of cracking. A uniaxial compressive stress–strain model has been developed utilizing the fiber reinforcing index to predict the stress–strain curves of GGFRC in compression. The fiber reinforcing index, which is a measure of the quantity of fiber reinforcement in the material, is used as a variable in the current model to observe how it impacts the material's behavior. This would help evaluate the material's behavior under uniaxial compressive loading conditions and then use that data to develop a mathematical model that can predict the material's response under other conditions. Finally, it can be concluded that there is a significant correlation between the experimental results and the proposed analytical model.

CONFLICT OF INTEREST STATEMENT


The authors declare no conflicts of interest.

[Home](#) [Air Quality, Atmosphere & Health](#) [Article](#)

Exploring the association between air pollution and spontaneous abortion through systematic review and bibliometric analysis

Published: 08 January 2024

Volume 17, pages 1107–1133, (2024) [Cite this article](#)[Air Quality, Atmosphere & Health](#)[Aims and scope](#)[Submit manuscript](#)

[Priyadharshini Babu](#) , [Vaishali Verma](#), [Swapna Sarika Khadanga](#), [Shailendra Kumar Yadav](#), [Dudam Bharath Kumar](#) & [Ayushi Gupta](#)

 565 Accesses  15 Altmetric  2 Mentions [Explore all metrics](#) →

Abstract

Air pollution has been recognized as a significant environmental risk factor with potentially adverse effects on women's reproductive health. This study presents the existing literature on air pollution exposure and its link to spontaneous abortion (SAB) utilizing a systematic literature review (SLR) and bibliometric analysis (BA). Firstly, SLR was employed to collect relevant articles based on specified inclusion/exclusion criteria and formulated research questions. Secondly, BA was used to map and assess research trends, current knowledge, and

Author information

Authors and Affiliations

Centre for Disaster Mitigation and Management (CDMM), Vellore Institute of Technology, Vellore, Tamil Nadu, 632014, India

Priyadharshini Babu

Department of Biotechnology, School of Engineering and Applied Sciences, Bennett University, Greater Noida, Uttar Pradesh, 201310, India

Vaishali Verma

Centre for Biotechnology, Siksha 'O' Anusandhan, Bhubaneswar, Odisha, 751030, India

Swapna Sarika Khadanga

Babasaheb Bhimrao Ambedkar University, Vidya Vihar, Raebareli Road, Lucknow, Uttar Pradesh, 226025, India

Shailendra Kumar Yadav

Department of Civil Engineering, Chaitanya Bharathi Institute of Technology, Gandipet, Hyderabad, 500075, India

Dudam Bharath Kumar

Knowledge Resource Centre, Azim Premji University, Bengaluru, Karnataka, 562125, India

Ayushi Gupta

Contributions

All authors contributed to the study conception and design. BP performed material preparation, data collection, and analysis. BP wrote the first draft of the manuscript, and all authors commented on previous versions of the manuscript. All authors read and approved the final manuscript.

Corresponding author



OPEN

A study on waste PCB fibres reinforced concrete with and without silica fume made from electronic waste

M. Vishnu Priyan¹✉, R. Annadurai¹, George Uwadiogwu Alaneme^{2,3}✉, Durga Prasad Ravella⁴, S. Pradeepkumar⁵ & Bamidele Charles Olaiya²

This research goal is to appraise the effect of electronic waste on concrete properties by examining the mechanical properties of concrete reinforced with waste printed circuit boards (PCBs). PCB fibres, each 50 mm long, were mixed in varying proportions (1–5% by weight of cement). Silica fume (SF) was used as a 12% weight replacement for cement to conserve the properties of PCB fibre-reinforced concrete while tumbling cement consumption. Following a 28-day curing period, the fresh and hardened characteristics of PCB fibre-reinforced concrete were juxtaposed with those of conventional concrete. The experimental results led to the conclusion that 5% by weight of cement is the most effective proportion of PCB fibres to include in both PCB fibre-reinforced concrete and silica fume-modified PCB fibre-reinforced concrete. The addition of PCB fibres and silica fume significantly increased the mechanical strength of the concrete, making it suitable for high-strength concrete applications. Based on a similar investigational research design, an artificial neural network model was created, and it played a critical role in predicting the mechanical properties of the concrete. The model produced accurate results, with an R-squared (R^2) value greater than 0.99.

Electronic waste (e-waste) is a significant issue worldwide, with millions of electronic devices becoming obsolete yearly¹. Over the next ten years, India is predicted to create 500% more e-waste than it does now, according to the UN Environment Programme (UNEP). Electrical waste equipment (EWE) is being manufactured more widely because of the quick technical improvements in electronic items. This leads to the production of novel products at competitive prices. Valuable metals, man-made chemicals, and hazardous materials that present serious threats to the environment and society are stored at EWE². Advanced countries have included legal and regulatory measures that encourage resource reuse in their waste management programs. On the other hand, a number of developing countries have not made comparable progress in this area^{3–5}. In emerging economies, households inefficiently dispose of electronic waste (EWE), resulting in pollution and health hazards. The act of disposing of material waste in neighbouring fields is a common occurrence, leading to the contamination of local sediments, dirt, dust, and vegetation due to inappropriate disposal of electronic trash, resulting in the presence of dangerous substances. This electronic trash consists primarily of screens of LCD (11.9%), computers (18.8%), cell phones (21.3%), and CRT monitors (7%), which are produced by both electrical devices and electronic instruments, manufacturing firms and residents. However, only a scant 10% of this electronic waste is actually being recycled^{2–4}. The management of this trash may be achieved by implementing recycling methods using diverse technologies, or alternatively, it can be appropriately dealt with via garbage dumps or incineration processes^{5,6}. Nevertheless, inadequate methods of waste disposal and insufficient equipment have the potential to have detrimental effects on both the natural environment and human health. The act of reusing electronic garbage, often referred to as e-waste, may be described as the process of repurposing a product in a manner that deviates from its original intended design and use^{2,7}. The implementation of prolonging the product's life answers,

¹Department of Civil Engineering, SRM Institute of Science and Technology, Kattankulathur, Chengalpattu 603203, Tamil Nadu, India. ²Department of Civil, School of Engineering and Applied Sciences, Kampala International University, Kampala, Uganda. ³Department of Civil Engineering, Michael Okpara University of Agriculture, Umudike, Umudike, Nigeria. ⁴Department of Civil Engineering, Chaitanya Bharathi Institute of Technology, Hyderabad, India. ⁵Ministry of Environment, Forest and Climate Change, Government of India, New Delhi, India. ✉email: vm3188@srmist.edu.in; alanemeg@kiu.ac.ug; tinz2020@gmail.com

An Evaluation of Mechanical and Fracture Characteristics of Geopolymer Concrete Incorporating Steel Fibers.

Feroz Shaik ¹, Thunuguntla Chaitanya Srikrishna ^{2*} and Lotla Sandeep Reddy ³

¹ Department of Civil Engineering, Warangal Institute of Technology and Science, Oorugonda, Warangal, Telangana State, India.

² Department of Civil Engineering, Chaitanya Bharathi Institute of Technology (A), Gandipet, Hyderabad, Telangana State, India.

³ Department of Civil Engineering, Sreenidhi Institute of Science and Technology, Ghatkesar, Telangana State, India.

*Corresponding Author email-id : chaitanya_civil@cbit.ac.in

Abstract. The present research aims to examine the impact of steel fiber inclusion (ranging from 0% - considered as reference, 0.08%, 0.16%, 0.24%, to 0.32%) on the mechanical and fracture characteristics of notched geopolymer concrete unreinforced beams (GCUB). These beams are prepared using fly ash and GGBFS (Ground Granulated Blast Furnace Slag), and the findings are compared with those from plain cement concrete unreinforced beams. The investigation encompasses various parameters including compressive strength, bending strength, split tensile strength, fracture energy (GF), crack mouth opening displacement (CMOD), and stress intensity factor (KIC). The primary focus is to assess how the inclusion of crimped steel fibers influences the ability of geopolymer concrete to arrest cracks. The outcomes obtained from the study underscore the effectiveness of crimped steel fibers in mitigating crack propagation and averting brittle fractures within notched geopolymer concrete unreinforced beams. The results indicate notable enhancements across all fracture and mechanical parameters upon the introduction of steel fibers. This points towards the positive impact and efficiency of steel fibers in augmenting the behavior of geopolymer concrete, making it more resistant to crack propagation and brittle failure.

Keywords: Geopolymer concrete; Steel fiber; Mechanical properties; Fracture energy; CMOD

1. Introduction

Concrete, a widely employed synthetic material globally, has manufacturing processes that lead to significant carbon dioxide emissions and depletion of natural resources [1]. The present global challenge revolves around environmental deterioration, with greenhouse gases serving as major contributors to this issue. Carbon dioxide-based gases, contributing to over 75% of global warming agents, pose a significant concern. Notably, the cement and concrete sectors account for nearly 8% of total carbon dioxide emissions [10,14].

To foster a more sustainable environment, the utilization of alternative cementitious materials is crucial. Opting for geological-origin materials or industrial byproducts as substitutes for cement can mitigate its adverse binding impacts [7]. An effective approach involves the utilization of alkaline activator solutions to enhance binding properties. Geopolymer concrete (GPC), formed from geological materials or activated industrial waste through alkaline solutions like sodium or potassium hydroxide and silicate solutions, offers a viable alternative [9,11,12].



Investigations on Strength and Durability Properties of Recycle Aggregate and Fly Ash in Concrete

Lotla Sandeep Reddy¹, Thunuguntla Chaitanya Srikrishna^{2*} and G.V.Praveen¹

¹Department of Civil Engineering, Sreenidhi Institute of Science and Technology, Ghatkesar, Telangana State, India.

² Department of Civil Engineering, Chaitanya Bharathi Institute of Technology (A), Gandipet, Hyderabad, Telangana State, India.

*Corresponding Author email-id : chaitanya_civil@cbit.ac.in

Abstract. In this investigation study the Natural Coarse Aggregate (NCA) were put back with Recycled Coarse Aggregate (RCA) at peculiar proportions, the mechanical performance and durability properties of concrete are examined. The inclusion of fly ash (FA) is also introduced as stand-in of Cement. The present investigation aims to determine the effect of RCA as an stand-in material to NCA and to analyze the fresh properties like workability, density and hardened properties like Compressive Strength, Flexure Strength, Split Tensile Strength and durability properties like Water permeability and Sorptivity. Mix is formulated for water cement ratio 0.40. The specimens were casted of replacing virgin aggregate with RCA by 10% and 20%, and cement with FA by 10%, 20% and 30%. All the specimens are cured for 7 and 28 days as per requirement later they are tested. The acquired data are then compared between the strength of NCA of concrete and the proportion of RCA and FA. The outcome view is in such a way that the workability of concrete will decline as the replacement of RCA increases, by which it should limited to a fixed percentage (10% or 20%). The density of concrete is not altered by the put back of FA, but raise in percentage of RCA replacement could alter the density of concrete. In case of Compressive, Flexure and Split tensile strength of concrete the optimum strength obtained for 10% FA and 10% RCA for 7 and 28 days was similar to that of 100% NCA and 0% FA and durability studies also gave the optimum results for the same replacement.

Keywords: Recycled Coarse Aggregate; FlyAsh; Mechanical properties; Sorptivity.

1. Introduction

Concrete is the primeutilized civil engineering building material. The main components which are required to produce the concrete are fine aggregate, coarse aggregate, cement, and water. It is employed in a wide range of civil engineering projects, including infrastructure, low and high-rise buildings, defense structures, and environmental protection structures. Concrete production necessitates the use of components such as cement, aggregates, and water. The term "sustainable" is becoming increasingly popular around the world[3]. Construction that is environmentally friendly, a fast remedy can have a direct impact on improving community livelihood problems.

The way to this aim requires first and foremost minimizing the environmental impact of concrete manufacture by substituting recycled mineral resources for virgin mineral materials, as well as lowering global CO₂ emissions. [4,5]. Recycling is the process of converting discarded materials into new products. The approach utilized here comprises a significant substitution of NCA for RCA



RESEARCH ARTICLE | SEPTEMBER 05 2023

Experimental investigation on durability aspects of hybrid fibre reinforced concrete under marine conditions

Daida Veronica Priyadharshini; G. V. V. Satyanarayana;
N. Ravi Dakshina Murthy 

+ Author & Article Information

AIP Conf. Proc. 2754, 150009 (2023)

<https://doi.org/10.1063/5.0167071>

The present paper aims to find the strength and durability properties of hybrid fiber reinforced concrete under marine conditions, and to investigate the effect of hybridization of fibres on properties of concrete. where the fibers to be used are steel fiber and polypropylene fiber and to find the proper corrosion less hybrid fiber reinforced concrete by adding the chemical admixture i.e CHYRSCO OPTIMA 9313 and MICRO SILICA to produce a moderate water reduction, better flow and retention of HYRC. Water to cement ratio increases there is a chance of high extend of having concrete permiability, so in this investigation water to cement ratio is about 0.38 % only. The literature study reveals that there is very little literature on the durability aspects of marine conditions on hybrid fibers reinforced concrete hence lot of research is to be done. Present experimental investigation is done up to M40 grade concrete mix design. The compressive strength is one of the most important features of concrete, Compressive strength was investigated, the mix design also affected the water-cement ratio The planned technique allows the designer to estimate characteristics such as compressive strength and workability of the concrete

Topics

 Your destination

Search

Book

x

RESEARCH ARTICLE | SEPTEMBER 05 2023

Design and analysis of multi-story building having visco-elastic dampers

J. Rohith Kumar; G. V. V. Satyanarayana; N. Ravi Dakshina Murthy [+ Author & Article Information](#)

AIP Conf. Proc. 2754, 040001 (2023)

<https://doi.org/10.1063/5.0167069>

As a result of urbanization, high rise structures with subversive parking and storage levels are becoming increasingly common. Seismic energy dissipation systems are presently used for a wide range of structures all around the world. Basements that are difficult to clean. The primary purpose is to evaluate the situation. The efficacy of horizontal dampers in the ground level of a high rise building on top of a basement. One of the various types of dampers available is visco-elastic dampers (VE). Dampers are used in this Equivalent static & Response spectrum analysis. An attempt has been made to determine the variance in natural period by integrating energy dissipation devices and comparing different models.

Topics

[Spectroscopy](#)

REFERENCES

1. Nasab, M. S. E., Javidan, M. M., Chun, S., & Kim, J. (2021, December). Experimental study on seismic retrofit of a RC frame using viscoelastic dampers. *In Structures* (Vol. 34, pp. 771–786). <https://doi.org/10.1016/j.istruc.2021.08.044>
[Google Scholar](#) [Crossref](#)
2. Dadkhah, E., Shiri, B., Ghaffarzadeh, H., & Baleanu, D. (2020). Visco-elastic dampers in structural buildings and

Kinaxis

 **A Leader**

x

RESEARCH ARTICLE | SEPTEMBER 05 2023

Experimental investigation on mix proportions of foam concrete to fix ingredients in low and medium densities



Pandrala Sanjana; G. V. V. Satyanarayana; N. Ravi Dakshina Murthy

[+ Author & Article Information](#)*AIP Conf. Proc.* 2754, 150007 (2023)<https://doi.org/10.1063/5.0167070>

Concrete is a building material that cannot be avoided in the construction business. Massive constructions need a significant volume of concrete and substantial foundations. By substituting normal-weight concrete with light, durable, environmentally friendly, and sustainable concrete, the structure's self-weight may be reduced. Foam concrete is a material that can meet all of the following criteria. Cement, fly ash, and foaming agent are all ingredients in foamed concrete, which is a cement-based slurry that has been physically blended with a stable and uniform foam. This research investigates the target densities of foamed concrete (FC). The purpose of this investigation is to assess foamed concrete of low and medium densities.

Topics

[Cement](#), [Surfactants](#)

REFERENCES

1. P. Gayatri and Satyanarayana G. V. V "Foam Concrete for Load Bearing Structures and Its Properties" 2021, *AIP Conference Proceedings*, Vol. 2358, No. 1, pp. 1–10.

[Google Scholar](#)

2. Akinkurolere, O.O., et al. "Water Absorption, Sorptivity and Permeability Properties of Concrete Containing Chemical and

Discharge estimation in a compound channel with converging and diverging floodplains using ANN-PSO and MARS

Divyanshu Shekhar^a, Bhabani Shankar Das^{ib a,*}, Kamalini Devi^{ib b}, Jnana Ranjan Khuntia^{ib d} and Tapas Karmaker^c

^a Department of Civil Engineering, National Institute of Technology, Patna 800005, India

^b Department of Civil Engineering, Chaitanya Bharathi Institute of Technology, Hyderabad, India

^c Department of Civil Engineering, Thapar Institute of Engineering and Technology, Patiala 147004, India

*Corresponding author. E-mail: bsd.nitrkl@gmail.com

 BSD, 0000-0003-1140-0432; KD, 0000-0002-5916-3256; JRK, 0000-0003-3943-4220

ABSTRACT

The discharge estimation in rivers is crucial in implementing flood management techniques and essential flood defence and drainage systems. During the normal flood season, water flows solely in the main channel. During a flood, rivers comprise a main channel and floodplains, collectively called a compound channel. Computing the discharge is challenging in non-prismatic compound channels where the floodplains converge or diverge in a longitudinal direction. Various soft computing techniques have nowadays become popular in the field of water resource engineering to solve these complex problems. This paper uses a hybrid soft computing technique – artificial neural network and particle swarm optimization (ANN-PSO) and multivariate adaptive regression splines (MARS) to model the discharge in non-prismatic compound open channels. The analysis considers nine non-dimensional parameters – bed slope, relative flow depth, relative longitudinal distance, hydraulic radius ratio, angle of convergence or divergence, flow aspect ratio, relative friction factor, and area ratio – as influencing factors. A gamma test is carried out to determine the optimal combination of input variables. The developed MARS model has produced satisfactory results, with a mean absolute percentage error (MAPE) of less than 7% and an R^2 value of more than 0.90.

Key words: ANN-PSO, gamma test, MARS, non-prismatic compound channel

HIGHLIGHTS

- Using traditional methods to estimate discharge in non-prismatic compound channels provides unsatisfactory results.
- Discharge is estimated in non-prismatic compound channels using two soft computing techniques ANN-PSO and MARS.
- Influencing parameters for the prediction of discharge are identified using the Gamma test.
- Different model performances have been carried out for different ranges of width ratio and relative flow depth.

NOMENCLATURE

Q_{fp}	discharges carried by the floodplain.
Q	measured discharge
Q_{mc}	discharges carried by the main channel
R_{fp}	hydraulic radius of the floodplain
R_{mc}	hydraulic radius of the main channel
S_0	bed slope of the channel
n	Manning's roughness coefficient
H	total flow depth over the main channel
h	bankfull depth of the main channel
P	wetted perimeter
R	hydraulic radius
A	area of the compound channel
f_r	relative friction factor
A_r	area ratio

This is an Open Access article distributed under the terms of the Creative Commons Attribution Licence (CC BY-NC-ND 4.0), which permits copying and redistribution for non-commercial purposes with no derivatives, provided the original work is properly cited (<http://creativecommons.org/licenses/by-nc-nd/4.0/>).

Turbulence modelling for depth-averaged velocity and boundary shear stress of a dense rigid grass bed open channel

Sarjati Sahoo ^{a,*}, Jnana Ranjan Khuntia ^b, Kamalini Devi ^b, B. Sree Sai Prasad^c and Kishanjit Kumar Khatua ^a

^a Department of Civil Engineering, National Institute of Technology, Rourkela, Odisha, India

^b Department of Civil Engineering, Chaitanya Bharathi Institute of Technology, Hyderabad, Telangana, India

^c Department of Civil Engineering, Indian Institute of Technology, Madras, Chennai, Tamilnadu, India

*Corresponding author. E-mail: sarjati.sahoo1991@gmail.com

 SS, 0009-0001-0005-3941; JRK, 0000-0003-3943-4220; KD, 0000-0002-5916-3256; KKK, 0000-0002-8843-211X

ABSTRACT

The present research focusses on a comparison of experimental and numerical approaches for flow over fixed artificial rigid grass bed channels. Various flow parameters like longitudinal velocity, depth-averaged velocity (DAV), boundary shear stress (BSS) and secondary current are analysed and compared with seven numerical models: standard, realizable and renormalization group (RNG) $k-\epsilon$ models and standard, shear stress transport (SST), generalized $k-\omega$ (GEKO) and Baseline (BSL) $k-\omega$ models. To evaluate the strength of the seven applied models, the error analysis has been performed. It is found that the RNG $k-\epsilon$ and SST $k-\omega$ models provided better results for both the DAV and BSS prediction, but the RNG $k-\epsilon$ model is found to be the most suitable for predicting the DAV and the SST $k-\omega$ model for BSS as compared to the other models. For the longitudinal velocity profiles, both the RNG $k-\epsilon$ and SST $k-\omega$ models are found to provide good agreement with experimental results at the centre of the channel, whereas the SST $k-\omega$ model is more accurate near the wall. Overall, the SST $k-\omega$ model has predicted the results with good accuracy for all the flow parameters considered in the present study.

Key words: ANSYS Fluent, experimental results, grass bed, $k-\epsilon$ and $k-\omega$ models, statistical error analysis

HIGHLIGHTS

- A comparative study of all the seven sub-models pertaining to the $k-\omega$ and $k-\epsilon$ groups was performed.
- DAV and BSS profiles are presented using the discussed turbulence models, CES and compared with the experimental results.
- Statistical error analysis is performed.
- The RNG $k-\epsilon$ model estimated the depth-averaged velocity more accurately, whereas the SST $k-\omega$ model is found to be more accurate in predicting the boundary shear stress.

1. INTRODUCTION

Hydraulic structures in open channels necessitate a thorough understanding of flow characteristics to ensure proper design. Parameters such as mean flow pattern, depth-averaged velocity (DAV) distribution, secondary flow properties, boundary shear stress (BSS), turbulent characteristics and conveyance capacity play a crucial role during the design process. In the study of turbulent flows in open channels, hydraulic engineers often rely on experimental and numerical investigations to understand the various flow components (Guo & Julien 2003; Yang *et al.* 2004; Sahu *et al.* 2014; Devi & Khatua (2016); Khuntia *et al.* (2018a,b); Tajnesaie *et al.* 2020; Khuntia *et al.* (2021); Devi *et al.* (2021); Qasim *et al.* 2022). Various research has been carried out on the flow and turbulent structure and it influences the riverine habitat (Bornette & Puijalon 2011), water quality (Dosskey *et al.* 2010), soil erosion and stability (El Bouanani *et al.* 2022; Ikhsan *et al.* 2022) and river planform disorderness (Nandi *et al.* 2022a).

With the advancement of computational techniques, numerical methods have become valuable tools for solving complex hydraulic engineering problems. Even with sophisticated turbulence models, accurately predicting turbulent structures and BSS in free surface flows remains a difficult task (Shnipov 1989; Yang *et al.* 2004; Yang & Lim 2005; Guo & Julien

This is an Open Access article distributed under the terms of the Creative Commons Attribution Licence (CC BY-NC-ND 4.0), which permits copying and redistribution for non-commercial purposes with no derivatives, provided the original work is properly cited (<http://creativecommons.org/licenses/by-nc-nd/4.0/>).